Characterization and Testing of Nanofluid Cooling Technology for Electronic Systems

Xue Zhengjun

NATIONAL UNIVERSITY OF SINGAPORE

2005

Characterization and Testing of Nanofluid Cooling Technology for Electronic Systems

Xue Zhengjun

(B. Eng, Shanghai Jiao Tong University)

A THESIS SUBMITTED

FOR THE DEGREE OF MASTER OF ENGINEERING

DEPARTMENT OF MECHANICAL ENGINEERING

NATIONAL UNIVERSITY OF SINGAPORE

2005

Name: Xue Zhengjun

Degree: Master of Engineering

Dept: Mechanical Engineering

Thesis Title: Characterization and Testing of Nanofluid Cooling Technology for Electronic Systems

Abstract

A Nanofluid is an innovative type of highly efficient heat transfer fluid, which was made by dispersing nanometer-sized metallic or non-metallic particles in various base fluids. With their superior thermal properties, nanofluids are expected to be a promising coolant candidate for thermal management systems of next generation high heat dissipation electronic systems.

In this research, one apparatus for thermal conductivity measurement using the steady-state parallel-plate method was fabricated. Nanofluids with different nanoparticle-base fluid combinations and different nanoparticle volumetric fractions were calibrated.

A microchannel heat sink (MCHS) liquid cooling test rig was used to investigate the thermal performance improvement of nanofluid-cooled liquid cooling systems. The thermal performance of the MCHS cooling system was measured and calculated in terms of junction-to-inlet and heatsink base-to-inlet thermal resistances. Thermal resistances and pressure drop across the MCHS with different working fluids under different flowrates ranging from 0.1 L/min to 0.8 L/min were measured and compared. Moreover, numerical simulations were conducted to evaluate the convective heat transfer enhancement of nanofluids within and beyond the range of the current experiments.

Keywords: Nanofluid, Thermal Conductivity, Microchannel Heat Sink, Thermal Contact Resistance, Electronics Cooling

Acknowledgements

First and foremost, the author would like to express his sincere appreciation and gratitude to his supervisors, Prof. Andrew Tay A. O. and Dr. Zhang Hengyun, for their invaluable guidance, suggestions and encouragement throughout the course of his candidature.

Also, the author would like to extend his thanks to the laboratory technologists of Nano/Microsystems Integration Laboratory and Thermal Process Laboratory 1 & 2 for their full support and great assistance in experiment preparation throughout the duration of this project.

Special thanks to his laboratory colleagues and friends for their kind help and enlightening advice during the two years' study and experimentation at NUS.

Last but not least, the author wants to express his deepest appreciation to his family members and girlfriend for their immense support, love and encouragement.

Table of Contents

Summary

Great advances of today's leading edge high performance and multi-functional electronic devices have led to great challenges in thermal management. Although various enhanced heat transfer mechanisms were introduced to meet the stringent requirements of electronic cooling systems, the poor thermal properties of conventional heat transfer fluid become one of the main constraints. The great development of emerging nanotechnology in nanopowder preparation process enabled us to disperse nanometer-sized particles in traditional heat transfer fluids to form an innovative type of heat transfer fluid, which was called nanofluid. With its remarkably high thermal conductivity, nanofluid was expected to be a promising candidate as the working medium for thermal management systems of next generation high heat flux electronic systems. This research intended to characterize the thermal conductivity of nanofluids and test the thermal performance improvement of liquid cooling system induced by the application of nanofluids.

One apparatus for thermal conductivity measurement using steady-state parallel-plate method was fabricated. Nanofluids with different nanoparticles-base fluid combination and different nanoparticles volumetric fractions were calibrated. Effective thermal conductivity values predicted by different theoretical models were compared with the obtained experiment results. Various mechanisms contributed to the significant increase in thermal conductivity of nanofluids were also discussed.

A microchannel heat sink (MCHS) liquid cooling test rig was used to investigate the thermal performance improvement of liquid cooling system utilizing nanofluids. Thermal performance of the nanofluid-cooled MCHS system was measured and calculated in terms of chip junction-to-heatsink inlet and heat sink base-to-heat sink inlet thermal resistances. Thermal resistances and pressure drop penalty across the MCHS with different working fluid under different flowrates ranging from 0.1L/min to 0.8/min were measured and compared. Numerical simulations of the MCHS liquid cooling system using commercial software (FLUENT) was conducted to evaluate the convective heat transfer enhancement of nanofluids within and out of current experiment range.

Extensive experiment and simulation results in this study strongly indicated the potential of nanofluids as a superior working media. Further, the nanofluid-cooled MCHS liquid cooling system was proved to be feasible and efficient for thermal management of high heat dissipation electronic systems.

Thesis Advisors:

1. Dr. Andrew A.O. Tay, Professor, Department of Mechanical Engineering, National University of Singapore.
2. Dr. Zhang Hengyun, Senior Research Engineer, Institute of Microelectronics.

List of Tables

List of Figures

Nomenclatures

Symbols

A	Surface area of upper plate, m^2
A_{ch}	Channel cross section area, m^2
A_h	Surface area of lower surface of hot plate, m^2
A_s	Surface area of spacers, m^2
b	Channel height, m
c_p	Specific heat at constant pressure, J/kg K
c_{pnf}	Specific heat of nanofluid at constant pressure, J/kg K
c_{pp}	Specific heat of particle at constant pressure, J/kg K
D_h	Hydraulic diameter, m
e	Relative uncertainty
e_k	Relative uncertainty of thermal conductivity
e_R	Relative uncertainty of thermal resistance
f_{app}	Apparent friction factor
h	Local heat transfer coefficient, $W/(m^2\text{-}^0C)$
H	Mean curvature
k_{eff}	Effective thermal conductivity, W/m-K
k'_{eff}	Thermal conductivity, W/m-K
k_l	Thermal conductivity of liquid, W/m K
k_{layer}	Thermal conductivity of liquid nanolayer, W/m-K
k_p	Thermal conductivity of particle, W/m-K

k_{pe}	Equivalent thermal conductivity of solid particle-liquid nanolayer structure, W/m-K
k_s	Thermal conductivity of spacer, W/m K
n	Empirical shape factor, $n = 3/\psi$
Nu	Nusselt number
p	Pressure, Pa
$\dot{q}$	Heat flux, W/m^2
Q	Heating power, W/m^2
r	Diameter of solid particle, m
R_{bi}	Inlet-to-heat sink base thermal resistance, ^{0}C/W
R_{bulk}	Coolant bulk thermal resistance resistance, ^{0}C/W
R_c	Contact thermal resistance, ^{0}C/W
$R_{heat\sin k}$	Thermal resistance of heat sink, ^{0}C/W
R_{jb}	Junction-to-heat sink base thermal resistance, ^{0}C/W
R_{ji}	Junction-to-inlet thermal resistance, ^{0}C/W
R_{jr}	Junction-to-reservoir thermal resistance, ^{0}C/W
R_{si}	Thermal test chip conductive thermal resistance, ^{0}C/W
R_{spr}	Thermal spreading resistance, ^{0}C/W
R_{cond}	Conduction thermal resistance, ^{0}C/W
R_{conv}	Convection thermal resistance, ^{0}C/W
R_{constr}	Constriction thermal resistance, ^{0}C/W
Re	Reynolds number

Re_i	Reynolds number at heat sink inlet
Re_o	Reynolds number at heat sink outlet
T	Temperature, ^{0}C
T_a	Ambient temperature, ^{0}C
T_h	Mean temperature of lower hot plate surface, ^{0}C
T_i	Temperature of the liquid at MCHS inlet port, ^{0}C
T_j	Thermal test chip junction temperature, ^{0}C
T_l	Mean temperature of upper cold plate surface, ^{0}C
T_r	Temperature of reservoir, ^{0}C
T_{ref}	Reference temperature, ^{0}C
w_{ch}	Channel width, m
w_w	Channel wall width, m
X	Axial distance along the channel, m
X^+	Dimensionless axial distance along the channel, $X/(\mathrm{Re}\,D_h)$

Greek Symbols

α	Channel aspect ratio, w_{ch}/b
β	Ratio of the liquid nanolayer thickness to nanoparticle radius, h/r
γ	Thermal conductivity ratio, k_{layer}/k_l
δ	Spacer thickness/distance between plates, m
δR	Overall uncertainty
μ	Dynamic viscosity of liquid, kg/m-s
μ_l	Dynamic viscosity of liquid, kg/m-s

μ_{nf}	Dynamic viscosity of nanofluid, kg/m-s
υ	Kinetic viscosity, m^2/s
ρ	Density, kg/m^3
σ	Surface tension, N/m
ϕ	Volumetric fraction, vol%
ψ	Sphericity, surface area/volume
ω	Angular velocity, rad/s

Subscripts

ch	Channel
f	Fluid
g	Gas
nf	Nanofluid
p	Particle
lam	Laminar
turb	Turbulent

CHARPTER 1: INTRODUCTION

1.1 Project Background

Since the first transistor was invented in 1947 and the first integrated circuit (IC) was developed independently twelve years later, the development of IC technology has largely kept pace with Moore's Law during the last four decades, with performance doubling roughly every 18 months. The ever-increasing demand for high performance, multifunctional and miniaturized IC devices has led to an exponential increase in transistor density, clock speed and, hence, a tremendous increase in the heat flux dissipated. Thermal management has increasingly become one of the main constraints in the development of leading edge highly integrated electronic devices and systems.

As the latest International Technology Roadmap for Semiconductors predicts (ITRS, 2003), cooling levels of next generation high performance electronic components such as processors, CMOS and Bipolar devices are projected to reach the 100~150W range and the dissipated heat flux may approach 100W/cm^2 in the near future. In the other hand, compared with the high heat dissipation, the upper junction temperature limit of most cost-performance and high-performance electronic components is lower than 100^{o}C (NEMI, 2002). Highly elevated junction temperatures and the associated thermal environment could lead to overheating, reducing component performance and drastic acceleration in failure rate, which was probably caused by thermally-induced mechanical creep in bonding materials, parasitic chemical reactions and dopant diffusion etc. It has been well documented that the failure rate of a silicon chip could be doubled for every 10^{o}C to 20^{o}C increase in junction temperature (Tummala, 2001). Therefore, providing high performance cooling solutions to sustain high heat flux and simultaneously maintain components working temperature within tolerable range has

become one of the biggest challenges in the thermal management of electronic systems.

In view of the great challenges in thermal management, various conventional and enhanced thermal management strategies have been introduced to meet the stringent cooling requirements of state-of-the-art IC devices. As it can be seen in Figure 1.1, different cooling techniques can be used to remove heat from chips but each technique and coolant leads to a distinct variation of the chip-to-fluid temperature difference with heat flux. At a typical allowable temperature difference of 60^{o}C, the combined free convection and radiation cooling of air is effective only at heat fluxes below 0.05W/cm^2 and forced convection cooling in air is unlikely to provide a heat removal capability in excess of 1W/cm^2. Consequently, large heat sinks are widely adopted to facilitate the dissipation of high heat fluxes from component surfaces. However, with the constraints in dimension, spreading resistance and low air-side heat transfer coefficient, the heat rejection limit of traditional fan-heatsink air cooling system can only go up to 50W/cm^2 (Saini and Webb, 2002). As shown in Figure 1.2, for electronic components with heat flux approaching or exceeding 10W/cm^2, attention should be turned to various direct and indirect liquid cooling strategies with or without phase change. For electronic components with extremely high heat flux which may be beyond 50W/cm^2, advanced cooling mechanisms such as pool boiling, jet impingement, spray cooling and microchannel heat sink have been proposed.

One major constraint in electronic cooling is the inherently poor thermal performance of conventional heat transfer fluids. Although various enhanced cooling strategies have been introduced, the poor thermal properties, especially the low thermal conductivity, of traditional coolants significantly limit the efficiency of heat removal mechanisms.

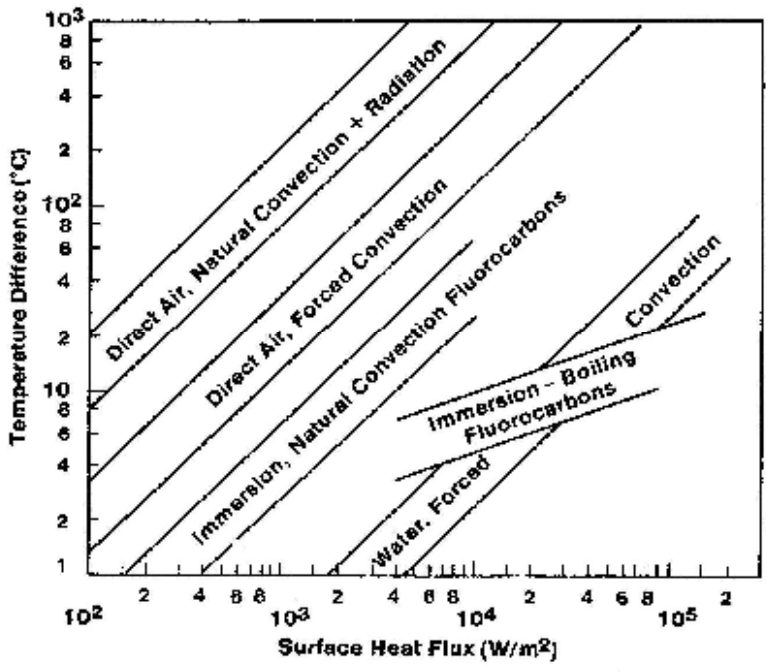

Figure 1.1: Temperature differences attainable as a function of heat flux for various heat transfer modes and coolants (Tummala et al., 1996-1997).

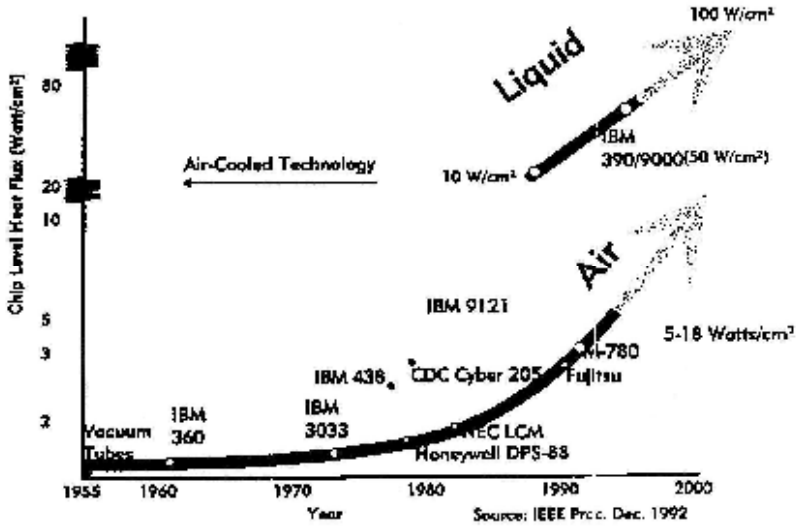

Figure 1.2: Evolution of air/liquid cooling capabilities (Tummala et al., 1996-1997).

Conventional heat transfer fluids have very low thermal conductivity especially when compared to most solids. As can be seen in Table 1.1, even for a good coolant such as water, its thermal conductivity is only around 0.62 W/m-K at room temperature and

1atm, which is at least one order of magnitude lower than solids. The thermal conductivity of copper at room temperature is about 700 times greater than that of water and about 3000 times higher than that of engine oil. The thermal conductivity of multi-walled carbon nanotubes at room temperature is about 20,000 times greater than that of engine oil. Thus, there is an urgent need for new and innovative heat transfer media to facilitate ultra high-performance cooling.

Table 1.1: Comparison of thermal conductivity values for representative solids and liquids at room temperature and 1atm.

Material		**Thermal Conductivity (W/m-K)**
Metallic Solids	Silver	429
	Copper	401
	Aluminum	237
Nonmetallic Solids	Diamond	3300
	Carbon nanotubes	3000
	Silicon	148
	Silicon Carbide	270
	Alumina (Al_2O_3)	40
Metallic Liquids	Mercury	9.05
Nonmetallic Liquids	Water	0.613
	Ethylene Glycol	0.253
	Engine Oil	0.145
	FC-77	0.057

Breakthroughs of today's cutting edge nanotechnology in nanopowder preparation and processing has enabled us to disperse nanometer-sized particles in usual heat transfer fluids such as water, engine oil and ethylene glycol to form an innovative class of high thermal conductivity fluids called nanofluids. The concept of nanofluids was first materialized by series of research works at Argonne National Laboratory, U.S.A. and probably S. U. S. Choi was the first one to call such suspensions "nanofluids", which is a description now.

It has long been recognized that suspensions of solid particles in liquids have great potential to become high efficient coolants. The key idea is to exploit the very high thermal conductivity of solid particles. In this context, numerous theoretical and experimental studies of the effective thermal conductivity of solid particle suspensions have been conducted since Maxwell's theoretical work was published more than 100 years ago (Maxwell, 1881). However, the vast majority of these studies have been confined to suspensions with millimeter- or micro-sized particles (Ahuja, 1975). Although such suspensions do indeed display the desired increase in thermal conductivity, they suffer from stability and rheological problems. In particular, the particles tend to quickly settle out of suspension, thereby causing severe clogging, especially in mini and microchannels. Further, the abrasive action of the particles may also cause erosion of components and considerable increase in pressure drop across passages.

The above bottleneck of slurries with micro or bigger size particles can be eliminated by utilizing particles of nanometer dimensions. Benefiting from the emerging nanotechnology, the mean diameter of nanoparticles suspended in nanofluids typically can be controlled within 100nm. Because of their ultra-fine size and large surface area-to-volume ratio, nanoparticles can be suspended in a base liquid uniformly and stably under the influence of several agitation forces, such as the Brownian force and the London-Van Der Waals force. Moreover, suspensions containing very low fraction of nanometer-sized particles, which was normally less than 5% volume, exhibited significant enhancement in effective thermal conductivity. For example, enhancements were recently reported for copper nanofluids, where just a 0.3% volume fraction of 10nm diameter copper nanoparticles led to an increase of up to 40% in the effective thermal conductivity of ethylene glycol (Eastman et al., 2001). Another

important issue is that with the small amount of nanoparticles added, the increase in viscosity of nanofluids is relatively low, leading to minor pressure drop penalty.

The remarkably high thermal conductivity can be attributed to several factors such as nanoparticles clustering, ballistic phonon transport, layering at the solid/liquid interface, the interaction and collision among particles and surface area enhancement. In addition, the suspended particles increase the surface area and heat capacity of the fluid. A significant improvement in the effective thermal conductivity is achieved as a result of decreasing the size of the suspended particles rather than using larger particles.

With all of the merits mentioned above, nanofluids are expected to be superior cooling media for thermal management of high heat flux electronic systems. Hence, extensive further research in this area is very important and desirable.

1.2 Motivation for the Work

Such unique thermal and flow properties of nanofluids stimulated more and more investigations on the mechanism of energy transport enhancement. Especially, with their remarkably high thermal conductivity, nanofluids were expected to be a promising candidate as the working medium for thermal management systems of next generation high heat flux electronic systems.

However, although various theoretical and experimental studies on the thermal conductivity enhancement of nanofluids are available in the literature, there is no theoretical model available that can predict the thermal conductivities of nanofluids accurately till now. Moreover, improvements in thermal performance of nanofluid-cooled systems have been rarely reported. In particular, the application of nanofluids

in micro-channel cooling system has never been published before.

Research on heat transfer application of nanofluids is still in its infancy. It is essential to pay more research effort in this area to develop a systematic understanding of the remarkable thermal transport properties of nanofluids.

1.3 Objectives of the Work

The current study is a collaborative project of the Department of Mechanical Engineering at National University of Singapore and the Microsystems, Modules & Components (MMC) department at Institute of Microelectronics, Singapore. It aims to study the feasibility and performance enhancement of nanofluid-cooled system as well as to characterize the thermal conductivity of nanofluids. It is an effort to advance the research towards thermal management of high heat flux electronic devices.

The thermal conductivity of various combinations of nanoparticles and base fluids at low volume fractions will be investigate experimentally using a steady-state parallel-plate apparatus. Various theoretical models will be evaluated using the experimental results obtained.

The convective heat transfer of nanofluids was characterized using a microchannel heat sink liquid cooling system. The thermal performance parameter used is the thermal resistance. Numerical simulation using commercial CFD software (FLUENT) will be extensively utilized to predict the thermal performance of different kinds of nanofluids within or beyond our current experimental range.

1.4 Organization of the Thesis

Chapter 1 provides a brief introduction to the thermal management of IC packages and the thermal management challenges in cooling next generation high heat dissipation IC devices. Nanofluid cooling technology is also briefly introduced. Motivation and objectives of the work are addressed.

Chapter 2 gives a review of the literature related to our current project. Various nanofluid synthesis methods, thermal conductivity measurement methodologies, experimental results as well as theories for predicting thermal conductivities of nanofluids are introduced. The mechanisms of thermal conductivity enhancement of nanofluids are also discussed. The theoretical models, numerical and experimental results in natural convection and forced convective heat transfer are summarized.

In Chapter 3 the experimental setup and procedures for measuring the thermal conductivity of nanofluids are described. Experimental results are compared with the values predicted by various theoretical models. Experiment errors are also examined.

The experimental setup, procedures and thermal performance of nanofluid-cooled microchannel heat sink systems are presented in Chapter 4.

Chapter 5 illustrates the numerical simulation of the thermal performance of microchannel heat sinks utilizing different nanofluids within and beyond the current experimental range.

Chapter 6 gives a summary of the main conclusions of this study. Suggestions for future research work are also given.

CHAPTER 2: LITERATURE REVIEW

2.1 Nanofluids Synthesis Techniques

2.1.1 Introduction

Preparation of nanofluids is the first key step in the application of nanofluid cooling technology. Reliable techniques for creating uniformly dispersed and long-time stable nanofluids are crucial to the success of all the applications. Also, in order to investigate the thermal properties and heat transfer characteristics of nanofluids, we should first possess robust preparation techniques.

The range of potentially useful combinations of nanoparticles and base fluids is enormous. Various nanoparticles of oxides, nitrides, metals, metal carbides, nonmetals and nanotubes can be dispersed into different base fluids such as water, ethylene glycol and engineering oils to form innovative nanofluids. Each application may have its most appropriate nanoparticle-fluid combination. Researchers have developed different synthesis techniques for nanoparticle production and dispersion, which can be generally divided into two categories, namely “single-step” method and “two-step” method (Eastman et al., 2004). Each method of nanofluid preparation has its own specific application area, advantages and limitations.

The process of synthesizing nanofluids should ensure proper nanoparticle size, dispersion uniformity, physical and chemical stability, and low particle agglomeration. To create a nanofluid the particles should be made small enough to be suspended by Brownian motion and be protected against aggregation. Although Brownian motions are intrinsically dispersive and in the absence of aggregative effects should produce diffusion of nanoparticles along lines suggested by the miscible liquids analogy, in

fact aggregations are particularly severe at volume fractions over 20% (Goldstein et al., 2000). Techniques for suppressing aggregation are greatly desirable.

Fortunately lots of effective auxiliary techniques such as controlling suspension pH values, electric charges, protective coatings, surface activate agents and long-duration ultrasonic vibrations are able to achieve and maintain the stability of nanofluids against sedimentation. Although all these techniques aim at changing the formation of particle clusters in order to obtain stable suspensions, how these techniques are used depends upon the particular application. The most common method is to add activators and dispersants, which are normally thiols, oleic acid and laurate salts (Xuan and Li, 2000). Selection of the suitable activators and dispersants mainly depends on the properties of the specific particle-liquid combination.

2.1.2 Two-step Method

The so called two-step method employs a two-step process to make nanofluids in which nanoparticles are first produced as a dry powder and the as-prepared nanoparticles are then dispersed into a base fluid in a second processing step.

Many processes have been developed recently to produce nanocrystalline materials. Current nanophase technology can produce large quantities of nanopowders with average particle sizes in the 10~100nm range. One typical nanopowder synthesis method is the inert gas–condensation (Granqvist et al., 1976), which involves the vaporization of a source material in a vacuum chamber and subsequent condensation of the vapor into nanoparticles via collisions with a controlled pressure of an inert gas such as helium. Ashly (1994) developed a chemistry-based solution-spray conversion process that started with water-soluble salts of the source materials. The solution is then turned into an aerosol and dried by a spray-drying system. Rapid vaporization of

the solvent and rapid precipitation of the solute keeps the composition identical to that of the starting solution. The precursor powder is then placed in a fluidized-bed reactor to evenly pyrolyze the mixture, drive off volatile constituents, and yield porous powders with a uniform homogeneous fine structure. The electrohydrodynamic spraying system, or called electrospray, operated in the cone-jet mode was first proposed by Chen et al. (1995) to produce monodispersed nanoparticles from a solution of desirable solute materials or colloidal suspensions. Airborne nanoparticles in the size range of 2~100nm can be generated with a production rate of up to 10 billion particles per second using this method. A fourth technique is to generate nanophase materials by condensation of metal vapors during rapid expansion in a supersonic nozzle. This method was first proposed by Hill et al. (1963) and later developed by Andres et al. (1981) and Brown et al. (1992).

Although a certain degree of agglomeration may occur in the nanoparticle preparation, storage and dispersion processes, it is well known that these agglomerates require very little energy to break up into smaller constituents. And thus it is possible that even agglomerated nanocrystalline powders can be successfully dispersed into fluids and result in good properties. This two-step process works well in many cases, especially for oxide and nonmetallic nanoparticles, which can be successfully dispersed in deionized water and ethylene glycol (Lee et al., 1999). Less success has been achieved when producing nanofluids containing high conductivity metallic nanoparticles by this technique (Eastman et al., 1997). Extra addition of surface activator or dispersant may be needed (Xuan et al., 2000). The nanofluids in our current study were also prepared using the two-step method. It worked well especially at low volumetric concentrations. An important advantage of this technique in terms of eventual commercialization of nanofluids is that the nanopowder preparation techniques have already been scaled up

to economically produce large quantities of nanopowders.

2.1.3 One-step Method

The second processing approach, referred to as the single-step method, has been used with success to produce nanofluids containing dispersed high thermal conductivity metal nanoparticles (Eastman et al. 1997, 2001). One successful technique is called the direct evaporation technique, which was first developed by Yatsuya and coworkers (1978), and later improved by Wagener and Günther (1999). During this process, nanoparticles were synthesized and dispersed into a fluid within a single step. As with the inert gas–condensation technique, the technique involves vaporization of a source material under vacuum conditions. In this case, however, condensation of the vapor to form nanoparticles occurs via contact between the vapor and a liquid. Nanoparticle agglomeration is minimized by flowing the liquid continuously. A significant limitation to the application of this technique is that the liquid must have low vapor pressure, typically less than 133 Pa (1 torr). Higher vapor pressures lead to gas condensation and the associated problems of increased nanoparticle agglomeration.

The chemical vapor condensation technique is another efficient choice, in which nanoparticles are formed by thermal decomposition of a metal-organic precursor entrained in a carrier gas passing through a furnace. It has recently been modified to synthesize and disperse non-agglomerated nanoparticles into fluids in a single step (Eastman et al., 2004). Compared with the direct-evaporation technique, chemical vapor condensation appears to offer advantages in terms of control of particle size, ease of scalability, and the possibility of producing novel core-shell nanostructures.

Zhu et al. (2004) recently modified the polyol process for copper nanoparticles preparation to produce copper-ethylene glycol nanofluids in a single step by reducing

copper sulfate pentahydrate ($CuSO_4 \cdot 5H_2O$) with sodium hypophosphite ($NaH_2PO_2 \cdot H_2O$) in ethylene glycol under microwave irradiation. The average size of the suspended copper nanoparticles can be well controlled under 20nm. It was found to be a fast and efficient single-step chemical method for preparing stable and nonagglomerated copper nanofluids. It was also expected that this method can be extended to other metallic nanofluids.

The single-step method can significantly reduce the agglomeration and improve the stability of nanofluid. However, at present the quantities of nanofluids that can be produced via this method are much more limited than two-step techniques, although, if desired, it is likely that those single-step techniques could also be scaled to an affordable cost range for the mass production of nanofluids.

2.2 Thermal Conductivity Measurement Methods

2.2.1 Steady-state Parallel-plate Methods

The one-dimensional, steady-state parallel-plate method was first proposed by Challoner and Powell (1956) and Wang et al. (1999) first used this method to measure the thermal conductivity of nanofluids. This method produces thermal conductivity data from measurements in a straight forward manner and requires only a small sample of liquid. Figure 2.1 shows the schematic of the experimental apparatus used. The fluid sample to be investigated is confined between two parallel horizontal plates made of a metal with high thermal conductivity, usually copper. The upper plate is supplied with a heating power Q uniformly distributed over the plate area. The two copper plates are separated by spacers with low thermal conductivity, normally glass. The liquid cell is housed in a larger cell made of aluminum. The lower plate is normally cooled by a high capacity liquid cooling system. Guide heaters are used to

minimize the heat loss to the ambient.

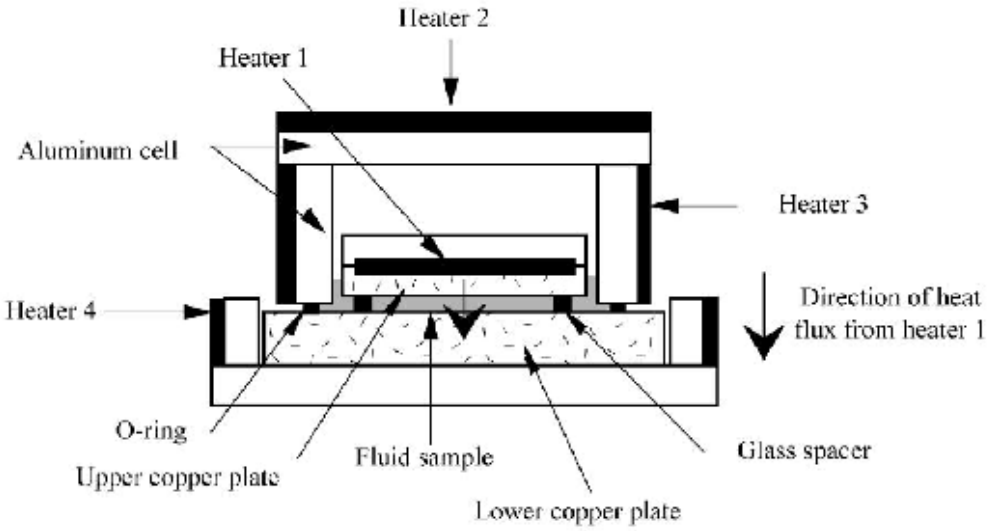

Figure 2.1: Schematic of thermal conductivity measurement apparatus using steady state parallel plate method (Wang et al., 1999).

Following the basic phenomenological relationship known as the law of Fourier, the basic equation to obtain thermal conductivity, k'_{eff}, is

$$k'_{eff} = -\frac{\dot{q}}{\nabla T} = \frac{Q\delta}{A\Delta T} \tag{2.1}$$

where $\dot{q}$ is the heat-flux, ∇T is the temperature gradient, Q is heating power, A is the surface area of the upper plate and δ is the distance between the two plates. The thermal conductivity of the liquid sample can be further corrected by taking the thermal conductivity of spacers into consideration. The effective thermal conductivity, k_{eff}, can be calculated as

$$k_{eff} = \frac{k'_{eff} \cdot A - k_s \cdot A_s}{A - A_s} \tag{2.2}$$

where k_s and A_s are the thermal conductivity and the total surface area of spacers respectively.

The steady-state parallel-plate method makes it possible to obtain accurate

measurements of the thermal conductivity of fluids over a wide range of temperatures and pressures. This method minimizes convection, allows proper consideration of radiation and other corrections due to the simple cell geometry and the possibility of measuring with different plate distances. For liquids under normal conditions, this simple apparatus can measure the thermal conductivity on a relative basis which can yield accuracy suitable for many practical applications.

2.2.2 Transient Hot-Wire Method

Recent advances in electronic instruments have helped to establish the transient hot-wire method as one of the most accurate techniques for measuring the thermal conductivity of fluids. The great advantage of this method is its almost complete elimination of the natural convection effect, whose unwanted presence greatly influences the accuracy of conventional steady-state thermal conductivity measurement instruments. In addition, this method is very fast relative to the steady-state techniques.

The major expositions of both theory and application of the modern transient hot-wire method were made by Kestin and Wakeham (1978), Roder (1981) and Johns et al. (1988). Masuda et al. (1993) and Lee et al. (1999) first adopted this method to measure the thermal conductivity of nanofluids. Later, it was extensively used in nanofluids thermal conductivity characterization. As it can be seen from Figure 2.2, a transient hot-wire system normally involves a high thermally conductive wire, typically platinum, suspended symmetrically in a liquid in a vertical cylindrical container. The wire serves both as heating element and thermometer.

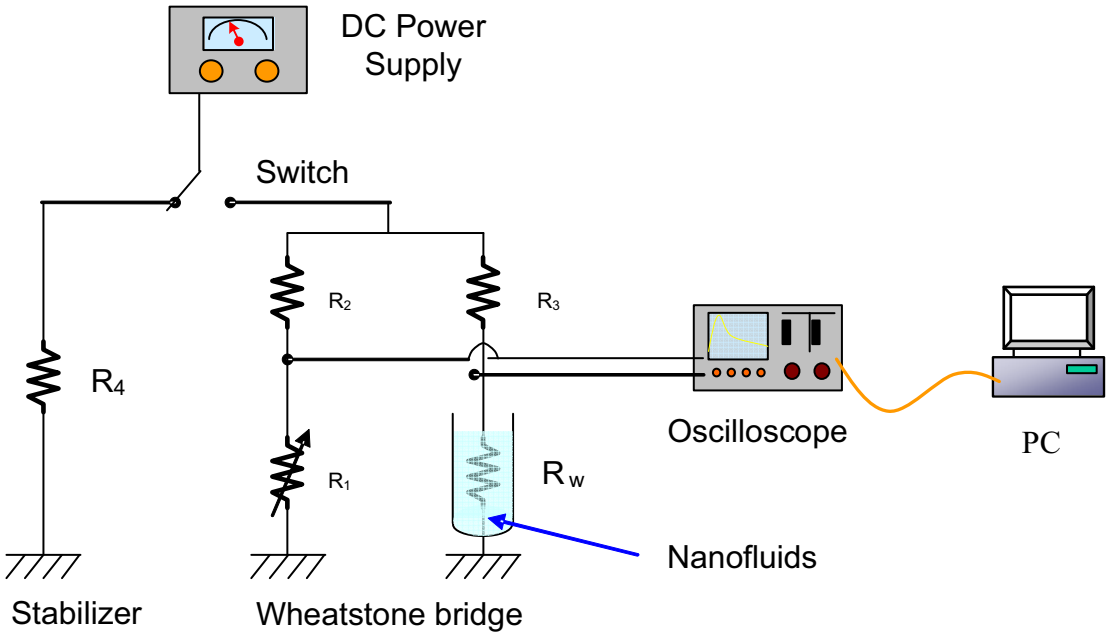

Fig 2.2: Schematic diagram of transient hot-wire apparatus for measuring thermal conductivities of nanofluids

The ideal mathematical model that one attempts to approximate is that of an infinitely long, vertical, line source of heat possessing zero heat capacity and infinite thermal conductivity is immersed in a medium at time $t = 0$. When a stepwise heat flux q per unit length is imposed, the energy is entirely conducted from the line source to the fluid. For the line source of radius r_o and a uniform initial temperature, the relationship between the temperature rise of the wire and the thermal conductivity of the fluid was based on a specific solution of Fourier's law (Carslaw and Jaeger, 1959).

$$T(t) - T_{ref} = \frac{q}{4\pi k} \ln\left(\frac{4K}{a^2 C} t\right) \qquad (2.3)$$

where $T(t)$ denotes the temperature of the wire in the fluids at time t, T_{ref} is the temperature of the cell, q is the applied electric power, k is the thermal conductivity, K is the thermal diffusivity of the fluid, a is the radius of the wire, and $\ln(c) = g$, where g is Euler's constant.

The relationship given by equation (2.3) implies a straight line for a plot of δT versus $\ln(t)$. In practice, systematic deviations occur at both short and long times. However, for each experimental measurement, there is a range of times over which equation (2.3) is valid, that is, the relationship between δT versus $\ln(t)$ relationship is linear. The slope of δT versus $\ln(t)$ is then obtained over the valid range, i.e., between times t_1 and t_2, and, using the applied power, the thermal conductivity can be determined from.

$$k = \frac{q}{4\pi(T_2 - T_1)} \ln\left(\frac{t_2}{t_1}\right) \qquad (2.4)$$

where $T_2 - T_1$ is the temperature rise of the wire between t_1 and t_2. From the temperature coefficient of the wire's resistance, the temperature rise of the wire's resistance can be determined by the change in its electrical resistance as the experiment progresses. The resistance change usually can be measured using a precise automatic Wheatstone bridge.

The end effect of the finite length wire used in the experiment can be experimentally minimized. A two-cell device can be employed for the compensation of end effects. Two wires are respectively immersed in two identical cells containing the same sample nanofluids. Both the wires are subject to the same heating current and the same end effects. Thus, the difference of the temperature rises of the two wires corresponds to the temperature rise of a finite section of an infinite wire. Therefore, the end effect is eliminated experimentally.

Despite the advantage of the transient hot-wire method, it is impossible to measure the thermal conductivity of the electrically conducting fluids because current flows through the liquids, the heat generation of the wire becomes ambiguous, and

polarization occurs on the surface of the wire. This method is thus normally restricted to electrically nonconducting fluids such as noble gases and organic liquids. A few attempts have thus far been made to expand the ordinary transient hot-wire method to measure electrically conducting liquids. Nagasaka and Nagashima (1981) used a thin platinum wire (diameter 40 μm) coated with a thin electrical insulation layer (thickness 7.5 μm) to measure the thermal conductivity of an NaCl solution and they analyzed the effects on the thermal conductivity measurement due to this thin insulation layer. A different approach to the wire-insulation problem was presented by Alloush et al. (1982). They considered metallic wire anodized at wire surface, forming a very thin layer of an insulating metallic oxide, uniform and not brittle. As those metallic nanoparticles and the suspending fluid such as water are electrica1ly conducting materials, the resulting nanofluids are likely to be electrically conducting too. Therefore the ordinary transient hot-wire method cannot be applied directly. Nagasaka and Nagashima's method was widely adopted in the reported experiments for characterizing the thermal conductivity of nanofluids.

2.2.3 Quasi-steady State Method

In order to measure the thermal conductivity of nanofluids, Wang et al. (2003a) proposed a special design based on the quasi-steady method to exclude the effect of local convection. In principle, this apparatus can provide simultaneous measurement of thermal conductivity and specific heat of the sample under testing. As can be seen in Figure 2.3, the testing suspension is kept in its original uniform temperature, T_0, before being heated. The sample fluid in the reservoir continuously flows through the parallel channel during testing. The analytical solution for this model was given by Carslaw and Jaeger (1959) as

$$k = q\delta/(2\Delta T) \tag{2.5}$$

$$C_p = q/[\rho l(dt/d\tau)] \tag{2.6}$$

where k is the effective thermal conductivity of liquid with particle inclusions, C_p is effective specific heat of sample fluid, q is the constant heat flux from the heating surface, δ is the thickness of the channel, $\Delta T = T_3 - T_4$ is the temperature difference between heating surface and insulated bottom surface at quasi-steady state, corresponding to Fourier number greater than 0.55. The Rayleigh number of testing medium was controlled to be less than 1000, so that liquid convection could be actually neglected. The uncertainty for the measured value of effective thermal conductivity and specific heat can be well controlled below 3%.

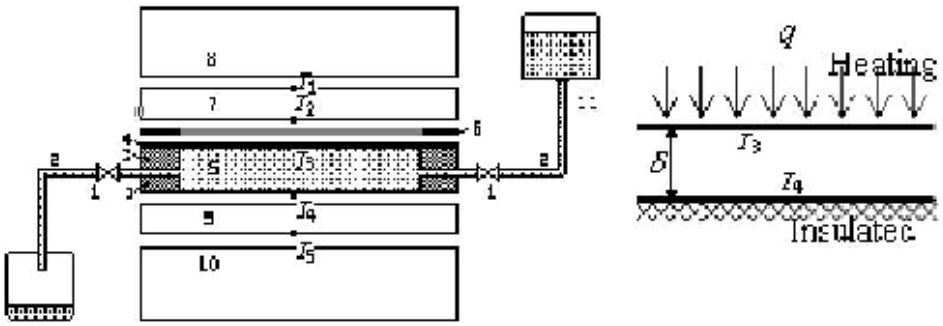

1.valve 2.ducting tube 3.supporter (insulator) 4.aluminum sheet 5.sample liquid 6.plane heater 7.9.heat-loss measuring layer 8.10.insulator 11.reservoir

Fig 2.3: Schematic diagram of apparatus for measuring thermal conductivities of nanofluids using quasi-steady state method (Wang et al., 2003a).

2.2.4 Temperature Oscillation Method

Das et al. (2003b) used a temperature oscillation technique to measure the effective thermal conductivity and thermal diffusivity of nanofluids with water as base fluid and Al_2O_3 and CuO nanoparticles as suspension material. The measurement of thermal

diffusivity and thermal conductivity is based on the energy equation for conduction given by

$$\frac{1}{\alpha}\frac{\partial T}{\partial t} = \nabla^2 T \tag{2.7}$$

The cylindrical fluid volume considered for analysis with its boundaries is shown in Figure 2.4 and the schematic of the total experimental setup is given in Figure 2.5.

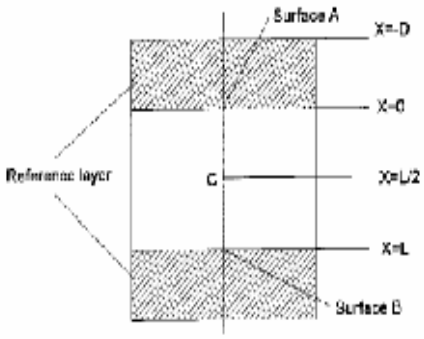

Fig 2.4: The fluid volume for analysis (Das et al., 2003).

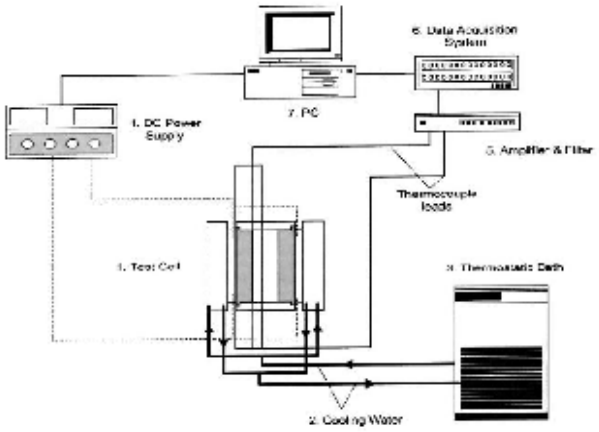

Fig 2.5: Schematic diagram of thermal conductivity measurement system using temperature oscillation method (Das et al., 2003).

At the surface A and B, periodic temperature oscillations are generated with an angular velocity given by

$$\omega = \frac{2\pi}{t_p} \tag{2.8}$$

Applying Laplace transformation, the solution of equation 2.7 in one dimension form can be written in complex form as

$$T_R^*(\zeta,\tau,\xi_L,) = T_m + u_0 e^{i(\tau+G_0)}\cosh\left(\zeta\sqrt{i}\right) + C\left[u_R e^{i(\tau+G_R)} - u_0 e^{i(\tau+G_0)}\cosh\left(\xi_L\sqrt{i}\right)\right]\frac{\sinh\left(\zeta\sqrt{i}\right)}{\sinh\left(\xi_L\sqrt{i}\right)} \tag{2.9}$$

where $C = \dfrac{\lambda}{\lambda_R}\sqrt{\dfrac{\alpha_R}{\alpha}}$

The complex amplitude ratio in this case between $x = -D$ (D being the thickness of reference layer) and $x = 0$ is given by

$$B_R^* = \cosh\left(\zeta_D\sqrt{i}\right) - C\sinh\left(\zeta_D\sqrt{i}\right)\times\left[\frac{\left(u_L/u_0\right)e^{i(G_L-G0)} - \cosh\left(\xi_L\sqrt{i}\right)}{\sinh\left(\xi_L\sqrt{i}\right)}\right] \tag{2.10}$$

The real phase shift and amplitude attenuation are given by

$$\Delta G_R = \arctan\left(\frac{\mathrm{Im}\left(B_R^*\right)}{\mathrm{Re}\left(B_R^*\right)}\right) \tag{2.11}$$

$$\frac{u_D}{u_0} = \sqrt{\mathrm{Re}\left(B_R^*\right)^2 + \mathrm{Im}\left(B_R^*\right)^2} \tag{2.12}$$

By measuring phase and amplitude of temperature oscillations at the two surfaces as well as at the center point, the thermal conductivity can be determined from above formula. This method was shown to be capable of providing thermal conductivity measurements with an uncertainty of less than 3%.

2.3 Experimental Study of Thermal Conductivity of Nanofluids

A number of exciting experimental results have been reported since the pioneering work of S. U. S. Choi in this field (Choi, 1995). A great improvement in the effective thermal conductivity as well as other key features of nanofluids have been observed which together make nanofluids a strong candidate for the next generation cooling medium.

2.3.1 Nonmetallic Nanoparticles

Masuda et al. (1993) first reported a 20% increase in the thermal conductivity of water with the addition of 3vol% Al_2O_3 nanoparticles. However, Lee et al. (1999) obtained an increase of only 8% at the same volume fraction. A subsequent study by Wang et al. (1999) also examined the behavior of Al_2O_3 nanoparticles in water but observed a 12% enhancement in thermal conductivity at the same nanoparticle loading percentage. The main cause of this discrepancy in behavior is thought to be the differences in average particle size in the three sets of samples. The Al_2O_3 nanoparticles used by

Masuda et al. had an average diameter of 13nm, compared with 38.4nm and 28nm in the following studies by Lee et al. and Wang et al., respectively.

Xie and co-workers (2002a) investigated the dependence of nanofluids effective thermal conductivity on base fluids. Nanosized $\alpha - Al_2O_3$ particles with a specific surface area (SSA) of $25m^2/g$ were dispersed into deionized water, glycerol, ethylene glycol and pump oil, respectively, at certain volume ratios. At the same volume fraction of 5vol%, a highest increase around 38% in effective thermal conductivity was observed for the Al_2O_3-pump oil nanofluid compared to that of the other fluids. Further, it was found that the thermal conductivity enhancement decreased with an increase in the thermal conductivity of the base fluids.

Water and ethylene glycol-based nanofluids containing dispersed CuO nanoparticles have shown significant enhancements in effective thermal conductivity than those containing Al_2O_3 nanoparticles. The study by Lee et al. (1999) observed a more than 20% improvement at a volume fraction of 4% for the CuO-ethylene glycol nanofluid. They also reported that for nanofluids using the same base liquid, the conductivity of the CuO suspension system is always higher than that of the Al_2O_3. Wang et al. (1999) reported a 16% enhancement in effective thermal conductivity of the 5vol% CuO-water nanofluid. Zhou and Wang (2002) observed a 17% increase in thermal conductivity for a loading of only 0.4 vol% CuO nanoparticles in water. These differences in behavior observed by different groups have not yet been reconciled. It cannot be simply explained by the particle size difference or surface area difference. The average diameter of the CuO nanoparticles in the studies of Zhou &Wang (50 nm) were actually reported to be larger than those in the study of Lee et al. (36 nm) and Wang et al. (23nm). Different particle surface treatment and nanofluid synthesis

methods used in their experiments may be responsible for the discrepancy in the measured effective thermal conductivity.

Xie et al. (2002b) studied the thermal conductivity of suspensions containing SiC nanoparticles. Three different type of α -SiC powder with average diameters of 26nm, 600nm and 900nm were dispersed in water and ethylene glycol, respectively. For all the measurements, the thermal conductivity enhancement ratio increased with the volume fraction of SiC nanoparticles but remained almost constant for the same fraction of same particles in different base fluids. For a given volume fraction, the thermal conductivity increase of nanofluids containing 600nm SiC powders is the highest within the range of experiment measurement uncertainty.

The recent important observation by Das et al. (2003) disclosed the strong temperature dependence of the effective thermal conductivity of nanofluids. Their study showed a two to four folder increase in thermal conductivity enhancement of CuO-water and Al_2O_3-water nanofluids, which took place only over a small temperature range of 20^oC to 50^oC. If further study proved that this temperature dependence occurs over a wide temperature range, this special property could make nanofluids particularly attractive for applications at elevated temperatures. In another word, nanofluids can sense hot spots and provide more rapid cooling in those regions.

2.3.2 Metallic Nanoparticles

Although fewer researches on nanofluids containing metallic nanoparticles have been published, those available results are much more encouraging. Nanofluids consisting of metallic nanoparticles have been observed to exhibit substantially improved thermal conductivity enhancements compared to nonparticle-containing fluids or nanofluids containing oxide particles.

Xuan and Li (2000) characterized the thermal conductivity of nanofluids with suspended copper nanophase powders (100nm) by using a transient hot-wire apparatus. For Cu-water nanofluids, the thermal conductivity enhancement varied from 34% to 78% with the volume fraction of nanoparticles increased from 2.5% to 7.5%.

The later successful experiment carried out by Eastman and co-workers (2001) showed that by dispersing pure copper nanoparticles of less than 10nm size in ethylene glycol, a phenomenal 40% increase in effective thermal conductivity can be attained with only 0.3 vol% addition of nanoparticles.

The more recent study by Patel et al. (2003) reported an up to 21% increase in thermal conductivity of gold and silver nanoparticles dispersed in water and toluene with particle volume fractions as low as 0.011 vol%. Besides, they again observed a significant enhancement associated with the increase of temperature range from 30^{o}C to 60^{o}C.

2.3.3 Nanotubes

Nanotubes exhibit a different behavior than nanoparticles when dispersed into a base liquid. For example, when multi-wall carbon nanotubes are added in water, they form a non-homogeneous and unstable two phase mixture. Suspension with large agglomerates of nanotubes present locally. Precipitation starts after several minutes. In order to obtain a homogeneous and stable solution, several procedures are usually adopted such as adding small amount of dispersant, special chemical treatment and ultrasonic vibration. Ultrasonic vibration can however, have two effects, it can break the nanotubes agglomerates to form a more uniform suspension, but it can also break them into smaller lengths.

Biercuk et al. (2002) first reported their work on an industrial polymer epoxy with

addition of single-wall carbon nanotubes in order to enhance its thermal properties. Samples loaded with 1 wt% unpurified single-wall carbon nanotubes demonstrated a 125% increase in thermal conductivity at room temperature. An additional 10% increase was observed when the carbon nanotubes were aligned by a magnetic field.

The successive experiment by Choi et al. (2001) reported the anomalous thermal conductivity enhancement of multi-wall carbon nanotubes-oil suspensions. By following a two step process, the suspended multi-walled carbon nanotubes with a mean diameter of ~25 nm and a length of ~50 μm were first produced by a chemical-vapor-deposition reactor and then dispersed into a synthetic poly (α-olefin) oil. For the 1 vol% carbon nanotubes-poly oil suspension, an increase exceeding 150% was observed. The measured thermal conductivity is anomalously greater than theoretical predictions and is nonlinear with nanotubes loadings even at very low volume fraction.

Assael et al. (2003) recently investigated the thermal conductivity enhancement of water with the addition of multi-wall carbon nanotubes. Sodium Dodecy Sulfate was employed as the dispersant and the thermal conductivity was characterized using a transient hot wire apparatus with a standard uncertainty better than 2%. For the 0.6 vol% nanotubes suspension, a 38% increase in effective thermal conductivity was observed.

2.4 Models for Predicting Thermal Conductivity of Nanofluids

A large body of literature has been contributed to the theoretical modeling of effective thermal conductivity of liquids containing suspended solid particles. The earliest study in this area can be traced back to Maxwell's theoretical work which was first published more than 100 years ago (Maxwell, 1881). Although Maxwell's theory was

originally used to calculate the effective electrical conductivity of a random suspension containing particles, it can be employed to model the effective thermal conductivity of liquid solid mixture due to the identity of mathematical formulations between these two transport phenomena. Maxwell's model indicates that the effective thermal conductivity of suspensions containing particles increases with the volume fraction of the solid particles. This model is only effective for dilute suspensions containing spherical particles and the influence of particle shape is not considered. However, for non-spherical particles, it is well known that the thermal conductivity of suspensions depends not only on the volume fraction of the particles, but also on the shape of the dispersed particles.

In order to incorporate the possible effects of particle surface area increase caused by non-spherical particle shapes, Hamilton and Crosser (1962) modified Maxwell's formula and developed an elaborate model for the effective thermal conductivity of two-component mixtures as a function of liquid and solid thermal conductivity, particle volume fraction and an empirical scaling factor taking the shape of the dispersed particles into account. This model shows that non-spherical shapes will increase thermal conductivity above that of spheres. An alternative expression for calculating the effective thermal conductivity of solid-liquid mixtures was introduced by Wasp in 1977. Wasp's model is a special case of Hamilton and Crosser model with sphericity equal to 1.

Jeffery (1973), Davis (1986), Lu and Lin (1996) also developed several theoretical models for predicting the effective thermal conductivity of liquid-solid two phase suspensions. Although most of the above mentioned models have been successfully verified by experimental data for suspensions with millimeter or micrometer sized particles at low concentrations, they often give much smaller or even contradictory

predictions compared to published experimental work when applied to fluids containing nanoparticles. The reason for the discrepancy is quite straight forward, because, in these theories, the effective thermal conductivity of liquid-solid particle suspensions depends only on the volume fraction and shape of the suspended particles, not on particle size. And from the results, the size of the particles has a dominant influence on the effective thermal conductivity.

A more successful model was developed by Xue (2003) based on Maxwell's theory and average polarization theory. A set of equations for calculating the effective thermal conductivity of nanofluids was provided. The predicted thermal conductivity values of nanotubes-oil nanofluid and Al_2O_3-water nanofluid are in good agreement with the published experimental results.

Based on the effective medium theory, Yu and Choi (2003) modified Maxwell's model by including the effect of the ordered liquid nanolayer at liquid and particle interface. This modified Maxwell model can successfully predict the effective thermal conductivity of binary suspension systems containing spherical nanoparticles. This study also suggested that in order to increase effective thermal conductivity of nanofluids, adding smaller particles could potentially be a better approach than simply increase the volume fraction of nanoparticles. However, this model does not consider the shape of nanoparticle and the predicted value is still much lower for ternary systems such as copper nanofluids with surfactants.

Wang et al. (2003) proposed an innovative method for modeling the effective thermal conductivity of nanofluids based on the effective medium approximation and the fractal theory for describing nanoparticle clusters and their radial distribution. The size and the surface adsorption of nanoparticles were taken into consideration. The thermal

conductivity values predicted by this method agree quite well with measured effective thermal conductivity of dilute suspensions of metallic oxide nanoparticles.

A brief summary of the currently available theoretical models for predicting the effective thermal conductivity of nanofluids is shown in Table 2.1.

Table 2.1: Summary of theoretical models for effective thermal conductivity prediction of a mixture.

Proposers	Model Expression	Remarks
Maxwell (1881)	$\frac{K_{eff}}{K_l} = 1 + \frac{3(\alpha-1)\phi}{(\alpha+2)-(\alpha-1)\phi}$	Only spherical particles are considered; Accurate to $o(\phi)$, applicable to low volume fraction.
Maxwell-Garnett model (Maxwell,1881)	$\frac{K_{eff}}{K_l} = \frac{(1-\phi)(k_p+2k_l)+3\phi k_p}{(1-\phi)(k_p+2k_l)+3\phi k_l}$	Applicable to suspensions with low concentration particle inclusions.
Bruggeman model (1935)	$\phi\left(\frac{k_p-k_{eff}}{k_p+2k_{eff}}\right)+(1-\phi)\left(\frac{k_l-k_{eff}}{k_l+2k_{eff}}\right)=0$	No limit on concentration of inclusions.
Hamilton & Crosser (1962)	$k_{eff} = k_l\left[\frac{k_p+(n-1)k_l-(n-1)\alpha(k_o-k_p)}{k_p+(n-1)k_o+\alpha(k_o-k_p)}\right]$	Spherical and non-spherical particles are considered, Accurate to $o(\phi)$, applicable to low volume fraction.
Jeffrey (1973)	$\frac{K_{eff}}{K_l} = 1+3\beta\phi+\phi^2\left(3\beta^2+\frac{3\beta^2}{4}+\frac{9\beta^3}{16}\frac{\alpha+2}{2\alpha+3}+\frac{3\beta^4}{2^6}+\cdots\right)$	Accurate to $o(\phi^2)$, High order terms represent pair interaction of randomly dispersed spheres.
Wasp (1977)	$\frac{k_{eff}}{k_l} = \frac{k_p+2k_l-2\phi(k_l-k_p)}{k_p+2k_l+\phi(k_l-k_p)}$	Special case of HC model with sphericity equal to 1.
Davis (1986)	$\frac{K_{eff}}{K_f} = 1+\frac{3(\alpha-1)}{(\alpha+2)-(\alpha-1)\phi}\left[\phi+f(\alpha)\phi^2+o(\phi^3)\right]$	Accurate to $o(\phi^2)$, high order terms represent pair interaction of randomly dispersed spheres.
Lu & Lin (1996)	$\frac{k_{eff}}{k_f} = 1+a\phi+b\phi^2$	Applicable to both spherical and non-spherical particles.
Xue (2003)	$9(1-\frac{\phi}{\lambda})\frac{k_{eff}-k_m}{2k_{eff}+k_m}+\frac{\phi}{\lambda}\left[\frac{k_{eff}-k_{c,x}}{k_{eff}+B_{2,x}(k_{c,x}-k_{eff})}+4\frac{k_{eff}-k_{c,y}}{2k_{eff}+(1-B_{2,x})(k_{c,y}-k_{eff})}\right]=0$	Elliptical particles are considered, only suitable for particles at nanometer size.
Yu & Choi (2003)	$k_{pe} = \frac{\left[2(1-\gamma)+(1+\beta)^3(1+2\gamma)\right]\gamma}{-(1-\gamma)+(1+\beta)^3(1+2\gamma)}k_p$ $k_{eff} = \frac{k_{pe}+2k_l+2(k_{pe}-k_l)(1+\beta)^3\phi}{k_{pe}+2k_l-(k_{pe}-k_l)(1+\beta)^3\phi}k_l$	Modified Maxwell model, nanoparticle liquid layering is considered.
Bonnecaze & Brady (1990)	N/A	Near and far field interactions among two or more particles are considered.

2.5 Potential Mechanisms of Thermal Conductivity Enhancement in Nanofluids

Various factors could potentially be responsible for the discrepancy between the predicted thermal conductivity values by macroscopic theoretical models and the experimental investigations. All the macroscopic models that we discussed earlier required the continuum assumption, which however may not be true for colloids with particles at nanometer scale. A number of microscopic mechanisms discussed in the literature as possible factors for anomalous thermal conductivity enhancement of nanofluids are examined in this section.

2.5.1 Microscopic Motions

Because of the small size of nanoparticles, microscopic motions induced by stochastic and inter-particle forces are able to increase the energy transport. However, microscopic forces acting on particles at nanometer scale such as the Van der Waals force and electrostatic force resulting from the electric double layer at the particle surface are difficult to calculate accurately. They are strongly affected by the chemical and electrical properties of the solid particle surface and hosting liquids.

Brownian motion and the induced particle collisions are another obvious type of motion that was thought to be a significant contributor to thermal conductivity increase. However, the calculation results of Wang et al. (1999) for the thermal conductivity increase induced by the rotational and translational motion of a spherical particle showed that up to a volume fraction of 10%, the thermal conductivity increase by the Brownian motion is less than 0.5% for the Al_2O_3 nanofluid evaluated in their experiment. More recently, Keblinski et al. (2002) showed that for a particle with diameter of 10nm in water at room temperature, it took $\tau_D \approx 2\times10^{-7} s$ to move a

distance equal to its size. The time required for heat to move in the liquid by the same distance is only $\tau_H \approx 4\times10^{-10} s$. The ratio of τ_D / τ_H is around 500 and decreases to ~25 even when the particle size is equal to the atomic size. This reveals that the thermal diffusion is much faster than the Brownian diffusion. Thus Brownian motion cannot contribute significantly to the thermal conductivity enhancement in nanofluids. However, it could play an important indirect role in producing nanoparticle clustering, which could significantly enhance the effective thermal conductivity.

2.5.2 Liquid Layering at Liquid/Particle Interface

The atomic structure of the liquid layer at the solid-liquid interface is much more ordered than that of bulk liquid. It is well known that materials with ordered structure like crystalline solids exhibit much better thermal conductivity than liquids. Therefore the liquid layering at the interface was expected to result in a better thermal conductivity.

Keblinski et al. (2002) calculated the thermal conductivity enhancement induced by the particle-layered-liquid structure (see Figure 2.6). To estimate an upper limit for this effect, the thermal conductivity of this interfacial liquid layer was set to be the same as the solid particle. By simple calculation, to double the effective volume of a particle with 10nm diameter would require a 2.5nm thick liquid layer. However, experimental (Henderson et al., 1984) and simulation (Yu et al., 2000) results have shown that a typical interfacial layer thickness is only of the order of 1nm. Thus, although the liquid layer at the interface may play a role in thermal transport, it is not that significant to account for the increase in thermal conductivity of nanofluids.

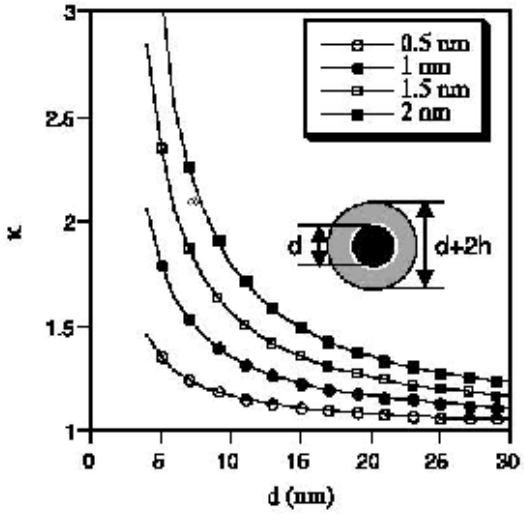

Fig 2.6: Effective thermal conductivity enhancement due to liquid layering at liquid/particle interface (k-excess thermal conductivity enhancement, b-particle diameter, h-liquid layer thickness).

2.5.3 Interfacial Resistance

According to the experimental results of Wilson et al. (2002), the values of the interfacial conductance of liquid-solid interface is of the order of 10MW/m^2-k, which corresponds to the equivalent matrix thickness of 10nm for a typical low thermal conductivity organic liquid or isotropic polymer. The length is of the order of the nanoparticle size, therefore it is important to study the influence of interfacial resistance on effective thermal conductivity of nanofluids.

Eastman et al. (2004) discussed the influence of interfacial resistance by using the effective medium theory for a small volume fraction of spherical particle in liquid. The effective composite thermal conductivity, k_{eff} can be expressed as,

$$\frac{k_{eff}}{k_{matrix}} - 1 = 3\phi \frac{\gamma - 1}{\gamma + 2} \tag{2.11}$$

where ϕ is the particle volume fraction and γ is the ratio of the particle radius to the equivalent matrix thickness. From the equation, the conductivity enhancement decrease with increasing interfacial resistance. However these predictions are totally opposite to the observed behavior of nanofluids, which indicates that more research on the liquid-solid interface is necessary. On the other hand, this reveals that the

influence of interfacial resistance is not significant and thus it is not the dominant factor contributing to the great effective thermal conductivity enhancement of nanofluids.

2.5.4 Heat Transportation in Nanoparticles

In crystalline solids such as nanoparticles used in nanofluids, heat is carried by phonons, that is, by the propagation of lattice vibrations. Such phonons are created at random, propagate in random directions, and are scattered by each other or by defects and thus justify the use of the macroscopic description of thermal transport. In metals, the heat is primarily carried by electrons, which also exhibit diffusive motion at the microscopic level. Therefore the diffusive thermal transport assumption in the above mentioned macroscopic theories is questionable.

Keblinski et al. (2002) and Eastman et al. (2004) discussed the nature of thermal transport in nanoparticles. Although it is difficult to envision how ballistic phonon transport could be more effective than very-fast-diffusion phonon transport, particularly to the extent of explaining the order of magnitude larger increase of thermal conductivity in Cu nanofluids, the other ballistic phonon effects could lead to a significant increase in thermal conductivity. As can be shown, the nanoparticles in a nanofluid are surprisingly close to each other even at very low volume fractions. For example, the surfaces of 10nm particles are only separated by 5nm at 5% volume fraction. Therefore the ballistic phonons initiated in one particle can persist in the liquid and reach a nearby particle even though the phonon mean free path in liquid is very short (~1-2nm). This process can further largely be agitated by the random Brownian motion of nanoparticles. Therefore this particular thermal transport process

in nanofluids is expected to be responsible for the major increase in effective thermal conductivity.

2.5.5 Effects of Nanoparticle Clustering

Clustering of particles into percolating patterns would greatly influence the effective thermal conductivity by introducing paths of lower thermal resistance. Although large clusters would most likely settle out of the fluid, local clustering is possible and indeed has been observed experimentally. The effective volume of a cluster can be much larger than the physical volume of the particles. Since within such clusters, heat can move very rapidly, the volume fraction of highly-conductive solid phase is larger than the volume of solid and may significantly increase thermal conductivity.

Keblinski et al. (2002) demonstrated that with decreasing volume fraction, the effective volume of the cluster increases, thus enhancing thermal conductivity (Figure 2.7). A further dramatic increase of effective thermal conductivity can take place if the particles do not need to be in physical contact, but just within a specific distance, allowing rapid heat flow between them. Such liquid-mediated clusters exhibit a very low packing fraction and thus a very large effective volume and in principle are capable of explaining the unusually large experimentally observed enhancements of effective thermal conductivity of nanofluids.

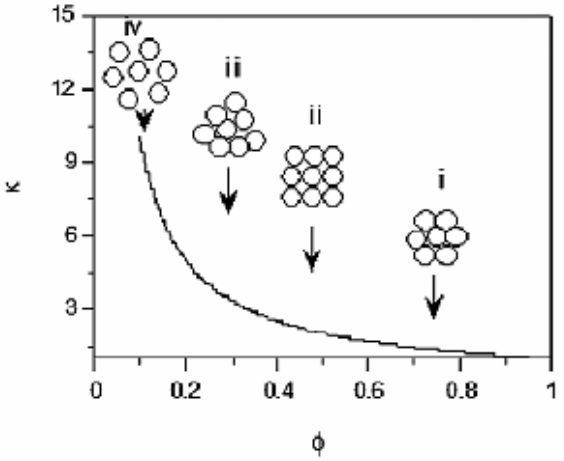

Fig 2.7: Effective thermal conductivity enhancement due to increased effective volume (k-excess thermal conductivity enhancement, ϕ -effective volume).

2.6 Other Important Thermal Properties

Although the thermal conductivity of nanofluids plays a very important role in heat transfer phenomena, the convective heat transfer coefficient or Nusselt number of the nanofluid flow system depends on many other properties such as density, specific heat and viscosity. Those factors will also significantly influence the heat transfer capability and pressure drop of a cooling system. Therefore a detailed examination of these properties is necessary.

2.6.1 Density

The density of a certain nanofluid can be calculated as,

$$\rho = (1-\phi)\rho_f + \phi\rho_p \tag{2.13}$$

where ϕ denotes the volume fraction of nanoparticles and ρ_f and ρ_p are the densities of base fluid and nanoparticle, respectively. Because the volume fraction of particles added is normally less than 5 percent, the increase in density of suspension is expected to be less than 10%.

2.6.2 Specific Heat

The specific heat of a nanofluid C_{pnf} can be calculated as

$$\rho C_{pnf} = (1-\phi)\rho_f C_{pf} + \phi\rho_p C_{pp} \tag{2.14}$$

where C_{pf} and C_{pp} are specific heats of base fluid and nanoparticles, respectively. From the equation a small decrease in specific heat is expected when typical solid particles are dispersed into liquids. Fortunately, the enhancement of molar capacity of nanostructured particles reduces the difference. Wang et al. (2001) recently reported that Al_2O_3 nanoparticles with average diameter around 20nm showed a 6% to 23% increase in heat capacity compared with the coarse-grained alumina in the temperature

range of 200~370K. Eastman and co-workers (2004) characterized the specific heat of water containing low volumetric fraction Al_2O_3 particles and they showed no measurable difference in specific heat compared with water alone.

2.6.3 Viscosity

Pak and Cho (1998) first reported that the viscosity of the water based Al_2O_3 (~100nm) nanofluid prepared using a two-step method was three times higher than that of water. Later, Wang et al. (1999) measured the viscosity of water-based Al_2O_3 nanofluids dispersed by different techniques and showed that nanofluids have lower viscosities when the particles are better dispersed. They also found that the 3 vol% Al_2O_3-water nanofluids showed an increase of around 20% to 30% in viscosity compared with that of the base fluid. Xuan & Li (2003b) measured the turbulent friction factor of water-based nanofluids containing copper nanoparticles (~100nm) in low volume fraction range between 0.3% and 2.0%. The friction factor for the nanofluids was found to be approximately the same as that of water. Those previous experimental results disclosed the strong dependence of viscosity of nanofluids on dispersion method, volumetric fraction and particle size.

Xuan and Roetzel (2000) proposed to use the Einstein model and Brinkman model for predicting the viscosity of nanofluids containing a low volume fraction of nanoparticles. The well known Einstein's model was initially for evaluating the effective viscosity of Newtonian fluids with a dilute suspension of small non-interacting rigid spherical particles. The formula yields $\mu_{nf} = (1 + 2.5\phi)\mu_f$, where μ_{nf} and μ_f denotes the viscosity of nanofluid and base fluid, respectively. This correlation is restricted to low volumetric fraction ($\phi < 5\%$) and the particles suspended should be very small and linear with volume fraction. The Einstein's model

was further extended by Brinkman as $\mu_{nf} = \mu_f /(1-\phi^{2.5})$.

Putra et. al. (2003) recently reported the viscosity of Al_2O_3-water and CuO-water nanofluids as a function of shear rate and showed Newtonian behavior of the nanofluids for a range of volume fractions between 1% and 4%.

Li et al. (2002) measured the viscosity of water based copper oxide (50nm) nanofluids with mass fraction between 2% and 10% and 30°C to 80°C temperature range by using capillary viscometers. The measured apparent viscosity of suspensions generally followed the values predicted by Brinkman's formula. The effect of nanoparticle concentration was not as obvious as temperature. However, the viscosity of nanofluids was 15% to 30% higher than water at higher particle concentrations.

2.7 Convective Heat Transfer of Nanofluids

Compared with the large body of literature on the effective thermal conductivity of nanofluids, less study involving fluid flow and heat transfer performance of nanofluids has been reported. However, the real worth of such highly efficient cooling media lies in its application under convective conditions. Heat transfer enhancement in a solid-liquid two-phase flow has been investigated for many years. Although all previous research are based on millimeter or micrometer-sized particles, nanofluids are expected to exhibit similar or better performance in convective heat transfer processes with their superior thermophysical properties.

2.7.1 Single Phase Heat Transfer of Nanofluids

Choi (1995) first quantitatively analyzed the potential benefits of nanofluids for augmenting heat transfer and reducing size, weight and cost of thermal apparatuses, at the same time, incurring little or no penalty in pressure drop.

Xuan and Roetzel (2000) first proposed two different approaches for deriving heat transfer correlation of the nanofluids based on the assumption that the nanofluid behaves more like a fluid rather than the conventional solid-fluid two phase mixtures. One is the conventional approach that nanofluids can be treated as common pure fluids by assuming that there exists no motion slip between the discontinuous phase of the dispersed nanoparticles and the continuous liquid and the local thermal equilibrium between the nanoparticles and the fluid. Another modified conventional approach is to use the dispersion model to include the effect of nanoparticle chaotic movements which increased the energy exchange rates in the fluid.

Xuan and Li (2000) analytically investigated the enhancement of the heat transfer mechanism of nanofluids by using the dispersion model. They concluded that the enhanced performance of the nanofluid resulted not only from its high thermal conductivity but also from the random movement and dispersion effect of the nanoparticles. A correlation of Nusselt number for turbulent flow through a tube was derived.

A. Ali et al. (2003) numerically investigated the heat and mass transfer between air and falling film desiccant with the addition of nanoparticles suspensions in parallel and counter flow configurations. The dehumidification and cooling rates of air were improved with an increase in the volume fraction of nanoparticles and dispersion factor, but the improvements were not significant due to the small thickness of the falling film desiccant.

Xuan and Li (2003) studied the characteristics of convective heat transfer and flow of water-Cu nanofluids in a tube. Both the convective heat transfer coefficient and the friction factor of the sample nanofluids for the turbulent flow were measured. Results

showed that the suspended nanoparticles remarkably enhanced the heat transfer process with smaller volume fraction of nanoparticles. A new type of convective heat transfer correlation was proposed to correlate experimental data of heat transfer of nanofluids.

Khaled and Vafai (2003) numerically investigated the flow and heat transfer inside thin films supported by flexible soft seals in the presence of suspended ultrafine nanoparticles. It was found that the increase in the coolant flow rate because of thermal expansion effects produced an additional cooling in the presence of suspended nanoparticles. Large fluctuation rates that can be generated in the flow during severe squeezing conditions tend to increase the chaotic motions of the particles in the fluid which in turn increases the energy transport in the coolant.

Khanafer et al. (2003) investigated the heat transfer enhancement in a two dimensional enclosure utilizing nanofluids by numerical simulation. A dispersion model was developed to incorporate the effect of the chaotic movement of nanoparticles. Their simulation results were found to be in excellent agreement with previously published work. In addition, an analysis of variance based on the thermophysical properties of nanofluids showed that the variances within different models have substantial effects on the results. A heat transfer correlation of average Nusselt number for various Grashof numbers and volume fractions was also presented.

Maïga et al. (2004) numerically investigated the hydrodynamic and thermal behaviors of nanofluids flowing inside a uniformly heated tube. Results have shown that the existence of nanoparticles has produced a considerable increase in heat transfer compared with that of the base liquid. Such heat transfer enhancement increased with the augmentation of the particle volume fractions. However, it is accompanied by a

major drawback on the wall shear stress. The authors also showed that the ethylene glycol- γ Al_2O_3 offers a better heat transfer enhancement than the water- γ Al_2O_3 nanofluid. The ethylene glycol based nanofluid was also observed to have a more pronounced adverse effect on the wall shear stress. For the turbulent flow regime, results have also shown that the heat transfer enhancement due to the presence of nanoparticles becomes more important with the increase of the Reynolds number.

Kim et al. (2004) analytically investigated the convective instability driven by buoyancy and the heat transfer characteristics of nanofluids. The Bruggeman model based on the mean field approach for expressing the thermal conductivity enhancement was chosen as a lower bound of the thermal conductivity relationship. The results showed that as the density and heat capacity of nanoparticles increase and the thermal conductivity and the shape factor of nanoparticles decrease, the convective motion in a nanofluid started more easily. The heat transfer coefficient of a nanofluid is enhanced with respect to the volume fraction of nanoparticles.

Roy et al. (2004) numerically investigated the flow and heat transfer characteristics of water- γ Al_2O_3 nanofluid in a radical laminar flow cooling system. Results indicated that considerable heat transfer enhancement was observed, even achieving a two fold increase in the case of applying a nanofluid with 10 vol% nanoparticles. On the other hand, the wall shear stress was also found to increase following the augmentation of particle volume concentration.

2.7.2 Two Phase Heat Transfer of Nanofluids

S. K. Das et al. (2003) first investigated the pool boiling characteristics of water-Al_2O_3 nanofluids. Nanoparticles were found to have pronounced and significant effect on deteriorating the boiling characteristics of the fluids. They pointed out that

nanoparticles were trapped on the heating surface during boiling process because the size of these particles are one to two orders of magnitude smaller than the surface roughness, thus plugging up the nucleation or boiling sites. Therefore the role of transient conduction of nanoparticles in pool boiling was probably overshadowed by the effect of trapped nanoparticles, which shifted the boiling characteristics in the negative direction. Consequently, an increase in the particle concentration resulted in more degradation in boiling performance which caused the surface temperature to rise further. The authors proposed that care should be taken in designing convective cooling systems with nanofluids to avoid occurrence of local boiling causing overheating of the surface.

This phenomenon was confirmed by Zhou and Liu (2004) for the convective heat transfer of $CaCO_3$ nanofluids within a copper tube even with the agitation of an acoustic cavitation field. They observed that nanoparticles deposited not only on the lower surface of the copper tube by gravity but also on the upper surface by absorption affinity because of its relatively smaller size. This caused the tube surface to become smooth, leading to a reduction in both single-phase convection and boiling heat transfer.

However, Yang (2003) reported a more encouraging result. He indicated that the deterioration effect caused by trapped nanoparticles can be eliminated through the use of a new advanced copper-graphite composite surface, in boiling of nanofluids.

You et al. (2003) studied the enhancement of critical heat flux in pool boiling from a flat square copper heater immersed in Al_2O_3-water nanofluid. An approximately 200% increase in critical heat flux was measured when nanofluid containing 0.005g/l

alumina particles is used as the cooling medium instead of pure water. However, the nucleate boiling heat transfer coefficients appear to be about the same.

Zhou (2004) experimentally investigated the pool boiling characteristic of acetone-based copper nanofluids with and without acoustic cavitation. The experimental results showed that single phase convection heat transfer was enhanced due to addition of copper nanoparticles, whereas the boiling heat transfer was reduced. This observation is consistent with previously published experimental work.

The application of nanofluid in heat pipe for CPU cooling system achieved more encouraging findings. Tsai et al. (2004) evaluated the effect of structural character of gold nanoparticles in nanofluid on heat pipe thermal performance. The thermal resistance of a conventional circular heat pipe with nanofluid or DI water was characterized. A significant reduction in thermal resistance of heat pipe with nanofluid was observed. The influence of nanoparticle size on the thermal performance of a vertical meshed heat pipe was also evaluated.

Chien et al. (2003) studied the performance of a disk-shaped miniature heat pipe with nanofluid as working medium, which is the aqueous solution of 17nm gold particles. The measured results showed that for the same charge volume, a significant reduction in thermal resistance of heat pipe was found with the application of nanofluid instead of DI water.

2.8 A Brief Review on Microchannel Heat Sink

In this project, we carried out a series of experiments to characterize the thermal performance enhancement of a nanofluid-cooled microchannel heat sink (MCHS) cooling system. A good understanding of the basic principles of microchannel heat

sink is crucial for carrying out performance analysis and evaluation. Thus a brief review of single-phase liquid-cooled microchannel heat sinks is also included.

The concept of microchannel heat sink was first introduced by Tuckerman and Pease (1981). A typical structure of microchannel heat sink is shown in Figure 2.8. Because heat transfer coefficient, h, is proportional to the reciprocal of characteristic length ($h = Nu \cdot k / D_h$), with small channel dimensions, extra high thermal performance can be achieved. For example, the total thermal conductance of a 251 μm wide and 1030 μm deep water-cooled silicon microchannel heat sink was found to be around $3\times10^{-6} m^2 K / W$ only (Harms et al., 1999).

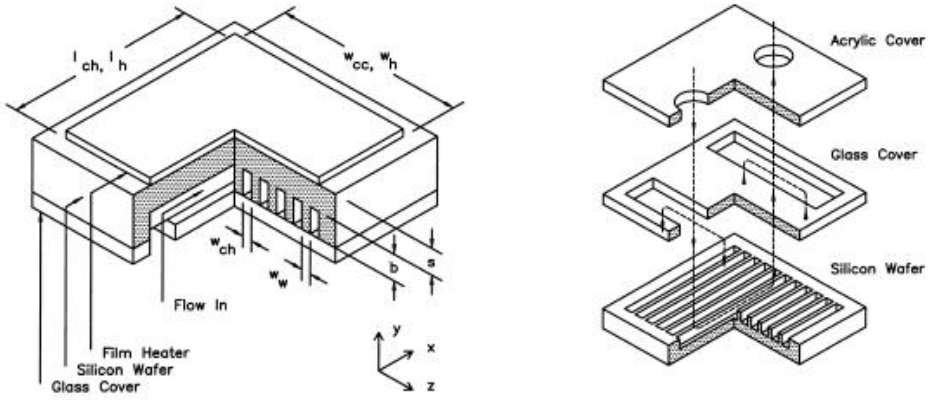

Fig 2.8: A typical liquid-cooled microchannel heat sink cooling system (Harms et al., 1999).

On the other hand, because of the small size of the flow passage, the pressure drop across MCHS is also significant, which in turn requires higher pumping power. Peng et al. (1994a) systematically investigated the pressure losses of water-cooled rectangular microchannels with hydraulic diameter, $133 < D_h < 343 \mu m$ and aspect ratio $1/3 < \alpha < 1$. The Poiseuille number, $f \mathrm{Re}_D$, was found not to be constant but to

decrease significantly with increasing Reynolds number and varied widely with D_h and α.

The later experiment of Peng and Peterson (1996) showed significant flow behavior deviations of microchannel from macro scale channel. Their results indicated that the flow in microchannel undergoes transition at a lower Reynolds number of 200 to 700, and fully turbulent convective heat transfer condition was reached when the Reynolds number ranged from 400 to 1500. Moreover, the transitional Reynolds number decreases with reductions in the microchannel dimensions. In addition, the transition range was observed to become smaller as well. They obtained the following updated correlations for heat transfer

$$Nu_{lam} = 0.1165\left[D_h/(w_{ch}+w_w)\right]^{0.81}\alpha^{0.79}\,\mathrm{Re}_D^{0.62}\,\mathrm{Pr}^{1/3} \tag{2.15}$$

$$Nu_{turb} = 0.072\left[D_h/(w_{ch}+w_w)\right]^{1.15}\left[1-2.421(\alpha-0.5)^2\right]\mathrm{Re}_D^{0.8}\,\mathrm{Pr}^{1/3} \tag{2.16}$$

The Nusselt number is proportional to thermal conductivity of the working medium by $k^{0.62}$ and $k^{0.8}$ in the above equations and the heat transfer coefficient is in turn proportional to $k^{1.62}$ and $k^{1.8}$. Therefore the application of high thermal conductivity coolant such as nanofluids will significantly improve the thermal performance of a microchannel heat sink cooling system.

The only available literature on the application of nanofluids in this area is from Lee and Choi (1996). They first mentioned that experiments were carried out in Argonne National Laboratory to study the feasibility and performance improvement of microchannel heat exchanger with nanofluid as coolant. The results indicated that the cooling rates of MCHS using nanofluids was dramatically enhanced compared with the cases of conventional water and liquid-nitrogen coolant. However, no detail information and experimental data are available.

Various theoretical analyses and optimization of the microchannel heat sink cooling system are available in the literature. Phillips (1988, 1990) developed a detailed thermal resistance model to study the performance of the microchannel heat sink within both the laminar and turbulent regimes. The model also included the effects of developing flow and variable viscosity. An optimization approach was also demonstrated. Samaiam (1989) used a quasi two dimensional differential equation to compute the optimum fin thickness and channel width of the heat sinks. The optimum designs can be achieved by making the aspect ratio as small as possible and simultaneously relaxing the constraint of $w_{ch} / w_w = 1$.

2.9 Closure

A literature review of the current stage of research and development of nanofluids is addressed in this chapter. Nanofluids synthesis methods, thermal conductivity measurement approaches and currently available experimental results of the effective thermal conductivity of nanofluids are extensively reviewed. Possible mechanisms that may contribute to the abnormally enhanced effective thermal conductivity of nanofluids are discussed in detail. Other thermophysical properties such as heat capacity and viscosity which are important to the fluid flow and heat transport are also addressed. Issues concerned with single phase and phase change convective heat transfer phenomena of nanofluids are discussed. Finally, a brief review of microchannel heat sinks is included.

CHAPTER 3: THERMAL CONDUCTIVITY CHARACTERIZATION OF NANOFLUIDS

3.1 Introduction

In this study the effective thermal conductivity of deionized water and ethylene glycol-based Al_2O_3, SiC and CuO nanofluids is characterized using the one-dimensional steady-state parallel-plate method. All the nanofluids studied were prepared in the laboratory following a two-step procedure except the CuO-water nanofluid, which was originally purchased from Nanotek Company with 15 wt% (2.67 vol%) nanoparticle concentration and diluted into different volume fractions for testing. For each nanoparticle and base fluid combination, nanofluids with different nanoparticle loadings were produced and tested to ensure a systematic investigation on particle volume fraction effects.

3.2 Nanofluids Preparation

The preparation of nanofluids is the first key step in thermal conductivity characterization. It must ensure proper dispersion of nanoparticles in the base liquid and proper treatment to attain the stability of suspension against sedimentation. In consideration of the high cost of the one-step method and the types of nanoparticles under testing, nanofluids in our current study were made following the so called two-step method, in which the nanoparticles were first produced and then dispersed into base fluids in a second step.

3.2.1 Nanoparticle Materials and Base Fluids

The alumina, silicon carbide and copper oxide nanoparticles with different morphology and size under our current investigations were sourced from professional

suppliers. These nanoparticles were produced using physical vapor synthesis method. The sizes of nanoparticles were well controlled and loose agglomerates were formed under atmospheric conditions, which are of the order of micrometers as can be seen in the SEM picture of 50nm SiC nanoparticles (Figure 3.1). However, when the nanoparticles were dispersed into the base fluids, these agglomerates can be easily broken to some extent giving particles of nanometer size. In the present study, ultrasonic vibration was employed to disperse the particles in the base fluids.

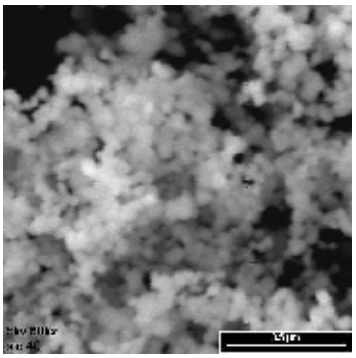

Figure 3.1: SEM image of 50nm SiC Nanoparticle.

The major physical and chemical properties of the base fluids and nanoparticles used in our current study are shown in the accompanying Table 3.1 and 3.2, respectively. Although we attempted to suspend various nanoparticles in FC-72 and FC-77, a proper method was not found in the current stage that can successfully suspend nanoparticles in these two base fluids.

Table 3.1: Physical and chemical properties of base fluids used in current experiments at room temperature and 1 atm.

Base Fluids	Color and Odor	Boiling Point (^{o}C)	Density (g/cm^{3})	Dynamic Viscosity (kg/m-s)	Thermal Conductivity (W/m-^{o}C)	Specific Heat (kJ/kg-K)
D.I. Water	Color less and odorless	100	0.998	0.001	0.604	4.18
Ethylene Glycol	Color less and odorless	197.6	1.11	0.02	0.26	2.40
FC-72	Color less and odorless	56	1.68	0.00064	0..057	1.10
FC-77	Color less and odorless	97	1.78	0.0013	0.063	1.10

Table 3.2: Physical and chemical properties of nanoparticles used in current experiments

	$\gamma - Al_2O_3$	CuO	$SiC(Amor.)$	$\beta - SiC$	$\beta - SiC$
AVS (nm)	60	20	10×100	20	45~55
Morphology	Powder	Powder	Powder	Powder	Powder
True Density (g/cm^3)	3.7	6.3~6.49	3.19	3.22	3.22
Bulk Density (g/cm^3)	0.16~0.4	0.79	0.061	0.069	0.068
SSA (m^2/g)	180	N/A	121~145	94	70~90
Color	White	Black	Black or Gray Black	black	Gray white
Purity	99.97%	>99%	>97.5%	>97%	>97.5%
Odor	odorless	odorless	odorless	odorless	odorless
Hazards Grade	Irritating respiratory systems	Irritating skin and respiratory system	Irritating eyes, skin & respiratory system	Irritating eyes, skin & respiratory system	Irritating eyes, skin & respiratory system
Handling & Storage	Nonflammable cool, dry Away from acids, alkali and oxidizing agents	Nonflammable cool, dry Away from acids, alkali and oxidizing agents	Away from oxidizing agents	Away from oxidizing agents	Away from oxidizing agents
Solubility in water	No	No	No	No	No
Dangerous Reaction	Exothermic with water	NA	Release CO & CO_2	Release CO & CO_2; metal fumes	Release CO & CO_2; metal fumes

3.2.2 Nanofluids Preparation Procedure

The two-step procedure for making the nanofluids used in our experiments is listed below:

a) Calculate and weigh the required nanoparticles and base fluid for nanofluid of a certain volume fraction.

b) Disperse the required amount of nanoparticles into certain pure base fluids and then mix with a magnetic agitator for one hour. A suitable dispersant may be added in this procedure for uniform dispersion.

c) Place the solution in the ultrasonic cleaner vibrating for another two hours.

It may be mentioned here that the true density of the particles is much larger than the

bulk density. Hence the volume of the solid was determined by calculating the equivalent weight of the solid using the true density. The weight of the air trapped inside is negligible.

In the current experiments, when making nanofluids containing SiC nanoparticles, an aqueous solution of Sodium Hydroxide (NaOH) was added as dispersant and the pH value of nanofluid was adjusted to be around 10. Because of the small amount of additives, normally less than 1%, its addition will not significantly influence the thermal conductivity of the base fluid itself and thus the real enhancement by using nanoparticles cannot be over shadowed. However, no third agent was added for the other nanofluids prepared in this study.

During the preparation procedure, the mixing processes significantly influence the dispersion uniformity and durability. Special attention should be drawn on these two procedures. The temperature of the ultrasonic bathing should be well controlled to avoid overheating, because it may induce or accelerate the chemical reaction between nanoparticles and base fluids. For example, when preparing the water-based Al_2O_3 nanofluids, high temperature enhanced the reaction of Al_2O_3 and water, which generates $Al(OH)_3$. In addition, when the nanofluids were placed in the ultrasonic bath, the container should be tightly sealed, especially for volatile liquids like FC-72 and FC-77. The leakage of vaporized base fluid may change the sample particle volume concentration.

As for the purchased CuO-water nanofluid, the amount of 15 wt% CuO-water nanofluid was first calculated according to the weight of nanoparticles needed. Extra deionized water was added to a certain amount of the original nanofluid according to the required nanoparticle volume concentration. Thereafter the diluted nanofluid

experienced a two hour ultrasonic vibration to ensure uniform dispersion.

3.2.3 Stability of As-prepared Nanofluids

In the current experiments, nanofluids containing Al_2O_3 or low volume fraction SiC (45~55nm) nanoparticles were well dispersed and little deposition were found even after being allowed to stand for two weeks. The original and diluted CuO-water nanofluids exhibited excellent dispersion stability and long time durability. Pictures of the 2 vol% Al_2O_3-water and 2 vol% CuO-water nanofluids prepared in the experiments are shown in Figures 3.2 and 3.3, respectively.

Figure 3.2: 2vol% Al_2O_3-water nanofluid

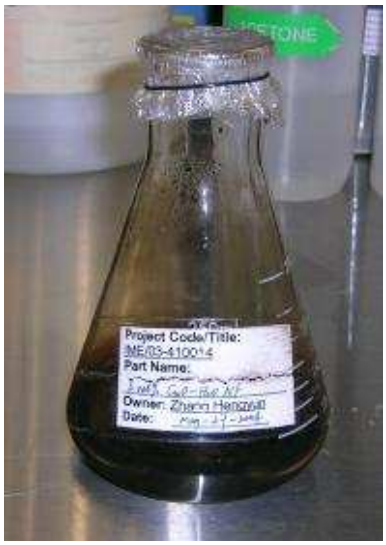

Figure 3.3: 2vol% CuO-water nanofluid

However, the 2 vol% and 3 vol% SiC-water nanofluids were less stable compared with other low fraction nanofluids. Sedimentation and layering can be clearly found after being placed stationary for a relatively long time period (Figure 3.4).

As mentioned earlier, we cannot successfully disperse nanoparticles into FC-72 and FC-77 in the current stage. Sedimentation appears almost immediately after mixing procedures, which indicates that special dispersant or treatment is necessary. Also, the 20 nm spherical and $10\times100nm$ needle-like amorphous SiC nanoparticles are difficult

to be dispersed into the base fluids used in our study, even with the same treatment as for the 40~50nm SiC nanoparticles. Probably due to its high viscosity, ethylene glycol based nanofluids are more stable than water and fluroinert liquid based nanofluids. For consistency in the current study, for each experiment freshly vibrated fluid was used for testing so that the experimental time of one to two hours does not bring out any sedimentation.

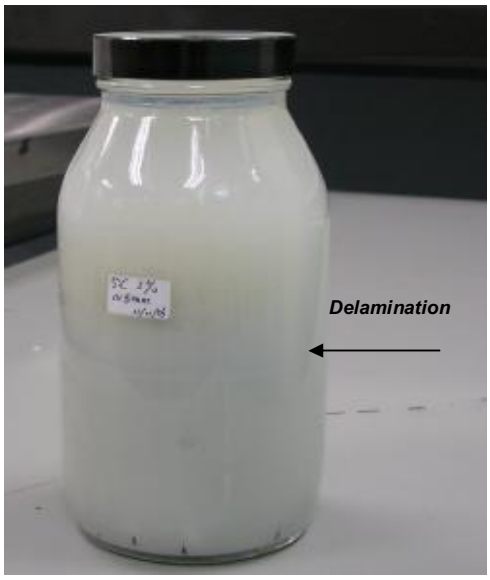

Figure 3.4: 2vol% SiC-water nanofluid after being placed stationary for two weeks.

3.3 Experiment Design and Operation Principles

3.3.1 Apparatus for Thermal Conductivity Testing

In the present experiments, one apparatus was fabricated for measuring the effective thermal conductivity of nanofluids. This apparatus was designed based on the one-dimensional steady-state parallel-plate method. This method interprets thermal conductivity value from the measurement in a straightforward manner, and it requires only a small amount of liquid sample. Figure 3.5 shows the schematic layout of the experimental apparatus, which generally follows the design of Challoner and Powell (1956).

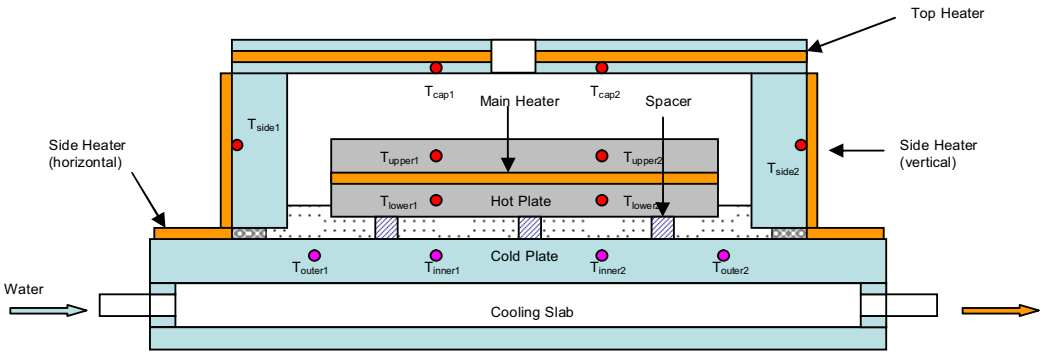

Figure 3.5: Schematic layout of the apparatus for liquid thermal conductivity measurement

The fluid sample is loaded in the gap between two parallel round copper plates, which are denoted as hot plate and cold plate respectively in Figure 3.5. The plate surfaces in contact with the test fluid are machined flat to a high degree of precision. The gap distance is kept fixed with the aid of three small identical PTFE spacers with thickness of 1mm or 2mm and a total footprint area of $10mm^2$. The liquid cell is housed in a large cylindrical aluminum cell. One neoprene rubber O-ring is placed between the aluminum cell and cold plate to prevent liquid leakage and provide insulation. The hot plate is centered and separated from the inside wall of the aluminum cell. The main heater, located in the middle of the hot plate, provides the heat flux from the lower surface of hot plate to the upper surface of the cold plate. Three guard heaters, viz. vertical side heater, horizontal side heater and top heater, are attached on the aluminum cell in order to control the temperature field surrounding the liquid cell and avoid heat loss to the ambient. The surface of liquid in the cell is slightly higher than the lower surface of the hot plate, which allows the free movement of liquid sample to accommodate the thermal expansion of the liquid. A cooling slab was applied below the cold plate to dissipate the heating power and maintain a temperature difference. A high performance pump and heat exchanger cooling system is employed, which uses water as its coolant. A small hole is drilled in

the center of the cap to let thermocouples and electrical wires for the main heater go through. However, it should be carefully sealed during the testing to prevent air circulation between the testing chamber and the ambient.

Calibrated T-type (Copper-Constantan) thermocouples are used to monitor the temperatures at different locations of the system as indicated in the layout. They are inserted in 0.89mm deep holes. Small slips of aluminum tapes are also inserted in these holes to fix up these thermocouples and make them touch the solid surface. The locations of the thermocouples in the hot and cold plates are very close to the lower surface of the hot plate and to the upper surface of the cold plate. Because the thermal conductivity of copper is much higher than that of the liquid, these thermocouples can accurately approximate the temperatures at the surface of the plates. A total of 12 thermocouples are used. Moreover, in order to prevent copper oxidization in the case of applying base and acid liquid samples, all the copper components of this apparatus are nickel-plated. The detail dimensions of this experimental apparatus can be found in the thesis of X. G. Li (2004). Figures 3.6 and 3.7 show the pictures of the fabricated experimental apparatus with sample loading and after final assembly.

Figure 3.6: Experiment apparatus with sample loading.

Figure 3.7: Assembled experiment apparatus.

3.3.2 Experimental System Construction

The schematic diagram of the entire experimental system for nanofluids thermal conductivity measurement is shown in Figure 3.8. During the testing, water is continuously circulated by a gear pump (HG0024 Micropump) following a simple closed loop. The water from the reservoir is pumped through the cooling slab of the fabricated thermal conductivity measurement apparatus and cooled down later by a high performance compact heat exchanger. The water is finally directed back to the reservoir after leaving the heat exchanger. Plastic pipes and brass connectors are used in the current experiment to construct all the water circuits.

Electrical supply of the main heater, three guard heaters and the gear pump is provided by power supplies with different output ranges. Their specifications can be found in Table 3.3.

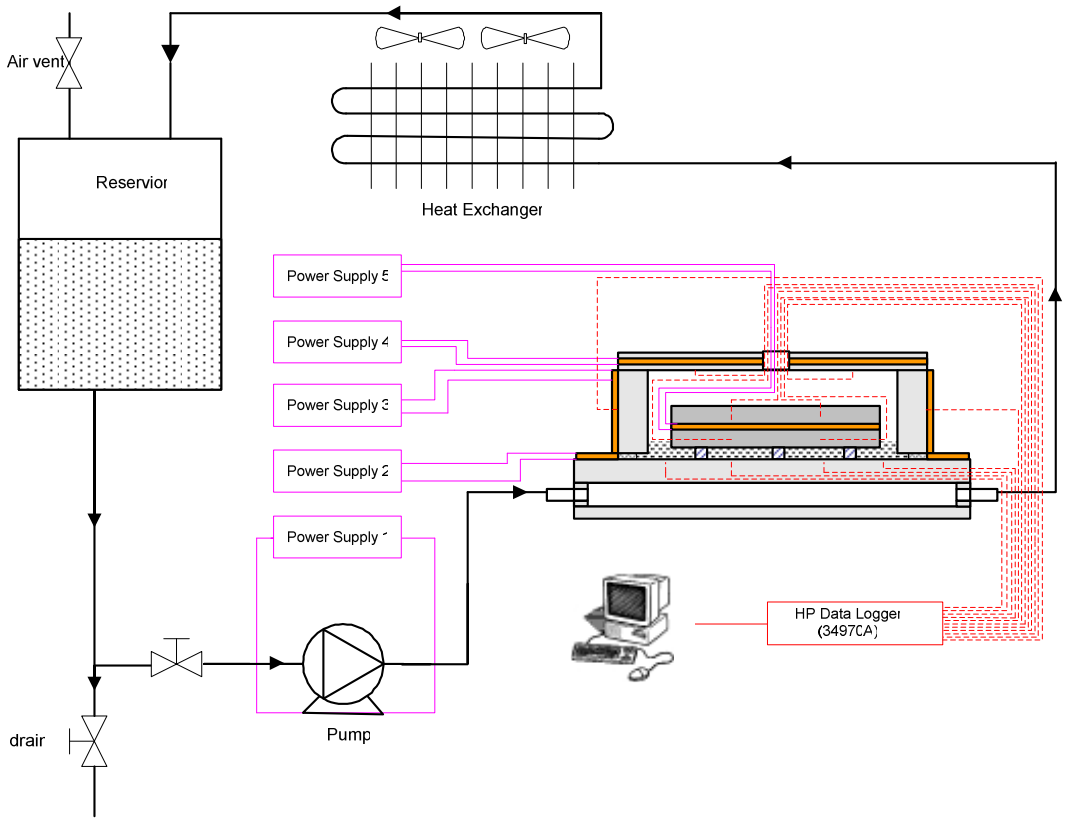

Figure 3.8: Schematic diagram of experiment system

Table 3.3: Specifications of power supplies

Item	Power Supply	Output Range
Main Heater	Keithley 228A programmable voltage/current source	0~100V (as a constant voltage source)
Side Compensate Heater (horizontal)	TTi PL330	0~32V (0~3A)
Side Compensate Heater (vertical)	Topward TPS-4000	2 X 0~30V (60V in Dual series mode)
Top Compensate Heater	TTi TSX1820P	0~18V (0~20A)
HG0024 Micropump	TTi PL330	0~32V (0~ 3A)

The Agilent Model 34970A data logger with a 20 channel armature multiplexer plug-in module (HP34901A) is used as the data acquisition unit. All the thermocouples are connected with the multiplexer module and routed to the built-in thermocouple reference junction. Hewlett-Packard Benchlink software is installed in the desktop to control the data logger and store the measured temperature data. Figure 3.9 shows a picture of the entire testing system.

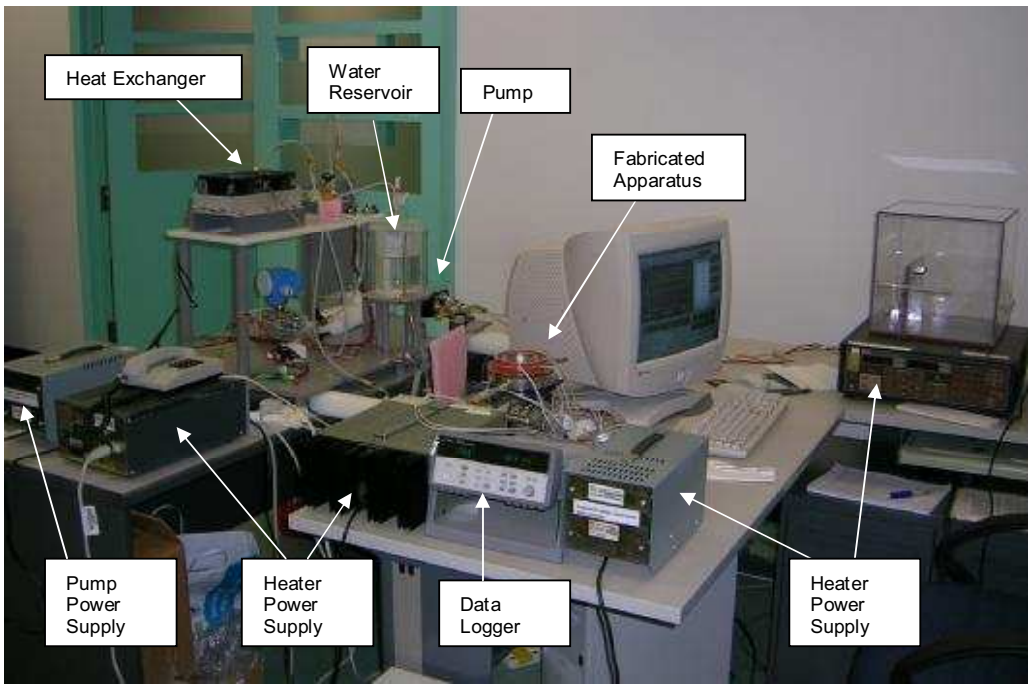

Figure 3.9: Picture of the experimental system.

3.3.3 Experiment Procedures

The experimental apparatus was assembled following the schematic of the apparatus setup. The seat and support of the apparatus were carefully adjusted to ensure its horizontality. The pipes, pump, compact heat exchanger and the cooling slab of the thermal conductivity measurement apparatus were connected following the schematic of the experimental setup. Hydraulic testing was carried out to check leakage problems before testing. All the thermocouples should be properly installed according to the apparatus setup and tested to be in good function. All the thermocouples were connected to the Agilent 34970A data logger for temperature measurement. Power supplies to the heaters, micro pump and heat exchanger fans were connected according to their corresponding power input requirements. All the power supplies were kept off during the preparation procedures.

The sample volume to be added was calculated according to the thickness of the PTFE spacer used. The fluid sample was put into the apparatus and the three spacers were carefully adjusted to be evenly distributed in the chamber. Gas bubbles were carefully avoided. The hotplate was placed in the center of the chamber. Its contact with the cell frame must be avoided. The cap of the apparatus was then tightened using screws. The cap center hole was carefully sealed to avoid air circulation between the chamber and the ambient.

During the thermal testing, the pump and heat exchanger fans were first turned on. The data logger was next activated to allow temperature monitoring. The power supplies for the main heater and other guard heaters were then switched on. The heating power of the main heater should be carefully adjusted to maintain enough temperature difference between the cold and hot plates of the apparatus. The power

input for different fluid varies. The recommended power inputs are given in Table A.1 of Appendix A. The heating power of the guard heaters should also be carefully adjusted to minimize the heat loss. Each experimental run should be conducted long enough to reach steady state (normally above 70 minutes) and the temperature reading deviation should be controlled to be less than 1%.

The experiment was stopped by turning off the temperature scanning process of the data logger first, and then turning off all the heaters, pump and heat exchanger fans. The detailed experimental procedure for characterizing the thermal conductivity can be found in Appendix C.

3.3.4 Data Reduction

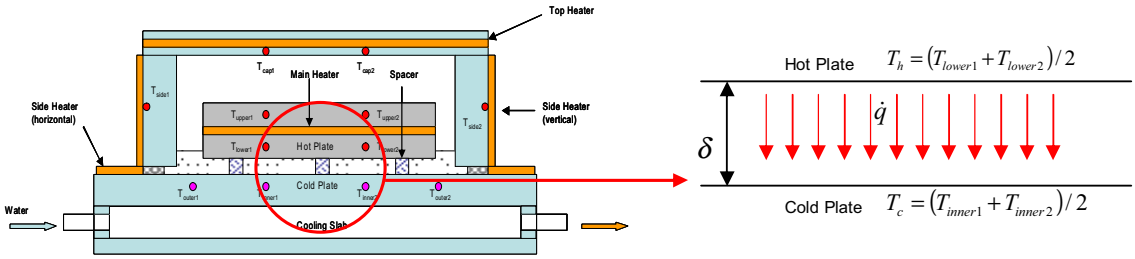

Figure 3.10: Thermal conductivity calculation theory

The effective thermal conductivity of the nanofluid sample can be calculated according to Fourier's law of heat conduction in one dimension, which states that heat flux is inversely proportional to the temperature gradient by a coefficient called thermal conductivity.

$$\dot{q} = -k\frac{dT}{dx} \tag{3.1}$$

Therefore the effective thermal conductivity in our experiment can be calculated as follows:

$$k = -\frac{Q \cdot dx}{A_h \cdot dT} = \frac{Q \cdot \Delta x}{A_h \cdot \Delta T} = \frac{Q \cdot \delta}{A_h \cdot (T_h - T_c)} \tag{3.2}$$

where,

$Q-$ Main heater heating power

$\delta-$ Thickness of PTFE spacer

A_h- Area of lower surface of hot plate

T_h- Mean temperature of lower hot plate surface, $(T_{lower1}+T_{lower2})/2$

T_c- Mean temperature of upper cold plate surface, $(T_{inner1}+T_{inner2})/2$

It might be mentioned here that the thermal conductivity calculated above is actually the average thermal conductivity ($\bar{k}$) of the sample within T_h and T_c temperature range.

$$\bar{k}=\frac{1}{T_h-T_c}\int_{T_c}^{T_h}k(T)dT \tag{3.3}$$

If k depends linearly on temperature, the average thermal conductivity $\bar{k}=k(\bar{T})$, where $\bar{T}=(T_h+T_c)/2$ is the average temperature. In most cases the linear approximation turns out to be adequate. If further correction for PTFE spacers is considered, the thermal conductivity of liquid sample can be modified as below.

$$k_{eff}=\frac{k\cdot A_h-k_s\cdot A_s}{A_h-A_s} \tag{3.4}$$

where,

A_s- Total footprint area of PTFE spacers

k_s- Thermal conductivity of PTFE spacers

3.3.5 Experimental System Calibration

The thickness of spacers was carefully measured before all the experiments using a digital caliper with accuracy of 0.001mm. These currently available PTFE spacers were measured to be 1.003mm and 2.006mm in thickness, respectively. Before applying the experiment system for nanofluid thermal conductivity measurement, it

was calibrated by measuring the thermal conductivity of D.I. water and ethylene glycol. The results were compared with the published data to examine the accuracy of our experimental system. Also, the influence of spacer thickness was studied.

Table 3.4: Thermal conductivity of DI water and ethylene glycol

Spacer	Thermal Conductivity (W/m-K)	
	D.I. water	Ethylene Glycol
1.003mm	0.636,0.639,0.632,0.634,0.632,0.635	—
Average	0.635	—
2.006mm	0.638, 0.641, 0.630,0.633, 0.642	0.268, 0.267
Average	0.636	0.268
Published Data	0.619 (at 303K and 1atm, J.P. Holman,2002)	0.253 (at 303K and 1atm, J.P. Holman, 2002)

The experimental results for the D.I. water and ethylene glycol with different spacers are listed in Table 3.4. It can be found from the results that our current experimental systems can provide quite reasonable measurement accuracy, whose uncertainty is only about 2~3% compared with the published data under the same conditions. Further, the results showed that the current experimental system with both 1.003mm and 2.006mm spacers can provide accurate measurements. However, thicker spacers are functionally more appropriate. Because in order to improve the measurement accuracy, a greater temperature difference between the hot plate and cold plate of the apparatus is preferred for the purpose of reducing the influence of thermocouple uncertainty. For the same temperature difference, the apparatus with thicker spacers needs relatively lower heat flux supply because thicker spacers increase the thickness of the liquid layer between the two plates, or in other words, it increases the thermal resistance between these two plates. Lower heating power can significantly reduce the influence of ambient temperature oscillation imposed on the heat exchanger and in turn on the measurement results. Also, for high thermal conductivity liquids such as water and water-based nanofluids, the required heating power for maintaining a

relatively large temperature difference using the 1.003mm thick spacers may exceed the voltage output range of the power supply for the main heater. In this case, a thicker spacer is also recommended. Therefore in consideration of the reasons mentioned above and for consistency, all the experiments for nanofluids were carried out using these 2.006mm spacers.

3.4 Results and Discussion

3.4.1 One Typical Experiment Run and Its Data Reduction

Using the experimental procedures and data reduction methods described earlier, a series of experiments for charactering the effective thermal conductivity of various nanofluids were carried out. One typical experiment run for testing the thermal conductivity of 1 vol% SiC-water nanofluid and its data reduction is shown in this section. The power inputs of the main heater and the guard heaters are shown in Table 3.5.

Table 3.5:Heater power inputs for thermal conductivity testing of 1 vol% SiC-water nanofluid

Sample under testing	1vol% SiC-water nanofluid		
Power Input	U (V)	I (A)	Q (W)
Main heater	42.00	0.414	17.39
Cap heater	19.50	0.64	12.56
Side heater (horizontal)	8.00	0.270	2.16
Side heater (vertical)	7.00	0.23	1.61

In this case, the whole experiment lasted for 6200 seconds. Figure 3.11 shows the temperature history of the positions in the experimental apparatus monitored using thermocouples. By carefully adjusting the heating power of the guard heaters, the temperature in the hot plate and the aluminum cell were well controlled to be close to each other and the temperature of the cold plate is also uniform, which indicates a low heat loss to the ambient. Figure 3.12 shows the change of temperature difference between hot and cold plate with time. It is quite stable after 2500 seconds and an

average temperature difference of 8.4°C is maintained thereafter. The detailed experimental data is tabulated in Appendix A (Table A.4).

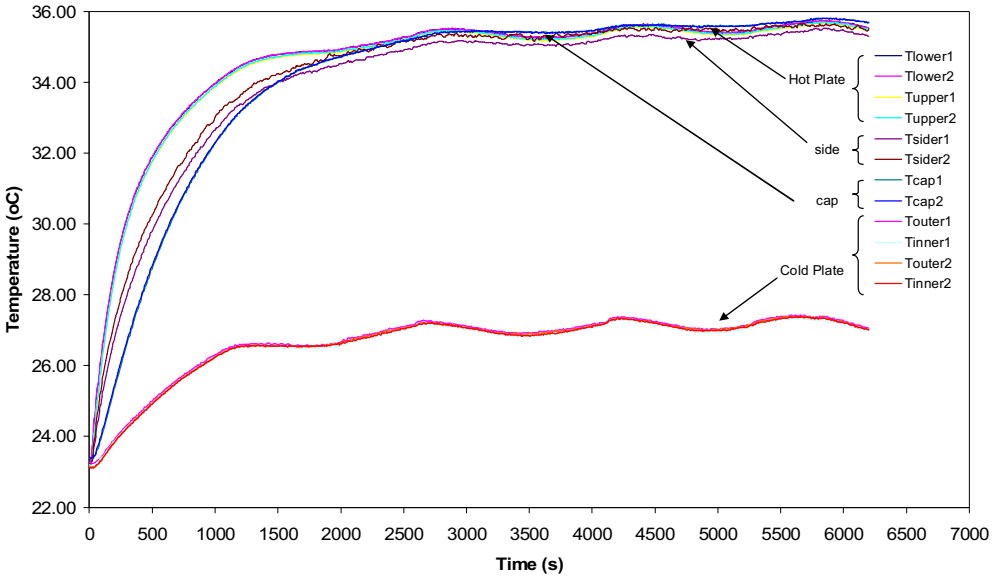

Figure 3.11: Temperature history at different location (1vol% SiC-water Nanofluid)

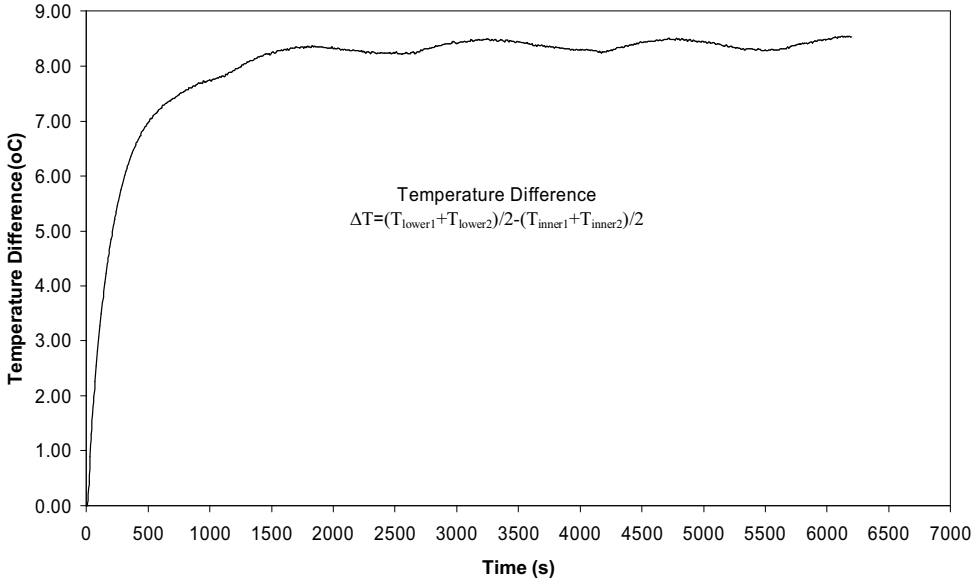

Figure 3.12: Temperature difference between hot plate and cold plate

The effective thermal conductivity of the sample is calculated using the temperature readings measured after the whole system has reached a stable state. Normally the average thermal conductivity value of the last 30 minutes can be considered as the

measurement result. Figure 3.13 shows the change of calculated effective thermal conductivity with time. In this case, the effective thermal conductivity calculated for 1 vol% SiC-water nanofluid is $0.662 W/m \cdot k$ and the standard deviation of the final result is about $0.009 W/m \cdot k$ (1.40%). The thermal conductivity ratio of 1 vol% SiC-water nanofluid over DI water is 1.072. It might be mentioned here that when calculating thermal conductivity ratio in all the cases, the thermal conductivity of pure base fluids used is the value obtained during calibration, i.e. 0.636 W/m-k for DI water and 0.268 W/m-k for ethylene glycol.

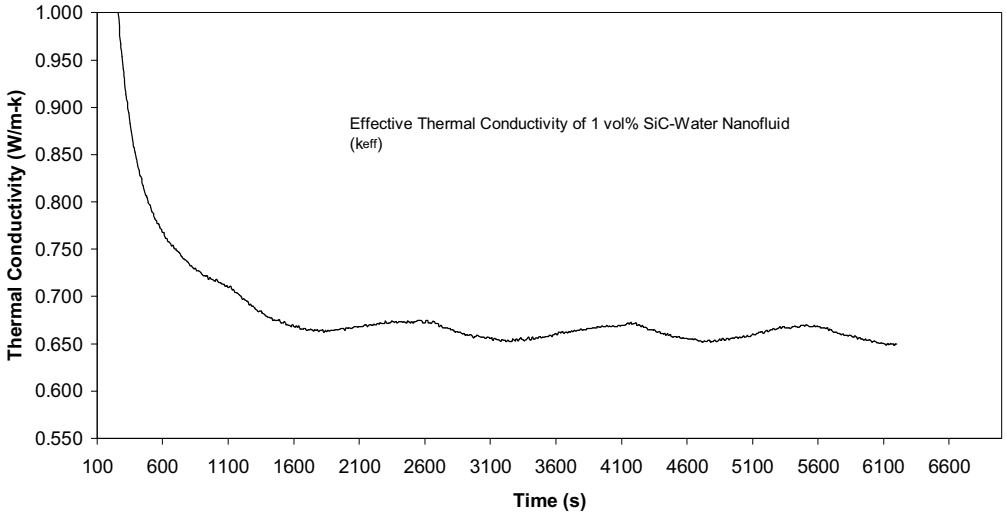

Figure 3.13: Changing of thermal conductivity with time (1vol% SiC-water nanofluid)

3.4.2 Summary of Experimental Results

The experimental results obtained in our current study are summarized in Table 3.6. For each sample, at least two replicants were provided. The details of all the available experimental data can be found in Appendix A (Table A.2~17). The recommended input voltage of the main heater and guard heaters for all kinds of nanofluids samples to obtain a temperature difference around 8°C or greater can be found in Table A.1 of Appendix A. All the experimental results were calculated exactly the same way as the sample case mentioned in the earlier section.

Table 3.6: Summary of experimental results.

Sample	Heating Power				Aver. Temp. Difference (°C)	Spacer Thickness (mm)	Thermal Conductivity (W/m-k)	Thermal Conductivity ratio (k_{eff}/k_l)
	Main Heater (W)	Cap Heater (W)	Side Heater (W)					
			Horiz.	Vert.				
D. I. Water	38.93	3.40	15.37	1.37	9.62	1.003	0.639	—
	30.86	2.64	12.05	0.85	7.78	1.003	0.632	—
	10.11	1.68	8.06	0.40	5.05	2.006	0.638	—
	10.11	1.68	8.06	0.40	5.10	2.006	0.633	—
	17.39	3.40	13.96	1.40	8.67	2.006	0.642	—
	17.30	2.08	13.96	1.61	8.57	2.006	0.644	—
Ethylene Glycol	9.49	2.79	14.60	1.40	11.18	2.006	0.267	—
	9,49	2.79	14.60	1.40	11.14	2.006	0.268	—
S_iC-H_2O NF								
1vol%	17.39	2.16	12.56	1.61	8.37	2.006	0.662	1.041
	17.39	2.16	12.56	1.61	8.39	2.006	0.660	1.038
2vol%	17.39	2.16	12.31	1.61	8.21	2.006	0.677	1.061
	17.39	2.16	12.31	1.61	8.21	2.006	0.682	1.072
3vol%	17.39	2.16	12.31	1.61	8.15	2.006	0.692	1.088
	17.39	2.16	12.31	1.61	8.42	2.006	0.692	1.088
4vol%	19.10	2.16	13.20	1.61	8.57	2.006	0.713	1.121
	19.10	2.16	13.20	1.61	8.56	2.006	0.713	1.121
Al_2O_3-H_2O NF								
1vol%	17.39	2.16	13.26	1.61	8.56	2.006	0.650	1.022
	17.39	2.16	13.26	1.61	8.55	2.006	0.650	1.022
2vol%	17.39	2.16	12.56	1.61	8.35	2.006	0.666	1.047
	17.39	2.16	12.56	1.61	8.37	2.006	0.664	1.044
3vol%	17.39	2.16	13.26	1.61	8.24	2.006	0.675	1.061
	17.39	2.16	13.26	1.61	8.24	2.006	0.675	1.061
4vol%	17.56	2.16	12.56	1.61	8.20	2.006	0.685	1.077
	17.56	2.16	12.56	1.61	8.22	2.006	0.686	1.079
CuO-H_2O NF								
1vol%	18.23	3.04	14.64	1.40	9.05	2.006	0.669	1.052
	18.23	3.04	14.64	1.40	8.96	2.006	0.661	1.039
2vol%	19.10	3.04	14.64	1.40	9.27	2.006	0.676	1.063
	19.10	3.04	14.64	1.40	9.27	2.006	0.674	1.060
15wt% (~2.7vol %)	19.10	3.61	16.08	1.40	9.21	2.006	0.683	1.074
	19.10	3.61	16.08	1.40	9.21	2.006	0.712	1.119
S_iC-EG NF								
1vol%	9.49	2.79	14.60	1.40	11.04	2.006	0.271	1.011
	9.49	2.79	14.60	1.40	10.94	2.006	0.274	1.022
2vol%	9.49	2.47	14.35	1.40	10.45	2.006	0.287	1.071
	9.49	2.47	14.35	1.40	10.71	2.006	0.284	1.060
3vol%	9.49	2.79	14.60	1.40	9.80	2.006	0.306	1.142
	9.49	2.47	13.26	1.40	9.85	2.006	0.304	1.134

Experimental results of the effective thermal conductivity of SiC-water nanofluids as a function of nanoparticle volume fraction are plotted in Figure 3.14. It can be found from the figure that the effective thermal conductivity of the nanofluids increases linearly with nanoparticle volume fraction. Figure 3.15 shows the ratio of effective thermal conductivity of SiC-water nanofluids at different volume fraction to that of pure DI water.

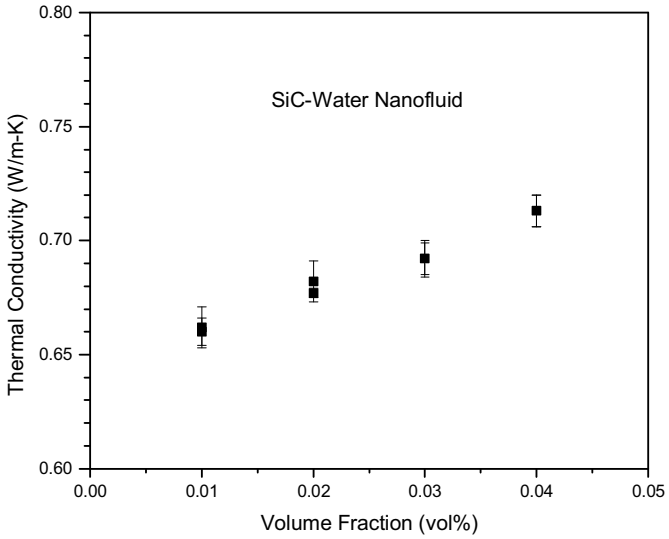

Figure 3.14: Effective thermal conductivity of SiC-water nanofluids

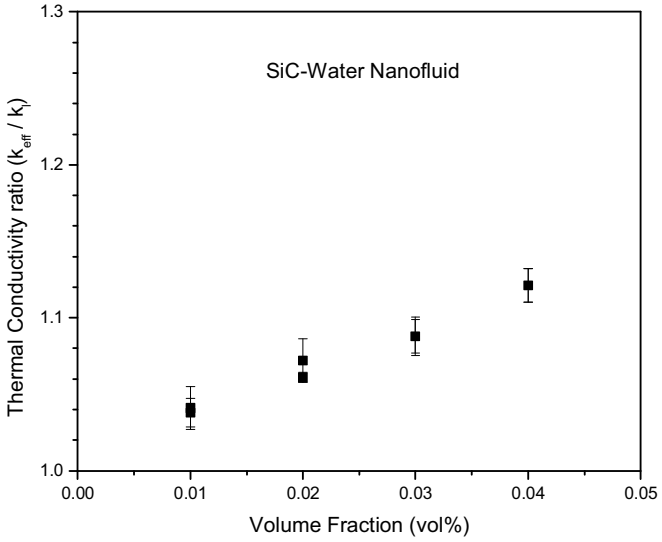

Figure 3.15: Ratio of thermal conductivity of SiC-water nanofluids to that of D.I. water

The absolute effective thermal conductivity of Al_2O_3-water nanofluids and the ratio of thermal conductivity of Al_2O_3-water nanofluids to that of D.I. water are demonstrated in Figure 3.16 and Figure 3.17, respectively. A similar linear trend of thermal conductivity increase is observed in this case.

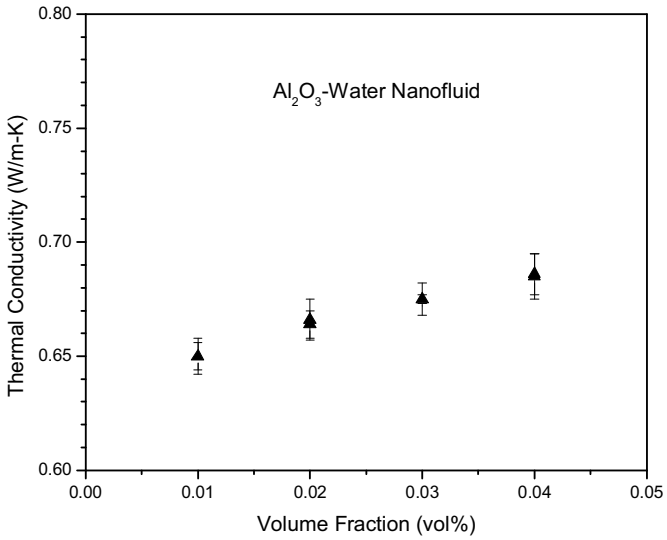

Figure 3.16: Effective thermal conductivity of Al_2O_3-water nanofluids

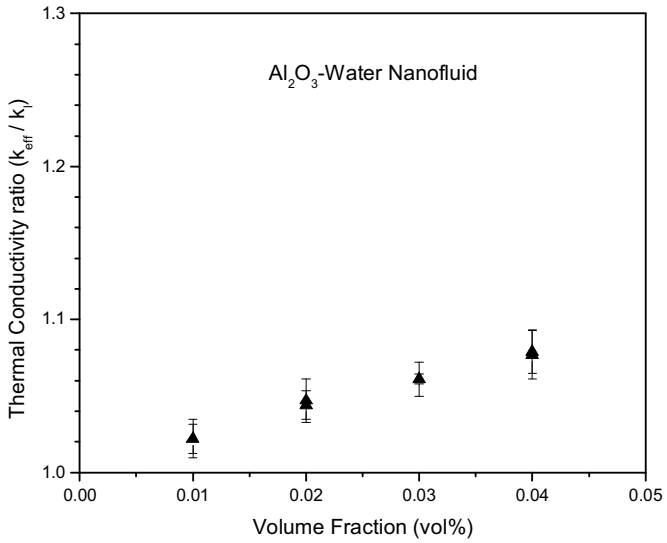

Figure 3.17: Ratio of thermal conductivity of Al_2O_3-water nanofluids to that of D.I. water

Figure 3.18 shows the effective thermal conductivity of the purchased CuO-water nanofluids and Figure 3.19 shows the ratio of thermal conductivity of CuO-water nanofluids to that of DI water. It can be seen from the figure that the two measurements taken for 15 wt% (2.7 vol%) CuO-water nanofluids have a large difference. One result is 0.712 W/m-K and the other is 0.683 W/m-K only. The higher value was measured just after the shipment and the lower one was taken one month later. Therefore one possible reason for the discrepancy is that some sedimentation had occurred after the as-purchased 15 wt% CuO-water nanofluid was placed stationary for a long time. In the latter experiments, the nanofluid sample under testing was taken from the upper part of the bottle containing the original 15 wt% nanofluid, which would most probably have a relatively lower particle volume fraction than 15 wt% (2.7 vol%). The effective thermal conductivities of the 15 wt% and the diluted 1 vol% and 2 vol% CuO-water nanofluids measured later are probably lower than the actual values because of their low nanoparticle volume fraction.

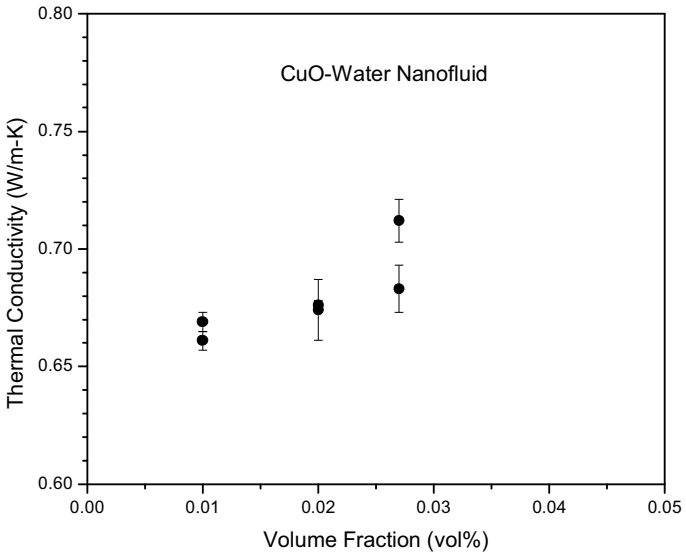

Figure 3.18: Effective thermal conductivity of CuO-water nanofluids

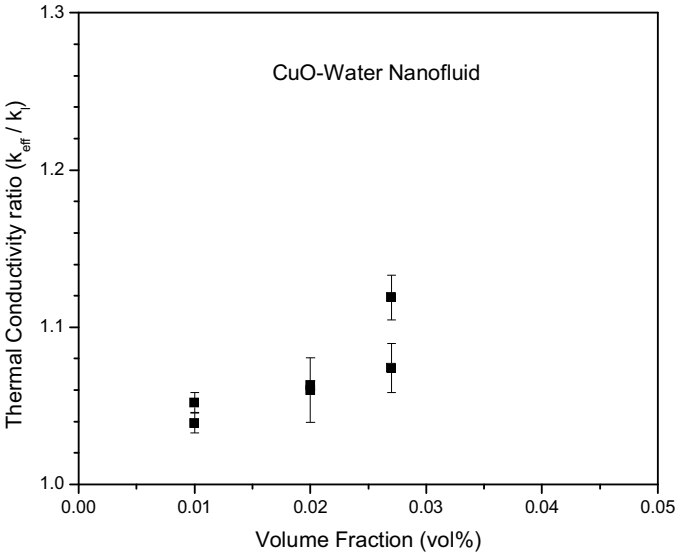

Figure 3.19: Ratio of thermal conductivity of CuO-water nanofluids to that of D.I. water

The effective thermal conductivity of SiC-ethylene glycol nanofluids as a function of SiC nanoparticle volume fraction is shown in Figure 3.20. The ratio of thermal conductivity of SiC-ethylene glycol nanofluids to that of pure ethylene glycol is shown in Figure 3.21.

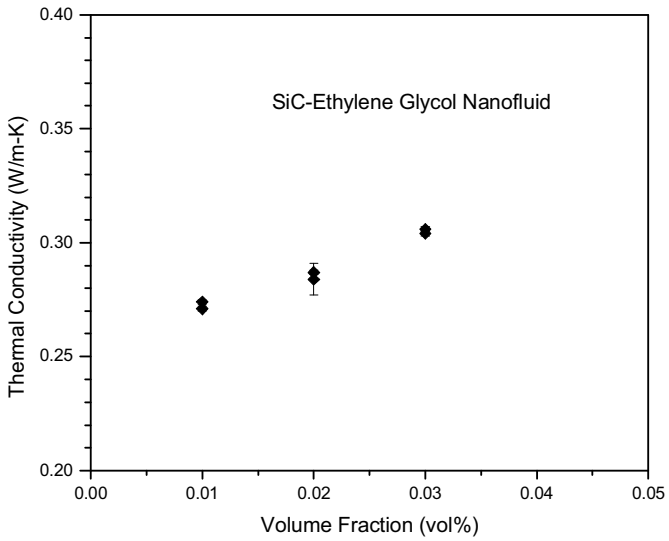

Figure 3.20: Effective thermal conductivity of SiC-ethylene glycol nanofluids

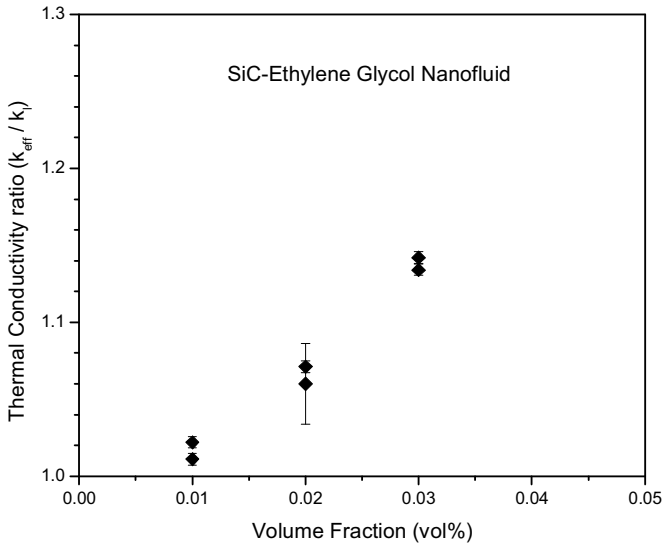

Figure 3.21: Ratio of thermal conductivity of SiC-ethylene glycol nanofluids to that of ethylene glycol

For all the nanofluids tested in our current study, the effective thermal conductivity increases linearly with the volume fraction of nanoparticles. However, for water based nanofluids, the thermal conductivity increases are different for different nanoparticles at a given volume fraction. The thermal conductivity increase of SiC-water nanofluids and CuO-water nanofluids is higher than Al_2O_3-water nanofluids. For example, at 2% volume fraction, the effective thermal conductivity of SiC-water nanofluid and Al_2O_3-water nanofluid increases 6.67% and 6.62%, respectively, whereas the thermal conductivity increase of Al_2O_3-water nanofluid is 4.55%. Probably due to the sedimentation problem mentioned earlier, the effective thermal conductivity of CuO-water nanofluid samples measured later is similar to that of SiC-water nanofluids at same volume fraction, although the size of CuO nanoparticles is smaller and a higher increase in effective thermal conductivity is expected. Among all the nanofluids measured, the thermal conductivity enhancement of SiC-ethylene glycol nanofluids is the highest. For example, the thermal conductivity of 3vol% SiC-ethylene glycol nanofluid increase 13.8%, however, that of the 3vol% SiC-water nanofluid increases 8.8% only. This result is expected as the stability of the ethylene glycol based

nanofluids prepared in our current experiments is better than the water based nanofluids.

3.4.3 Comparison with Experimental Results from Literature and Theoretical Model Prediction

From the experimental results in the present study, a linear variation of effective thermal conductivity increase is observed, which agrees with the results reported in literature. However, the effective thermal conductivity of Al_2O_3-water nanofluids in our experiment is different from the reported values. Masuda et al. (1993) reported that the effective thermal conductivity of 3 vol% Al_2O_3-water nanofluid is 20% higher than that of pure DI water. Wang et al. (1999) obtained a 12% increase at the same volume fraction. The experiment result of Lee et al. (1999) shows an 8% increase, whereas the thermal conductivity increase observed in our present experiments is about 6.1%. The size of the Al_2O_3 nanoparticle used in different experiments may be responsible for the discrepancy. The average diameter of the Al_2O_3 nanoparticles used in the experiments of Masuda et al. is 13nm, and those in the experiments of Wang et al. and Lee et al. are 28nm and 38 nm, respectively. However, the average diameter of the alumina nanoparticles used in our current study is about 60nm. It is possible that the size of the nanoparticles significantly influences the effective thermal conductivity of nanofluids.

CuO-water nanofluids were reported to have more significant enhancements in effective thermal conductivity than those water based nanofluids containing Al_2O_3 nanoparticles. This phenomenon was again proved by the results of our experiment. The effective thermal conductivity of the fresh 15 wt% (2.7 vol%) CuO-water nanofluid is 0.712 W/m-K and that of 3 vol% Al_2O_3-water nanofluid is 0.675W/m-K. The effective thermal conductivity of the fresh 15 wt% CuO-water nanofluid in our

study shows excellent agreement with that reported by Lee et al. (1999) and Das et al. (2002). The particle size in the experiments of Lee et al., Das et al. and the present study is 18.6nm, 28.6nm and 20nm, respectively.

The thermal conductivity increase of SiC-water nanofluids in our experiments is close to that of the 26nm and 900nm SiC-water nanofluids but lower than that of the 600nm SiC-water nanofluids reported by Xie et al. (2002b). A similar nanofluid preparation method of Xie et al. was used in our current experiments. However, the average diameter of SiC nanoparticles used in present study is around 50nm.

As to the effective thermal conductivity of SiC-ethylene glycol nanofluids, the experimental results in the present study is different from the values reported by Xie et al. (2002b), which is lower than that of nanofluids containing 600nm SiC nanoparticles and higher than that of those containing 26nm and 900nm SiC nanoparticles.

Figure 3.22-25 show the comparison between the experimental results and the value predicted by Hamilton and Crosser model (HC model) on the thermal conductivity ratio of nanofluids. In the calculation, thermal conductivity of SiC, Al_2O_3 and CuO is chosen as 90W/m-K, 36W/m-K and 15W/m-K, respectively. Because the particle shape is spherical in our current experiments, the shape factor in the HC model is set to be 3.0. For the SiC-water nanofluids and CuO-water nanofluids, the predicted value is close to the experimental results. However, the HC model overestimates the thermal conductivity increase of Al_2O_3-water nanofluids and underestimates that of the SiC-ethylene glycol nanofluids. This clearly suggests that the HC model, which only accounts for the particle shape, is not sufficient to explain the heat transfer processes in nanofluids.

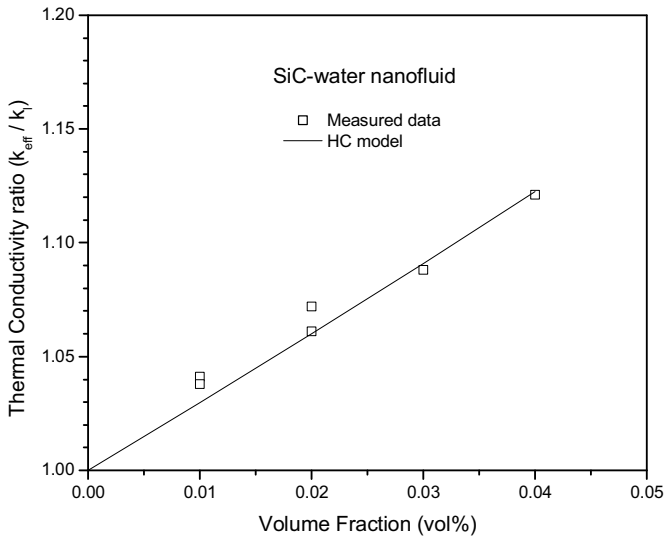

Figure 3.22: Experimental results and HC model predictions for SiC-water nanofluids

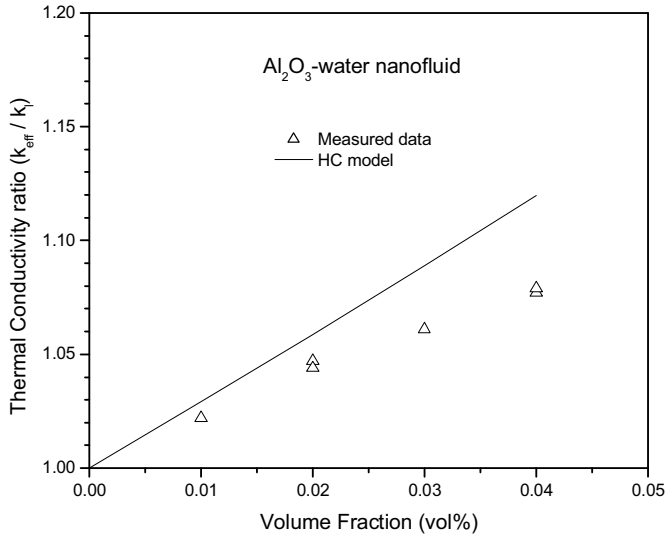

Figure 3.23: Experimental results and HC model predictions for Al_2O_3-water nanofluids

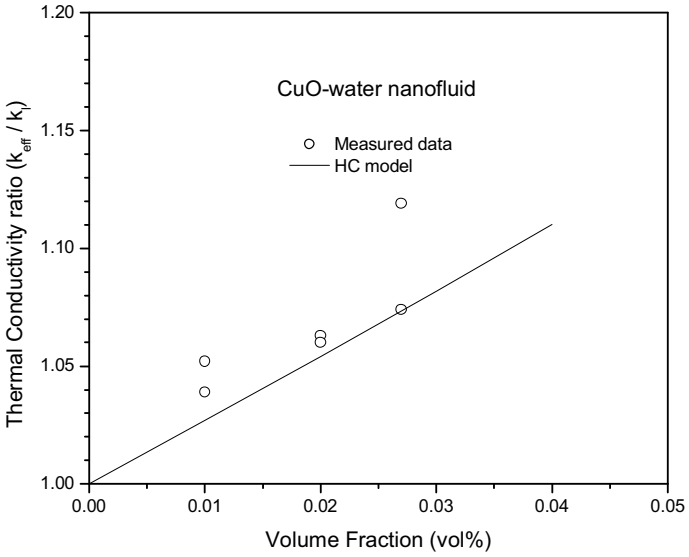

Figure 3.24: Experimental results and HC model predictions for CuO-water nanofluids

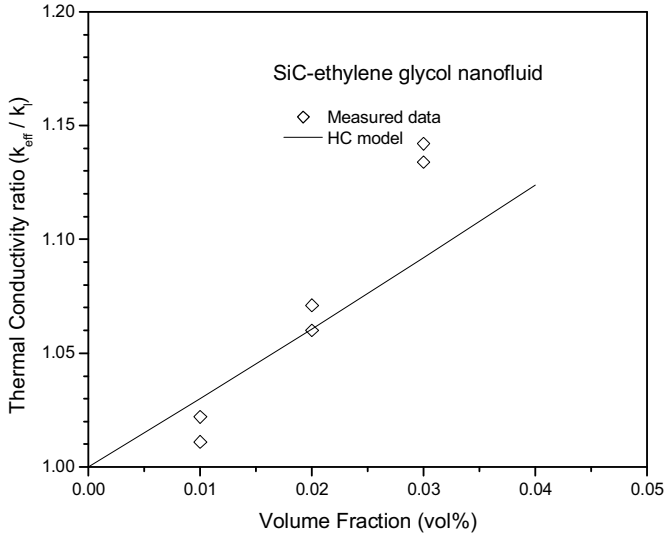

Figure 3.25: Experimental results and HC model predictions for SiC-ethylene glycol nanofluids

3.4.4 Error Analysis

There are altogether 12 T-type thermocouples installed in the experiment apparatus to monitor the temperature. Four thermocouples near the lower surface of the hot plate and upper surface of the cold plate are used in the measurement of the thermal conductivity. All the thermocouples were calibrated against Master Mercury-in-glass

thermometers using a Hakke Water Bath. The calibration range was from 20°C to 100°C. In this work, although the absolute value of temperature is to be measured, it is more important to measure accurately the temperature difference of the thermocouples. The measurement uncertainty of the calibrated T-type thermocouples is around 0.1°C, therefore the uncertainty of the temperature difference between the hot and cold plate is about 0.2°C. During the experiments, the temperature difference across the liquid layer was normally maintained to be greater than 8°C for the purpose of minimizing the influence of temperature measurement uncertainty on experimental results.

Defects in alignment of hot and cold plates make a first-order contribution to the inaccuracy, therefore the plate surfaces in contact with the test fluid were machined flat to a high degree of precision and the thickness of spacers were carefully examined using a digital caliper to ensure uniformity. The accuracy of the caliper used is ±0.001mm. PTFE spacers, 2.006mm in thickness, were used in all the experiments for characterizing the thermal conductivity of nanofluids. However, if the correction due to spacers is considered, the ideal spacer material will hold the same thermal conductivity as the liquid sample under test. The thermal conductivity of PTFE spacers is about 0.27W/m-K. The deformation of spacers under the weight of the hot plate is calculated in Table 3.7. Its variation is negligible.

Table 3.7: PTFE spacer deformation calculation

Young's Module (N/m^2)	Weight of hot plate (kg)	Stress (N/m^2)	Strain
399895906	0.911	1404	3.51E-06

Generally, a temperature gradient between two plates induces not only thermal conduction but also leads to convection and radiation. In addition, parasitic heat losses also need to be taken into account. In the present apparatus, the effects of convection

were made negligibly small by putting the plates in a horizontal position, heating from above and by using a small gap distance. According to Wakeham et al. (1991), a spacer thickness greater than 2mm will greatly enhance the natural convection. To eliminate heat losses, three guard heaters were used to raise the temperature of the aluminum cell to that of the upper copper plate in order to eliminate convection and radiation losses from the upper copper plate. Heating powers of guard heaters were carefully adjusted. The temperature difference between the upper hot plate and the wall of the aluminum cell was well controlled to be less than $0.5^{o}C$, and the temperature uniformity in the hot and cold plates was better than $0.2^{o}C$. Although it is not ideal to carry out this kind of thermal experiment in an air conditioned laboratory, the room temperature was well controlled to be $21\pm1^{o}C$. To reduce the radiation effect, the plate surfaces were polished and protected against oxidation with nickel plating, which provides low emissivity. Moreover, because liquid based nanofluid is almost opaque and highly absorbable, the heat transferred from the hot plate to cold plate by radiation is considered to be negligible.

Attempts were made to characterize low thermal conductivity and low viscosity samples such as FC-77 and air using our current apparatus. However significant oscillation was observed. Because the main heater heating power was relatively small compared with the heating powers of the guard heaters for balancing heat loss from the top and side. Therefore small fluctuations of ambient temperature will significantly influence the experimental results. Although we can increase the heating power and maintain a higher temperature difference, it will drastically enhance the natural convection due to the low viscosity. The experimental result will be much less than their actual thermal conductivity value.

When results are calculated from experimental measurements, the effect of individual measurement uncertainties on the result can be estimated by uncertainty analysis using the root-sum-square method (Moffat, 1988). The result, R, is a function of a set of measurements, which can be written as

$$R = R\left(x_1, x_2, ...x_n\right) \tag{3.5}$$

where x_1 to x_n are the measured variables.

The overall uncertainty can be calculated as

$$\delta R = \left[\sum_{i=1}^{n}\left(\frac{\partial R}{\partial x_i}\delta x_i\right)^2\right]^{1/2} \tag{3.6}$$

And the relative uncertainty is

$$e = \frac{\delta R}{R} = \left[\sum_{i=1}^{n}\left(\frac{1}{R}\frac{\partial R}{\partial x_i}\delta x_i\right)^2\right]^{1/2} \tag{3.7}$$

The thermal conductivity in the present study can be presented as

$$k = \frac{Q\cdot\Delta x}{A_h\cdot\Delta T} \tag{3.8}$$

The independent parameter measured in experiment is temperature difference ΔT, which is equal to $\left(t_h - t_c\right)$. The relative uncertainty in obtaining the thermal conductivity, e_k, can be derived as follows:

$$\Delta k = \left[\left(\frac{\partial k}{\partial \Delta T}\Delta\left(\Delta T\right)\right)^2 + \left(\frac{\partial k}{\partial Q}\Delta Q\right)^2\right]^{1/2} = \left[\left(-\frac{Q\Delta x}{A_h\Delta T^2}\Delta\left(\Delta T\right)\right)^2 + \left(\frac{\Delta x}{A_h\Delta T}\Delta Q\right)^2\right]^{1/2} \tag{3.9}$$

So,

$$e_k = \left[\left(\frac{\Delta\left(\Delta T\right)}{\Delta T}\right)^2 + \left(\frac{\Delta Q}{Q}\right)^2\right]^{1/2} \tag{3.10}$$

One typical set of experimental data of 2vol% SiC-EG is selected to evaluate the accuracy of the experiment. The accuracy of the main heater heating power provided

by Keithly 228A voltage/current source equipment is 0.1W (0.1V in voltage and 0.001A in current). The uncertainty of the measured temperature difference is up to 0.2°C. The total uncertainty of experiment results are calculated in Table 3.8.

Table 3.8 Analysis of experimental uncertainty for thermal conductivity

ΔT (°C)	Q (W)	$\Delta(\Delta T)$ (°C)	ΔQ (W)	e_k
8.35	17.39	0.2	0.1	2.46%

3.5 Numerical simulation

A two dimensional steady state numerical simulation using commercial software FLUENT was carried out to characterize the system error due to natural convection. Since the temperature dependent thermal properties of D.I. water is well published, it was chosen as the liquid sample in the current numerical simulation. The effects of natural convection were examined by comparing the thermal conductivity value inputted in the numerical model and the value calculated using equation 3.2 according to the simulation results.

3.5.1 Governing Equations

In this simulation, fluid sample was modeled as a pure incompressible Newtonian fluid with temperature dependent viscosity and thermal conductivity. As the fabricated experimental apparatus is axisymmetric, only half of the cross section is studied. The detailed geometry is shown in Figure 3.26.

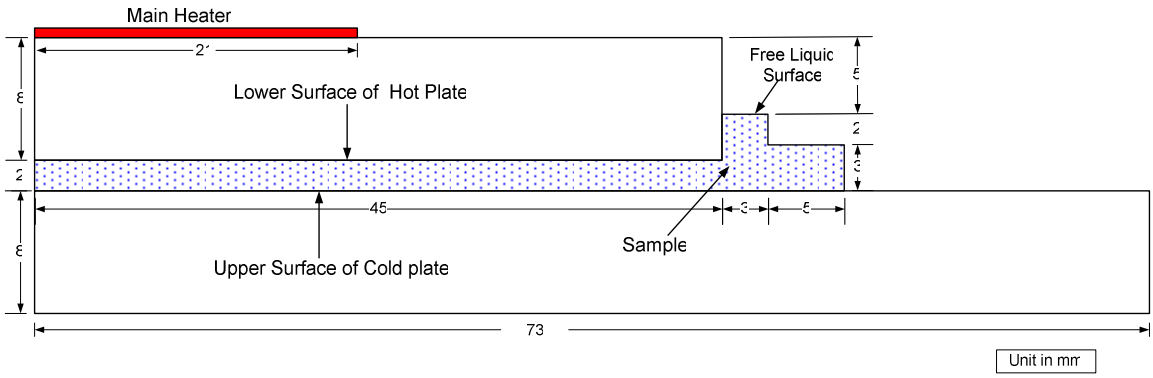

Figure 3.26: Half cross section of the fabricated experiment apparatus

The governing equations of this simplified model are given below.

- Continuity Equation

$$\nabla \cdot \mathbf{v} = 0 \tag{3.11}$$

where $\mathbf{v}$ is the velocity vector.

- Momentum equation

Here we treat the nanofluids as an incompressible Newtonian fluid with temperature dependent viscosity, therefore the stress tensor $\mathbf{T} = -P\mathbf{I} + \nabla\bullet(\mu\nabla\mathbf{v})$. The momentum equation thus can be written as

$$\rho\frac{D\mathbf{v}}{Dt} = -\nabla p + \rho\mathbf{g} + \nabla\bullet(\mu\nabla\mathbf{v}) \tag{3.12}$$

In the cylindrical coordinate system the above governing equation can be written as,

$$\frac{1}{r}\frac{\partial}{\partial r}(\rho r v_r) + \frac{\partial}{\partial z}(\rho v_z) = 0 \tag{3.13}$$

$$\rho\left(v_r\frac{\partial v_r}{\partial r} + v_z\frac{\partial v_r}{\partial z}\right) = -\frac{\partial p}{\partial r} + \left[\frac{\partial}{\partial r}\left(\mu\frac{1}{r}\frac{\partial}{\partial r}(r v_r)\right) + \frac{\partial}{\partial z}\left(\mu\frac{\partial v_r}{\partial z}\right)\right] \tag{3.14}$$

$$\rho\left(v_r\frac{\partial v_z}{\partial r} + v_z\frac{\partial v_z}{\partial z}\right) = -\frac{\partial p}{\partial z} + \left[\frac{1}{r}\frac{\partial}{\partial r}\left(\mu r\frac{\partial v_z}{\partial r}\right) + \frac{\partial}{\partial z}\left(\mu\frac{\partial v_z}{\partial z}\right)\right] + \rho g \tag{3.15}$$

When modeling the effect of natural convection on the experiments, the Boussinesq approximation model was used to get faster convergence. Inasmuch as the temperature difference in the testing system is less than 30°C, the density variation of liquid is relatively small. This model treats density as a constant value in all solved equations, except for the buoyancy term in the momentum equation:

$$(\rho - \rho_o)g \approx -\rho_o\beta(T - T_o)g \tag{3.16}$$

where,

ρ_o — (constant) density of the flow,

T_o — operating temperature,

β — volume thermal expansion coefficient.

Equations are obtained using the Boussinesq approximation $\rho = \rho_o\left(1-\beta\Delta T\right)$ to eliminate ρ from the buoyancy term. This approximation is accurate as long as changes in actual density are small; specifically, the Boussinesq approximation is valid when $\beta\left(T-T_o\right)<<1$.

- Energy equation

  The energy equation for Newtonian fluids with temperature dependent thermal conductivity is

$$\rho C_p \frac{DT}{Dt} = \nabla\bullet\left(k\nabla T\right)+\mu\Phi_v \tag{3.17}$$

where Φ_v is the dissipation term. Because of its small magnitude in natural convection, the heat dissipation term is neglected in the current simulation.

Therefore in the cylindrical coordinate system, the energy equation can be written as,

$$\rho C_p\left(v_r\frac{\partial T}{\partial r}+v_z\frac{\partial T}{\partial z}\right)=\frac{1}{r}\frac{\partial}{\partial r}\left(kr\frac{\partial T}{\partial r}\right)+\frac{\partial}{\partial z}\left(k\frac{\partial T}{\partial z}\right) \tag{3.18}$$

3.5.2 Boundary Conditions

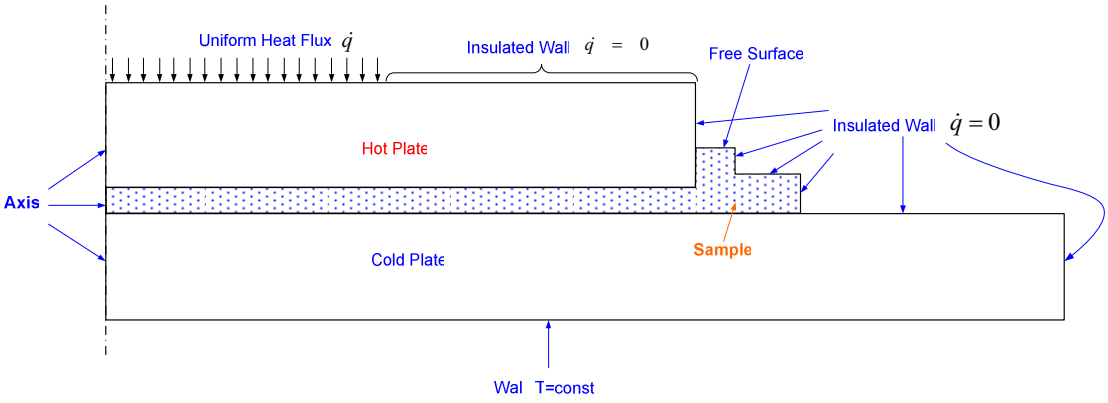

Figure 3.27: Boundary conditions of numerical simulation

The boundary conditions are listed below,

- Left boundary ($r = 0$)

  A symmetric boundary condition was applied.

$$\frac{\partial v_z}{\partial r} = 0 \ , \ v_r = 0 \tag{3.19}$$

- Bottom ($z = 0$)

  Because a high performance cooling system was employed, a constant temperature boundary condition was applied.

$$T = 300K \ \text{ for all r at z=0} \tag{3.20}$$

- Free liquid surface.

  This boundary condition can be modeled by a typical pillbox approach, for which at the interface

$$\mathbf{n} \cdot \left(\mathbf{T_l} - \mathbf{T_g} \right) = 2H\sigma\mathbf{n} - \nabla_s \sigma \tag{3.21}$$

  where H is the mean curvature, σ is the surface tension and ∇_s is the surface gradient operator. The stress caused by surface tension and interfacial tension gradient are negligible for the purpose of simplification in the current case. The normal velocity in our current simulation is assumed to be zero at the free surface. The tangential stress balance was simplified to the following result. At the free surface,

$$\mu_l \frac{\partial v_{r,l}}{\partial z} = \mu_g \frac{\partial v_{r,g}}{\partial z} \tag{3.22}$$

  Or,

$$\frac{\partial v_{r,l}}{\partial z} = \frac{\mu_g}{\mu_l} \frac{\partial v_{r,g}}{\partial z} \tag{3.23}$$

  where the subscripts l and g represent the liquid and gas phase, respectively. The viscosity of liquid is much larger than gas, therefore $\partial v_{r,l} / \partial z \approx 0$ at the free surface.

Thus the boundary condition $\partial v_r / \partial z = 0$ was used at the free surface in this case.

- Other boundaries

Because of the use of compensate heaters, heat losses at the other boundaries were minimized. Therefore all the other boundaries are assumed to be adiabatic boundaries. Heat loss due to radiation is also neglected.

3.5.3 Simulation Results and Discussion

Figure 3.28 shows the mesh of the two dimensional model built in this work. A coarse mesh was applied for solid domains and a very fine mesh was used for the liquid phase. Three layers of fine mesh in the solid side are attached at the solid-liquid interface to smooth the mesh size variation.

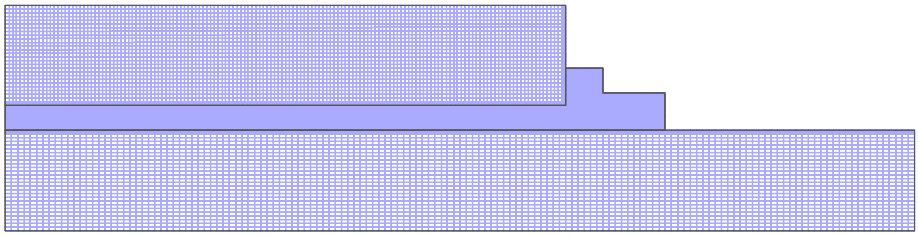

Figure 3.28 Mesh of numerical model

The numerical model was used to characterize the system error when pure DI water was applied. In order to account for the temperature-related variation of thermal conductivity and viscosity, three term polynomial fitting equations are used in the numerical model for predicting these two parameters. These two polynomial fitting equations are shown as follows,

$$k = -0.53164 + 0.00605225T - 0.0000075T^2 \quad (3.24)$$

$$\mu = 0.029099 - 0.00016913T + 0.00000025T^2 \quad (3.25)$$

The numerical simulation results of one typical case are shown in the following. The simulation inputs are summarized in Table 3.9.

Table 3.9: Simulation input of one typical case

Main heater heating power (W)	Cold plate temperature (K)	Operating temperature in Boussinesq model (K)	Thermal expansion coefficient (1/K)
17.39	300	303	0.0003817

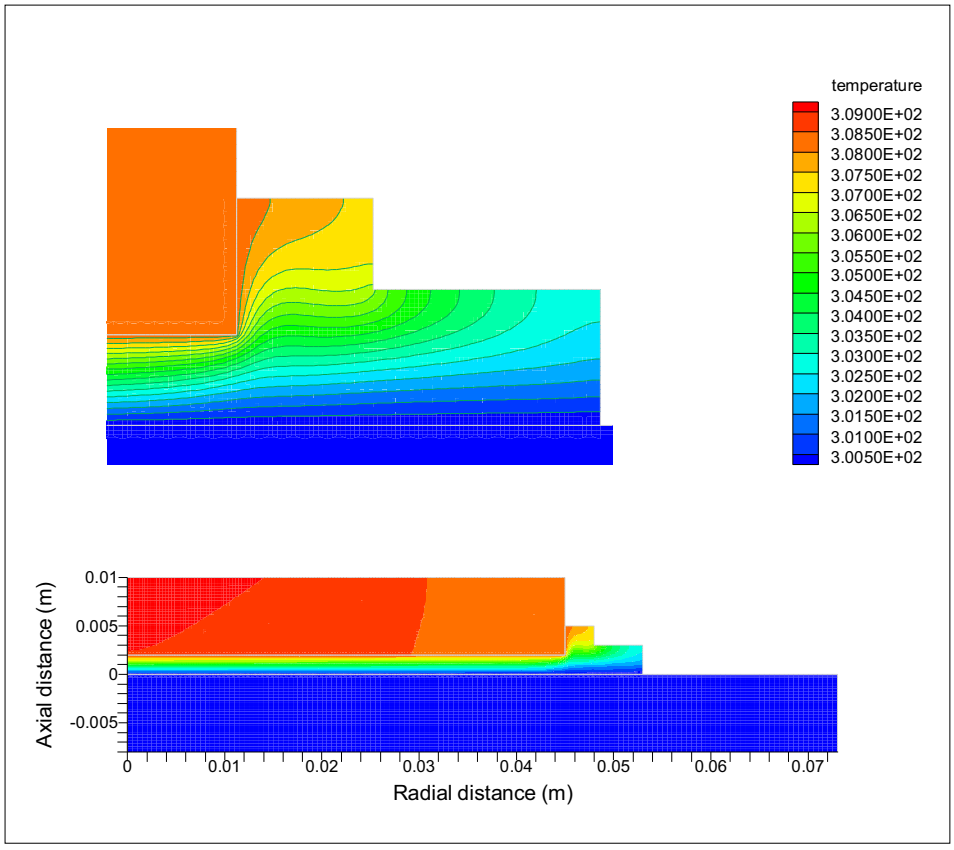

Figure 3.29: Temperature contour of the apparatus

The temperature contour of this case is shown in Figure 3.29. It can be found that the temperature distribution within the gap between two plates is uniform along the radial direction and linear along the axial direction. In the area near the peripheral side of the chamber, the temperature variation is not linear any more due to the natural convection.

Figure 3.30 shows the temperature variation along axial direction at the radial position where those two thermocouples for cold and hot plate temperature measurement locate. Due to the high thermal conductivity of copper, the temperature gradient in the

cold and hot plate is very small. It can also be found from the plot that the temperature distribution in the liquid sample is quite linear.

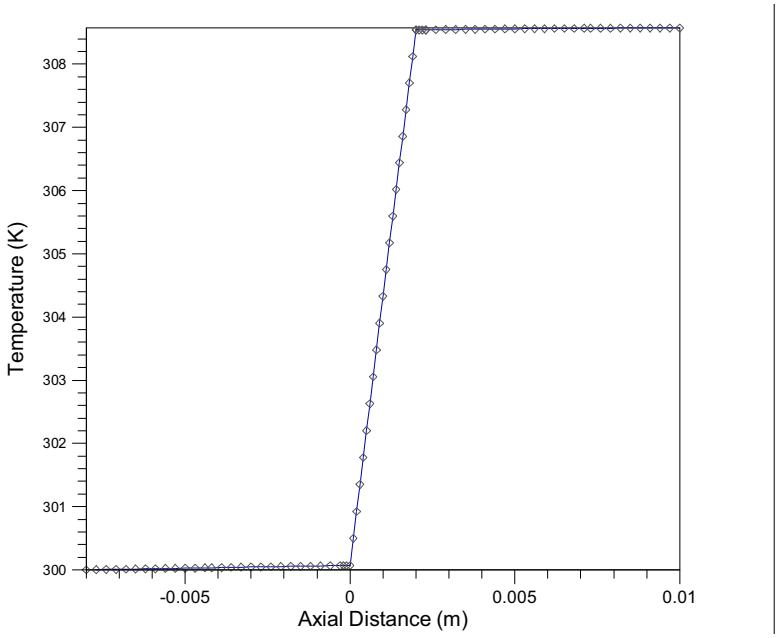

Figure 3.30: Temperature distribution at $r = 0.027m$

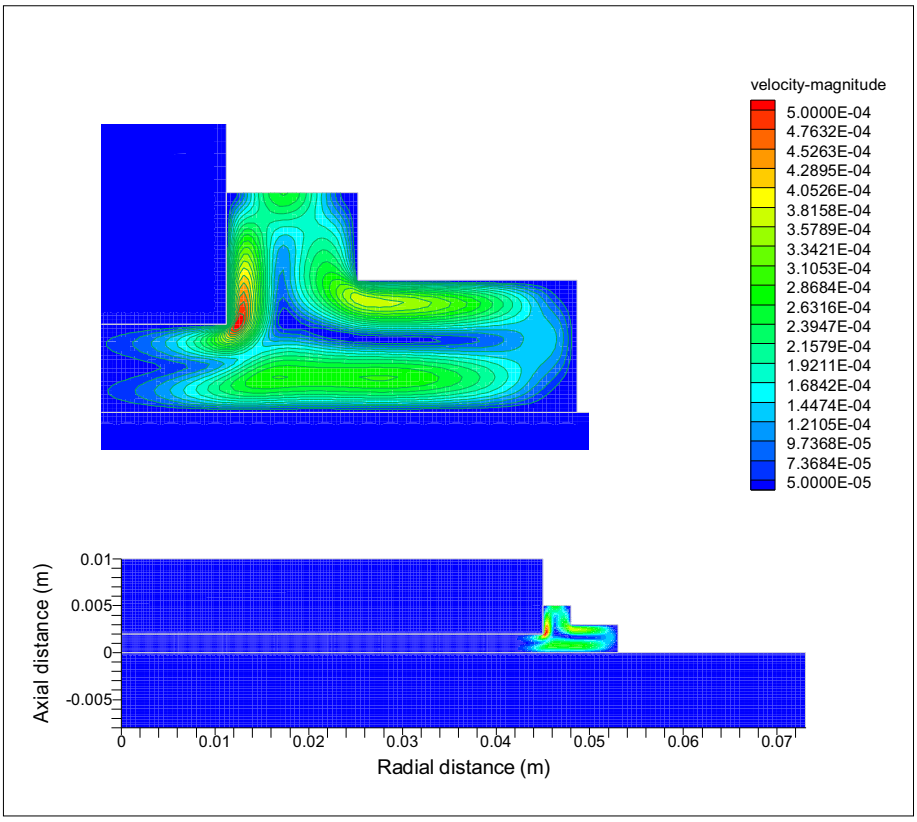

Figure 3.31: Velocity magnitude contour of the experimental apparatus

The velocity contour is shown in Figure 3.31. Because the liquid sample enclosed in the apparatus is heated from the upper plate, the natural convection of fluid is successfully suppressed within the plate gap. Although the effect is more significant in the zone that near the liquid free surface and peripheral side of the cell chamber, the velocity magnitude is of the order of 10^{-4} m/s only.

The velocity vector plot colored by its magnitude is shown in Figure 3.32. The streamline which is coincident with path line at steady state is also shown in the region where natural convection is significant.

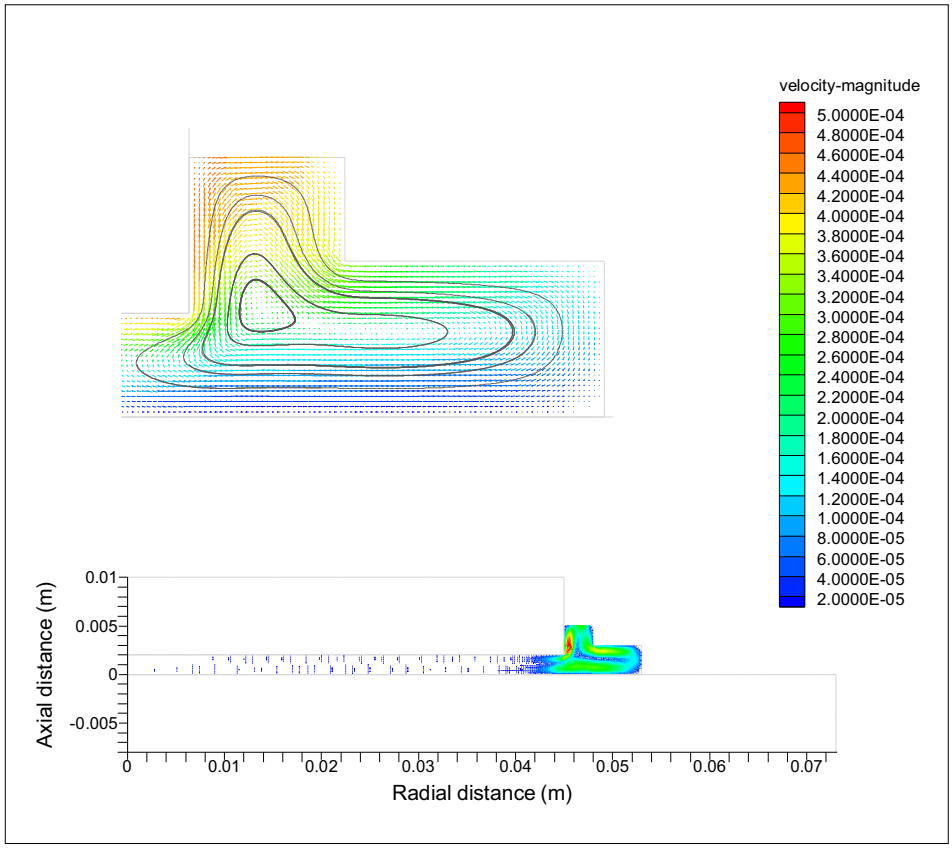

Figure 3.32: Velocity vector plot of simulation results

The effects of natural convection are examined by comparing the thermal conductivity value inputted in the numerical model and the value calculated using

equation 3.2 according to the simulation results. Temperatures at the same positions as the thermocouples are extracted from the simulation results. The Simulation results and system error at different main heater heating power are listed in Table 3.10. The published thermal conductivity value of water at mean temperature was used as the comparison criteria. From Figure 3.33, we can find that the calculated thermal conductivity value increase with the heating power, which indicates a greater error when heating power increase. This is probably due to the enhancement of natural convection when heating power and temperature difference increase. However, it might be mentioned here that although the system error is lower at low heating power levels such as 5W and 10W, their corresponding experimental results show a significant oscillation. Because of their low heating power and small temperature difference, the heating power of guard heaters are comparable to the main heater or even larger. The temperature difference between sample and the ambient is also small in these cases, therefore the temperature change of ambient impose significant influence on the effect of guard heaters. Guard heaters in turn may cool or heat the liquid sample according to the change of ambient temperature. Because the heating and cooling effects of guard heaters are significant compared to the main heater heating power, it altered the experiment results substantially.

Table 3.10: Summary of simulation results

Heating Power (W)	5	10	15	17.39	20	25	30	35	40	45
Temperature Difference (^{o}C)	2.50	4.99	7.40	8.48	9.60	11.53	13.24	14.63	15.92	17.18
Thermal Conductivity (W/m-K)	0.629	0.630	0.637	0.645	0.655	0.681	0.712	0.752	0.790	0.823
Published Data (W/m-K)	0.613	0.617	0.620	0.622	0.623	0.626	0.628	0.630	0.632	0.633
System Error	2.6%	2.2%	2.7%	3.8%	5.1%	8.8%	13.3%	19.3%	25.0%	29.9%

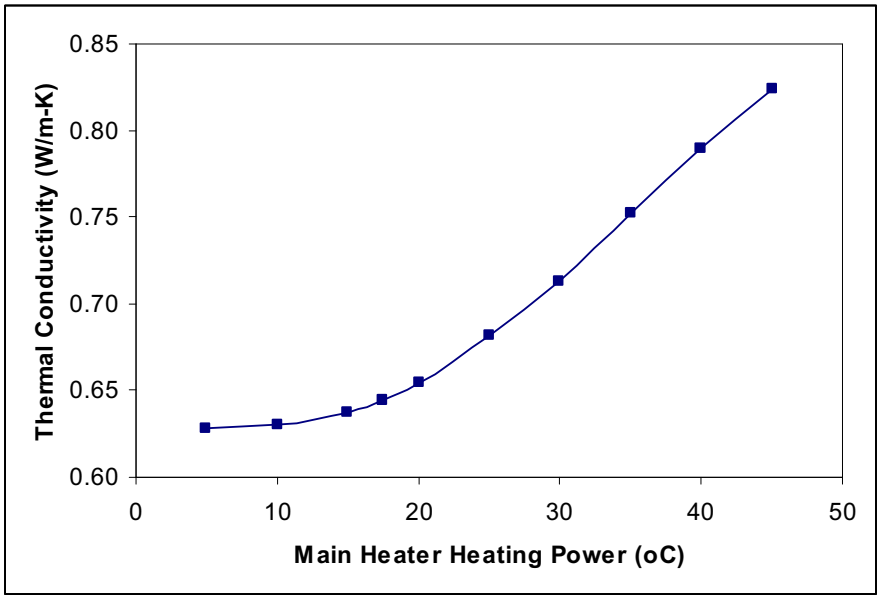

Figure 3.33: Plot of simulation results

3.6 Closure

The set-up and operating principles of our current experimental system for characterizing the effective thermal conductivity of nanofluids based on the one-dimensional steady-state parallel plate method are described in this chapter. Nanofluid preparation procedures and stability are discussed. Experimental results of various water and ethylene glycol based nanofluids prepared in our experiments are presented and analyzed. The system uncertainty and measurement error are also discussed. Moreover, the effects of natural convection are characterized numerically using commercial software.

CHAPTER 4: EXPERIMENTAL CHARACTERIZATION OF NANOFLUID-COOLED MICROCHANNEL HEAT SINK COOLING SYSTEM

4.1 Introduction

Great advances of today's IC technology have led to the extreme increase in heat dissipation of state-of-the-art IC chips, which most conventional cooling methods are inadequate to meet. The innovative microchannel cooling techniques, which was first proposed by Tuckerman and Peace, is among the most promising ways to meet the challenges. With its significantly high thermal conductivity, nanofluid is also expected to greatly improve the capability of liquid cooling systems. It comes naturally that the combination of these two innovative techniques may bring out a significant improvement in cooling ability. However, although numerous previous theoretical and experimental studies on the thermal conductivity of nanofluids have been published, thermal performance improvement of nanofluid cooling systems has seldom been reported. This chapter presents an experimental study of a nanofluid-cooled microchannel heat sink (MCHS) cooling system.

4.2 Design of Experiment and Operating Principles

4.2.1 Thermal Test Section

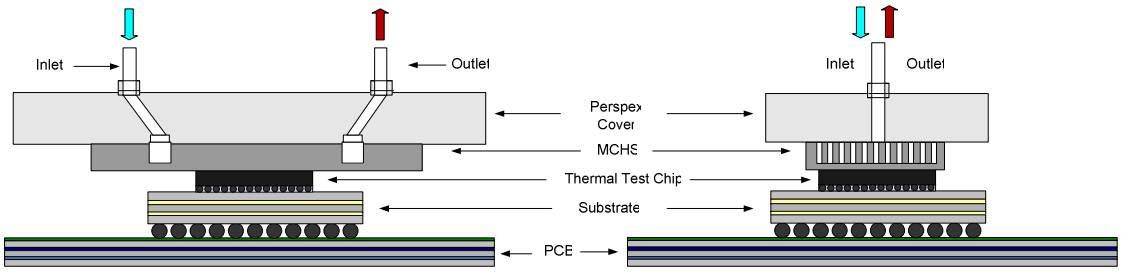

Figure 4.1: Schematic diagram of the thermal test section (side and cross section view)

Figure 4.1 shows a schematic diagram of the thermal test section, which consists of an aluminum microchannel heat sink, a heat sink cover and a thermal test board. The microchannel heat sink used in the experiment has a typical straight fin and rectangular channel design. It was fabricated by precision machining on an $52 \times 24 \times 2.8\ mm^3$ aluminum block. The footprint of the finned area is $15.0 \times 12.2\ mm^2$. The detailed dimensions and parameters of the MCHS used is shown in Figure 4.2 and is summarized in Table 4.1.

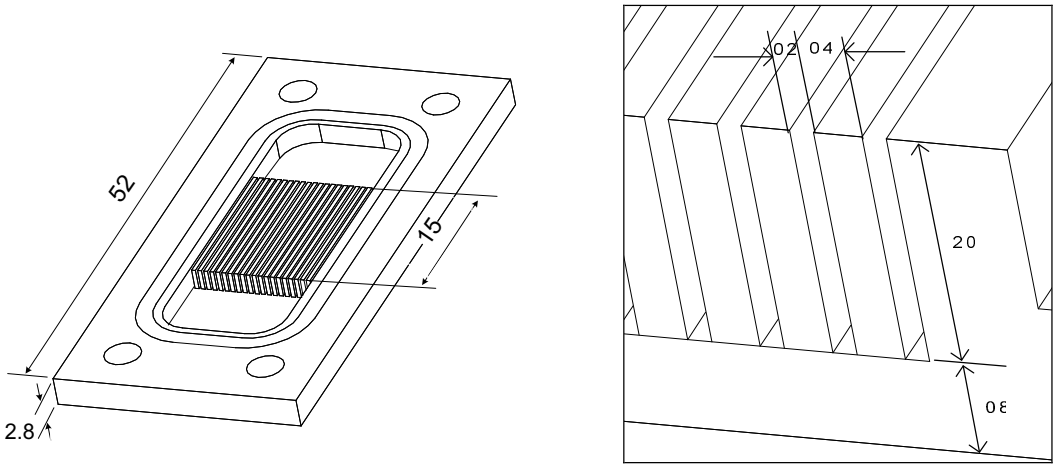

Figure 4.2: Dimensions of MCHS (unit in mm)

Table 4.1: Summary of MCHS parameters

Fin Height (mm)	Fin Thickness (mm)	Fin Length (mm)	Heat Sink Base (mm)	Channel Number
2	0.4	15	0.8	21
Channel Width (mm)	Channel number	Heat Sink Length (mm)	Heat Sink Width (mm)	Heat Sink Thickness (mm)
0.4	21	52	24	2.8

One copper and one aluminium single channel heat sink (SCHS) are used in the experiments in order to characterize the thermal contact resistance between thermal test chip and heat sink. The dimensions of the SCHS are the same as MCHS except the thickness of the single channel heatsink base was 1mm higher than the MCHS. Three holes of diameter 1mm are drilled in the middle and downstream of the heat sink to

allocate thermocouples. Figure 4.3 shows pictures of the copper single channel heat sink.

Figure 4.3: Picture of the copper single channel heat sink.

A $50\times50\times10\,mm^3$ perspex heat sink cover with two ¼" NPT connectors is used to lead and enclose the liquid flow passing through the MCHS. A Viton O-ring lays in the groove peripherally along the heatsink to eliminate leakage. Four M2 screws are used to attach the aluminum heat sink to the perspex cover. Two more screws may be used in the middle of the heat sink to minimize undesirable liquid bypass between the cover and heat sink fin tips.

The MCHS and its perspex cover are attached as the cooling solution of a thermal test chip in the form of a flip chip ball grid array (FCBGA) package. The 12×12 mm thermal test chip is attached on a substrate with 208 peripheral bumps, and the substrate is connected with PCB by 352 solder balls. The PCB with connectors on one side provide the input and output connections for the thermal test chip. The thermal test chip consists of four equally sized silicon dies. Each die has a built-in resistor for heating and a built-in thermal test diode for junction temperature measurement. The four built-in resistors are connected in series to ensure uniform heating. The total resistance of these four resistors is about 75.49 Ohms. The temperature rise in the chip is measured based on the resistance change of thermal diodes. A picture of the thermal test board used in the current experiment is shown in Figure 4.4.

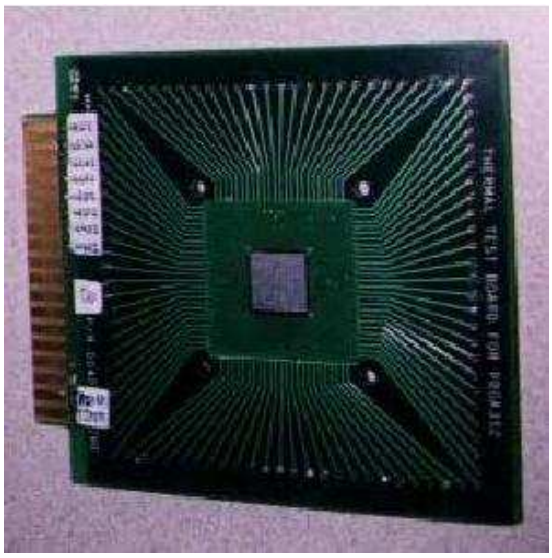

Figure 4.4: Picture of the thermal test board

The MCHS with perspex cover are bolted with the thermal test board by four spring-loaded screws. Thermal grease (Arctic Silver) is applied as thermal interface material to reduce thermal contact resistance between heatsink and thermal test chip. Lengths of the four springs are well controlled to ensure uniform and constant pressure load. One picture of the assembled thermal test section is shown in Figure 4.5.

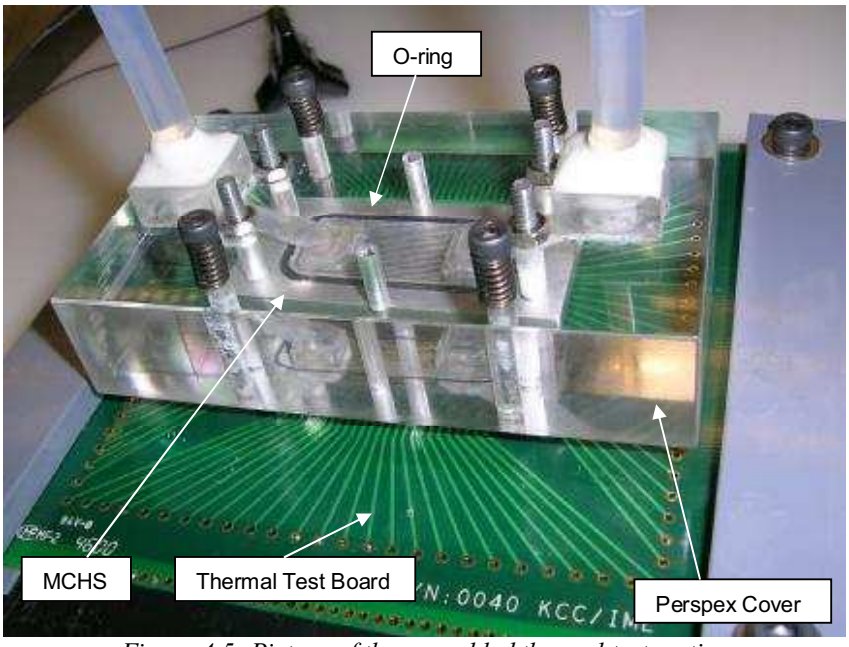

Figure 4.5: Picture of the assembled thermal test section

4.2.2 Construction of Experimental System

One microchannel heat sink cooling system has been developed in-house and is shown schematically in Figure 4.6. In this system, coolant from the reservoir is continuously circulated by a HG0024 micropump. Two ball valves are installed between the reservoir and micropump to control the volumetric flowrate. A 10 micron-sized mesh filter is installed after the pump to reduce sediment and agglomerated particles. To protect the pump in case of flow clogging in the filter, a by-pass loop is connected after the pump to the reservoir. Two flow meters are connected in parallel to measure the volumetric flow rate. Starting from the reservoir, the coolant is pumped through the filter, flow meters and enters the thermal test section. The heated coolant is cooled down by a compact heat exchanger, and finally directed back to the reservoir. Plastic pipes and brass connectors are used in the current experiment to construct all the coolant circuits. The pressure drop across the test section was measured by a PMD 235 differential pressure transducer. The ambient, reservoir, heat sink inlet and outlet temperatures are measured by four calibrated T-type thermocouples. The picture of the whole experimental system is shown in Figure 4.7.

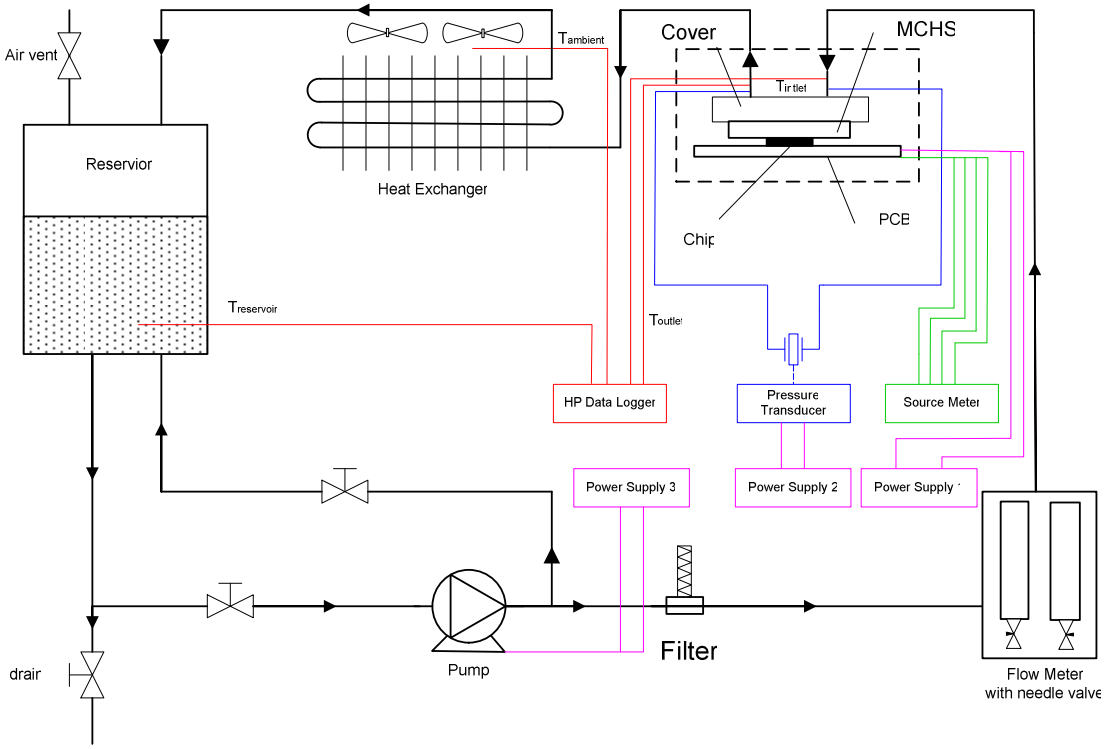

Figure 4.6: Schematic diagram of MCHS cooling system.

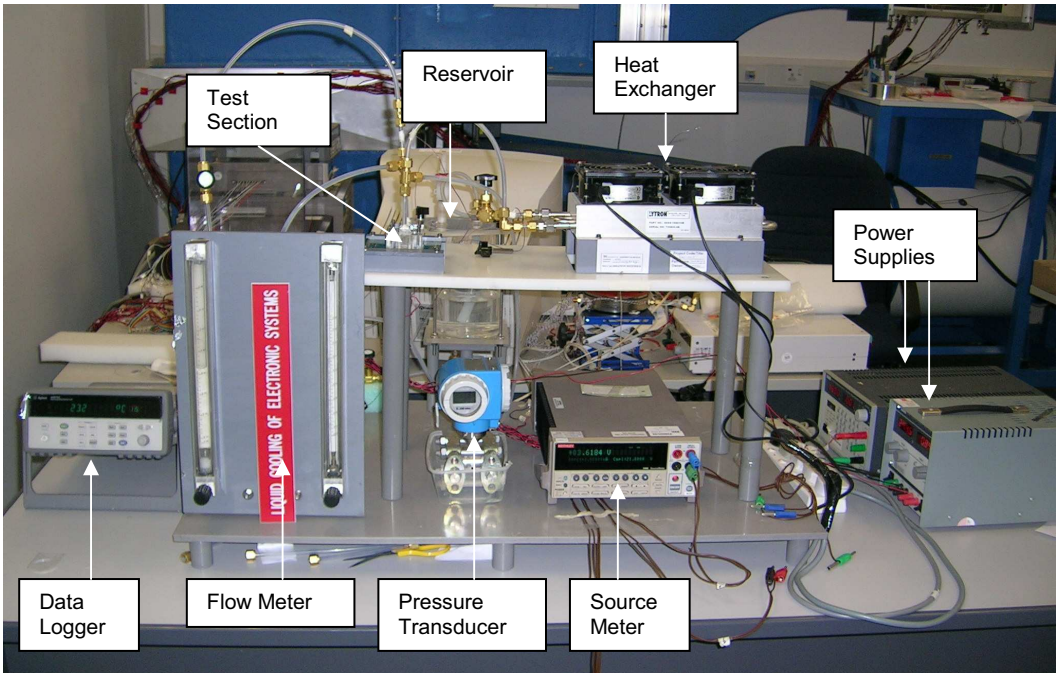

Figure 4.7: Picture of MCHS cooling system.

4.2.3 Instrumentation and Measurements

4.2.3.1 Micropump

Coolant in the cooling system is circulated by a HG0024 micropump (Figure 4.8) operated at 24VDC with a maximum input current of 3A. Its speed ranges from 500rpm to 4500rpm. The gears of the pump are made of PTFE, which allows various kinds of coolants to be utilized.

Figure 4.8: Picture of the HG0024 Micropump

4.2.3.2 Heat Exchanger

A compact copper tube-fin heat exchanger (Type: Lytron AS04) is used to dissipate the heat from the coolant to ambient air. The operation voltage for two exchanger fans is 230VAC. Figure 4.9 shows the side and top view of this compact heat exchanger.

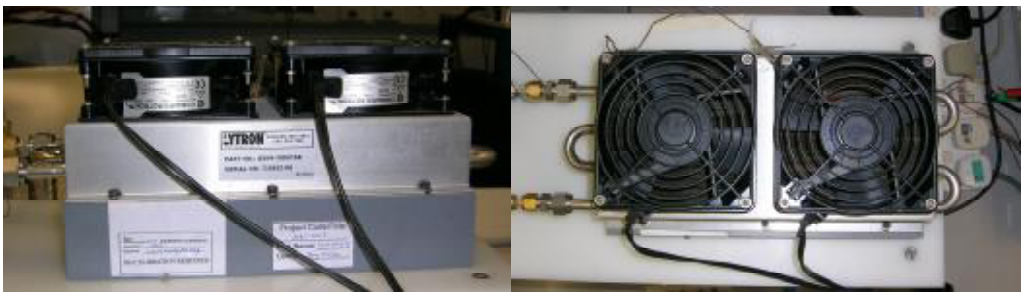

Figure 4.9: Picture of the side and top views of compact heat exchanger

4.2.3.3 Power Supplies

The power supplies used in this experiment is summarized in Table 4.2.

Table 4.2: Specifications of power supplies

Item	Power Supply	Output Range
Thermal Test Board	Keithley 228A programmable voltage/current source	0~100V (as a constant voltage source)
Pressure Transducer	TTi TSX1820P	0~18V (0~20A)
HG0024 Micropump	TTi PL330	0~32V (0~ 3A)

4.2.3.4 Flow Meter

Figure 4.9 shows the picture of two volumetric flow meters, which can be used independently or connected in parallel to measure the volumetric flow rate. The flowrate measurement ranges of those two flow meters are 0.08~0.80 l/min and 0.04~0.20 l/min. Thus a maximum measurement range from 0.04 l/min to 1.0 l/min is achievable when these two flow meters are connected in parallel. Flow meters are calibrated before all the experiments. The detail calibration data can be found in Table B.1 of Appendix B. The maximum measurement error after calibration is estimated to be 2.5%.

Figure 4.10: Picture of volumetric flow meters

4.2.3.5 Pressure Transducer

The pressure drop across the microchannel heatsink is measured by a PMD 235 piezoresistive differential pressure transducer with a digital display. Figure 4.11 shows

a picture of it. During the experiment, two ports from the transducer are connected before and after the test section to measure the pressure drop. The pressure transducer was factory-calibrated with an accuracy of ±2% at the nominal value of 0.5bar. The operation voltage of the pressure transducer is around 16 VDC and the measurement range of the pressure transducer is 0~500mbar.

Figure 4.11: Picture of the pressure transducer

4.2.3.6 Temperature Measurement

The junction temperature of each silicon die in the thermal test chip is measured by its built-in thermal diode. Average of the four temperature measurements is taken as the junction temperature of the thermal test chip. The temperatures are measured by the voltage drop of the thermal diodes. All the thermal diodes of the thermal test chip were calibrated in an oven and the k factors of the four diodes were obtained before all the experiments. The detailed calibration data can be found in Table B.2 of Appendix B. The measurement error of the thermal diodes is estimated to be less than $\pm 0.2\,^{o}C$ after calibration. The voltage drop of the thermal diodes is measured by a Keithley 2400 source meter. The source current is set to be 1mA in all the experiments. Figure 4.12 shows a picture of the source meter.

Figure 4.12: Picture of Keithley 2400 source meter

The temperatures of ambient, reservoir, MCHS inlet and outlet as well as the SCHS base are measured by T-type (copper-constantan) thermocouples. The temperature measurements are taken by a data acquisition system which consists of a data acquisition unit and a desktop computer. The Hewlett Packard Model 34970A data logger installed with a HP34901A 20-channel armature multiplexer plug-in model is used as the data acquisition unit. This module features 20 channels of 300V switching, built-in thermocouple reference junction, and connection to the internal multi-meter. Hewlett-Packard Benchlink software is installed in the desktop to control the data logger, record temperature readings and monitor the temperature variation during the experiment to ensure that the readings are taken in a steady state. Figure 4.13 shows a picture of the data logger. The thermocouples as well as the data logger are calibrated using a Hakke water bath and master mercury-in-glass thermometer. The regression equation of each thermocouple is obtained. The measurement uncertainty is about $\pm 0.1^{o}C$ after calibration.

Figure 4.13: HP 34970A data logger

4.2.4 Experimental Procedures and Data Reduction

4.2.4.1 Experimental Procedures

Prior to the thermal testing, a series of preparation procedures was carried out. Firstly, power supplies to the thermal test board, heat exchanger fans, micro pump and pressure transducer were connected according to their respective power input requirements. The source meter was connected to the thermal test board for the measurement of diode forward-bias voltages which can be used to calculate chip temperature. All power supplies should be kept off during the entire preparation procedures. Secondly, the piping system, as well as the flow meter and pressure transducer, was assembled following the schematic diagram of the experimental setup. The MCHS was assembled with the Perspex cover plate, whose inlet and outlet were connected with the piping system. Hydraulic testing was then carried out to check for possible leakage problems. Air trapped in the ports of pressure transducer should be carefully removed to avoid measurement errors. Finally, the MCHS was assembled with the thermal test board using spring-loaded screws. Thermal interface material was applied between the MCHS and thermal test chip to reduce thermal contact resistance. Tubes and connectors should be carefully adjusted to assure a torque-free mounting between the thermal test board and the MCHS.

The thermal testing was started by switching on the power supplies of all the equipments except the power supply for chip heating. The data acquisition system was turned on to monitor the system temperatures and pressures. The experimental system was first run about 20 minutes at a medium flow rate without chip heating to get the initial chip diode readings. The heating power of thermal test chip was then turned on to measure the thermal performance of the MCHS cooling system at different flow rates starting from 1.0 l/min to 0.1 l/min. During the thermal testing, pressure drop

across the MCHS, inlet and outlet temperature, heat sink base temperature, ambient temperature and diode forward-bias voltages were measured. Since the temperature readings had been found to deviate by less than 1% after running around 40 minutes at a given flowrate, both pressure drop and chip temperatures were first recorded after running the test for the first 20 minutes and then recorded every 5 minutes until steady-state was reached.

The thermal testing of MCHS cooling system was stopped by switching off all the power supplies. It should be mentioned here that when turning off the power supplies, the power supply for the heating of the thermal test chip must be deactivated first.

The detailed experimental procedures for characterizing the thermal performance of the liquid-cooled MCHS cooling system can be found in Appendix D.

4.2.4.2 Data Reduction

The thermal performance of the microchannel heat sink liquid cooling system is characterized by the thermal resistance based on the temperature difference between chip junction and microchannel heatsink inlet (R_{ji}). Its calculation is given by the following equation.

$$R_{ji} = \frac{T_j - T_i}{Q} \tag{4.1}$$

where,

T_j —junction temperature of the thermal test chip

T_i —temperature of the liquid at the MCHS inlet

Q —thermal test chip heating power

Although the most important characteristic for comparison is the junction-to-inlet thermal resistance, the junction-to-ambient thermal resistance (R_{ja}) and junction-to-reservoir thermal resistance (R_{jr}) are also calculated in the experimental results for reference. Their calculations are given by equation 4.2 and 4.3.

$$R_{ja} = \frac{T_j - T_a}{Q} \tag{4.2}$$

$$R_{jr} = \frac{T_j - T_r}{Q} \tag{4.3}$$

where,

T_a —temperature of ambient

T_r —temperature of reservoir

When single channel heat sinks are used in the experiments for characterizing the thermal contact resistance, the thermal resistance based on the temperature difference between chip junction and heat sink base is given by equation 4.4.

$$R_{jb} = \frac{T_j - T_b}{Q} \tag{4.4}$$

where, T_b is the temperature at heat sink base.

Thus the thermal resistance between heat sink inlet and heat sink base R_{bi} can be calculated from equation 4.5.

$$R_{bi} = \frac{T_b - T_i}{Q} \tag{4.5}$$

The thermal contact resistance R_c can be calculated as

$$R_c = R_{jb} - R_{si} - R_{bb} \tag{4.6}$$

where R_{si} is the thermal resistance of the silicon chip and R_{bb} is the thermal resistance between the heatsink bottom surface and the location where the heat sink base thermocouples are located.

4.3 Experimental Results and Discussion

Thermal performances of the nanofluid-cooled MCHS cooling system were characterized experimentally in this study. The nanofluids used in the current experiments were mainly water-based Al_2O_3 and SiC nanofluids. In order to exclude the effects of thermal contact resistance variation due to different installation of MCHS, a D.I water test run at several flow rates was carried out first after each individual reinstallation. Only when results of the test run were in good agreement with previous installations, would the successive testing for nanofluids be carried out. Otherwise, the test section was reassembled and reinstalled. During the experiments, the thermal and hydraulic performance of nanofluids with different nanoparticle volume fractions were examined and compared. During every change of nanofluids, different volume fraction or different type, the whole system was cleaned up using D.I. water. The experimental results obtained are shown in the following sections.

4.3.1 Experimental Results of Al_2O_3-water Nanofluids

The experimental results of the MCHS cooling system using water-based Al_2O_3 nanofluids are summarized in Table 4.3. The experimental results for D.I. water are also included for comparison.

Table 4.3: Experiment results summary of Al_2O_3-water Nanofluids

Microchannel Heat Sink

DI water	Flowrate (l/min)	0.072	0.159	0.239	0.33	0.424	0.516	0.61	0.709
	R_{ji} (K/W)	0.472	0.388	0.362	0.350	0.341	0.334	0.329	0.324
	R_{jr} (K/W)	0.477	0.384	0.358	0.346	0.336	0.331	0.326	0.321
	R_{ja} (K/W)	0.521	0.448	0.420	0.416	0.398	0.387	0.385	0.375
	Pressure Drop (mbar)	4.8	11.1	19.6	29.6	40.6	53.9	68.3	84.1
0.7vol% Al_2O_3-Water Nanofluid	Flowrate (l/min)	0.072	0.159	0.239	0.33	0.424	0.516	0.61	0.709
	R_{ji} (K/W)	0.432	0.355	0.332	0.322	0.314	0.308	0.305	0.302
	R_{jr} (K/W)	0.425	0.350	0.326	0.319	0.310	0.304	0.301	0.297
	R_{ja} (K/W)	0.458	0.404	0.388	0.384	0.371	0.364	0.365	0.355
	Pressure Drop (mbar)	5.4	12.1	20.5	29.8	39.6	49.5	61.2	74.5
2vol% Al_2O_3-Water Nanofluid	Flowrate (l/min)	0.256	0.344	0.415	0.488	0.583	0.665	0.753	
	R_{ji} (K/W)	0.337	0.313	0.301	0.295	0.289	0.284	0.281	
	R_{jr} (K/W)	0.334	0.311	0.301	0.293	0.285	0.281	0.278	
	R_{ja} (K/W)	0.408	0.380	0.367	0.361	0.350	0.339	0.342	
	Pressure Drop (mbar)	38.1	54.1	70.0	81.5	97.9	110.1	124.0	
3vol% Al_2O_3-Water Nanofluid	Flowrate (l/min)	0.227	0.354	0.482	0.595	0.679	0.777		
	R_{ji} (K/W)	0.343	0.304	0.288	0.280	0.275	0.274		
	R_{jr} (K/W)	0.344	0.301	0.284	0.277	0.273	0.272		
	R_{ja} (K/W)	0.424	0.394	0.375	0.350	0.339	0.350		
	Pressure Drop (mbar)	71.4	87.5	97.8	110.4	121.0	137.9		

Figure 4.14 shows the junction-to-inlet thermal resistance (R_{ji}), junction-to-reservoir thermal resistance (R_{jr}) and junction-to-ambient thermal resistance (R_{ja}) of the water-

cooled MCHS cooling system. Probably due to the low heat transfer coefficient at the air side of the heat exchanger, the ambient temperature is much lower than the reservoir and heat sink inlet temperature, and therefore R_{ja} is much higher than R_{ji} and R_{jr}. As can be seen in Figure 4.6, the coolant is cooled further when it passes by the tubes after it leaves the reservoir. Therefore the temperature at the heat sink inlet is slightly lower than the temperature at the coolant reservoir, and thus R_{ji} is slightly higher than R_{jr}. Furthermore, because this experiment was carried out in an air-conditioned room, the ambient air temperature was normally 22 ^{o}C with ± 1^{o}C variation. Thus, as can be seen in the figure, the oscillation of ambient temperature may significantly influence the junction-to-ambient thermal resistance and make the R_{ja} curve unsmooth.

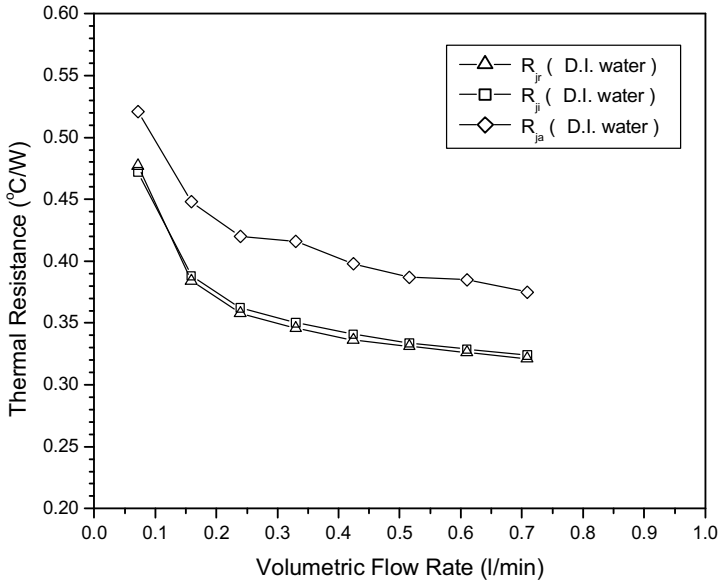

Figure 4.14: Thermal resistances of D.I. water-cooled MCHS cooling system

The pressure drop across the MCHS as a function of volumetric flow rates is shown in Figure 4.15. It increases monotonically with the increase of volumetric flow rate.

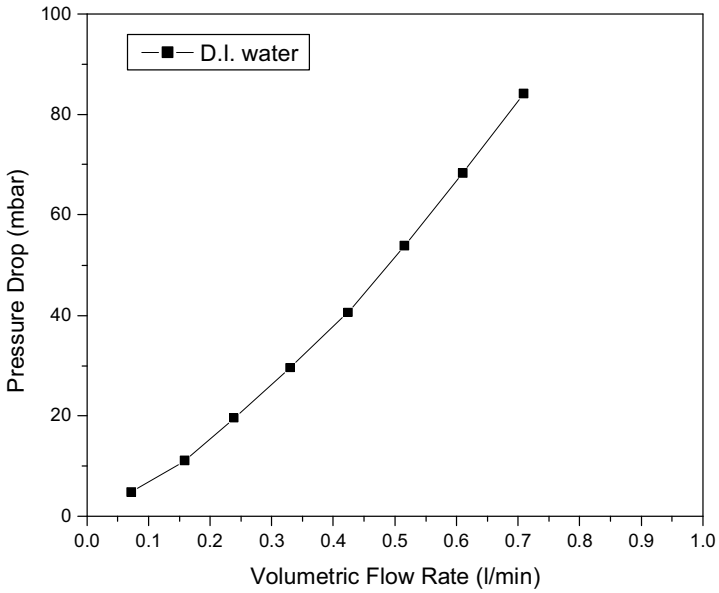

Figure 4.15: Pressure drop across the MCHS (D.I. water)

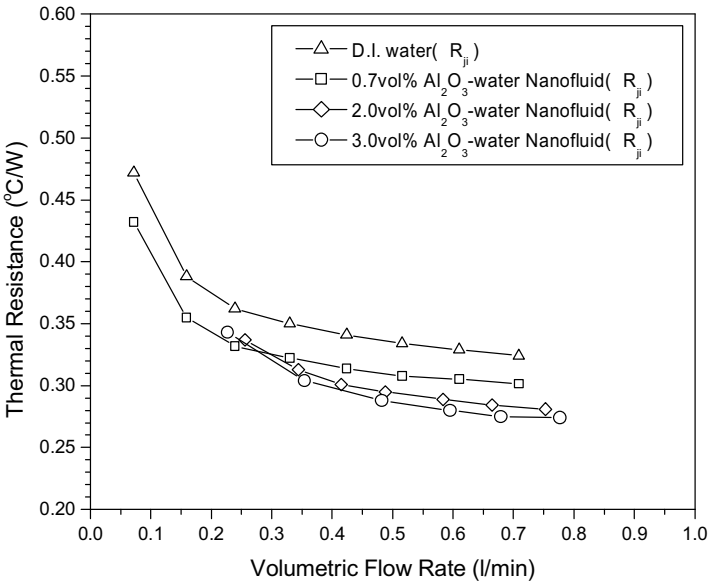

Figure 4.16: R_{ji} of Al_2O_3-water nanofluid-cooled MCHS cooling system

The junction-to-inlet thermal resistance of the MCHS liquid cooling system using D.I. water, 0.7vol%, 2.0vol% and 3.0vol% Al_2O_3-water nanofluids are shown in Figure 4.16. The R_{ji} for alumina nanofluids is much smaller than that for D.I. water at the same volumetric flow rate. For nanofluids at a specific flow rate, R_{ji} decreases with the increase of nanoparticle fraction, this is probably due to the increase of thermal

conductivity as nanoparticle volume fraction increases. The decrease of R_{ji} in percentage for 0.7 vol%, 2.0 vol% and 3.0 vol% Al_2O_3-water nanofluids over D.I water is shown in Figure 4.17. Generally, a 6%, 12% and 15% improvement in R_{ji} for 0.7 vol%, 2.0 vol% and 3.0 vol% Al_2O_3-water nanofluids, respectively, was observed.

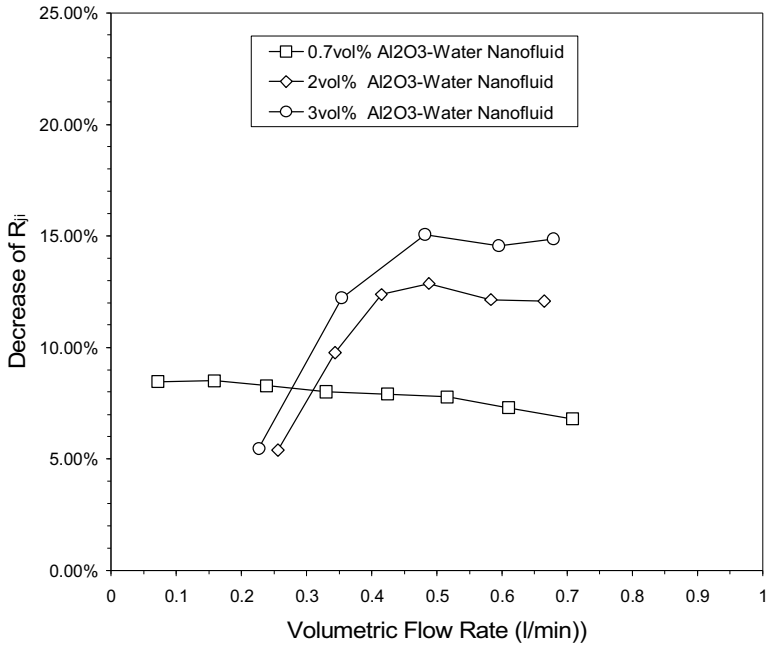

Figure 4.17: Improvement of R_{ji} in Al_2O_3-water nanofluid-cooled MCHS cooling system

Figure 4.18 shows the pressure drop across the microchannel heat sink when D.I. water and Al_2O_3-water nanofluids were used. As expected, the pressure drop increases with the volumetric fraction of nanoparticles. It might be mentioned here that when 2vol% and 3vol% Al_2O_3-water nanofluids were used in the experiment, the pump works unsteadily when the volumetric flow rate was reduced to less than 0.4 *l*/min. Therefore it can be seen in Figure 4.16-18 that at low volumetric flow rates, the junction-to-inlet thermal resistances for 2vol% and 3vol% Al_2O_3-water nanofluids are slightly higher than 0.7vol% Al_2O_3-water nanofluid and their respective pressure drop significantly increase. This is probably caused by the unsteady operation of the micro pump.

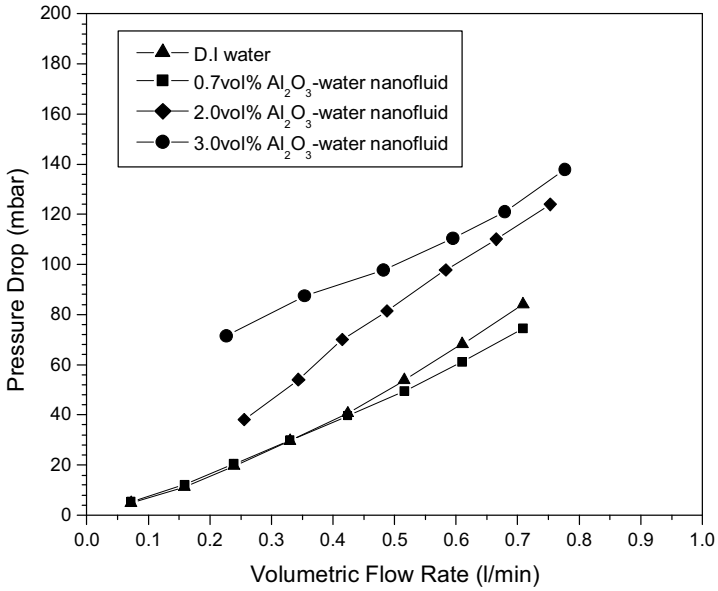

Figure 4.18: Pressure drop across the MCHS (Al_2O_3-water nanofluids)

4.3.2 Experimental Results of SiC-Water Nanofluids

The experimental results of SiC-water nanofluids and D.I. water are summarized in Table 4.4.

Table 4.4: Experiment results summary of SiC-water Nanofluids

Microchannel Heat Sink									
DI Water	Flowrate (l/min)	0.072	0.159	0.239	0.33	0.424	0.516	0.610	0.709
	R_{ji} (K/W)	0.472	0.388	0.362	0.350	0.341	0.334	0.329	0.324
	R_{jr} (K/W)	0.477	0.384	0.358	0.346	0.336	0.331	0.326	0.321
	R_{ja} (K/W)	0.521	0.448	0.420	0.416	0.398	0.387	0.385	0.375
	Pressure Drop (mbar)	4.8	11.1	19.6	29.6	40.6	53.9	68.3	84.1
1vol% SiC-Water Nanofluid	Flowrate (l/min)	0.071	0.106	0.247	0.389	0.532	0.698	0.862	
	R_{ji} (K/W)	0.446	0.363	0.314	0.299	0.290	0.282	0.278	
	R_{jr} (K/W)	0.443	0.359	0.311	0.297	0.289	0.282	0.279	
	R_{ja} (K/W)	0.474	0.399	0.368	0.359	0.353	0.337	0.336	
	Pressure Drop (mbar)	6.2	10.8	26.1	42.7	63.8	93.3	125.5	

The junction-to-inlet thermal resistances of 1vol% SiC-water nanofluid and D. I. water are shown in Figure 4.19. As can be seen in Figure 4.20, a 12% decrease in R_{ji} was

observed in the experiment. As the effective thermal conductivity of SiC-water has been shown in the previous chapter to be relatively higher than that of Al_2O_3-water nanofluids at the same particle volume fraction, the decrease of R_{ji} for 1vol% SiC-water nanofluid is approximately the same as that of 2vol% Al_2O_3-water nanofluid at the same volumetric flow rate.

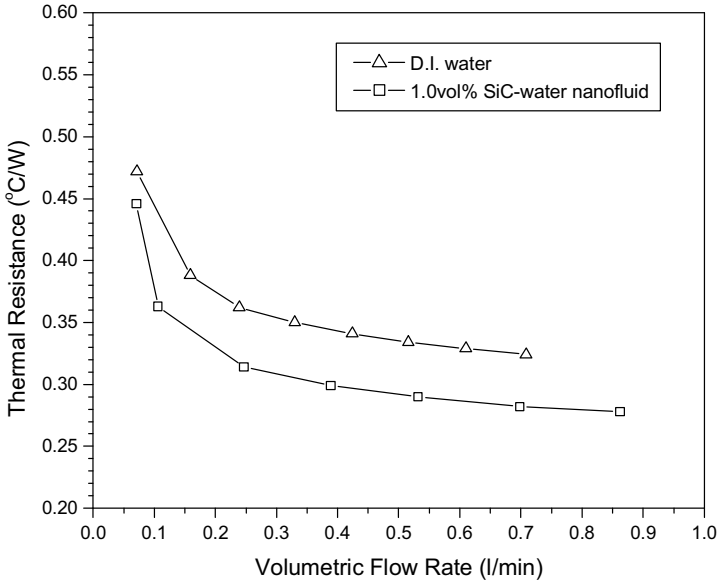

Figure 4.19: R_{ji} of 1vol% SiC-water nanofluid-cooled MCHS cooling system

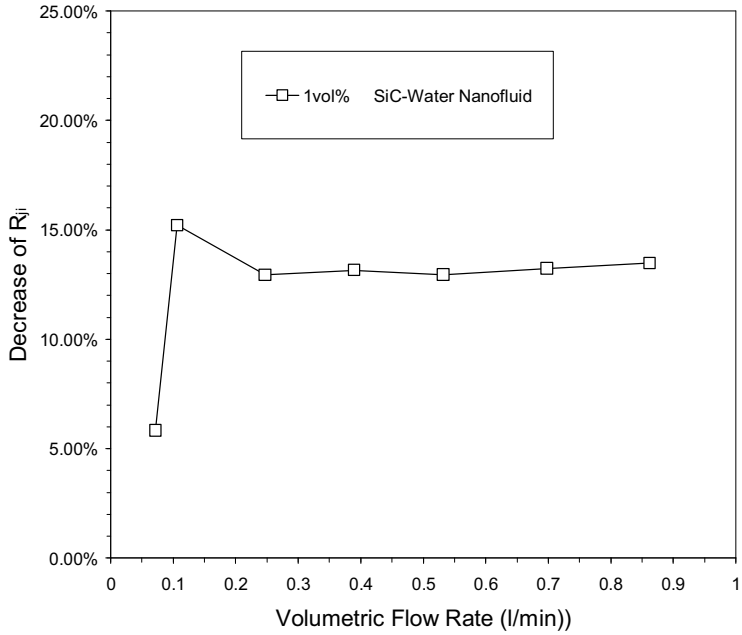

Figure 4.20: Improvement of R_{ji} in SiC-water nanofluid-cooled MCHS cooling system

The pressure drop across the MCHS for 1vol% SiC-water nanofluid is shown in Figure 4.21. Its magnitude is between that of 0.7vol% and 2.0vol% Al_2O_3-water nanofluids at the same volumetric flow rate.

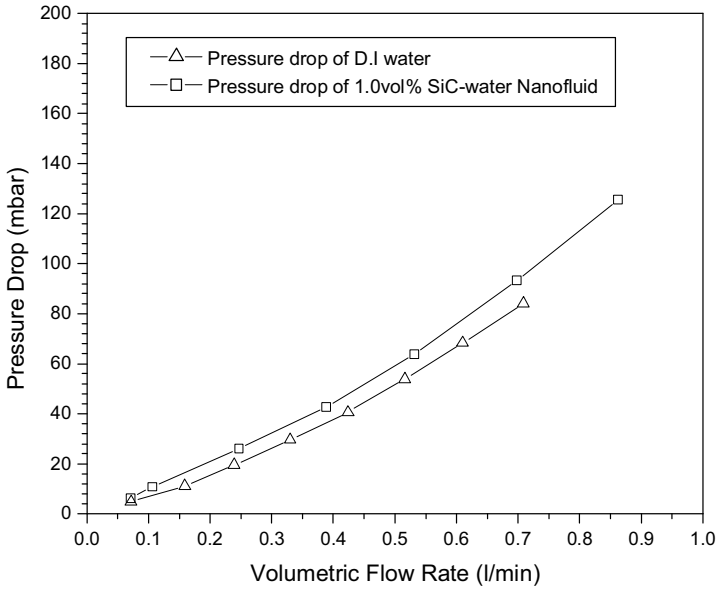

Figure 4.21: Pressure drop across the MCHS (1vol%SiC-water nanofluids)

The thermal testing for 2vol% and 3vol% SiC-D.I. water nanofluids was terminated due to the clogging of the MCHS. Figure 4.22 shows the junction-to-inlet thermal resistance of the MCHS cooling system when 2vol% and 3vol% SiC-water nanofluids were used. The volumetric flow rate of 2vol% and 3vol% SiC-water nanofluids were set at 0.862 *l*/min and 0.532 *l*/min respectively. As can be seen from Figure 4.22, R_{ji} for 2vol% SiC-water nanofluid is much larger than that for D.I. water at the same flow rate, which indicates the occurrence of MCHS clogging. This was further confirmed by the abnormal increase in pressure drop. As can be seen in Figure 4.23, the pressure drop across the MCHS for 2vol% SiC-water nanofluid is around 300 mbar, which is about two times larger than that for D.I. water at the same flow rate. Although the R_{ji} for 3vol% SiC-water nanofluid at 0.352 *l*/min is smaller than that for D.I. water, a continuous increase in pressure drop can be found in Figure 4.23. This

again indicates that clogging of microchannel heat sink occurred during the testing. Figure 4.24 shows a picture of the clogged MCHS. This picture was taken when the 3vol% SiC-water nanofluid was used for MCHS cooling system.

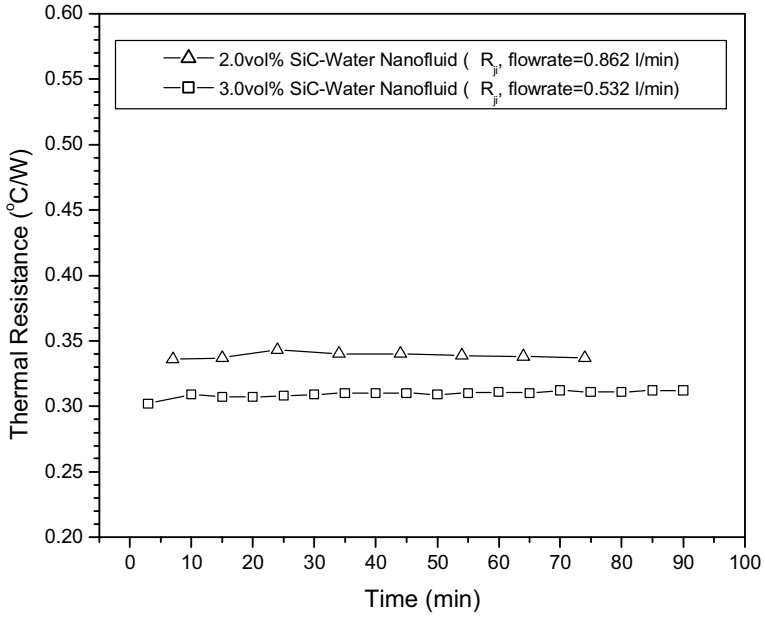

Figure 4.22: R_{ji} as a function of time (2vol% and 3vol% SiC-water nanofluids)

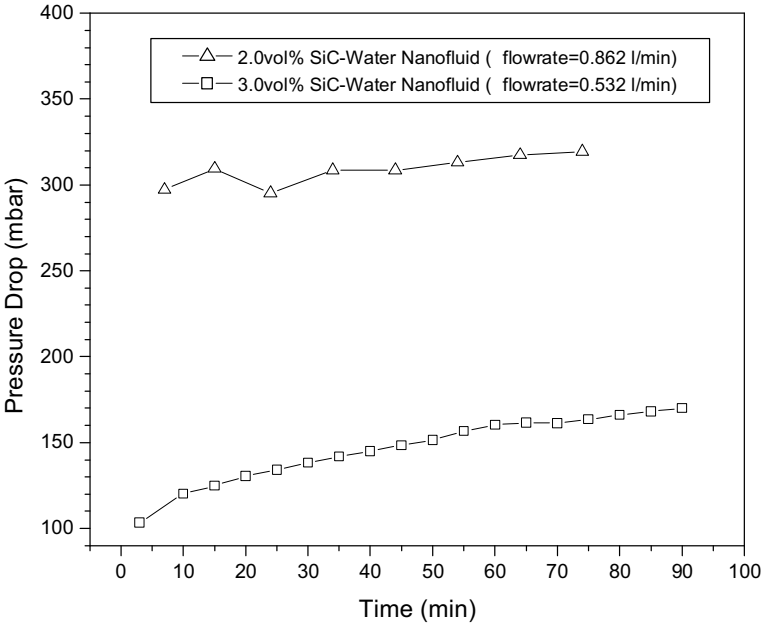

Figure 4.23: Pressure drop across the MCHS as a function of time (2vol% and 3vol% SiC-water nanofluids)

Figure 4.24: A picture of the clogged MCHS

It might be mentioned here that those two alumina nanofluids were made by the same method as the 1vol% SiC-DI water nanofluid and maintained at the same pH value, however sediment and clogging happened during the testing for nanofluids with high volumetric fractions. These two unsuccessful experiments indicate that the stability and uniformity of nanofluids is of extreme importance to the thermal performance and reliability of MCHS cooling systems using nanofluids. It also discloses an urgent demand in the improvement of nanofluid preparation techniques.

4.3.3 Experimental Results of Nanofluids at High Temperature

According to the experimental results reported by Das et al. (2003b), the effective thermal conductivity of nanofluids increases significantly with the increase of working temperature. In order to investigate the thermal performance of nanofluid-cooled MCHS cooling system at high working temperature, two heat exchanger fans were switched off in our current experiments to elevate the working temperature of the coolant. By turning off the heat exchanger fans, the cooling effect of compact heat exchanger significantly reduces, and thus the temperature of the coolant in the reservoir and that entering the MCHS is elevated. The junction-to-inlet thermal resistance of MCHS cooling system thus increases significantly. In consideration of the high junction-to-inlet thermal resistance and the highest tolerable working temperature of the thermal test chip, the flow rate of coolant at high temperature

working conditions were set to be around the highest available flow rate. Thermal resistances, junction temperature as well as the pressure drop of the MCHS cooling system at the high volumetric flow rate are summarized in Table 4.5.

Table 4.5: Summary of the experiment results at high working temperature

Heat Sink	Coolant	Flowrate (l/min)	Fans	T_j (°C)	R_{ji} (K/W)	Pressure Drop (mbar)
MCHS	D.I. water	0.709	On	43.1	0.324	84.1
MCHS	D.I. water	0.709	Off	60.4	0.285	58.7
MCHS	1vol% SiC-Water Nanofluid	0.698	On	41.4	0.282	93.3
MCHS	1vol% SiC-Water Nanofluid	0.698	Off	61.3	0.313	60.4
MCHS	0.7vol% Al_2O_3-Water Nanofluid	0.709	On	43.2	0.297	74.5
MCHS	0.7vol% Al_2O_3-Water Nanofluid	0.709	Off	63.3	0.277	59.7

As shown in Table 4.5, the junction-to-inlet thermal resistance of MCHS is decreased from 0.324 °C/W to 0.285 °C/W when D.I. water is used. This is mainly due to the thermal conductivity increase of D.I. water with the increase of working temperature. R_{ji} of the MCHS utilizing 0.7vol% Al_2O_3-water nanofluid decreases from 0.297 °C/W to 0.277 °C/W. However, it is difficult to tell if the enhancement of the thermal performance is due to the increase of thermal conductivity of base fluid only or due to the effect by both base fluid and nanoparticle. For 1vol% SiC-water nanofluid, the junction-to-inlet resistance observed is larger than its low temperature counterpart, which is contrary to what was expected. Another experimental run for a higher volumetric flow rate at 0.862 *l*/min was carried out for double checking. A similar behaviour was observed. No convincing reasons have been found to explain this abnormal phenomenon. Probably because the viscosity of coolant decreases with the increase of working temperature, the pressure drop across the MCHS decreases at certain flow rates for D.I water and nanofluids.

4.3.4 Experimental Results of Single Channel Heat Sink

The thermal contact resistance between the thermal test chip and aluminium MCHS played an important role in the overall thermal resistance. Therefore its variation between different working temperature and different assemblies was characterized. Since the optimized aluminium MCHS base was only 0.8mm in thickness, too thin to allocate thermocouples for temperature measurement, one single channel heatsink made of the same material as the MCHS was used to characterize the thermal contact resistance. Another single channel heat sink made of copper was also used in the experiment to characterize the temperature effect on thermal contact resistance. The dimensions of the SCHSs are the same as the MCHS except that the single channel has no fin structure and the thickness of the single channel heatsink base was 1mm higher than that of the MCHS in order to seat thermocouples. The bottom surfaces of those two heat sinks were finished at the same surface smoothness requirement.

The experimental results for the aluminium single channel heat sink are summarized in Table 4.6. Figure 4.25 shows the junction-to-inlet and junction-to-base thermal resistance of water-cooled MCHS at two different installations. During the assembly of the thermal test section and thermal test board, the length of screw springs is set to be 7mm in both of these two cases. It can be found from the results that the variation of R_{ji} is around 2~5%, which shows good agreement between these two installations. The results show better agreement at high volumetric flow rates. The difference of R_{jb} is around 0.018^{o}C/W, or about 10%. However, its influence on R_{ji} is less than 3% for all the flow rates.

Table 4.6: Experiment results summary of aluminium single channel heat sink

Aluminium Single Channel Heat Sink

D.I. water_1	Flowrate (l/min)	0.072	0.159	0.239	0.33	0.424	0.516	0.61	0.709
	R_{ji} (K/W)	1.490	1.104	0.926	0.801	0.729	0.671	0.625	0.593
	R_{bi} (K/W)	0.207	0.203	0.201	0.199	0.199	0.198	0.192	0.192
	R_{jr} (K/W)	1.503	1.103	0.925	0.798	0.727	0.670	0.621	0.592
	R_{ja} (K/W)	1.568	1.197	1.013	0.870	0.824	0.730	0.705	0.669
	Pressure Drop (mbar)	0.7	2.2	4.4	7.8	11.7	16.9	23.2	30.3
D.I. water_2	Flowrate (l/min)	0.072	0.159	0.239	0.33	0.424	0.516	0.61	0.709
	R_{ji} (K/W)	1.233	1.014	0.875	0.771	0.692	0.652	0.610	0.585
	R_{bi} (K/W)	0.180	0.179	0.176	0.176	0.174	0.176	0.172	0.177
	R_{jr} (K/W)	1.250	1.012	0.872	0.768	0.689	0.649	0.607	0.582
	R_{ja} (K/W)	1.321	1.085	0.959	0.863	0.784	0.733	0.684	0.671
	Pressure Drop (mbar)	1.0	1.9	4.4	7.5	11.4	16.7	23.0	30.0
D.I. water_3	Flowrate (l/min)	0.159	0.424	0.709					
	R_{ji} (K/W)	1.014	0.692	0.585					
	R_{bi} (K/W)	0.179	0.174	0.177					
	Pressure Drop (mbar)	1.9	11.4	30.0					
	Spring Length (mm)	7							
	Flowrate (l/min)	0.159	0.424	0.709					
	R_{ji} (K/W)	1.021	0.698	0.590					
	R_{bi} (K/W)	0.183	0.182	0.183					
	Pressure Drop (mbar)	2.0	11.4	30.0					
	Spring Length (mm)	9							
	Flowrate (l/min)	0.159	0.424	0.709					
	R_{ji} (K/W)	1.001	0.717	0.612					
	R_{bi} (K/W)	0.197	0.193	0.195					
	Pressure Drop (mbar)	2.1	11.7	30.1					
	Spring Length (mm)	11							

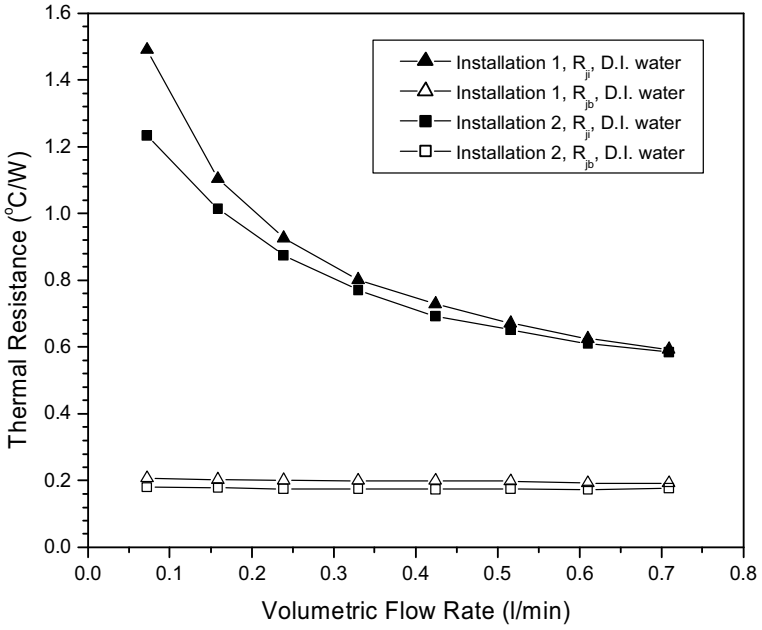

Figure 4.25: R_{ji} and R_{jb} for aluminium SCHS at two different installations

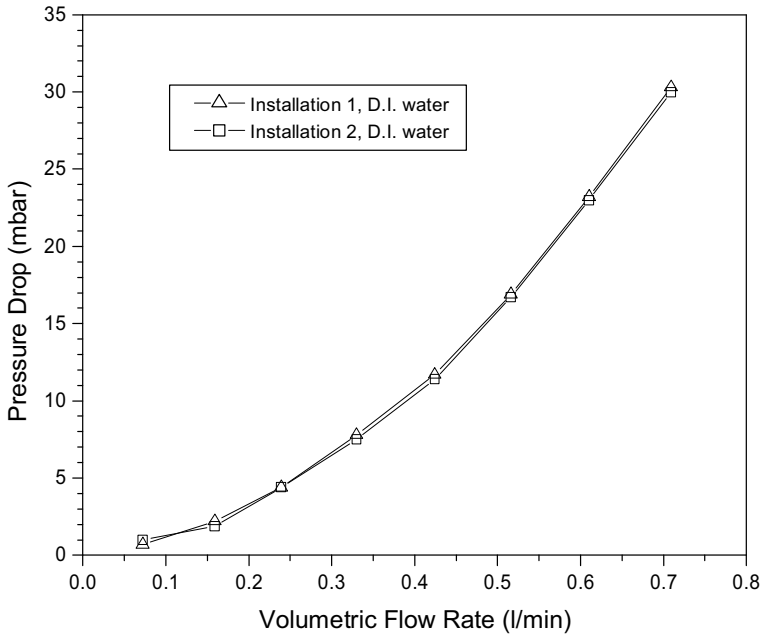

Figure 4.26: Pressure drop for aluminium SCHS at two different installations

The pressure drop across SCHS in these two cases is shown in Figure 4.26. The pressure drop is affected by the assembly of heat sink and heat sink cover only. Current experimental results show no significant difference between these two

installations. For the SCHS, the pressure drop is insensitive to the assembly force between the SCHS and its cover.

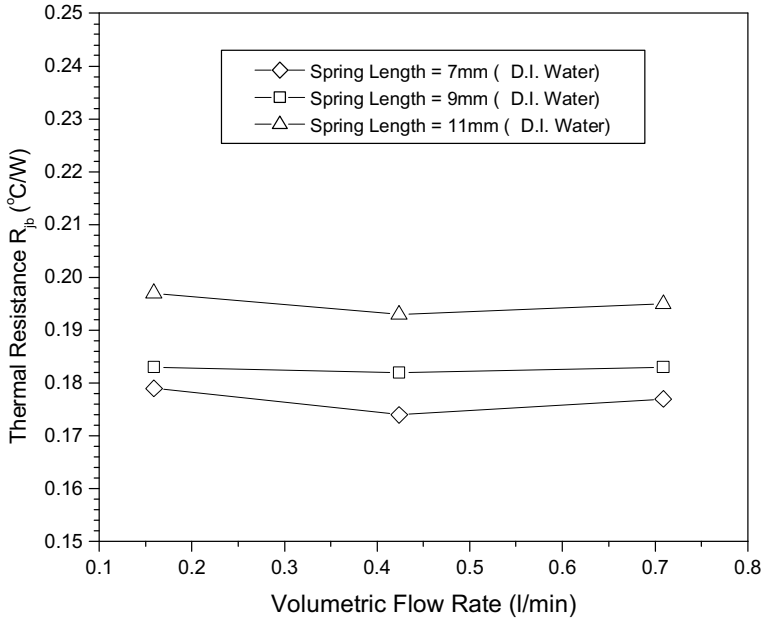

Figure 4.27: R_{jb} of aluminium SCHS at different mounting pressure conditions

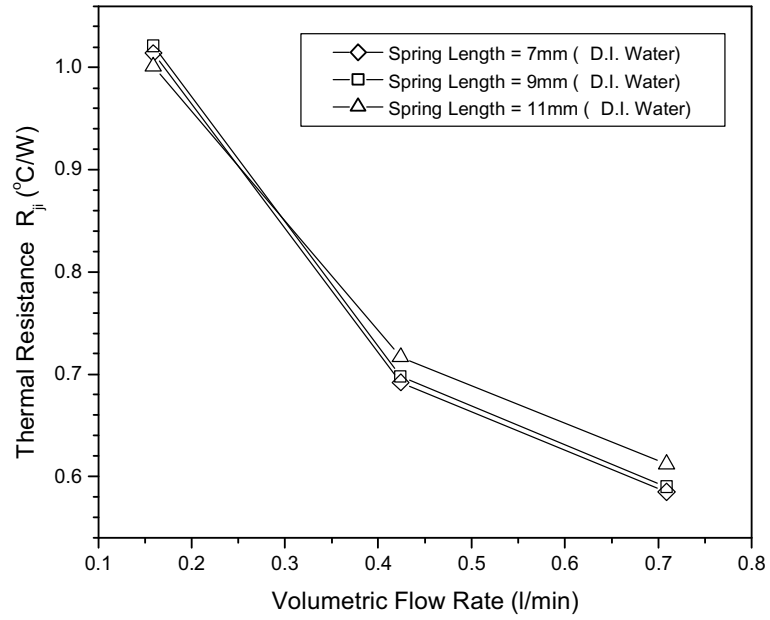

Figure 4.28: R_{ji} of aluminium SCHS at different mounting pressure conditions

Since thermal grease was used as the thermal interface material in the current experiments to reduce the thermal contact resistance, the effect of mounting pressure on thermal contact resistance was characterized in current experiments by adjusting the length of the spring. As the thermal test section is mounted onto the thermal test board by four spring-loaded screws, the adjustment of spring length directly changed the mounting force. This experiment was carried out by first adjusting the length of the spring to 11mm and decreasing it later to 9mm and 7mm. The heating power was set to be constant. As the thermal resistance of silicon chip R_{si} and the thermal resistance from heat sink bottom surface to the position of heat sink base thermocouple R_{bb} are constant, the difference in R_{jb} indicates exactly the difference of thermal contact resistance between the upper surface of the silicon chip and the lower surface of the heat sink. Figure 4.27 shows the R_{jb} of the SCHS cooling system for different spring lengths at three different flow rates. R_{jb} and R_c decrease with the increase of mounting pressure. However, the variation of thermal contact resistance imposes small effects on R_{ji} due to its relatively small magnitude (Figure 4.28).

The experimental results for copper single channel heat sink are summarized in Table 4.7. As can be seen from the table, R_{jb} of the copper SCHS when D.I. water was used as coolant is about 0.114 ^{o}C/W, which is lower than the value measured for the aluminium SCHS. This discrepancy is mainly due to the difference of R_{bb}, because the thermal conductivity of copper is two times that of aluminium.

Table 4.7: Experiment results summary of copper single channel heat sink

Copper Single Channel Heat Sink

D.I. Water	Flowrate (l/min)	0.069	0.146	0.234	0.327	0.418	0.511	0.610	0.699
	R_{ji} (K/W)	0.981	0.778	0.676	0.594	0.525	0.483	0.439	0.414
	R_{jr} (K/W)	0.999	0.774	0.675	0.592	0.521	0.480	0.437	0.412
	R_{ja} (K/W)	1.050	0.857	0.741	0.658	0.593	0.551	0.502	0.481
	R_{jb} (K/W)	0.117	0.115	0.115	0.114	0.114	0.113	0.111	0.110
	Pressure Drop (mbar)	0.8	1.9	4.3	7.5	11.6	16.7	23.1	30.4
1vol% SiC-Water Nanofluid	Flowrate (l/min)	0.340	0.417	0.514	0.589	0.677	0.779		
	R_{ji} (K/W)	0.578	0.515	0.477	0.446	0.424	0.398		
	R_{jr} (K/W)	0.576	0.515	0.475	0.445	0.424	0.398		
	R_{ja} (K/W)	0.635	0.569	0.544	0.513	0.494	0.463		
	Pressure Drop (mbar)	9.0	13.0	17.4	23.1	28.9	38.5		
2vol% SiC-Water Nanofluid	Flowrate (l/min)	0.340	0.417	0.514	0.589	0.677	0.779		
	R_{ji} (K/W)	0.588	0.516	0.481	0.452	0.428	0.403		
	R_{jr} (K/W)	0.588	0.514	0.481	0.451	0.427	0.402		
	R_{ja} (K/W)	0.643	0.584	0.544	0.513	0.498	0.461		
	Pressure Drop (mbar)	7.9	12.3	16.3	21.9	28.5	37.3		
4vol% Al_2O_3-Water Nanofluid	Flowrate (l/min)	0.343	0.463	0.525	0.630	0.754			
	R_{ji} (K/W)	0.802	0.702	0.648	0.598	0.573			
	R_{jr} (K/W)	0.798	0.699	0.645	0.594	0.571			
	R_{ja} (K/W)	0.867	0.773	0.716	0.665	0.647			
	Pressure Drop (mbar)	15.2	21.8	28.5	36.7	49.1			

Figure 4.29 shows R_{ji} of the copper SCHS at different volumetric flow rates for water and nanofluids. The pressure drop across SCHS is shown in Figure 4.30. It can be found from the figure that the thermal resistance for 1vol% and 2vol% SiC-water nanofluid is almost the same as that for D.I. water at the same flow rate. Probably due to the small heat transfer area and low heat transfer coefficient within the SCHS, the

thermal performance enhancement induced by the improvement of effective thermal conductivity of nanofluids is relatively small compares to the total thermal resistance. Therefore no significant improvement can be found in the experimental results. However, for 4 vol% Al_2O_3-water nanofluid, its respective junction-to-inlet thermal resistance is much larger than that for D.I water. Sedimentation in some flow dead zones of heat sink was found for these two cases.

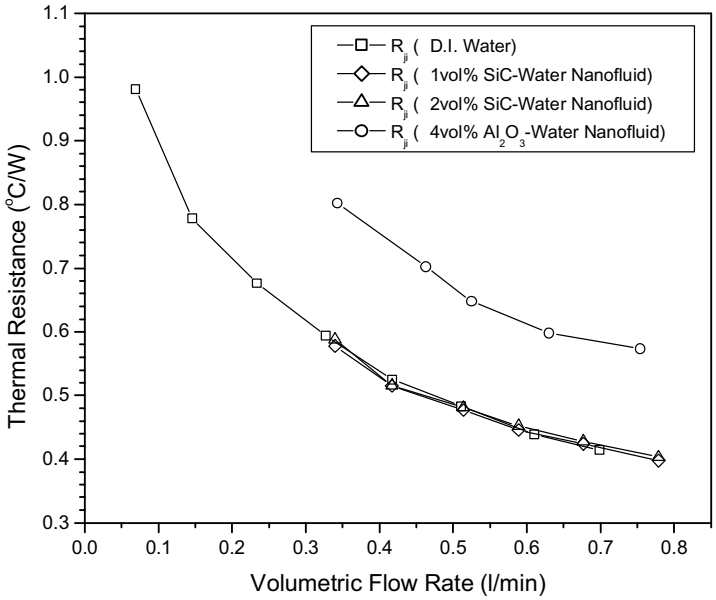

Figure 4.29: R_{ji} of copper SCHS for different coolants

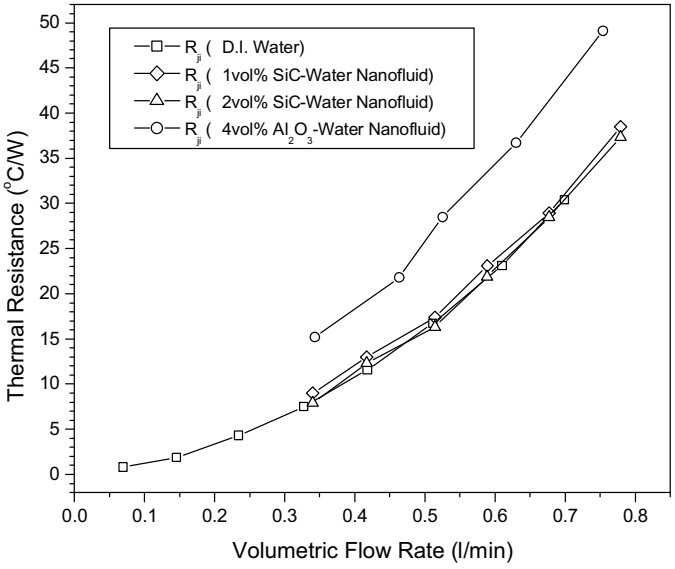

Figure 4.30: Pressure drop of copper SCHS for different coolants

4.3.5 Error Analysis

The effect of individual measurement uncertainties on the experimental results can be estimated by uncertainty analysis using the root-sum-square method (Moffat, 1988). In the current experiments, the results are expressed in the form of thermal resistance. For example, according to the equation 4.1, the junction-to-inlet thermal resistance R_{ji} can be presented as,

$$R_{ji} = \frac{T_j - T_i}{Q} = \frac{\Delta T_{ji}}{Q} \tag{4.7}$$

where $\Delta T_{ji} = T_j - T_i$ is the temperature difference between chip junction and heat sink inlet. The independent parameter measured in the experiment is temperature difference ΔT_{ji} and heating power Q. The overall uncertainty can be calculated as

$$\Delta R_{ji} = \left[\left(\frac{\partial R_{ji}}{\partial \Delta T_{ji}} \Delta \left(\Delta T_{ji} \right) \right)^2 + \left(\frac{\partial R_{ji}}{\partial Q} \Delta Q \right)^2 \right]^{1/2} = \left[\left(\frac{1}{Q} \Delta \left(\Delta T_{ji} \right) \right)^2 + \left(-\frac{T_j - T_i}{Q^2} \Delta Q \right)^2 \right]^{1/2} \tag{4.8}$$

So, the relative uncertainty in obtaining the thermal resistance, e_R, can be derived as follows:

$$e_R = \left[\left(\frac{\Delta \left(\Delta T_{ji} \right)}{\Delta T_{ji}} \right)^2 + \left(\frac{\Delta Q}{Q} \right)^2 \right]^{1/2} \tag{4.9}$$

One typical set of experimental data of D.I. water-cooled MCHS cooling system is selected to evaluate the accuracy of the experiment. The accuracy of the main heater heating power provided by Keithly 228A voltage/current source equipment is 0.1W (0.1V in voltage and 0.001A in current). The heat loss to the ambient through the substrate of thermal test chip is estimated to be around 1%. The uncertainty of the measured temperature for T_j and T_i is about 0.2°C, thus the uncertainty of temperature

difference ΔT_{ji} is about 0.4°C. The total uncertainty of experimental results is calculated and shown in Table 4.8.

Table 4.8 Analysis of experimental uncertainty for thermal conductivity

T_j (°C)	T_i (°C)	ΔT_{ji} (°C)	$\Delta\left(\Delta T_{ji}\right)$ (°C)	Q (W)	ΔQ (W)	$e_{R_{ji}}$
44.0	24.6	19.4	0.4	59.893	0.60	2.29%

4.4 Closure

In this chapter, the setup and operatiing principles of one microchannel heat sink cooling system is presented in detail. The thermal performance of nanofluids-cooled MCHS system is measured and compared using the thermal resistance as the performance parameter. A significant improvement in junction-to-inlet thermal resistance for Al_2O_3-water and SiC-water nanofluids were observed. The variation of thermal contact resistance due to reinstallation and different mounting pressures were investigated using two single channel heat sinks. Feasibility, stability and reliability of the nanofluids-cooled MCHS cooling system are discussed.

CHARPTER 5: NUMERICAL SIMULATION OF MICROCHANNEL HEAT SINK COOLING SYSTEM

5.1 Introduction

With the great improvement in today's computational resources, numerical simulation has become one of the indispensable tools in modeling and optimization of electronic cooling systems. In this study, the numerical simulation of microchannel heat sink was carried out using commercial CFD software FLUENT. By building a 3-D numerical model, we can predict the thermal performance and relative hydrodynamic requirements of MCHS cooling systems at different flow rates and with different coolants. In this chapter, the thermal resistance network of the MCHS cooling system and a theoretical thermal and hydrodynamic analysis of the MCHS are presented. In the numerical simulation, the model is first validated by comparing the simulation results with the available experimental results for a water-cooled MCHS cooling system. Then the thermal performance enhancement of the MCHS cooling system using SiC-water nanofluids and Al_2O_3-water nanofluids is predicted. The thermal performance of MCHS cooling system using nanofluids out of the range of the current experiments is also studied.

5.2 Theoretical Analysis

5.2.1 Thermal Resistance Network Analysis

The total thermal resistance or the junction-to-inlet thermal resistance of a microchannel heat sink cooling system is defined as

$$R_{ji} = \frac{T_j - T_i}{Q} \tag{5.1}$$

where T_j is the junction temperature of the thermal test chip, T_i is the temperature of coolant at the MCHS inlet and Q is the heating power of the thermal test chip. The junction-to-inlet thermal resistance can be further expressed as a sum of four thermal resistances.

$$R_{ji} = R_{si} + R_c + R_{heat\sin k} + R_{bulk} \tag{5.2}$$

where R_{si} , R_c , $R_{heat\sin k}$ and R_{bulk} denote the thermal test chip conduction, interface contact, heat sink and coolant bulk thermal resistances of the MCHS cooling system, respectively. Figure 5.2 shows a schematic diagram of the thermal resistance network for the MCHS cooling system.

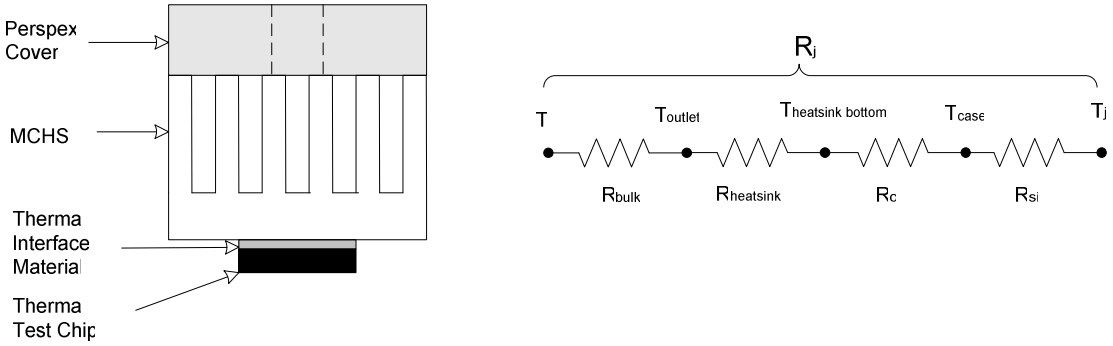

Figure 5.1: Thermal resistance network of MCHS cooling system

The conduction thermal resistance (R_{si}) of the silicon thermal test chip is given by

$$R_{si} = \frac{t}{k_{si} A_{si}} \tag{5.3}$$

where t and A_{si} are the thickness and footprint area of silicon thermal test chip, k_{si} is the thermal conductivity for silicon.

The thermal contact resistance between the upper surface of the thermal test chip and the bottom surface of the MCHS is referred as R_c . Because thermal grease was applied

in our current experiments as thermal interface material, R_c actually includes the thermal contact resistance between thermal test chip and thermal grease layer, the thermal resistance of thermal grease layer and the thermal contact resistance between thermal grease layer and heat sink bottom.

The heat sink thermal resistance ($R_{heat\sin k}$) is related to the temperature difference between the highest temperature of the heat sink bottom surface and the microchannel heat sink outlet coolant temperature. Here the heat sink thermal resistance is a combination of four thermal resistances of the MCHS.

$$R_{heat\sin k} = R_{spr} + R_{cond} + R_{constr} + R_{conv} \tag{5.4}$$

R_{spr} is the thermal spreading resistance. Because the surface area of thermal test chip is smaller than the bottom surface of MCHS, the heat flow will be redistributed to a near-uniform heat flux in some distance above the heat sink bottom surface. Thus a thermal spreading resistance is introduced here to account for this redistribution effect. The heat conduction between the heat sink base and the base of the microchannels and fins adds a conduction thermal resistance R_{cond}. R_{constr} is the constriction thermal resistance that accounts for the constriction effect at the fin base. The constriction effect is associated with the need to funnel the heat flow into the base of fins, because the base areas of fins are much less than the heat sink base. For high aspect ratio MCHS like the one used in our current experiments, the constriction effect is significant. The convective thermal resistance R_{conv} is related to the heat conduction through the fin and the convective heat transfer between fin surfaces, channel base surfaces and the coolant. R_{conv} is determined by calculating the parallel thermal resistances of heat flow through the fin surfaces and through the channel base surfaces. For the heat conduction

within the fins, fin efficiency is normally calculated in order to take the nonuniform distribution of temperature along the fin into consideration. In the fin efficiency model, the Biot number is normally assumed to be high because the temperature gradient across the fin width is small comparing with that along the fin length.

The bulk thermal resistance (R_{bulk}) that is associated with the coolant's bulk temperature rise from the heat sink entrance to heat sink outlet is defined as

$$R_{bulk} = \frac{1}{\dot{m}C_p} \tag{5.5}$$

where $\dot{m}$ and C_p are mass flow rate and specific heat of the coolant, respectively.

5.2.2 Hydrodynamic Analysis

The geometric parameters of a MCHS including channel aspect ratio (α), channel cross section area (A_{ch}), channel perimeter (C_{ch}) are specified as follows,

$$\alpha = w_{ch} / b \tag{5.6}$$

$$A_{ch} = w_{ch} b \tag{5.7}$$

$$C_{ch} = 2\left(w_{ch} + b\right) \tag{5.8}$$

where w_{ch} and b are the width and height of the microchannel, respectively. The microchannel mean velocity (U_m) and the inlet/outlet mean velocity (U_i, U_o) are defined as,

$$U_m = Q_f /(NA_{ch}) \tag{5.9}$$

$$U_i = Q_f / A_i \tag{5.10}$$

$$U_o = Q_f / A_o \tag{5.11}$$

where Q_f, N, A_i and A_o are the volumetric flow rate, number of channels, heatsink inlet area and heat sink outlet area, respectively.

The hydraulic diameter (D_h), Reynolds number (Re) and the dimensionless axial distance for the hydrodynamic entrance region (x^+) are given by

$$D_h = 4A_{ch} / C_{ch} \tag{5.12}$$

$$\mathrm{Re} = U_m D_h / \nu \tag{5.13}$$

$$X^+ = X / (D_h \,\mathrm{Re}) \tag{5.14}$$

where X is the axial distance along the channel.

Shah and London (1978) reported the correlations of the apparent friction factor (f_{app}) for the developing and fully developed laminar flow in a rectangle channel, and later Nakamura et al. (1979) provided a correction for the temperature-dependent viscosity. These correlations for different flow regions are given as follows:

$$f_{app}\,\mathrm{Re} = (\mu_w / \mu_m)^{0.58} 16 / G + k_\infty / 4X^+, \qquad x^+ \geq 0.1 \tag{5.15}$$

$$f_{app}\,\mathrm{Re} = 11.3\left(X^+\right)^{-0.202} \alpha^{-0.094}, \qquad 0.02 \leq x^+ \leq 0.1 \tag{5.16}$$

$$f_{app}\,\mathrm{Re} = 5.26\left(X^+\right)^{-0.434} \alpha^{-0.010}, \qquad 0.001 \leq x^+ \leq 0.02 \tag{5.17}$$

where G and k_∞ are given by

$$G = 2/3 + (11/24)\alpha(2-\alpha) \tag{5.18}$$

$$K_\infty = -0.906\alpha^2 + 1.693\alpha + 0.649 \tag{5.19}$$

Because f_{app} is a function of x^+, the pressure drop across the microchannel is given in the integral form as

$$\Delta p_{ch} = 2\rho U_\infty^2 \int_0^{l_{ch}/(D_h \mathrm{Re})} f_{app}\,\mathrm{Re}\, dX^+ \tag{5.20}$$

where, U_∞ is the coolant velocity at the microchannel entrance.

The pressure drop at the inlet and outlet plenum due to the bend of coolant flow is given by

$$\Delta p_b = 0.5\rho U_m^2 k_b \tag{5.21}$$

where,

$$k_b = \begin{cases} 1.53 & \mathrm{Re}_b \le 4000 \\ 0.7(2\times10^5 / \mathrm{Re}_i)^{0.2} & \mathrm{Re}_b \ge 4000 \end{cases} \tag{5.22}$$

Re_b can be the Reynolds number at heat sink inlet or outlet plenum (Re_i or Re_o). Re_i and Re_o are given by

$$\mathrm{Re}_i = U_i D_i / \nu \tag{5.23}$$

$$\mathrm{Re}_o = U_o D_o / \nu \tag{5.24}$$

where, U_i, U_o are the mean velocities at heat sink inlet and outlet pipe, respectively. D_i and D_o are the diameter of the inlet and outlet pipe, respectively.

The friction pressure drop at the inlet and outlet pipes, the contraction and expansion pressure drops at the entrance and exit of microchannels are not discussed in detail here, because their magnitudes are relatively small compared to the pressure drop due to the bending effect and the friction pressure drop in the microchannel.

The parameters of the MCHS used in our current study are summarized in Table 5.1. The calculation results of the pressure drop across the thermal test section in our current experiment are shown in Table 5.2.

Table 5.1: Summary of MCHS geometry parameters

w_{ch} (mm)	b (mm)	α	A_{ch} (mm^2)	C_{ch} (mm)	D_h (mm)	l_{ch} (mm)	D_i (mm)	D_o (mm)	N
0.2	2	0.1	0.4	4.4	0.364	15	6	6	21

Table5.2: Calculation results of the pressure drop across thermal test section

Flow rate (l/min)	0.1	0.2	0.3	0.4	0.5	0.6	0.7	0.8	0.9	1.0
U_m (m/s)	0.198	0.397	0.595	0.794	0.992	1.190	1.389	1.587	1.786	1.984
Re	105	210	315	421	526	631	736	841	946	1052
Δp (Pa)	716	1596	2614	3758	4992	6307	7699	9029	10504	12033

5.2.3 Thermal Performance Analysis

The dimensionless axial distance (x^*) for the thermal entrance region is defined as

$$X^* = X/(D_h \,\mathrm{Re}\,\mathrm{Pr}) \tag{5.25}$$

The correlations for the local Nusselt number in laminar flow from Shah and London (1978) are shown as following

$$Nu = 8.24 - 16.8\alpha + 25.4\alpha^2 - 20.4\alpha^3 + 8.70\alpha^4 \qquad x^* \geq 0.1 \tag{5.26}$$

$$Nu = 3.35\left(X^*\right)^{-0.130} \alpha^{-0.120}\,\mathrm{Pr}^{-0.038} \qquad 0.013 \leq x^* \leq 0.1 \tag{5.27}$$

$$Nu = 1.87\left(X^*\right)^{-0.300} \alpha^{-0.056}\,\mathrm{Pr}^{-0.036} \qquad 0.005 \leq x^* \leq 0.013 \tag{5.28}$$

The local heat transfer coefficient is defined as

$$h = Nuk_c / D_h \tag{5.29}$$

where k_c is the thermal conductivity of coolant.

As shown in Equation 5.29, the local heat transfer coefficient is proportional to coolant thermal conductivity and the reciprocal of hydraulic diameter of flow passage. Thus, decreasing the dimension of heat sink channels to micrometer size can significantly improve the local heat transfer coefficient. In the other hand, due to their high thermal conductivity, the application of nanofluids can improve the thermal performance of MCHS cooling systems further.

5.3 Numerical Model

5.3.1 Model Geometry

The geometry of microchannel heat sink and heat sink cover under study is symmetric, therefore only half of the MCHS was built in the numerical model in order to save computational effort. For simplificity, the heatsink cover was treated as adiabatic, therefore only the inlet and outlet flow passages were included in the model. Because the thermal test chip is in the form of FCPGA package, it was built as a silicon block ($12.8\times12.8\times0.65mm^3$) attached on the bottom surface of the heatsink in the geometric model. Figure 5.2 shows the 3-D geometric model built for the numerical simulation.

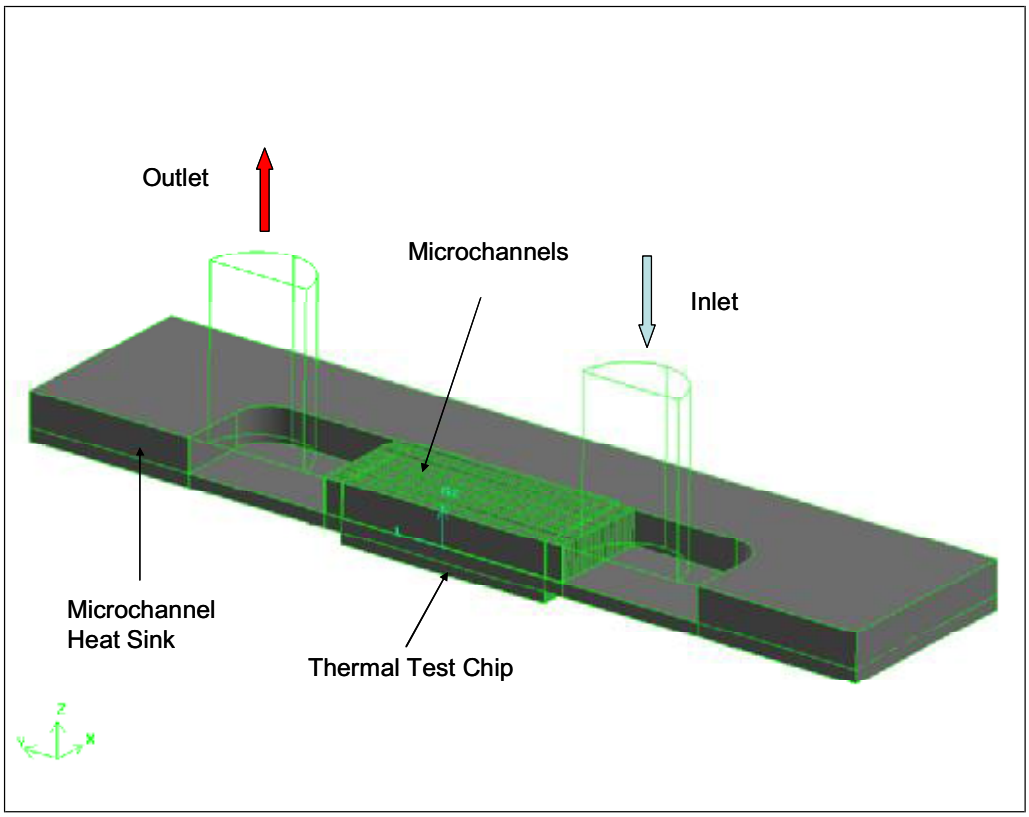

Figure 5.2: Geometric model of MCHS cooling system

A nonuniform mesh system has been generated in the numerical model (Figure 5.3). The size of grids is much finer in the domain with microchannels and heat sink fin structures. Altogether, 241825 elements were generated in this model.

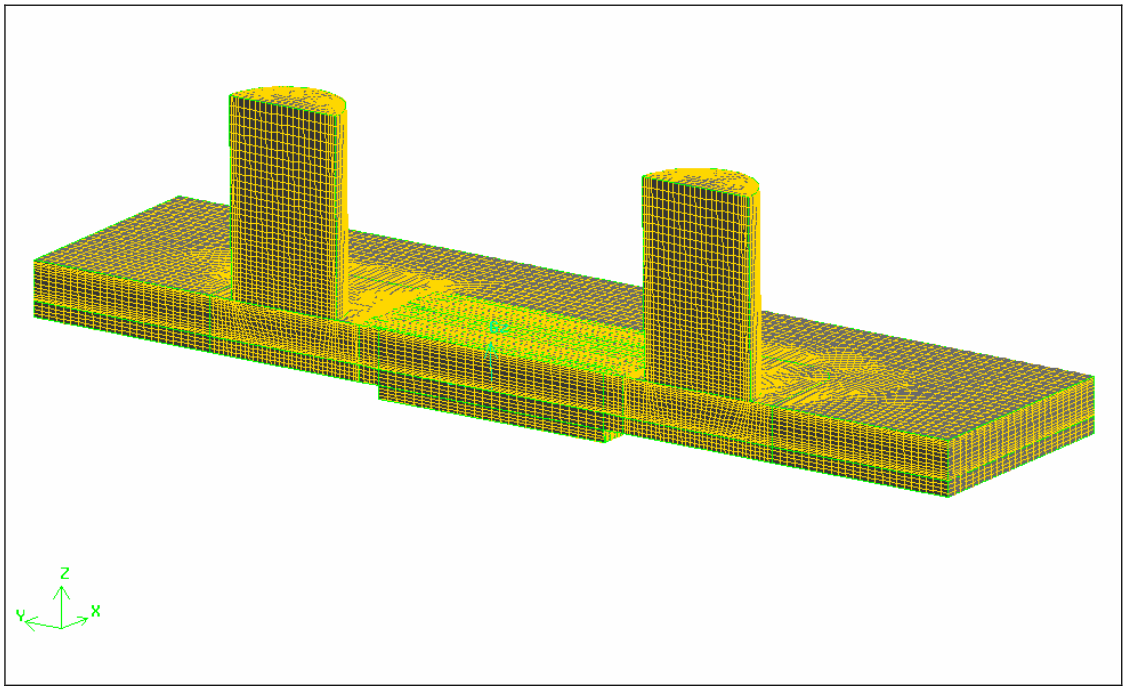

Figure 5.3: Mesh of the numerical model

As shown in Figure 5.4, eight horizontal elements and fifteen vertical elements were assigned in each microchannel. The mesh size used in the channel is not uniform. There are more grids near walls than in the center in order to capture the boundary layers. Three grids were assigned for each fin along the width direction. To ensure the computational accuracy, a grid independence study is carried out for microchannels. By doubling the elements in both channel length, width and depth directions, the deviations of these two simulation results are found to be less than 3% in pressure drop and 0.3% in thermal resistances. Therefore, the current mesh scheme was utilized in all the numerical simulation cases.

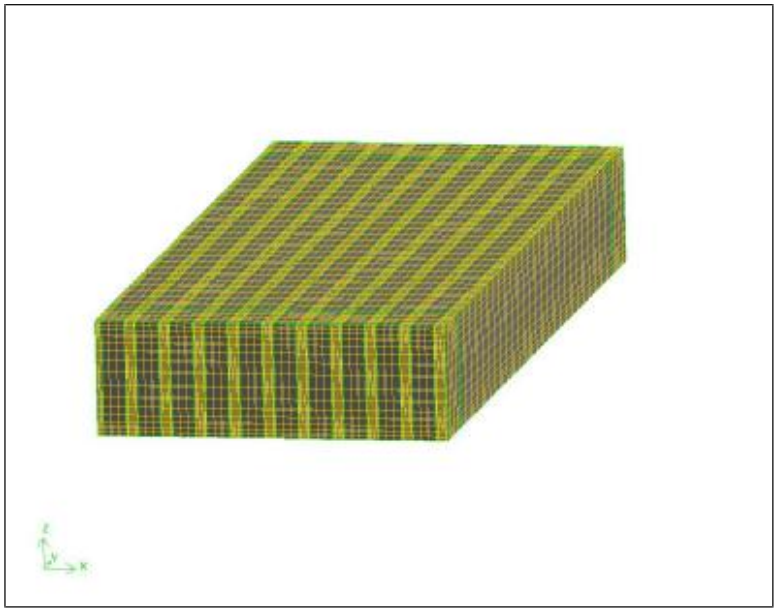

Figure 5.4: Mesh of microchannels and heat sink fins.

5.3.2 Governing Equations

The coolants in the numerical simulation were treated as incompressible Newtonian fluids but with changes of thermal and hydrodynamic properties such as thermal conductivity, viscosity and density. The temperature dependence of coolant viscosity and thermal conductivity were also considered. Thus, the governing equations are shown as follows:

- Equation of continuity

$$\nabla \cdot \mathbf{v} = 0 \tag{5.30}$$

- Equation of momentum (Navier-Stokes equations)

$$\rho \mathbf{v} \bullet \nabla \mathbf{v} = -\nabla p + \rho \mathbf{g} + \nabla \bullet \left(\mu \nabla \mathbf{v} \right) \tag{5.31}$$

- Equation of energy

$$\rho C_p \left(\mathbf{v} \bullet \nabla T \right) = \nabla \bullet \left(k \nabla T \right) + \mu \Phi_v \tag{5.32}$$

where Φ_v is the dissipation term. As the velocity gradient is small in our cooling system, the dissipation term is neglected.

In the Cartesian coordinate system, the above mentioned governing equations are given as follows:

$$\begin{cases} \dfrac{\partial v_x}{\partial x}+\dfrac{\partial v_y}{\partial y}+\dfrac{\partial v_z}{\partial z}=0 \\ \rho\left(v_x\dfrac{\partial v_x}{\partial x}+v_y\dfrac{\partial v_x}{\partial y}+v_z\dfrac{\partial v_x}{\partial z}\right)=-\dfrac{\partial p}{\partial x}+\left[\dfrac{\partial}{\partial x}\left(\mu\dfrac{\partial v_x}{\partial x}\right)+\dfrac{\partial}{\partial y}\left(\mu\dfrac{\partial v_x}{\partial y}\right)+\dfrac{\partial}{\partial z}\left(\mu\dfrac{\partial v_x}{\partial z}\right)\right]+\rho g_x \\ \rho\left(v_x\dfrac{\partial v_y}{\partial x}+v_y\dfrac{\partial v_y}{\partial y}+v_z\dfrac{\partial v_y}{\partial z}\right)=-\dfrac{\partial p}{\partial y}+\left[\dfrac{\partial}{\partial x}\left(\mu\dfrac{\partial v_y}{\partial x}\right)+\dfrac{\partial}{\partial y}\left(\mu\dfrac{\partial v_y}{\partial y}\right)+\dfrac{\partial}{\partial z}\left(\mu\dfrac{\partial v_y}{\partial z}\right)\right]+\rho g_y \\ \rho\left(v_x\dfrac{\partial v_z}{\partial x}+v_y\dfrac{\partial v_z}{\partial y}+v_z\dfrac{\partial v_z}{\partial z}\right)=-\dfrac{\partial p}{\partial z}+\left[\dfrac{\partial}{\partial x}\left(\mu\dfrac{\partial v_z}{\partial x}\right)+\dfrac{\partial}{\partial y}\left(\mu\dfrac{\partial v_z}{\partial y}\right)+\dfrac{\partial}{\partial z}\left(\mu\dfrac{\partial v_z}{\partial z}\right)\right]+\rho g_z \\ \rho C_p\left(v_x\dfrac{\partial T}{\partial x}+v_y\dfrac{\partial T}{\partial y}+v_z\dfrac{\partial T}{\partial z}\right)=\dfrac{\partial}{\partial x}\left(k\dfrac{\partial T}{\partial x}\right)+\dfrac{\partial}{\partial y}\left(k\dfrac{\partial T}{\partial y}\right)+\dfrac{\partial}{\partial z}\left(k\dfrac{\partial T}{\partial z}\right) \end{cases} \tag{5.33}$$

5.3.3 Boundary Conditions

- Inlet

The inlet is set as velocity inlet in FLUENT. A fully developed tube flow velocity profile at the inlet is assigned using the user defined function (UDF) ability of FLUENT. The velocity profile in the inlet is given as

$$\mathbf{v}=2\mathbf{v}_m(1-(r/R)^2) \tag{5.34}$$

where $\mathbf{v}_m$ is the coolant mean velocity at the inlet.

- Outlet

The outlet is set as pressure outlet. As only the pressure drop across the MCHS is of interest, the reference pressure at outlet is set as zero.

- Heat source

A Neumann boundary condition is assigned here to represent the constant heat flux generate by the thermal test chip. In all the simulations, the heating power of the thermal test chip is set to be 60W, therefore a heat flux of 36.62W/cm^2 is assigned on the bottom surface of thermal test chip in the numerical model.

- Other surfaces

By assuming that the heat loss from the thermal test chip and MCHS to ambient negligible, the other outer surfaces such as the side walls of MCHS and thermal test chip in the model are set as adiabatic walls.

5.3.4 Coolant Properties

The thermophysical and hydrodynamic properties of coolants are functions of temperature. Since temperature gradients exist in the fluid flow field, it is clear that the properties are not constant. However, except for D.I. water, the properties change of nanofluids with temperature in the present study is not available. Therefore the thermal conductivities of nanofluids used in the numerical simulation were assumed to be constant at the values measured in the experiments. This may underestimate the thermal performance of nanofluid-cooled MCHS cooling system, because the effective thermal conductivity of nanofluids shows strong temperature dependence (Das et al., 2003). The density of nanofluids can be calculated using the following equation

$$\rho = (1-\phi)\rho_f + \phi\rho_p \tag{5.35}$$

Previous experimental results have shown that the viscosity of nanofluids depends significantly on the dispersion method, volumetric fraction and particle size. According to the experiment results of Li et al. (2002), the viscosity of nanofluids generally follows Brinkman's theory for viscosity of solid-fluid mixture in low particle fraction region. Therefore the Brinkman's formula (Equation 5.36) was adopted in our current numerical model.

$$\mu_{nf} = \mu_f / (1-\phi^{2.5}) \tag{5.36}$$

One available equation for calculating the specific heat of nanofluids is given by

$$\rho C_{pnf} = (1-\phi)\rho_f C_{pf} + \phi\rho_p C_{pp} \tag{5.37}$$

This equation shows a decrease in specific heat with the increase of particle loading. However, Eastman et al. (2004) reported that the specific heat of nanofluids containing low volumetric fraction particles showed no measurable difference compared with that of the pure base fluid. Therefore the specific heat of nanofluids was set to be the same as that of the pure base fluids in the numerical model. A comparison of simulation results using specific heat of base fluid and using the value given by equation 5.37 will be discussed in the next section.

5.3.5 Simulation Results Calculation

The pressure drop (Δp) across the thermal test section is calculated as the pressure difference between the facet average pressure of inlet port (p_i) and outlet port (p_o).

$$\Delta p = p_i - p_o \tag{5.38}$$

$$p_i = \frac{1}{A_i}\int_{A_i} p dA_i \tag{5.39}$$

$$p_i = \frac{1}{A_o}\int_{A_o} p dA_o \tag{5.40}$$

In line with the experiments, the junction temperature used in the calculation of R'_{ji} was evaluated based on the four diode locations, which are at the centers of four dies on the chip. The inlet coolant temperature (T_i) in all numerical simulations were set to be 300K. The thermal resistance between the inlet coolant and thermal test chip in the numerical simulation (R'_{ji}) is calculated as

$$R'_{ji} = \frac{T'_j - T_i}{Q} \tag{5.41}$$

where, T'_j is the average temperature of the positions where thermal diodes are located and Q is the thermal test chip heating power, which was set to be 60W in all the simulations.

One should be aware here that the thermal contact resistance was not included in this numerical model. From the previous experimental results for aluminium single channel heat sink, the average junction-to-heatsink base thermal resistance (R_{jb}) is about 0.20°C/W. The thermal resistance of silicon chip (R_{si}) is about 0.026°C/W. The numerical simulation of aluminium single channel heat sink shows that the thermal resistance between the heat sink bottom and the position where the heat sink base thermocouples are located is less than 0.005°C/W. Therefore the thermal contact resistance (R_c) is estimated to be about 0.17°C/W. Thus, the junction-to-inlet thermal resistance of numerical simulation is calculated as

$$R_{ji} = R_{ji}^{'} + R_c \tag{5.42}$$

5.4 Simulation Results and Discussion

5.4.1 Validation of Numerical Model

Validation of the numerical model was carried out by comparing the simulation and experimental results for water-cooled MCHS cooling system. In order to take the temperature-dependent thermal and hydrodynamic properties of D.I. water into account, polynomial regression equations given by equations (5.43) and (5.44) for thermal conductivity and viscosity, respectively, in the current experiment temperature range were used in the numerical model.

$$k = -0.53164 + 0.00605225T - 0.0000075T^2 \tag{5.43}$$

$$\mu = 0.029099 - 0.00016913T + 0.00000025T^2 \tag{5.44}$$

The experimental and numerical simulation results for D.I. water-cooled MCHS cooling system are summarized in Table 5.3.

Table 5.3: Experiment, simulation and theoretical results of MCHS cooling system using water

Experiment	Flowrate (l/min)	0.072	0.159	0.239	0.33	0.424	0.516	0.61	0.709
	R_{ji} (K/W)	0.472	0.388	0.362	0.350	0.341	0.334	0.329	0.324
	Pressure Drop (mbar)	4.8	11.1	19.6	29.6	40.6	53.9	68.3	84.1
Numerical Simulation	Flowrate (l/min)	0.072	0.159	0.239	0.33	0.424	0.516	0.61	0.709
	R_{ji} (K/W)	0.426	0.355	0.334	0.320	0.313	0.308	0.304	0.301
	Pressure Drop (mbar)	5.09	12.7	20.5	30.8	41.0	52.2	64.2	77.9

5.4.1.1 Pressure Drop

The results from experiment, numerical simulation and theoretical analysis for the pressure drop across the thermal test section are plotted in Figure 5.5. The pressure drop values predicted by theoretical analysis and numerical simulation are quite similar. Their difference is within 2%. However, the measured pressure drop across the thermal test section measured in the experiment is slightly lower than the value predicted by numerical simulation at low volumetric flow rates and higher than the predicted value at high volumetric flow rates. The pressure drop discrepancy between experiment and simulation results is betweeb 2% to 8%.

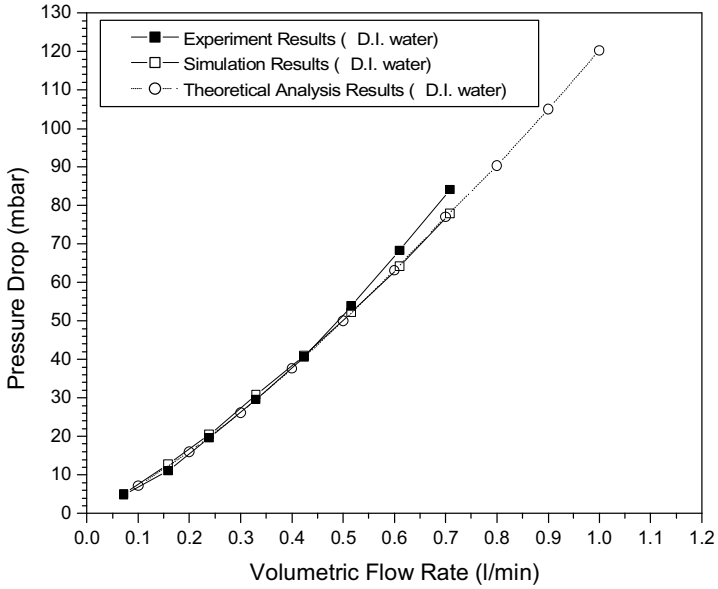

Figure 5.5: Experiment, numerical simulation and theoretical analysis results for pressure drop across the thermal test section.

5.4.1.2 Junction-to-inlet Thermal Resistance (R_{ji})

Figure 5.6 shows the junction-to-inlet thermal resistance measured in experiments and calculated by numerical simulation. The results from numerical simulation are about 6% lower than the experimental results.

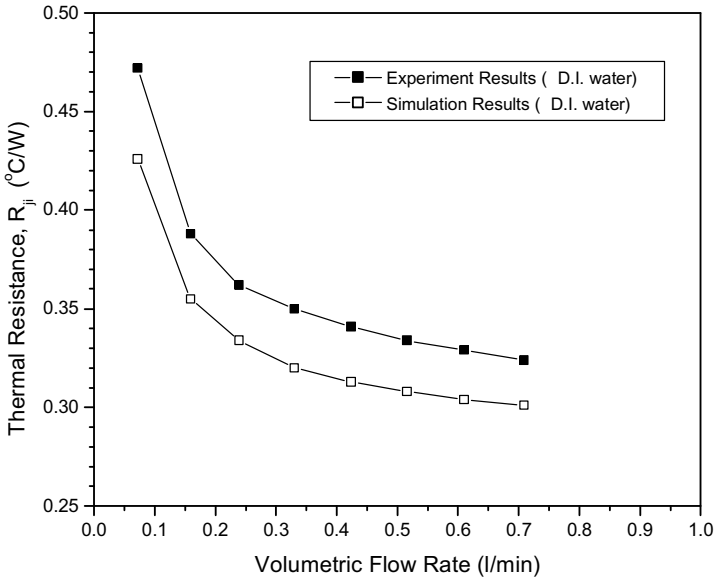

Figure 5.6: Comparison of R_{ji} from experiments results and numerical simulation

One possible reason for the discrepancy is that because the MCHS was attached with the heat sink cover by four screws, the nonuniform tightening of these screws may cause the heat sink to bend. The bending effect may cause the coolant flow by pass between the microchannel heat sink fin tips and the heat sink cover. It in turn reduces the cooling effect of MCHS by reducing the coolant flow rate through the microchannels.

5.4.1.3 Discussion

Figure 5.7 and 5.8 show the temperature distribution of MCHS and inlet/outlet ports when D.I. water was used as coolant with flow rate of 0.516 *l*/min.

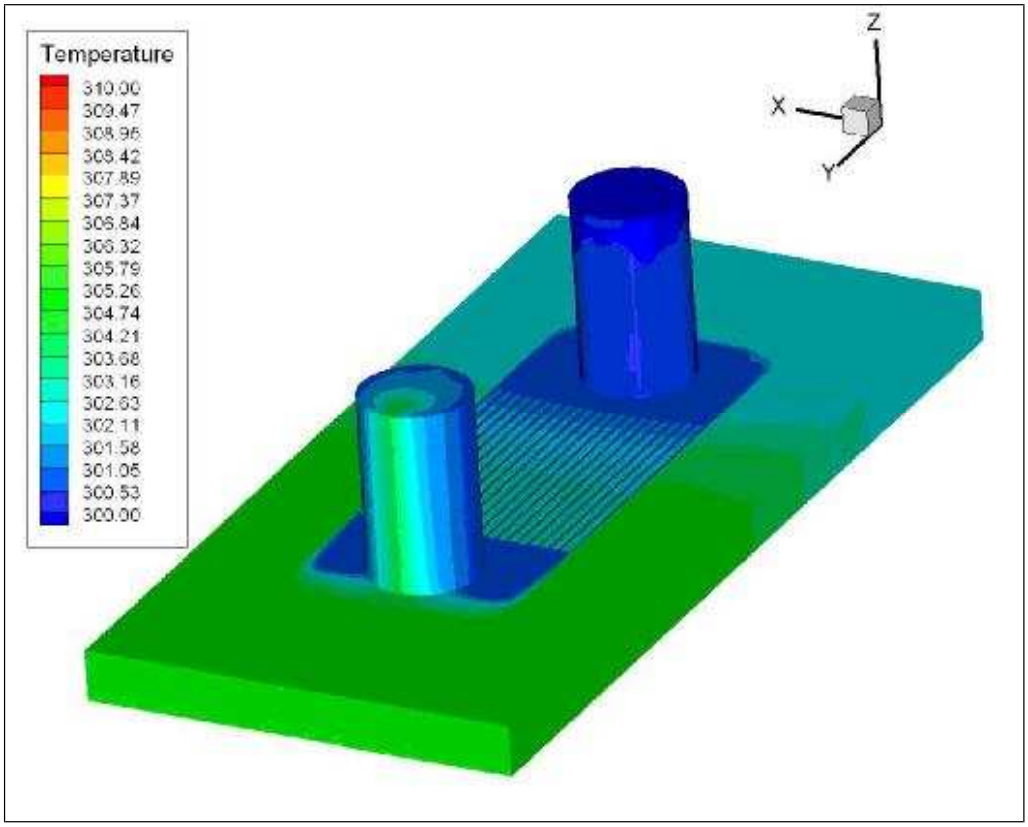

Figure 5.7: Temperature distribution of water-cooled MCHS at 0.516 l/min-1

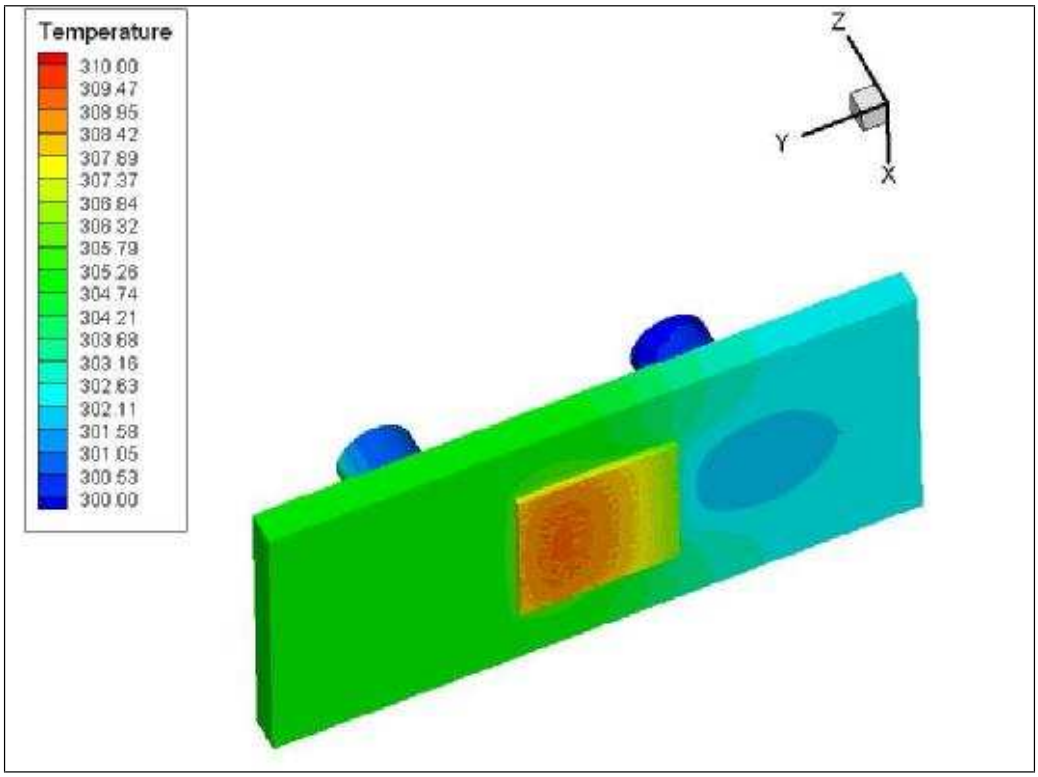

Figure 5.8: Temperature distribution of water-cooled MCHS at 0.516 l/min-2

Figure 5.9 shows the temperature contour of the bottom surface of the thermal test chip. It can be found that the point with highest temperature is located slightly downstream from the center of the thermal test chip. The positions of thermal diodes are labeled by "+" in Figure 5.9. The average temperature of these four points was used as T_j in the calculation of R_{ji} in order to allow the comparison between experimental measurements and simulation results.

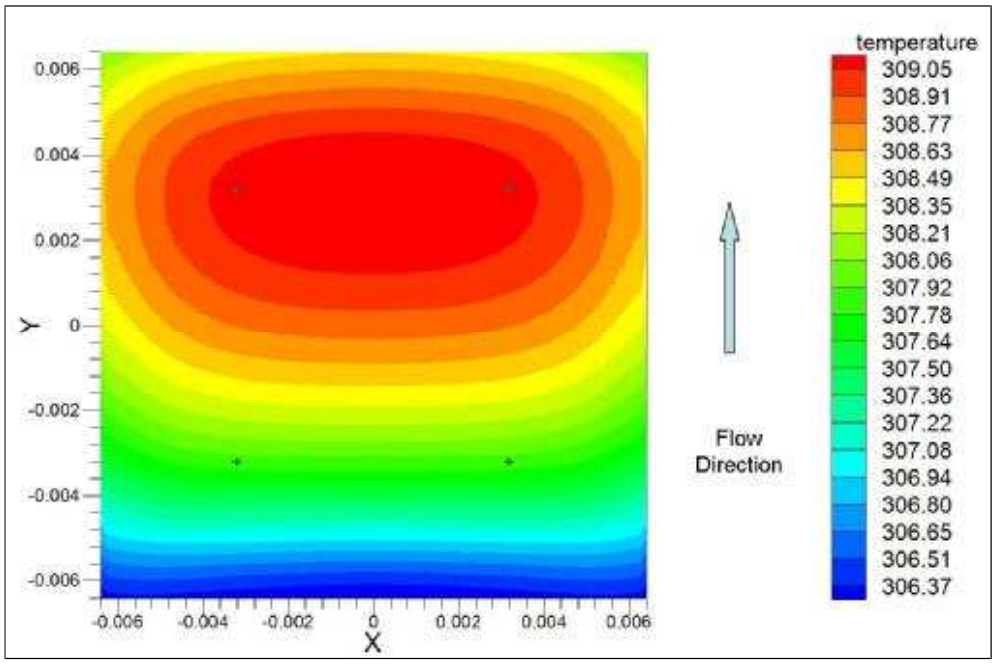

Figure 5.9: Temperature contour of the bottom surface of thermal test chip

Figure 5.10 and 5.11 show temperature and pressure contours of the central surface. It can be seen from Figure 5.11 that the major pressure drop occurs in the microchannel. Figure 5.12 shows the velocity magnitude contour of a cross section located 1mm from the heat sink base along the fin height direction. A typical flow developing region is observed in the microchannel entrance region. The units for velocity in this contour figure is m/s. Figure 5.13 shows the streamline of coolant flow in microchannel heat sink as well as the inlet/outlet port.

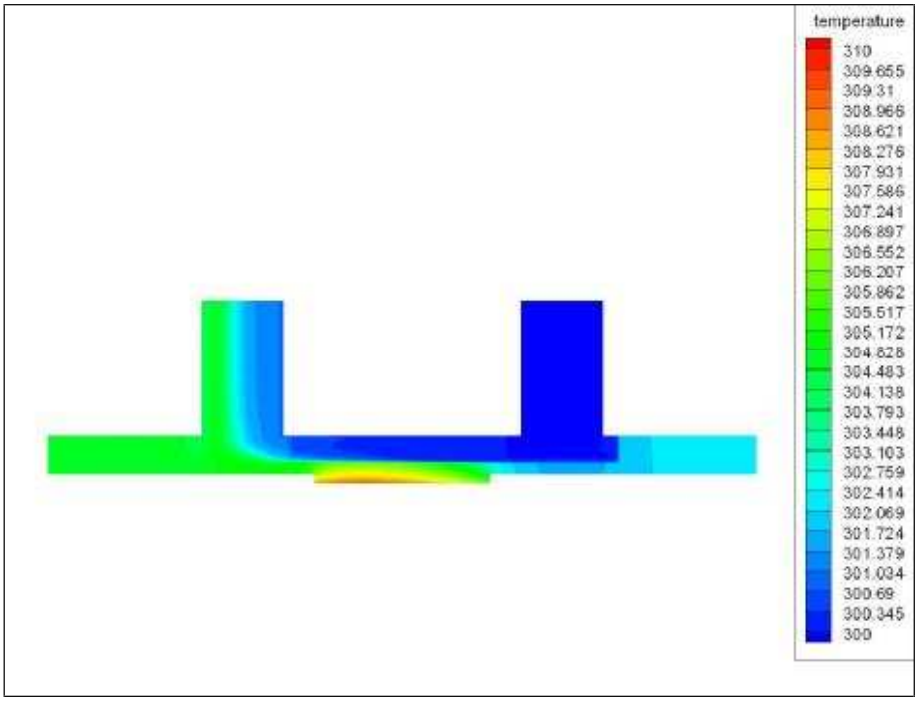

Figure 5.10: Temperature contour of the central surface

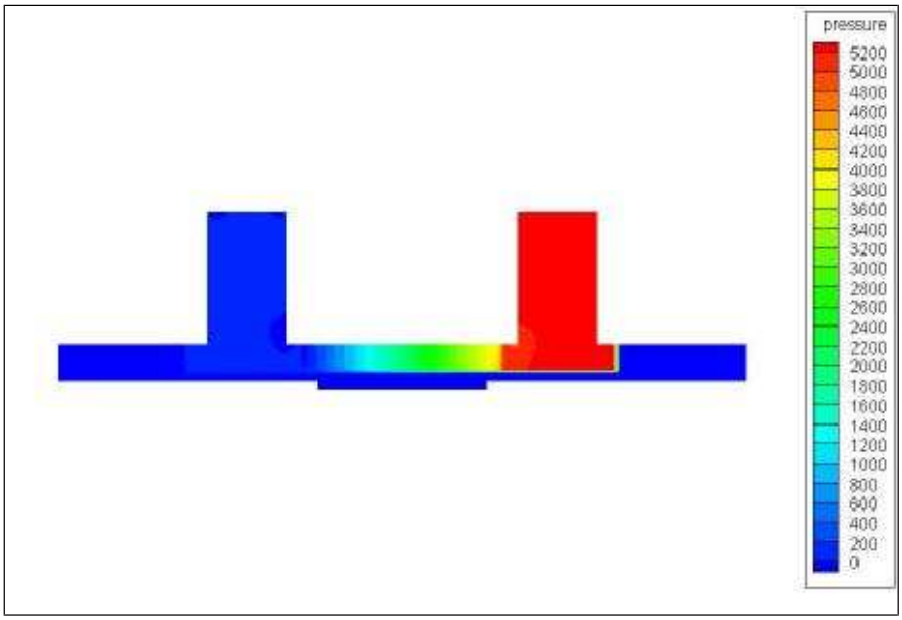

Figure 5.11: Pressure contour of the central surface

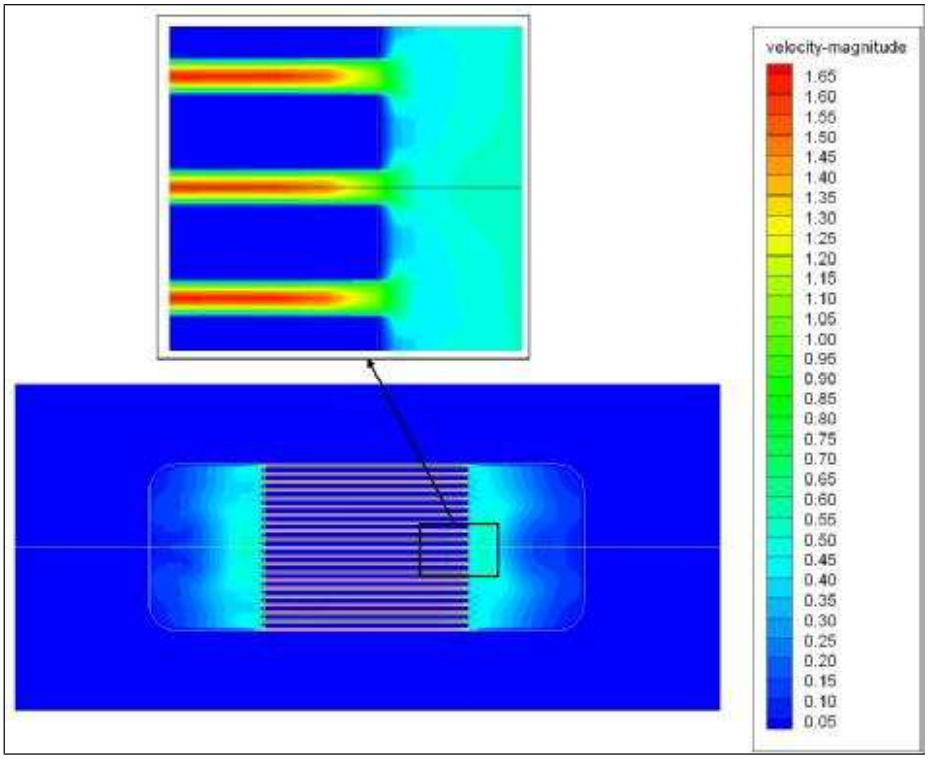

Figure 5.12: Velocity magnitude contour of cross section 1mm from heat sink base plane.

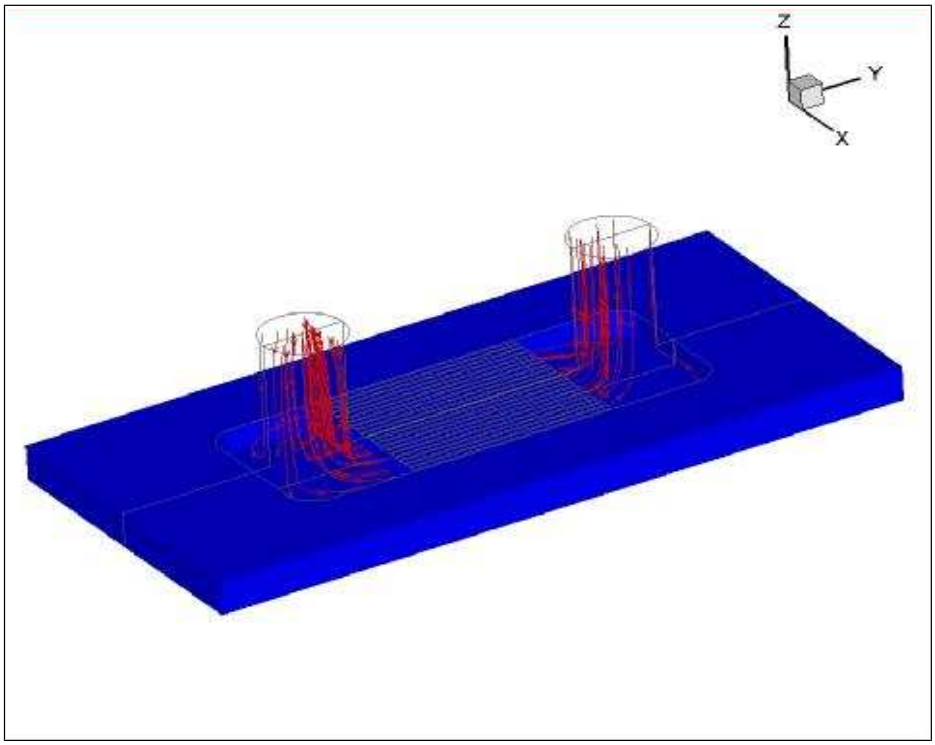

Figure 5.13: Streamline of coolant in MCHS and inlet/outlet ports.

5.4.2 Simulation Results for Nanofluids

5.4.2.1 Al_2O_3-water Nanofluids

The properties of 1~4 vol% Al_2O_3-water nanofluids are summarized in Table 5.4. It might be mentioned here that only the viscosity ratio between nanofluids and their base fluid are provided in the table. The actual viscosity of nanofluids are inputted in the numerical model using polynomial equations calculated according to the viscosity ratio and the temperature dependent viscosity of D.I. water. The simulation results for MCHS cooling system using 1~4 vol% Al_2O_3-water nanofluids are listed in Table 5.5.

Table 5.4: Properties summary of Al_2O_3-water nanofluids

Volume Fraction ϕ	1%	2%	3%	4%
Density ρ (kg/m^3)	1020.44	1047.51	1074.58	1101.64
Specific Heat C_P (kJ/kg-K)	4182	4182	4182	4182
Dynamics Viscosity ratio μ_{nf} / μ_f	1.00001	1.000057	1.000156	1.00032
Effective Thermal Conductivity k_{eff} (W/m-K)	0.650	0.664	0.675	0.686

Table 5.5: Summary of simulation results for Al_2O_3-water nanofluids

D.I. water	Flowrate (l/min)	0.1	0.2	0.3	0.4	0.5	0.6	0.7	0.8	0.9	1.0
	R_{ji} (K/W)	0.389	0.342	0.324	0.314	0.309	0.305	0.301	0.298	0.296	0.294
	ΔP (mbar)	7.5	16.6	27.0	38.2	50.0	62.9	76.5	91.3	107.0	123.5
1vol% Al_2O_3-Water Nanofluid	Flowrate (l/min)	0.1	0.2	0.3	0.4	0.5	0.6	0.7	0.8	0.9	1.0
	R_{ji} (K/W)	0.384	0.338	0.320	0.312	0.306	0.302	0.299	0.296	0.294	0.291
	ΔP (mbar)	7.5	16.7	27.2	38.5	50.4	63.4	77.7	92.0	107.6	126.2
2vol% Al_2O_3-Water Nanofluid	Flowrate (l/min)	0.1	0.2	0.3	0.4	0.5	0.6	0.7	0.8	0.9	1.0
	R_{ji} (K/W)	0.380	0.336	0.319	0.310	0.305	0.301	0.297	0.295	0.292	0.290
	ΔP (mbar)	7.6	16.8	27.3	38.6	50.9	63.9	78.0	92.4	108.9	124.6
3vol% Al_2O_3-Water Nanofluid	Flowrate (l/min)	0.1	0.2	0.3	0.4	0.5	0.6	0.7	0.8	0.9	1.0
	R_{ji} (K/W)	0.377	0.334	0.317	0.309	0.303	0.300	0.296	0.293	0.291	0.289
	ΔP (mbar)	7.6	16.9	27.4	38.8	51.8	64.3	78.7	94.8	109.2	126.7

4vol% Al_2O_3-Water Nanofluid	Flowrate (l/min)	0.1	0.2	0.3	0.4	0.5	0.6	0.7	0.8	0.9	1.0
	R_{ji} (K/W)	0.374	0.332	0.316	0.308	0.303	0.299	0.295	0.292	0.290	0.288
	ΔP (mbar)	7.6	17.0	27.6	39.0	51.5	64.8	79.0	94.5	110.5	128.6

The junction-to-inlet thermal resistances for the MCHS cooling system using D.I. water and Al_2O_3-water nanofluids are plotted in Figure 5.14, respectively. The R_{ji} of MCHS cooling system using Al_2O_3-water nanofluids are less than that for D.I. water. For each specific volumetric flow rate within the present simulation range, R_{ji} decreases with the increase of nanoparticle volume fraction. This is mainly due to the increase of the effective thermal conductivity of nanofluids when particle volume fraction increases.

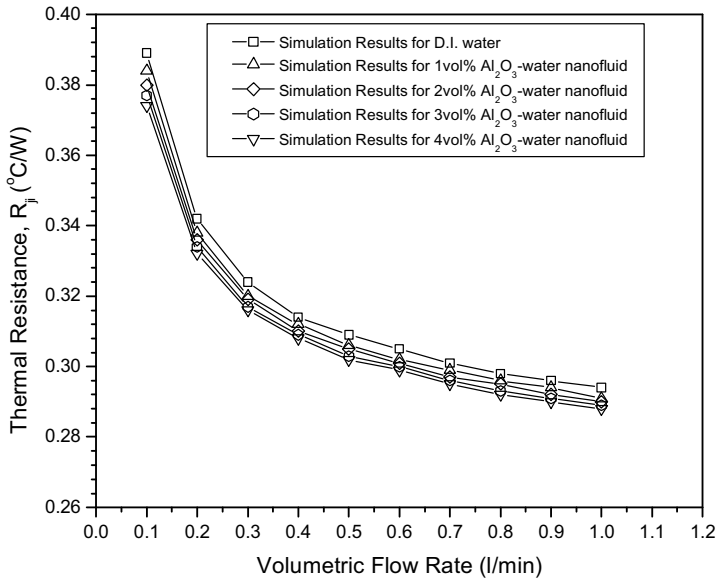

Figure 5.14: R_{ji} of D.I. water and Al_2O_3-water nanofluid-cooled MCHS cooling system.

Figure 5.15 shows the simulation results for pressure drop across the thermal test section when D.I. water and Al_2O_3-water nanofluids were used. As the viscosity increase for low volume fraction nanofluids over that of pure D.I. water is relatively small, no significant difference in pressure drop was observed.

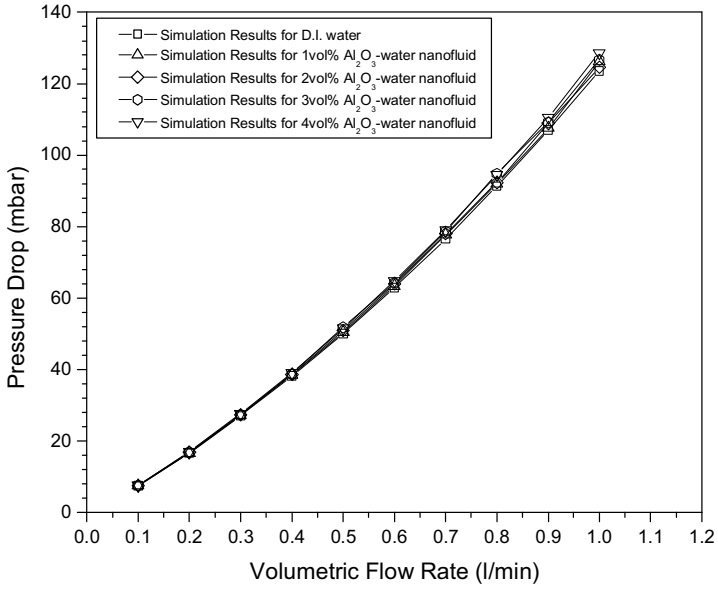

Figure 5.15: Pressure drop of D.I. water and Al_2O_3-water nanofluid cooled MCHS cooling system.

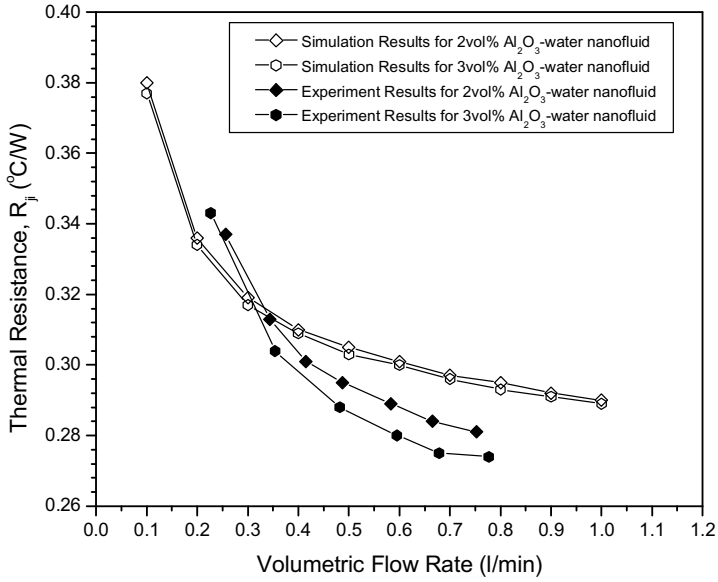

Figure 5.16: Experiment and simulation results of R_{ji} for MCHS cooling system using 2~3vol% Al_2O_3-water nanofluids.

Figure 5.16 shows the junction-to-inlet thermal resistance results for 2vol% and 3vol% Al_2O_3-water nanofluids from experiment and numerical simulation. It can be seen that the numerical simulation results for R_{ji} are 3~6% higher than that of the experimental results. One possible reason for the discrepancy is that the current numerical model

hasn't included the temperature effect on the effective thermal conductivity of nanofluids, which have been reported to be highly temperature dependent. The enhancement of convective heat transfer due to the existence of nanoparticles may also be considered as one important effect that accounts for this discrepancy.

The experimental results for pressure drop across the thermal test section are much larger than the simulation results at the same volumetric flow rates (Figure 5.17). As the viscosity of nanofluids depends greatly on the uniformity of nanoparticle dispersion, it is suspected that the agglomeration of nanoparticles in the prepared nanofluids significantly increases the viscosity of nanofluids and thus the pressure drop across the test section.

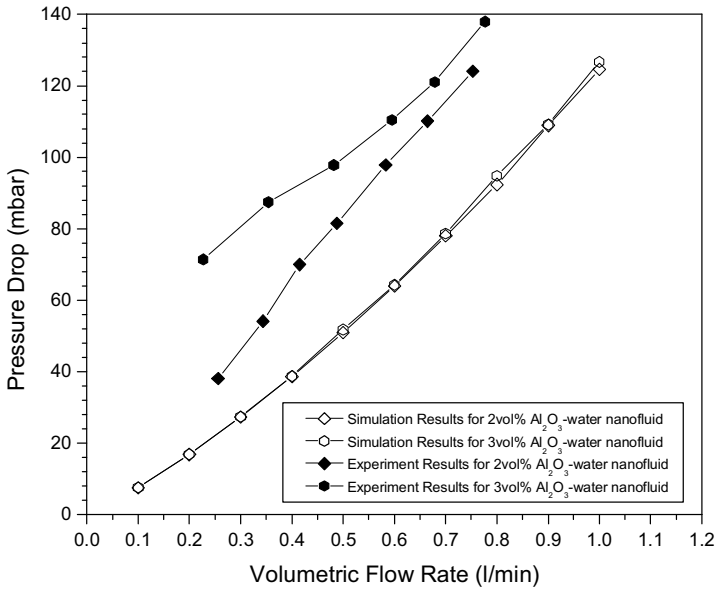

Figure 5.17: Experiment and simulation results of pressure drop across thermal test sectionfor MCHS cooling system using 2~3vol% Al_2O_3-water nanofluids.

The simulation results of R_{ji} using the specific heat of the base fluid and using the value given by equation 5.37 for MCHS cooling system utilizing 2vol% and 3vol% Al_2O_3-water nanofluids are plotted in Figure 5.18. The specific heat of nanofluids predicted by Equation 5.37 decreases with the increase of nanoparticle fraction. The

decrease in specific heat may overshadow the thermal performance improvement induced by the enhancement in effective thermal conductivity of nanofluids. For example, the R_{ji} predicted by using specific heat calculated from equation 5.37 for 2vol% and 3vol% Al_2O_3-water nanofluids are almost the same at the same volumetric flow rate, although the effective thermal conductivity of 3vol% Al2O3-water nanofluid are about 1.7% higher than that of 2vol% Al_2O_3-water nanofluid. The simulation results show that the junction-to-inlet thermal resistances predicted using specific heat given by Equation 5.37 are about 3~5% higher than the value predicted using specific heat of base fluid and about 7~10% higher than the experiment results. Therefore, this phenomenon can also be treated as one indication that Equation 5.37 underestimates the actual specific heat of the nanofluids.

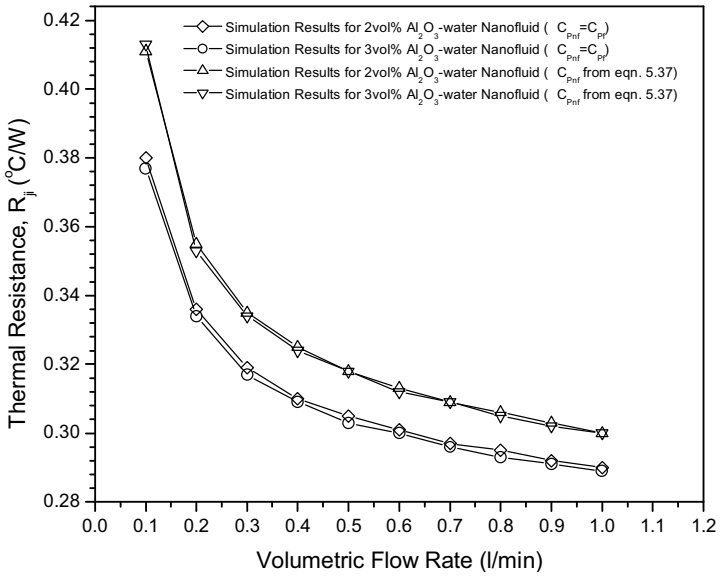

Figure 5.18: Comparison of simulation results for MCHS cooling system using different coolant specific heat value.

5.4.2.2 SiC-water nanofluids

The thermophysical and hydrodynamic properties of 1~4vol% SiC-water nanofluids are summarized in Table 5.6. The numerical simulation results for a MCHS cooling system using 1~4vol% SiC-water nanofluids are tabulated in Table 5.7.

Table 5.6: Properties summary of SiC-water nanofluids

Volume Fraction ϕ	1%	2%	3%	4%
Density ρ (kg/m^3)	1015.34	1037.31	1059.28	1081.24
Specific Heat C_P (kJ/kg-K)	4182	4182	4182	4182
Dynamics Viscosity ratio μ_{nf} / μ_f	1.00001	1.000057	1.000156	1.00032
Effective Thermal Conductivity k_{eff} (W/m-K)	0.661	0.680	0.692	0.713

Table 5.7:Summary of simulation results for SiC-water nanofluids

D.I. water	Flowrate (l/min)	0.1	0.2	0.3	0.4	0.5	0.6	0.7	0.8	0.9	1.0
	R_{ji} (K/W)	0.389	0.342	0.324	0.314	0.309	0.305	0.301	0.298	0.296	0.294
	ΔP (mbar)	7.5	16.6	27.0	38.2	50.0	62.9	76.5	91.3	107.0	123.5
1vol% SiC-Water Nanofluid	Flowrate (l/min)	0.1	0.2	0.3	0.4	0.5	0.6	0.7	0.8	0.9	1.0
	R_{ji} (K/W)	0.383	0.337	0.320	0.311	0.305	0.302	0.298	0.296	0.293	0.291
	ΔP (mbar)	7.5	16.7	27.1	38.4	51.1	63.4	77.4	91.9	107.1	123.9
2vol% SiC-Water Nanofluid	Flowrate (l/min)	0.1	0.2	0.3	0.4	0.5	0.6	0.7	0.8	0.9	1.0
	R_{ji} (K/W)	0.380	0.335	0.318	0.310	0.304	0.300	0.298	0.294	0.292	0.290
	ΔP (mbar)	7.6	16.8	27.3	38.6	51.7	63.8	78.1	92.8	108.3	124.8
3vol% SiC-Water Nanofluid	Flowrate (l/min)	0.1	0.2	0.3	0.4	0.5	0.6	0.7	0.8	0.9	1.0
	R_{ji} (K/W)	0.377	0.333	0.317	0.308	0.303	0.299	0.296	0.293	0.291	0.289
	ΔP (mbar)	7.6	16.8	27.4	38.8	51.9	64.1	78.7	93.4	108.7	126.1
4vol% SiC-Water Nanofluid	Flowrate (l/min)	0.1	0.2	0.3	0.4	0.5	0.6	0.7	0.8	0.9	1.0
	R_{ji} (K/W)	0.375	0.331	0.315	0.307	0.302	0.297	0.295	0.291	0.290	0.288
	ΔP (mbar)	7.6	16.9	27.5	39.0	52.2	65.5	78.9	94.9	109.4	127.5

Figure 5.19 and 5.20 show the junction-to-inlet thermal resistance and pressure drop of the MCHS cooling system at different flow rates when 1~4vol% SiC-water nanofluids are used. A similar trend in R_{ji} and ΔP as for Al_2O_3-water nanofluids was found. For example, at 0.5 *l*/min volumetric flow rate, the decrease of R_{ji} for 1~4vol% SiC-water nanofluids over that for pure D.I. water are about 1.3%, 1.6%,1.9% and 2.3%,

respectively, and the increase of pressure drop for 1~4vol% SiC-water nanofluids over that for pure D.I. water are about 2.2%, 3.4%, 3.8% and 4.4%, respectively.

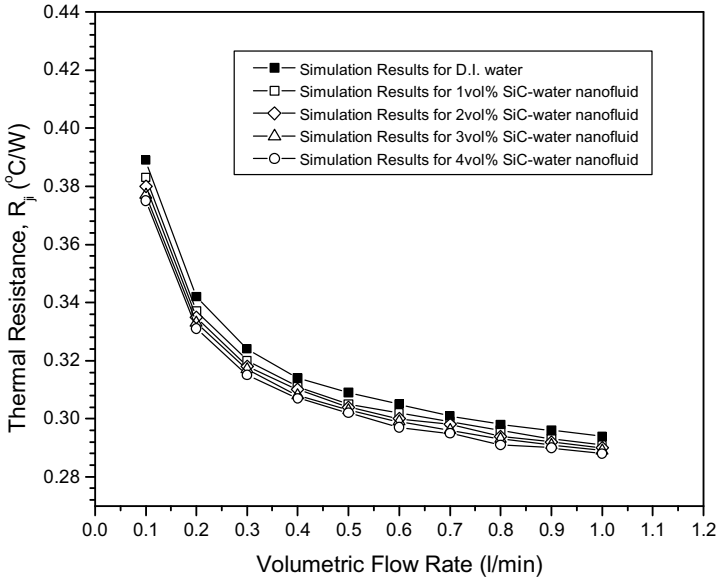

Figure 5.19: R_{ji} of D.I. water and SiC-water nanofluid-cooled MCHS cooling system

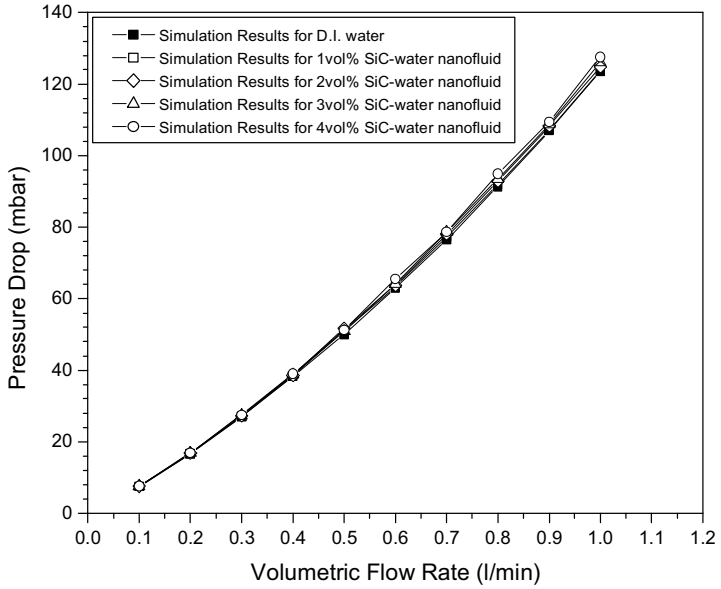

Figure 5.20: Pressure drop of D.I. water and SiC-water nanofluid-cooled MCHS cooling system.

Figure 5.21 shows the experimental and simulation results for junction-to-inlet thermal resistance of the MCHS cooling system for 1vol% SiC-water nanofluid. The simulation results for R_{ji} are again 4~6% higher than experiment results. Again, not

accounting for the effect of temperature on the thermal conductivity of SiC-water nanofluids and the dispersion effect of nanoparticles may lead to the underestimation of the thermal performance of the nanofluid-cooled MCHS cooling system.

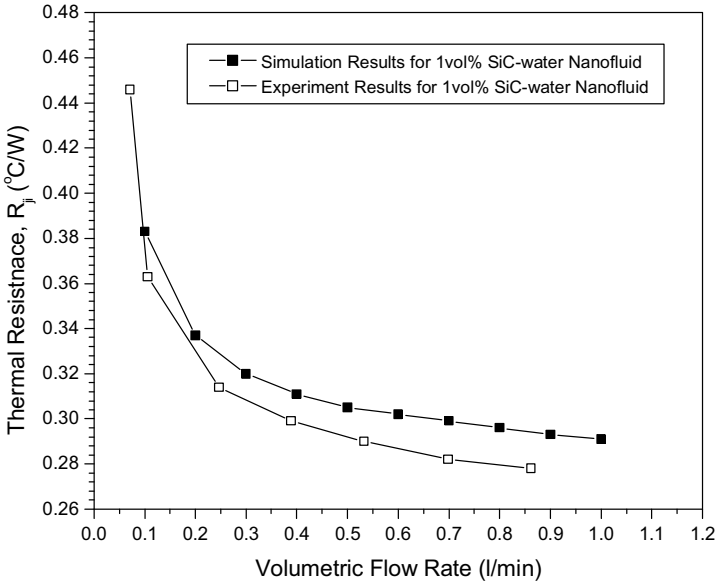

Figure 5.21: Experiment and simulation results of R_{ji} for MCHS cooling system using 1 vol% SiC-water nanofluid.

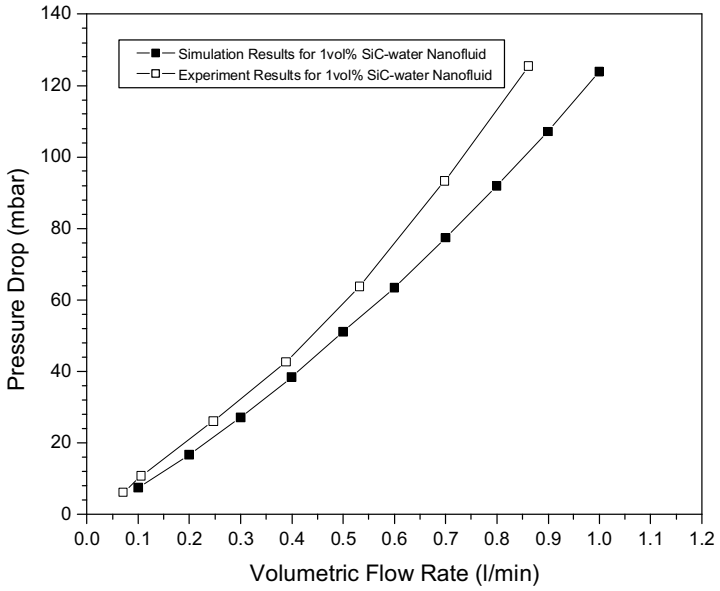

Figure 5.22: Experimenalt and simulation results of pressure drop across thermal test section for MCHS cooling system using 1vol% SiC-water nanofluid.

The pressure drop across the thermal test section from the numerical simulation and experiment is plotted in Figure 5.22. The value predicted by the numerical simulation is much lower than the experimental results. This may be caused by the increase of nanofluid viscosity due to agglomeration and sedimentation of nanoparticles, which is mainly related to nanofluid preparation method, nanoparticle size, experiment duration and procedure.

5.5 Closure

In this chapter, analyses on thermal resistance network, thermal and hydrodynamic performance of MCHS cooling system are presented. The numerical simulation approach is discussed in detail. The simulation results are first validated using the experimental results for the D.I. water-cooled MCHS cooling system. The junction-to-inlet thermal resistance and pressure drop of the MCHS cooling system utilizing various nanofluids are predicted.

CHARPTER 6: CONCLUSION

In this project, the effective thermal conductivities of D. I. water and ethylene glycol-based SiC, Al_2O_3 and CuO nanofluids were characterized experimentally using a fabricated apparatus based on the one dimensional steady-state parallel-plate method. A 2~14% increase in effective thermal conductivity was observed for the nanofluids studied. One microchannel heat sink cooling system was constructed in this study to investigate the thermal performance improvement induced by the application of various nanofluids. A 6~14% improvement in junction-to-inlet thermal resistance for Al_2O_3-water and SiC-water nanofluids over that for D.I. water were observed. Numerical simulations are extensively utilized in order to study the thermal performance of MCHS cooling system using various coolants within and beyond the range of our current experiments. By building a 3-D numerical model, the junction-to-inlet thermal resistance and pressure drop of the MCHS cooling system using various nanofluids are predicted. With a small pressure drop penalty, significant improvements in thermal performance of MCHS cooling systems using nanofluids are found from the simulation results. The currently available experimental and simulation results strongly indicate the great potential of nanofluids as coolants.

The development of heat transfer application based on nanofluids is still in its infancy. It is essential to do more research in this area. Although our current experimental and numerical results are reasonably good, further improvements can be expected.

- Nanofluids preparation technique

The preparation technique of nanofluids is extremely important to the stability, thermal and hydrodynamic properties of nanofluids. Its further development is greatly desired.

- Theoretical model for effective thermal conductivity

Although various theoretical models are proposed for predicting the effective thermal conductivity of nanofluids, to date, there is no model that can make accurate estimations. Further research in this area is necessary.

- Optimization of MCHS design

The flow path design of the heat sink can be improved further to reduce dead zones which probably may cause the sedimentation of nanoparticles.

- Optimization of cooling system

The design and operation of the MCHS cooling system can be optimized for nanofluids to reduce the possibility of sedimentation. For example, adding a mixing device in the coolant reservoir may help to reduce the sedimentation in the reservoir.

- Effect of nanoparticles in convective heat transfer

In the current numerical simulation, nanofluids were treated as Newtonian fluids. In order to consider the effect of nanoparticles, a diffusion model proposed by Xuan and Roetzel (2000) may be incorporated into the numerical model for a more accurate prediction of convective heat transfer of nanofluids.

REFERENCES:

Ahuja, A. S., "Augmentation of Heat Transport in Laminar Flow of Polystyrene Suspension: Experiments and Results", Journal of Applied Physics, Vol.46, No.8, pp. 3408-3416, 1975.

Ali, A., K. Vafai and A. R. A. Khaled, "Comparative Study between Parallel and Counter Flow configurations between Air and Falling Film Desiccant in the Presence of Nanoparticle Suspension", International Journal of Energy Research, pp.725-745, 2003.

Alloush, A., W. B. Gosney and W. A. Wakeham, "A Transient Hot-Wire Instrument for Thermal Conductivity Measurements in Electrically Conducting Liquids at Elevated Temperatures", International Journal of Thermophysics, Vol.3, pp.225, 1982.

Andres, R. P., R. S. Bowles, J. J. Kolstad and J. M. Calo, "Generation of Molecular Clusters of Controlled Size", Surface Science, Vol.106, pp.117-124, 1981.

Ashly, S., "Small-scale Structure Yields Big Property Payoffs", Mechanical Engineering, Vol.116, No.2, pp.52-57, 1994.

Assael, M. J., C. F. Chen, I. Metaxa and W. A. Wakeham, "Thermal Conductivity of Suspensions of Carbon Nanotubes in Water", 15th Symposium on Thermophysical Properties, Boulder CO, June 22-27, 2003.

"Assembly and Packaging", International Technology Roadmap for Semiconductors (ITRS) 2003 edition, http://public.itrs.net/Files/2003ITRS/Home2003.htm, pp.4-8, 2003.

Biercuk, M. J., M. C. Llaguna, M. Radosavljevic, J. K. Hyun and A. T. Johnson, "Carbon Nanotube Composites for Thermal Management", Applied Physics Letters, Vol.80, No.15, pp.2767-2769, 2002.

Brown, D. P., J. N. Chung and C. T. Crowe, "A Numerical Simulation of Nanocluster Formation in Supersonic Expansion Flows", Micromechanical Systems, ASME, New York, Dsc-vol.40, pp.211-225, 1992.

Bonnecaze R. T. and J. F. Brady, "A Method for Determining the Effective Conductivity of Dispersions of Particles", Proceedings of the Royal Society of London, Series A, Vol.430, pp.285-313, 1990.

Bruggeman, D. A. G., "Berechnung Verschiedener Physikalischer Konstanten von Heterogenen Suibstanzedn, I. Dielektrizitatskonstanten und Leitfahigkeiten der Mischkorper aus Isotropen Substanzen", Annalen der Physik, Vol.24, pp.636-679,

1935.

Carslaw, H. S. and J. C. Jaeger, "Conduction of Heat in Solids", 2nd edition, Oxford University Press, New York, pp. 510, 1959.

Challoner, A. R. and R. W. Powell, "Thermal Conductivity of Liquids: New Determinations for Seven Liquids and Appraisal of Existing Values", Proceeding of the Royal Society of London, Series A, Vol.238, No.112, pp. 90-106, 1956.

Chen, D. R., D. Y. H. Pui and S. L. Kaufman, "Electrospraying of Conducting Liquids for Monodisperse Aerosol Generation in the 4 nm to 1.8 μm Diameter Range", Journal of Aerosol Science, Vol.26, No.6, pp.963-977, 1995.

Chien, H. T., C. I. Tsai, P. H. Chen and P. Y. Chen, "Improvement On Thermal Performance of A Disk-shaped Miniature Heat Pipe with Nanofluid", ICEPT2003, pp.389-391, 2003.

Choi, U. S., "Enhancing Thermal Conductivity of Fluids with Nanoparticles: Developments and Applications of Non-Newtonian Flows", Vol.231/MD-Vol.66, pp.99-105, New York: The American Society of Mechanical Engineers, Nov. 1995.

Choi, U. S., Z. G. Zhang, W. Yu, F. E. Lockwood and E. A. Grulke, "Anomalous Thermal Conductivity Enhancement in Nanotube Suspensions", Applied Physics Letters, Vol.79, pp.2252-2254, 2001.

Das, S. K., N. Putra and W. Roetzel, "Pool Boiling Characteristics of Nano-fluids", International Journal of Heat and Mass Transfer, Vol.46, pp.856-862, 2003a.

Das, S. K., N. Putra, P. Thiesen and W. Roetzel, "Temperature Dependence of Thermal Conductivity Enhancement of Nanofluids", Journal of Heat Transfer, Vol.125, pp.567-574, 2003b.

Davis, R. H., "The Effective Thermal Conductivity of a Composite Material with Spherical Inclusions," International Journal of Thermophysics, Vol.7, pp.609-662, 1986.

Eastman, J. A., S. U. S. Choi, L.J. Thompson and S. Lee, "Enhanced Thermal Conductivity through the Development of Nanofluids", Nanocrystalline and Nanocomposite Materials II, Materials Research Society, pp.3-11, 1997.

Eastman, J. A., U. S. Choi, S. Li, "Development of Energy-Efficient Nanofluids for Heat Transfer Applications", Research Briefs Argonne National Laboratory, 2000.

Eastman, J. A., S. U. S. Choi, S. Li, W. Yu and L. J. Thompson, "Anomalously Increased Effective Thermal Conductivities of Ethylene Glycol-based Nanofluids Containing Copper Nanoparticles", Applied Physics Letter, Vol.78, Num.6, pp.718-720, 2001.

Eastman, J. A., S. R. Phillpot, S. U. S. Choi, P. Keblinski, “Thermal Transport in Nanofluids”, Annual Review of Materials Research, Vol.34, pp. 219-246, Aug. 2004.

Goldstein, R. J., D. D. Joseph and D. H. Pui, “Convective Heat Transfer in Nanofluids”, University of Minnesota, Sept. 2000.

Granqvist C. G., R. A. Buhrman, “Ultrafine Metal Particles”, Journal of Applied Physics, Vol.47, pp.2200-2219, 1976.

Hamilton R. L. and O. K. Crosser, "Thermal Conductivity of Heterogeneous Two-Component Systems", I & EC Fundamentals, Vol.1, No.3, pp.187-191,1962.

Harms, T. M., M. Kazmierczak and F. M. Gerner, “Developing Convective Heat Transfer in Deep Rectangle Microchannels”, International Journal of Heat and Fluid Flow, Vol.20, pp. 149-157, 1999.

Healy, J. J. , J. J. de Groot J. Kestin, “The Theory of the Transient Hot-wire Technique for Measuring Thermal Conductivity”, Physica B+C, Vol.82, pp.392-408, 1976.

Henderson, J. R. and F. van Swol, “On the Interface between a Fluid and a Planar Wall: Theory and Simulations of a Hard Sphere Fluid at a Hard Wall”, Molecular Physic, Vol.51, pp.991-1010, 1984.

Hill, P. G., H. Witting and E. P. Demetri, “Condensation of Metal Vapors During Rapid Expansion”, Journal of Heat Transfer, Vol.85, No.4 , pp. 303-317, Nov. 1963.

Holman, J. P., “Heat Transfer”, Singapore: McGraw Hill, 2002.

Incropera, F. P. and D. P. DeWitt, “Fundamentals of heat and mass transfer”, New York, Singapore: John Wiley & Sons, 2002.

Jeffrey, D. J., “Conduction through a Random Suspension of Spheres”, Proceedings of the Royal Society of London, Series A, Vol.335, No.1602, pp.355-367, 1973.

Johns, A. I., A. C. Scott, J. T. R. Watson and D. Ferguson, “Measurement of the Thermal Conductivity of Gases by the Transient Hot Wire Method”, Philosophical Transactions of the Royal Society of London, Series A, Mathematical and Physical Sciences, Vol. 325, No. 1585, pp.295-356, Jun. 1988.

KakaÇ, S. and Y. Yener, “Convective Heat Transfer”, United States: CRC Press, 1995.

Keblinski, P., S. R. Phillpot, S. U. S. Choi and J. A. Eastman, “Mechanisms of Heat Flow in Suspensions of Nano-sized Particles (Nanofluids)”, International Journal of Heat and Mass Transfer, Vol.45, pp.855-863, 2002.

Kestin, J. and W. A. Wakeham, “A Contribution to the Theory of the Transient Hot-

wire Technique for Thermal Conductivity Measurement", Physica, Vol.92A, pp.102-116, 1978.

Khaled, A.–R. A., K. Vafai, "Cooling Enhancements in Thin Films Supported by Flexible Complex Seals in the Presence of Ultrafine Suspensions", Journal of Heat Transfer, Vol.125 , pp.916-925, October 2003.

Khanafer, K., K. Vafai and M. Lightstone, "Buoyancy-driven Heat Transfer Enhancement in a Two-dimensional Enclosure Utilizing Nanofluids", International Journal of Heat and Mass Transdfer, Vol.46, pp.3639-3653, 2003.

Kim J., Kang, Y. T. and C. K. Choi, "Analysis of Convective Instability and Heat Transfer Characteristics of Nanofluids", Physics of Fluids, Vol.16, No.7, pp.2395-2401, 2004.

Komarneni, S., Parker, J.C., Wollenberger, H. J. (Eds.), Nanophase and Nanocomposite Materials II. Material Research Society, Pittsburg, PA, pp.3-11, 1993.

Lee, S. P. and U. S. Choi, "Application of Metallic Nanoparticle Suspensions in Advanced Cooling Systems: Recent Advances in Solids/Structures and Application of Metallic Materials," PVP-Vol. 342/MD-Vol.72, pp.227-234, New York: The American Society of Mechanical Engineers, November 1996.

Lee, S., S. U.-S. Choi, S. Li and J. A. Eastman, "Measuring Thermal Conductivity of Fluids Containing Oxide Nanoparticles", Journal of Heat Transfer, Vol.121, pp.280-289, May 1999.

Li, J. M., Z. L. Li, B. X. Wang, "Experimental Viscosity Measurements for Copper Oxide Nanoparticle Suspensions", Tsinghua Science and Technology, Vol.7, No.2, pp.198-201, April 2002.

Liu, K. V., U. S. Choi and K. E. Kazas, "Measurement of Pressure Drop and Heat Transfer in Turbulent Pipe Flows of Particulate Slurries", Argonne National Laboratory Report, ANL-88-15, 1988.

Lu, S. Y. and H. C. Lin, "Effective Conductivity of Composites Containing Aligned Spheroidal Inclusions of Finite Conductivity", Journal of Applied Physics, Vol.7, pp.6761-6769, 1996.

Maïga, S. E. B., C. T. Nguyen, N. Galanis and G. Roy, "Heat Transfer Behaviours of Nanofluids in a Uniformly Heated Tube", Superlattices and Microstructures, Vol.35, pp.543-557, 2004.

Masuda H., A. Ebata, K. Teramae and N. Hishinuma, "Alteration of Thermal Conducitvity and Viscosity of Liquid by Dispersing Ultra-fine Particles (Dispersion of $\gamma - Al_2O_3$, SiO_2 and TiO_2 Ultra-fine Particles)", Netsu Bussei, Vol.4, pp.227-233, 1993.

Maxwell, J. C., "A Treatise on Electricity and Magnetism", 2nd Ed., 1, Clarendon Press, Oxford, U. K., pp.435, 1881.

Moffat, R. J., "Describing the Uncertainties in Experimental Results", Experimental Thermal and Fluid Science, Vol.1, pp.3-17, 1988.

Moore, G. E., "Progress in Digital Integrated Electronics", IEEE International Electron Devices Meeting, Digest of Technical Papers, pp.11-13, Dec. 1975.

Nagasaka, Y. and A. Nagashima, "Absolute Measurement of the Thermal Conductivity of Electrically Conducting Liquids by the Transient Hot-wire Method", Journal of Physics E: Scientific Instruments, Vol.12, pp.1435-1440, 1981.

"National Electronics Manufacturing Technology Roadmaps, December 2002 (NEMI 2002)", National Electronics Manufacturing Initiative, Herndon, Virginia, USA, 2002.

Pak, B. C. and Y. I. Cho, "Hydrodynamic and Heat Transfer Study of Dispersed Fluids with Submicron Metallic Oxide Particles", Experimental Heat Transfer, Vol.11, pp.151-170, 1998.

Patel H. E., S. K. Das, T. Sundararajan, A. S. Nair, B. George, T. Pradeep, "Thermal Conductivities of naked and monolayer protected metal nanoparticle based nanofluids: manifestation of anomalous enhancement and chemical effects", Applied Physics Letters, Vol.83, pp.2931-2933,2003 .

Peng, X. F. and G. P. Peterson, "Convective Heat Transfer and Flow Friction for Water Flow in Microchannel Structures", International Journal of Heat and Mass Trnasfer, Vol.39, No.12, pp.2599-2608, 1996.

Philips, R. J., "Forced-Convection Liquid-Cooled Microchannel Heat Sinks", Master Thesis, Massachusetts Institute of Technology, Cambridge, MA, USA, 1988.

Philips, R. J., "Microchannel Heat Sinks", Advances in Thermal Modeling of Electronic Components and Systems, Vol.2, pp.109-184, 1990.

Putra, N., W. Roeztel, and S. K. Das, "Natural Convection of Nano-fluids", Heat and Mass Transfer, Vol.39, pp.775-784, 2003.

Roder, H. M., "A Transient Hot Wire Thermal Conductivity Apparatus for Fluids", Journal of Research of the National Bureau of Standards, Vol.86, No.5, pp.457-493, 1981.

Roy G., C. T. Nguyen and P. R. Lajoie, "Numerical Investigation of Laminar Flow and Heat Transfer in a Radial Flow Cooling System with the Use of Nanofluids", Superlattices and Microstructures, Vol.45, pp.497-511,2004.

Saini M. and R. L. Webb, “Thermal Performance Limits of Forced Convection Air Cooled Plain Fin Heat Sinks for Computer Cooling”, Proceeding of ITherm’02 Conference, 2002, pp.1-8, 2002.

Samalam, V. K., “Convective Heat Transfer in Microchannels”, Journal of Electronic Materials, Vol.18, No.5, pp.611-617, 1989.

Shin, S. and S. H. Lee, “Thermal Conductivity of Suspensions in Shear Flow Fields”, International Journal of Heat and Mass Transfer, Vol.43, pp.4275-4284, 2000.

Sohh, C. W. and M. M. Chen, “Microconvective Thermal conductivity in disperse two phase mixture as observed in a low velocity Couette Flow Experiment”, Journal of Heat Transfer, Vol.103, pp.47-51, 1981.

Taylor, G. I., “Dispersion of Soluble Matter in solvent flowing through a tube”, Proceeding of Royal Society, A, Vol.219, pp.186-203, 1953.

Tsai, C. Y., H. T. Chien, P. P. Ding, B. Chan, T. Y. Luh and P. H. Chen, “Effect of Structural Character of Gold Nanoparticles in Nanofluid on Heat Pipe Thermal Performance”, Materials Letters, Vol.58, pp.1461-1465, 2004.

Tummala, Rao R., co-editor and author, “Microelectronics Packaging Handbook”, Chapman Hall, 1996-1997.

Tummala Rao R., “Fundamentals of Microsystems Packaging”, McGraw-Hill Professional, 1st ed., May 8, pp. 214-216, 2001.

Tuckerman, D. B. and R. F. W. Pease, “High-Performance Heat Sinking for VLSI”, IEEE Electron Device Letters, Vol.EdL-2, No.5, pp.126-129, 1981.

Wagener M. and B. Günther, “Sputtering in Liquids: a Versatile Process for the Production of Magnetic Suspensions”, Journal of Magnetism and Magnetic Materials, vol.201, pp.41, 1999.

Wakeham W.A., A. Nagashima, and J.V. Sengers (ed), “Measurement of the Transport Properties of Fluids”, CRC Press, 1991.

Wang B. X., L. P. Zhou, X. F. Peng, “A Fractal Model for Predicting the Effective Thermal Conductivity of Liquid With Suspension of Nanoparticles”, International Journal of Heat and Mass Transfer, Vol.46, pp.2665-2672, 2003a.

Wang B. X., L. P. Zhou, X. F. Peng and X. X. Zhang, “Enhancing the Effective Thermal Conductivity of Liquid with Dilute Suspensions of Nano Particles”, 15th Symposium on Thermophysical Properties, Jun. 22-27. 2003b.

Wang, L., Z. Tan, S. Meng, D. L and G. Li, "Enhancement of Molar Heat Capacity of

Nanostructured Al_2O_3", Journal of Nanoparticle Research, Vol.3, pp. 483-487, 2001.

Wang, X. W., X. F. Xu, Stephen U. S. Choi, "Thermal Conductivity of Nanoparticle-Fluid Mixture", Journal of Thermophysics and Heat Transfer, Vol.13, No.4, pp.474-480, 1999.

Wasp, F. J., "Solid-Liquid Flow Slurry Pipeline Transportation", Trans Tech Publications, Berlin, 1977.

Xie H. Q., J. C. Wang, T. G. Xi, Y. Liu and F. Ai, "Dependence of the Thermal Conductivity of Nanoparticle-fluid Mixture on the Base Fluid", Journal of Materials Science Letter, Vol.21, pp.1469-1471, 2002a.

Xie H. Q., J. C Wang, T. G. Xi, Y. Liu and F. Ai, "Thermal Conductivity of Suspension Containing SiC particles", Journal of Materials Science Letter, Vol.21, pp. 193-195, 2002b.

Xuan, Y. M. and Q. Li, "Heat Transfer Enhancement of Nanofluids", International Journal of Heat and Fluid Flow, Vol.21, pp.58-64, 2000.

Xuan, Y. M. and W. Roetzel, "Conceptions for Heat Transfer Correlation of Nanofluids", International Journal of Heat and Mass Transfer, Vol.43, pp.3701-3707, 2000.

Xuan, Y. M., Q. Li and W. F. Hu, "Aggregation Structure and Thermal Conductivity of Nanofluids", AIChE Journal (Thermodynamics), Vol.49, No.4, pp.1038-1043, 2003.

Xuan, Y. M. and Qiang Li, "Investigation on Convective Heat Transfer and Flow Features of Nanofluids", Journal of Heat Transfer, Vol.125, pp.151-155, 2003.

Xue, L., Keblinski, P., Phillpot S. R., S. U. S. Choi, J. A. Eastman, "Effect of Liquid Layering at the Liquid-Solid Interface on Thermal Transport", International Journal of Heat and Mass Transfer, Vol.47, pp.4277-4284, 2004.

Xue Q. Z., "Model for Effective Thermal Conductivity of Nanofluids", Physics Letters A, Vol.307, pp.313-317, 2003.

Yang, W. J., "Convective Heat Transfer in Nanofluids", ME, The University of Michigan, Ann Arbor, 2003.

Yatsuya S, Y. Tsukasaki, K. Mihama, R. Uyeda, "Preparation of Extremely Fine Particles by Vacuum Evaporation onto a Running Oil Substrate", Journal of Crystal Growth, Vol.45, pp.490, 1978.

Yeh, L. T. and R. C. Chu, "Thermal Management of Microelectronic Equipment", New York: ASME Press, 2002.

You, S. M., K. H. Kim and J. H. Kim, "Effect of Nanoparticles on Critical Heat Flux of Water in Pool Boiling Heat Transfer", Applied Physics Letters, Vol.83, No.16, pp.3374-3376, 2003.

Yu, C. J., A. G. Richter, A. Datta, M. K. Durbin, P. Dutta, "Molecular Layering in a Liquid on a Solid Substrate: an X-ray Reflectivity Study", Physica B, Vol.283, pp.27-31, 2000.

Yu, W. and S. U. S. Choi, "The Role of Interfacial Layers in the Enhanced Thermal Conductivity of Nanofluids: A Renovated Maxwell Model", Journal of Nanoparticle Research, Vol.5, pp.167-171, 2003.

Zhang, H. Y., D. Pinjala, Y. K. Joshi, T. N. Wong, K. C. Toh, "Thermal Modeling and Design of Liquid Cooled Heat Sinks Assembled with Flip Chip Ball Grid Array Packages", Proceedings of Electronic Components and Technology Conference 2003, pp.431-437, 2003.

Zhou, D. W. and D. Y. Liu, "Heat Transfer Characteristics of Nanofluids in an acoustic Cavitation Field", Heat Transfer Engineering, Vol.25, No.6, pp.90-100, 2004.

Zhou, D. W., "Heat Transfer Enhancement of Copper Nanofluid with Acoustic Cavitation", International Journal of Heat and Mass Transfer, Vol.47, pp.3109-3117, 2004.

Zhou, L. P. and B. X. Wang, "Experimental Research on the Thermophysical Properties of Nanoparticle Suspensions Using the Quasi-Steady Method", Proceeding of Annual Chinese Engineering Thermophysics, pp.889-892, 2002 (in Chinese).

Zhu, H. T., Y. S. Lin and Y. S. Yin, "A Novel One-Step Chemical Method for Preparation of Copper Nanofluids", Journal of Colloid and Interface Science, Vol.277, pp.100-103, 2004.

Appendix A: Experiment Data of Nanofluids Thermal Conductivity Characterization

Table A.1 Recommended Heater Power Supply

Sample	Main Heater			Cap Heater			Side Heater (horizontal)			Side Heater (vertical)			Spacer Thickness (mm)	Temperature Difference (^{o}C)
	U (V)	I (A)	P (W)	U (V)	I (A)	P (W)	U (V)	I (A)	P (W)	U (V)	I (A)	P (W)		
D. I. Water	42.0	0.414	17.39	8.0	0.26	2.08	20.50	0.681	13.96	7.0	0.23	1.61	2.06	8.57
S_iC-H_2O NF														
1vol%	42.0	0.414	17.39	8.0	0.26	2.08	19.50	0.64	12.56	7.0	0.23	1.61	2.06	8.37
2vol%	42.0	0.414	17.39	8.0	0.26	2.08	19.30	0.64	12.31	7.0	0.23	1.61	2.06	8.21
3vol%	43.0	0.424	18.23	8.0	0.26	2.08	19.50	0.64	12.31	7.0	0.23	1.61	2.06	8.24
4vol%	44.0	0.434	19.10	8.0	0.26	2.08	20.0	0.66	13.20	7.0	0.23	1.61	2.06	8.57
Al_2O_3-H_2O NF														
1vol%	42.0	0.414	17.39	8.0	0.26	2.08	20.0	0.66	13.20	7.0	0.23	1.61	2.06	8.56
2vol%	42.0	0.414	17.39	8.0	0.26	2.08	19.50	0.64	12.56	7.0	0.23	1.61	2.06	8.35
3vol%	42.0	0.414	17.39	8.0	0.26	2.08	20.0	0.66	13.20	7.0	0.23	1.61	2.06	8.24
4vol%	42.0	0.414	17.39	8.0	0.26	2.08	19.50	0.64	12.56	7.0	0.23	1.61	2.06	8.20
CuO-H_2O NF														
1vol%	43.00	0.424	18.23	9.50	0.32	3.04	21.00	0.70	14.64	7.0	0.20	1.40	2.06	~8
2vol%	44.00	0.434	19.10	9.50	0.32	3.04	21.00	0.70	14.64	7.00	0.20	1.61	2.06	~8
2.7vol%	44.0	0.434	19.10	9.0	0.31	2.79	22.0	0.73	16.80	7.0	0.23	1.61	2.06	8.82
S_iC-EG NF														
1vol%	31	0.306	9.49	9.00	0.31	2.79	21.00	0.695	14.60	7.00	0.20	1.61	2.06	10.98
2vol%	31	0.306	9.49	8.50	0.29	2.47	20.80	0.690	14.35	7.00	0.20	1.61	2.06	10.47
3vol%	31	0.306	9.49	7.00	0.24	1.68	19.50	0.647	12.62	7.00	0.20	1.61	2.06	9.70

Table A.2: D.I. water

Power Input												Sample Under Testing	Date
Main Heater			Cap Heater			Side Heater (Horizontal)			Side Heater (Vertical)				
U (V)	I (A)	Q_{main} (W)	U (V)	I (A)	Q_{cap} (W)	U (V)	I (A)	Q_{side1} (W)	U (V)	I (A)	Q_{side2} (W)		
32.00	0.316	10.11	7.00	0.24	1.68	15.50	0.52	8.06	4.00	0.10	0.40	D.I. water	5-May-04

Time (S)	Cold Plate Temperature (oC)				Hot Plate Temperature (oC)				Side Temperature (oC)		Cap Temperature (oC)		dT (°C)	Thermal Conductivity (W/m-k)	
	T_{outer1}	T_{inner1}	T_{outer2}	T_{inner2}	T_{lower1}	T_{lower2}	T_{upper1}	T_{upper2}	T_{side1}	T_{side2}	T_{cap1}	T_{cap2}			
	103(°C)	104(°C)	105(°C)	106(°C)	107(°C)	108(°C)	109(°C)	110(°C)	113(°C)	114(°C)	115(°C)	116(°C)		K	K_{eff}
0	22.78	22.73	22.74	22.72	22.75	22.73	22.80	22.80	22.97	23.03	23.44	23.42	0.02	198.688	203.480
250	23.64	23.59	23.64	23.63	26.81	26.85	26.10	26.11	26.23	26.22	24.52	24.51	3.22	0.987	1.004
500	24.46	24.40	24.46	24.44	28.42	28.45	28.06	28.08	27.89	27.74	25.93	25.92	4.02	0.791	0.804
750	25.07	25.01	25.07	25.08	29.42	29.42	29.21	29.22	28.89	28.69	27.18	27.17	4.37	0.727	0.738
1000	25.14	25.10	25.17	25.17	29.89	29.91	29.83	29.84	29.46	29.20	28.11	28.11	4.76	0.668	0.677
1250	25.07	25.03	25.11	25.14	30.05	30.06	30.10	30.10	29.75	29.55	28.87	28.85	4.97	0.640	0.649
1500	25.21	25.16	25.26	25.24	30.16	30.15	30.20	30.21	29.97	29.86	29.40	29.38	4.96	0.642	0.651
1750	25.35	25.27	25.38	25.33	30.27	30.27	30.30	30.30	30.15	30.08	29.82	29.83	4.97	0.639	0.648
2000	25.55	25.46	25.56	25.54	30.45	30.45	30.48	30.49	30.37	30.33	30.18	30.18	4.95	0.642	0.651
2250	25.70	25.66	25.72	25.72	30.62	30.62	30.65	30.66	30.57	30.45	30.47	30.46	4.93	0.644	0.653
2500	25.68	25.62	25.73	25.72	30.73	30.74	30.80	30.81	30.70	30.54	30.70	30.68	5.07	0.627	0.636
2750	25.48	25.42	25.55	25.52	30.64	30.64	30.76	30.78	30.66	30.62	30.84	30.80	5.17	0.615	0.623
3000	25.62	25.51	25.65	25.60	30.62	30.65	30.71	30.71	30.68	30.65	30.90	30.92	5.08	0.626	0.635
3250	25.69	25.61	25.72	25.73	30.70	30.71	30.77	30.76	30.79	30.71	31.02	31.01	5.03	0.632	0.640
3500	25.71	25.62	25.73	25.72	30.77	30.77	30.85	30.87	30.80	30.64	31.08	31.05	5.10	0.623	0.631
3750	25.51	25.45	25.55	25.52	30.67	30.68	30.81	30.81	30.73	30.54	31.07	31.05	5.19	0.612	0.621
4000	25.36	25.29	25.42	25.38	30.53	30.53	30.67	30.68	30.61	30.59	31.06	31.03	5.19	0.612	0.621
4250	25.41	25.34	25.45	25.41	30.48	30.49	30.58	30.60	30.63	30.59	31.05	31.02	5.11	0.622	0.630
4500	25.52	25.45	25.57	25.52	30.54	30.54	30.61	30.63	30.69	30.69	31.09	31.06	5.05	0.629	0.638
4750	25.68	25.61	25.71	25.70	30.65	30.63	30.69	30.72	30.79	30.67	31.13	31.11	4.99	0.638	0.647
5000	25.68	25.62	25.70	25.69	30.76	30.76	30.84	30.84	30.81	30.70	31.14	31.11	5.11	0.622	0.631
5250	25.50	25.43	25.53	25.52	30.67	30.65	30.78	30.83	30.75	30.70	31.17	31.14	5.18	0.613	0.622
5500	25.45	25.37	25.51	25.47	30.57	30.58	30.69	30.71	30.74	30.80	31.16	31.13	5.15	0.617	0.625
5750	25.54	25.46	25.59	25.54	30.58	30.58	30.65	30.67	30.74	30.71	31.14	31.11	5.08	0.626	0.635

Table A.3: Ethylene glycol

Power Input												Sample Under Testing	Date
Main Heater			Cap Heater			Side Heater (Horizontal)			Side Heater (Vertical)				
U (V)	I (A)	Q_{main} (W)	U (V)	I (A)	Q_{cap} (W)	U (V)	I (A)	Q_{side1} (W)	U (V)	I (A)	Q_{side2} (W)		
30.7	0.303	9.30	9.00	0.31	2.79	21.00	0.70	14.60	7.00	0.20	1.40	Pure Ethylene glycol	26-July-04

Time (S)	Cold Plate Temperature (oC)				Hot Plate Temperature (oC)				Side Temperature (oC)		Cap Temperature (oC)		dT (°C)	Thermal Conductivity (W/m-k)	
	T_{outer1}	T_{inner1}	T_{outer2}	T_{inner2}	T_{lower1}	T_{lower2}	T_{upper1}	T_{upper2}	T_{side1}	T_{side2}	T_{cap1}	T_{cap2}			
	103(°C)	104(°C)	105(°C)	106(°C)	107(°C)	108(°C)	109(°C)	110(°C)	113(°C)	114(°C)	115(°C)	116(°C)		K	K_{eff}
0	21.92	21.94	21.96	21.96	22.03	22.04	22.05	22.04	22.14	22.11	22.35	22.35	0.09	33.471	34.273
250	22.86	22.81	22.85	22.80	27.24	27.26	26.45	26.45	27.67	28.21	24.26	24.34	4.45	0.677	0.687
500	23.76	23.70	23.73	23.71	30.47	30.50	29.98	30.00	30.54	31.17	26.89	26.96	6.78	0.444	0.448
750	24.38	24.31	24.32	24.31	32.56	32.60	32.25	32.30	32.17	32.80	29.16	29.20	8.27	0.364	0.366
1000	24.83	24.76	24.75	24.73	33.93	33.96	33.74	33.79	33.22	33.79	30.97	31.00	9.21	0.327	0.329
1250	25.16	25.06	25.08	25.02	34.87	34.88	34.74	34.81	33.96	34.51	32.46	32.48	9.83	0.306	0.307
1500	25.39	25.31	25.26	25.26	35.48	35.51	35.44	35.48	34.55	35.12	33.60	33.60	10.21	0.295	0.296
1750	25.53	25.41	25.39	25.37	35.89	35.93	35.87	35.91	35.09	35.24	34.48	34.49	10.52	0.286	0.287
2000	25.61	25.50	25.49	25.48	36.21	36.24	36.20	36.29	35.39	35.55	35.22	35.21	10.73	0.281	0.281
2250	25.74	25.64	25.63	25.60	36.49	36.48	36.45	36.53	36.03	35.99	35.77	35.78	10.87	0.277	0.277
2500	25.83	25.73	25.69	25.69	36.63	36.65	36.66	36.70	36.39	36.40	36.28	36.27	10.93	0.276	0.276
2750	25.84	25.72	25.72	25.71	36.78	36.81	36.82	36.89	36.68	36.65	36.72	36.71	11.08	0.272	0.272
3000	25.88	25.78	25.76	25.75	36.90	36.93	36.95	37.01	36.82	36.87	37.04	37.01	11.15	0.270	0.270
3250	25.95	25.82	25.83	25.77	36.98	37.01	37.05	37.10	36.95	36.90	37.28	37.26	11.20	0.269	0.269
3500	25.99	25.87	25.86	25.83	37.07	37.08	37.11	37.17	37.01	36.90	37.44	37.43	11.23	0.268	0.268
3750	25.96	25.86	25.84	25.80	37.09	37.10	37.14	37.20	37.04	36.98	37.56	37.52	11.27	0.267	0.267
4000	25.98	25.86	25.84	25.82	37.13	37.14	37.18	37.23	37.03	37.02	37.69	37.65	11.29	0.267	0.267
4250	26.00	25.88	25.86	25.84	37.13	37.17	37.19	37.26	36.95	36.91	37.76	37.70	11.29	0.267	0.267
4500	25.96	25.86	25.87	25.84	37.16	37.16	37.20	37.26	36.88	36.84	37.78	37.70	11.31	0.266	0.266
4750	26.00	25.86	25.86	25.83	37.16	37.17	37.23	37.27	36.67	36.62	37.75	37.69	11.32	0.266	0.266
5000	25.91	25.79	25.75	25.75	37.08	37.09	37.14	37.19	36.47	36.44	37.64	37.55	11.31	0.266	0.266
5250	25.83	25.71	25.70	25.68	37.01	37.04	37.08	37.14	36.45	36.39	37.60	37.52	11.33	0.266	0.266

Table A.4: 1 vol% SiC-water Nanofluid

Power Input												Sample Under Testing	Date
Main Heater			Cap Heater			Side Heater (Horizontal)			Side Heater (Vertical)				
U (V)	I (A)	Q_{main} (W)	U (V)	I (A)	Q_{cap} (W)	U (V)	I (A)	Q_{side1} (W)	U (V)	I (A)	Q_{side2} (W)		
42.00	0.414	17.39	19.50	0.64	12.56	8.00	0.270	2.16	7.00	0.23	1.61	1 vol% SiC-H_2O NF fresh	13-May-04

Time (S)	Cold Plate Temperature (oC)				Hot Plate Temperature (oC)				Side Temperature (oC)		Cap Temperature (oC)		dT (°C)	Thermal Conductivity (W/m-k)	
	T_{outer1}	T_{inner1}	T_{outer2}	T_{inner2}	T_{lower1}	T_{lower2}	T_{upper1}	T_{upper2}	T_{side1}	T_{side2}	T_{cap1}	T_{cap2}			
	103(°C)	104(°C)	105(°C)	106(°C)	107(°C)	108(°C)	109(°C)	110(°C)	113(°C)	114(°C)	115(°C)	116(°C)		K	K_{eff}
0	23.28	23.21	23.14	23.13	23.18	23.15	23.15	23.13	23.24	23.25	23.38	23.42	-0.01	-607.38	-622.05
250	24.13	24.07	24.05	24.04	29.51	29.52	29.32	29.34	27.42	27.92	25.98	26.10	5.46	1.002	1.019
500	25.00	24.92	24.93	24.91	31.89	31.89	31.76	31.77	29.81	30.26	28.74	28.83	6.97	0.784	0.796
750	25.73	25.65	25.67	25.65	33.13	33.14	33.02	33.05	31.43	31.77	30.78	30.83	7.48	0.730	0.741
1000	26.31	26.21	26.25	26.22	33.96	33.97	33.87	33.89	32.64	33.01	32.27	32.30	7.75	0.706	0.716
1250	26.59	26.54	26.56	26.56	34.55	34.54	34.45	34.48	33.48	33.76	33.33	33.34	7.99	0.684	0.694
1500	26.59	26.52	26.55	26.55	34.79	34.78	34.70	34.73	34.02	34.23	34.00	34.01	8.25	0.663	0.672
1750	26.57	26.49	26.54	26.54	34.86	34.87	34.78	34.81	34.31	34.51	34.44	34.46	8.35	0.654	0.664
2000	26.67	26.61	26.65	26.62	34.94	34.93	34.87	34.86	34.53	34.75	34.72	34.72	8.31	0.657	0.667
2250	26.89	26.79	26.86	26.81	35.06	35.08	34.98	35.00	34.71	34.92	34.95	34.96	8.27	0.661	0.671
2500	27.10	27.02	27.06	27.04	35.26	35.26	35.18	35.20	34.90	35.18	35.16	35.15	8.23	0.664	0.673
3000	27.11	27.04	27.06	27.06	35.45	35.47	35.41	35.42	35.13	35.32	35.44	35.42	8.41	0.650	0.659
3250	26.96	26.86	26.92	26.91	35.38	35.38	35.29	35.33	35.11	35.27	35.41	35.41	8.50	0.643	0.652
3500	26.92	26.82	26.91	26.83	35.26	35.26	35.18	35.21	35.05	35.24	35.41	35.40	8.44	0.648	0.657
3750	27.01	26.90	26.96	26.93	35.28	35.26	35.19	35.22	35.04	35.30	35.40	35.40	8.36	0.654	0.663
4000	27.17	27.07	27.13	27.09	35.39	35.37	35.29	35.33	35.12	35.38	35.45	35.44	8.30	0.658	0.668
4250	27.36	27.28	27.32	27.31	35.59	35.60	35.51	35.53	35.30	35.50	35.60	35.62	8.29	0.659	0.669
4500	27.23	27.14	27.22	27.20	35.59	35.61	35.54	35.57	35.31	35.54	35.62	35.60	8.43	0.649	0.658
4750	27.07	26.98	27.07	27.01	35.49	35.49	35.40	35.45	35.21	35.48	35.58	35.57	8.49	0.644	0.653
5000	27.02	26.93	27.00	27.00	35.40	35.40	35.34	35.38	35.23	35.49	35.58	35.58	8.44	0.648	0.657
5250	27.16	27.08	27.16	27.12	35.45	35.44	35.37	35.40	35.28	35.46	35.60	35.59	8.34	0.655	0.665
5500	27.39	27.30	27.34	27.32	35.59	35.60	35.53	35.54	35.33	35.58	35.68	35.67	8.29	0.660	0.669
5750	27.35	27.28	27.36	27.34	35.69	35.70	35.61	35.66	35.48	35.61	35.76	35.75	8.38	0.652	0.661
6000	27.26	27.17	27.21	27.21	35.68	35.67	35.60	35.63	35.47	35.57	35.76	35.78	8.48	0.644	0.653
6200	27.05	26.97	27.01	27.01	35.53	35.52	35.46	35.48	35.29	35.49	35.69	35.67	8.53	0.641	0.650

Table A.5: 2 vol% SiC-Water Nanofluid

Power Input												Sample Under Testing	Date
Main Heater			Cap Heater			Side Heater (Horizontal)			Side Heater (Vertical)				
U (V)	I (A)	Q_{main} (W)	U (V)	I (A)	Q_{cap} (W)	U (V)	I (A)	Q_{side1} (W)	U (V)	I (A)	Q_{side2} (W)		
42.00	0.414	17.39	19.30	0.64	12.31	8.00	0.270	2.16	7.00	0.23	1.61	2 vol% SiC-H_2O NF fresh	13-May-04

Time (S)	Cold Plate Temperature (oC)				Hot Plate Temperature (oC)				Side Temperature (oC)		Cap Temperature (oC)		dT (°C)	Thermal Conductivity (W/m-k)	
	T_{outer1}	T_{inner1}	T_{outer2}	T_{inner2}	T_{lower1}	T_{lower2}	T_{upper1}	T_{upper2}	T_{side1}	T_{side2}	T_{cap1}	T_{cap2}		K	K_{eff}
	103(°C)	104(°C)	105(°C)	106(°C)	107(°C)	108(°C)	109(°C)	110(°C)	113(°C)	114(°C)	115(°C)	116(°C)			
0	22.81	22.74	22.71	22.66	22.63	22.59	22.56	22.56	22.79	22.81	23.04	23.04	-0.09	-60.403	-61.868
250	24.31	24.21	24.20	24.19	29.34	29.38	29.08	29.08	27.70	28.26	25.38	25.50	5.16	1.059	1.078
500	25.33	25.32	25.32	25.31	31.93	31.97	31.78	31.82	30.29	30.86	28.13	28.25	6.64	0.824	0.837
750	26.16	26.09	26.13	26.10	33.30	33.33	33.19	33.21	31.95	32.18	30.29	30.39	7.23	0.757	0.768
1000	26.57	26.51	26.55	26.53	34.11	34.15	34.03	34.07	33.08	33.32	31.92	32.01	7.60	0.719	0.730
1250	26.60	26.54	26.57	26.60	34.48	34.50	34.41	34.46	33.74	33.93	33.01	33.07	7.92	0.690	0.700
1500	26.71	26.62	26.68	26.66	34.65	34.66	34.59	34.63	34.13	34.32	33.71	33.76	8.01	0.682	0.692
1750	26.69	26.61	26.68	26.67	34.72	34.73	34.67	34.71	34.43	34.54	34.23	34.24	8.09	0.676	0.686
2000	26.71	26.60	26.69	26.66	34.77	34.77	34.73	34.74	34.60	34.68	34.59	34.57	8.14	0.672	0.681
2250	26.71	26.65	26.72	26.69	34.80	34.81	34.74	34.77	34.73	34.76	34.89	34.89	8.14	0.671	0.681
2500	26.73	26.63	26.71	26.69	34.83	34.84	34.79	34.81	34.85	34.85	35.12	35.13	8.18	0.669	0.678
2750	26.68	26.61	26.68	26.65	34.83	34.82	34.77	34.80	34.88	34.85	35.14	35.14	8.20	0.667	0.677
3000	26.62	26.55	26.63	26.60	34.78	34.76	34.71	34.76	34.89	34.87	35.22	35.22	8.20	0.667	0.677
3250	26.58	26.51	26.59	26.57	34.74	34.74	34.70	34.74	34.89	34.84	35.21	35.19	8.21	0.666	0.676
3500	26.60	26.51	26.59	26.58	34.75	34.73	34.69	34.73	34.87	34.83	35.18	35.18	8.19	0.667	0.677
3750	26.59	26.50	26.58	26.56	34.74	34.74	34.70	34.74	34.87	34.84	35.19	35.17	8.21	0.665	0.675
4000	26.57	26.48	26.58	26.56	34.74	34.75	34.68	34.72	34.84	34.82	35.17	35.16	8.22	0.665	0.674
4250	26.59	26.51	26.58	26.56	34.74	34.74	34.68	34.72	34.83	34.77	35.16	35.15	8.21	0.666	0.676
4500	26.61	26.53	26.61	26.60	34.75	34.74	34.69	34.72	34.85	34.79	35.14	35.13	8.18	0.668	0.678
4750	26.60	26.51	26.59	26.57	34.74	34.74	34.70	34.73	34.84	34.81	35.15	35.16	8.20	0.666	0.676
5000	26.53	26.44	26.54	26.51	34.71	34.72	34.66	34.69	34.76	34.75	35.15	35.13	8.24	0.663	0.673
5250	26.35	26.27	26.39	26.36	34.58	34.59	34.55	34.59	34.61	34.57	35.05	35.03	8.27	0.661	0.670
5500	26.37	26.28	26.37	26.35	34.51	34.52	34.47	34.50	34.54	34.47	34.97	34.94	8.21	0.666	0.676
5750	26.33	26.26	26.33	26.34	34.49	34.50	34.44	34.48	34.47	34.41	34.89	34.88	8.19	0.667	0.677
5890	26.30	26.22	26.31	26.29	34.47	34.46	34.42	34.45	34.44	34.39	34.86	34.84	8.21	0.666	0.675

Table A.6: 3 vol% SiC-Water Nanofluid

Power Input												Sample Under Testing	Date
Main Heater			Cap Heater			Side Heater (Horizontal)			Side Heater (Vertical)				
U (V)	I (A)	Q_{main} (W)	U (V)	I (A)	Q_{cap} (W)	U (V)	I (A)	Q_{side1} (W)	U (V)	I (A)	Q_{side2} (W)		
43.00	0.424	18.23	8.00	0.27	2.16	20.00	0.660	13.20	7.00	0.23	1.61	3 vol% SiC-H_2O NF fresh	13-May-04

Time (S)	Cold Plate Temperature (oC)				Hot Plate Temperature (oC)				Side Temperature (oC)		Cap Temperature (oC)		dT (°C)	Thermal Conductivity (W/m-k)	
	T_{outer1}	T_{inner1}	T_{outer2}	T_{inner2}	T_{lower1}	T_{lower2}	T_{upper1}	T_{upper2}	T_{side1}	T_{side2}	T_{cap1}	T_{cap2}		K	K_{eff}
	103(°C)	104(°C)	105(°C)	106(°C)	107(°C)	108(°C)	109(°C)	110(°C)	113(°C)	114(°C)	115(°C)	116(°C)			
0	23.62	23.54	23.51	23.46	23.33	23.29	23.27	23.25	23.76	23.89	24.37	24.36	-0.19	-30.088	-30.821
250	25.11	25.09	25.04	25.05	31.50	31.57	31.38	31.35	28.40	29.03	27.15	27.20	6.46	0.887	0.902
500	25.89	25.88	25.85	25.87	33.67	33.75	33.60	33.60	30.81	31.26	29.90	29.96	7.84	0.732	0.743
750	26.17	26.14	26.14	26.14	34.61	34.66	34.53	34.55	32.28	32.65	31.75	31.80	8.50	0.674	0.684
1000	26.20	26.19	26.23	26.23	34.99	35.04	34.93	34.95	33.19	33.40	32.95	32.96	8.80	0.651	0.660
1250	26.35	26.27	26.31	26.31	34.42	34.46	34.37	34.39	33.71	34.00	33.70	33.70	8.15	0.704	0.714
1500	26.69	26.61	26.63	26.62	34.74	34.80	34.68	34.70	34.12	34.45	34.22	34.22	8.16	0.703	0.713
1750	26.93	26.88	26.94	26.89	35.05	35.08	34.99	35.00	34.47	34.76	34.61	34.61	8.18	0.701	0.711
2000	27.20	27.14	27.18	27.15	35.30	35.34	35.24	35.27	34.81	35.12	34.95	34.95	8.17	0.701	0.712
2250	27.33	27.26	27.31	27.31	35.55	35.60	35.51	35.51	35.03	35.24	35.25	35.24	8.29	0.691	0.701
2500	27.18	27.14	27.17	27.16	35.58	35.61	35.52	35.55	35.25	35.38	35.40	35.39	8.45	0.678	0.688
2750	26.95	26.88	26.96	26.95	35.45	35.49	35.41	35.42	35.35	35.43	35.51	35.52	8.56	0.670	0.679
3000	26.83	26.73	26.81	26.77	35.28	35.33	35.23	35.25	35.24	35.35	35.49	35.50	8.55	0.670	0.680
3250	26.87	26.79	26.86	26.82	35.23	35.27	35.16	35.18	35.19	35.37	35.49	35.47	8.44	0.679	0.689
3500	27.03	26.94	27.03	26.96	35.31	35.34	35.25	35.26	35.25	35.44	35.53	35.53	8.38	0.684	0.694
3750	27.23	27.12	27.19	27.16	35.47	35.49	35.39	35.44	35.39	35.64	35.64	35.64	8.34	0.687	0.697
4000	27.46	27.39	27.43	27.43	35.70	35.71	35.63	35.64	35.62	35.78	35.80	35.81	8.30	0.691	0.701
4250	27.36	27.31	27.37	27.33	35.77	35.79	35.73	35.75	35.65	35.79	35.87	35.88	8.46	0.678	0.688
4500	27.12	27.07	27.10	27.08	35.62	35.68	35.59	35.60	35.59	35.66	35.85	35.85	8.57	0.669	0.678
4750	26.98	26.89	26.97	26.94	35.44	35.48	35.40	35.40	35.49	35.62	35.80	35.78	8.54	0.671	0.681
5000	27.06	26.98	27.05	27.01	35.40	35.42	35.34	35.34	35.43	35.57	35.71	35.71	8.42	0.681	0.691
5250	27.18	27.11	27.18	27.15	35.46	35.50	35.43	35.42	35.45	35.64	35.72	35.71	8.35	0.686	0.696
5430	27.38	27.32	27.39	27.34	35.63	35.67	35.58	35.60	35.61	35.82	35.85	35.86	8.32	0.689	0.699

Table A.7: 4 vol% SiC-Water Nanofluid

Power Input												Liquid Under Test	Date
Main Heater			Cap Heater			Side Heater (Horizontal)			Side Heater (Vertical)				
U (V)	I (A)	Q_{main} (W)	U (V)	I (A)	Q_{cap} (W)	U (V)	I (A)	Q_{side1} (W)	U (V)	I (A)	Q_{side2} (W)		
44.00	0.434	19.10	8.00	0.27	2.16	20.00	0.660	13.20	7.00	0.23	1.61	4vol% SiC-H2O NF fresh	14-May-04

Time (S)	Cold Plate Temperature (oC)				Hot Plate Temperature (oC)				Side Temperature (oC)		Cap Temperature (oC)		dT (°C)	Thermal Conductivity (W/m-k)	
	T_{outer1}	T_{inner1}	T_{outer2}	T_{inner2}	T_{lower1}	T_{lower2}	T_{upper1}	T_{upper2}	T_{side1}	T_{side2}	T_{cap1}	T_{cap2}			
	103(°C)	104(°C)	105(°C)	106(°C)	107(°C)	108(°C)	109(°C)	110(°C)	113(°C)	114(°C)	115(°C)	116(°C)		K	Ke
0	23.29	23.21	23.17	23.13	22.97	22.93	22.91	22.91	23.16	23.20	23.30	23.28	-0.22	-26.982	-27.640
240	24.65	24.59	24.56	24.56	29.73	29.77	29.54	29.55	27.60	28.14	26.13	26.17	5.17	1.161	1.182
500	25.69	25.68	25.69	25.70	32.62	32.63	32.49	32.53	30.54	30.90	29.40	29.47	6.94	0.866	0.880
750	26.11	26.08	26.10	26.13	33.82	33.81	33.69	33.73	32.26	32.47	31.55	31.60	7.71	0.779	0.791
1000	26.30	26.26	26.28	26.30	34.39	34.38	34.26	34.32	33.29	33.47	32.94	32.94	8.11	0.741	0.752
1250	26.33	26.29	26.38	26.36	34.62	34.61	34.52	34.54	33.86	34.04	33.75	33.75	8.29	0.724	0.735
1750	26.76	26.72	26.81	26.77	35.07	35.04	34.95	35.00	34.64	34.79	34.75	34.74	8.31	0.722	0.733
2000	27.10	27.03	27.07	27.04	35.36	35.33	35.24	35.27	34.99	35.22	35.07	35.09	8.31	0.722	0.733
2250	27.29	27.24	27.31	27.31	35.61	35.61	35.52	35.56	35.32	35.60	35.42	35.42	8.34	0.720	0.731
2500	27.60	27.55	27.60	27.60	35.92	35.90	35.80	35.84	35.60	35.66	35.70	35.70	8.34	0.720	0.731
2750	27.54	27.51	27.58	27.57	36.07	36.05	35.96	36.00	35.78	35.81	35.91	35.91	8.52	0.705	0.715
3000	27.37	27.33	27.38	27.40	36.01	36.00	35.91	35.95	35.75	35.80	35.93	35.94	8.64	0.695	0.706
3250	27.15	27.11	27.18	27.17	35.83	35.83	35.72	35.77	35.74	35.89	35.96	35.95	8.69	0.691	0.701
3500	27.21	27.13	27.23	27.20	35.76	35.73	35.66	35.69	35.77	35.87	35.96	35.96	8.58	0.700	0.710
3750	27.36	27.30	27.36	27.36	35.85	35.83	35.76	35.79	35.87	36.05	36.04	36.04	8.51	0.706	0.716
4000	27.59	27.51	27.59	27.54	36.03	36.00	35.91	35.94	35.95	36.09	36.16	36.15	8.49	0.707	0.718
4250	27.71	27.64	27.72	27.69	36.16	36.15	36.06	36.12	36.08	36.24	36.31	36.30	8.49	0.707	0.718
4500	27.79	27.74	27.79	27.79	36.31	36.28	36.20	36.25	36.16	36.30	36.36	36.36	8.53	0.704	0.714
4750	27.48	27.46	27.53	27.51	36.22	36.20	36.11	36.16	36.15	36.22	36.38	36.35	8.73	0.688	0.698

Table A.8: 1 vol% Al_2O_3-Water Nanofluid

Power Input												Liquid Under Test	Date
Main Heater			Cap Heater			Side Heater (Horizontal)			Side Heater (Vertical)				
U (V)	I (A)	Q_{main} (W)	U (V)	I (A)	Q_{cap} (W)	U (V)	I (A)	Q_{side1} (W)	U (V)	I (A)	Q_{side2} (W)		
42.00	0.414	17.39	20.00	0.663	13.26	8.00	0.270	2.16	7.00	0.23	1.61	1vol% Al_2O_3-H2O NF fresh	18-May-04

Time (S)	Cold Plate Temperature (oC)				Hot Plate Temperature (oC)				Side Temperature (oC)		Cap Temperature (oC)		dT (°C)	Thermal Conductivity (W/m-k)	
	T_{outer1}	T_{inner1}	T_{outer2}	T_{inner2}	T_{lower1}	T_{lower2}	T_{upper1}	T_{upper2}	T_{side1}	T_{side2}	T_{cap1}	T_{cap2}			
	103(°C)	104(°C)	105(°C)	106(°C)	107(°C)	108(°C)	109(°C)	110(°C)	113(°C)	114(°C)	115(°C)	116(°C)		K	Ke
0	23.32	23.26	23.22	23.20	23.15	23.10	23.08	23.11	23.14	23.12	23.18	23.20	-0.11	-51.328	-52.574
250	24.18	24.14	24.10	24.11	29.68	29.69	29.45	29.45	27.73	28.14	26.13	26.20	5.55	0.984	1.001
500	24.84	24.76	24.78	24.76	31.92	31.93	31.78	31.80	30.07	30.34	28.95	29.01	7.17	0.763	0.775
750	25.46	25.37	25.41	25.38	33.03	33.02	32.90	32.93	31.71	32.00	30.99	31.02	7.65	0.714	0.725
1000	26.05	25.94	26.00	25.95	33.85	33.87	33.77	33.80	32.96	33.12	32.51	32.52	7.91	0.691	0.701
1250	26.63	26.50	26.55	26.51	34.50	34.52	34.43	34.45	33.81	33.87	33.57	33.57	8.00	0.683	0.693
1500	26.98	26.89	26.93	26.92	35.07	35.08	34.99	35.03	34.57	34.50	34.44	34.45	8.18	0.669	0.678
1750	27.10	27.00	27.02	27.01	35.42	35.42	35.33	35.39	35.00	35.02	34.97	34.99	8.42	0.649	0.659
2000	26.83	26.75	26.80	26.80	35.41	35.43	35.37	35.40	35.18	35.19	35.27	35.30	8.65	0.632	0.641
2250	26.72	26.59	26.68	26.65	35.31	35.32	35.26	35.28	35.17	35.14	35.36	35.37	8.69	0.629	0.637
2500	26.84	26.71	26.79	26.76	35.30	35.31	35.24	35.27	35.33	35.38	35.51	35.50	8.57	0.638	0.647
2750	27.04	26.91	27.00	26.95	35.45	35.44	35.37	35.41	35.43	35.54	35.64	35.66	8.52	0.642	0.651
3000	27.27	27.17	27.22	27.21	35.64	35.65	35.58	35.60	35.57	35.55	35.76	35.76	8.46	0.646	0.655
3250	27.12	27.02	27.09	27.09	35.74	35.72	35.67	35.72	35.66	35.53	35.87	35.87	8.67	0.630	0.639
3500	26.92	26.84	26.86	26.87	35.59	35.60	35.55	35.57	35.56	35.50	35.80	35.81	8.74	0.625	0.634
3750	26.73	26.62	26.67	26.67	35.42	35.40	35.37	35.40	35.41	35.33	35.71	35.71	8.77	0.623	0.632
4000	26.64	26.50	26.59	26.55	35.22	35.23	35.16	35.19	35.25	35.12	35.57	35.58	8.70	0.628	0.637
4250	26.80	26.66	26.78	26.73	35.25	35.26	35.20	35.23	35.36	35.48	35.62	35.60	8.56	0.638	0.647
4500	26.99	26.88	26.97	26.92	35.41	35.41	35.34	35.37	35.47	35.50	35.72	35.70	8.51	0.642	0.651
4750	27.20	27.09	27.15	27.14	35.56	35.58	35.52	35.53	35.56	35.74	35.75	35.76	8.46	0.646	0.655
5000	27.32	27.24	27.30	27.29	35.79	35.81	35.74	35.78	35.72	35.66	35.90	35.91	8.54	0.640	0.649
5110	27.23	27.16	27.20	27.22	35.80	35.81	35.73	35.80	35.70	35.56	35.87	35.89	8.61	0.635	0.643

Table A.9: 2 vol% Al_2O_3-Water Nanofluid

Power Input												Liquid Under Test	Date
Main Heater			Cap Heater			Side Heater (Horizontal)			Side Heater (Vertical)				
U (V)	I (A)	Q_{main} (W)	U (V)	I (A)	Q_{cap} (W)	U (V)	I (A)	Q_{side1} (W)	U (V)	I (A)	Q_{side2} (W)		
42.00	0.414	17.39	19.50	0.64	12.56	8.00	0.270	2.16	7.00	0.23	1.61	2vol% Al_2O_3-H2O NF fresh	19-May-04

Time (S)	Cold Plate Temperature (oC)				Hot Plate Temperature (oC)				Side Temperature (oC)		Cap Temperature (oC)		dT (°C)	Thermal Conductivity (W/m-k)	
	T_{outer1}	T_{inner1}	T_{outer2}	T_{inner2}	T_{lower1}	T_{lower2}	T_{upper1}	T_{upper2}	T_{side1}	T_{side2}	T_{cap1}	T_{cap2}			
	103(°C)	104(°C)	105(°C)	106(°C)	107(°C)	108(°C)	109(°C)	110(°C)	113(°C)	114(°C)	115(°C)	116(°C)		K	Ke
0	22.52	22.51	22.48	22.49	22.39	22.39	22.37	22.36	22.44	22.48	22.47	22.49	-0.11	-49.026	-50.217
250	23.73	23.75	23.71	23.75	29.04	29.10	28.88	28.89	26.85	27.47	25.33	25.43	5.32	1.028	1.046
500	24.44	24.45	24.48	24.52	31.55	31.59	31.47	31.49	29.44	29.92	28.31	28.36	7.09	0.771	0.784
750	25.09	25.07	25.12	25.12	32.71	32.78	32.66	32.69	31.14	31.60	30.46	30.52	7.64	0.715	0.726
1000	25.72	25.69	25.76	25.75	33.51	33.56	33.44	33.50	32.41	32.86	32.03	32.04	7.82	0.699	0.709
1250	26.29	26.26	26.33	26.32	34.24	34.26	34.19	34.23	33.41	33.54	33.19	33.21	7.96	0.687	0.697
1500	26.54	26.50	26.56	26.55	34.71	34.72	34.66	34.69	34.05	34.09	34.01	34.03	8.19	0.667	0.677
1750	26.51	26.46	26.52	26.54	34.84	34.85	34.82	34.86	34.41	34.42	34.45	34.47	8.35	0.655	0.664
2000	26.54	26.49	26.58	26.56	34.89	34.91	34.86	34.89	34.56	34.62	34.77	34.76	8.37	0.653	0.662
2250	26.77	26.70	26.76	26.77	35.00	35.03	34.98	35.00	34.77	34.96	34.99	35.01	8.28	0.660	0.669
2500	26.96	26.93	27.03	27.01	35.20	35.21	35.16	35.19	34.99	35.16	35.21	35.21	8.24	0.664	0.673
2750	27.10	27.09	27.13	27.12	35.42	35.43	35.37	35.41	35.17	35.18	35.41	35.41	8.32	0.657	0.666
3000	26.94	26.89	26.98	26.97	35.39	35.39	35.35	35.38	35.21	35.15	35.46	35.46	8.46	0.646	0.655
3250	26.94	26.90	26.97	26.95	35.32	35.32	35.27	35.31	35.24	35.20	35.55	35.52	8.40	0.651	0.660
3500	27.14	27.08	27.16	27.13	35.40	35.39	35.33	35.37	35.24	35.27	35.56	35.56	8.29	0.659	0.669
3750	27.41	27.32	27.39	27.38	35.56	35.57	35.51	35.54	35.38	35.41	35.63	35.64	8.22	0.665	0.675
4000	27.36	27.29	27.38	27.38	35.66	35.68	35.62	35.66	35.46	35.46	35.69	35.69	8.34	0.656	0.665
4250	27.20	27.15	27.25	27.23	35.63	35.64	35.61	35.64	35.44	35.42	35.71	35.69	8.45	0.647	0.656
4500	27.08	27.00	27.09	27.04	35.49	35.49	35.43	35.47	35.36	35.43	35.65	35.66	8.46	0.646	0.655
4750	27.03	26.96	27.07	27.04	35.38	35.39	35.34	35.38	35.31	35.55	35.63	35.62	8.38	0.652	0.661
5000	27.22	27.14	27.21	27.21	35.47	35.48	35.42	35.46	35.34	35.26	35.66	35.63	8.30	0.659	0.668
5140	27.26	27.22	27.28	27.28	35.54	35.54	35.48	35.51	35.39	35.46	35.67	35.66	8.29	0.659	0.668

Table A.10: 3 vol% Al_2O_3-Water Nanofluid

Power Input												Liquid Under Test	Date
Main Heater			Cap Heater			Side Heater (Horizontal)			Side Heater (Vertical)				
U (V)	I (A)	Q_{main} (W)	U (V)	I (A)	Q_{cap} (W)	U (V)	I (A)	Q_{side1} (W)	U (V)	I (A)	Q_{side2} (W)		
42.00	0.414	17.39	20.00	0.663	13.26	8.00	0.270	2.16	7.00	0.23	1.61	3vol% Al_2O_3-H2O NF fresh	19-May-04

Time (S)	Cold Plate Temperature (oC)				Hot Plate Temperature (oC)				Side Temperature (oC)		Cap Temperature (oC)		dT (°C)	Thermal Conductivity (W/m-k)	
	T_{outer1}	T_{inner1}	T_{outer2}	T_{inner2}	T_{lower1}	T_{lower2}	T_{upper1}	T_{upper2}	T_{side1}	T_{side2}	T_{cap1}	T_{cap2}			
	103(°C)	104(°C)	105(°C)	106(°C)	107(°C)	108(°C)	109(°C)	110(°C)	113(°C)	114(°C)	115(°C)	116(°C)		K	Ke
0	22.46	22.44	22.45	22.43	22.52	22.50	22.48	22.51	22.58	22.62	22.67	22.66	0.07	74.883	76.685
250	23.61	23.56	23.57	23.58	28.80	28.85	28.65	28.64	26.82	27.37	25.48	25.55	5.26	1.040	1.059
500	24.69	24.66	24.69	24.72	31.43	31.46	31.34	31.35	29.54	29.91	28.57	28.65	6.76	0.809	0.822
750	25.32	25.28	25.33	25.35	32.72	32.78	32.67	32.69	31.36	31.57	30.78	30.83	7.43	0.735	0.747
1000	25.57	25.52	25.60	25.60	33.38	33.44	33.33	33.38	32.52	32.71	32.24	32.26	7.85	0.696	0.707
1250	26.00	25.95	25.99	26.00	33.88	33.91	33.82	33.86	33.31	33.45	33.26	33.26	7.91	0.691	0.701
1500	26.48	26.40	26.47	26.46	34.34	34.38	34.29	34.33	34.00	34.11	34.00	34.00	7.93	0.689	0.700
1750	26.91	26.82	26.89	26.88	34.79	34.82	34.75	34.78	34.50	34.53	34.57	34.59	7.96	0.687	0.697
2000	27.08	27.03	27.09	27.11	35.15	35.16	35.08	35.12	34.87	34.96	35.03	35.03	8.09	0.676	0.686
2250	27.00	26.95	27.02	27.02	35.23	35.24	35.16	35.22	34.91	34.97	35.10	35.11	8.25	0.663	0.672
2500	26.83	26.77	26.86	26.85	35.15	35.16	35.11	35.15	35.00	35.11	35.17	35.16	8.34	0.656	0.665
2750	26.94	26.88	26.97	26.94	35.09	35.12	35.06	35.10	35.10	35.18	35.31	35.30	8.20	0.667	0.677
3000	27.16	27.11	27.15	27.14	35.25	35.27	35.21	35.23	35.26	35.18	35.47	35.45	8.13	0.672	0.682
3250	27.42	27.34	27.40	27.40	35.45	35.48	35.40	35.42	35.43	35.44	35.64	35.63	8.09	0.675	0.685
3500	27.49	27.42	27.51	27.51	35.64	35.65	35.55	35.60	35.61	35.57	35.82	35.81	8.18	0.668	0.678
3750	27.42	27.35	27.43	27.42	35.65	35.68	35.61	35.64	35.62	35.62	35.86	35.86	8.28	0.660	0.670
4000	27.24	27.17	27.25	27.23	35.54	35.55	35.51	35.52	35.46	35.50	35.75	35.74	8.34	0.655	0.664
4250	27.07	26.99	27.07	27.06	35.35	35.39	35.32	35.35	35.45	35.44	35.71	35.70	8.34	0.655	0.665
4500	27.16	27.09	27.18	27.16	35.32	35.34	35.27	35.31	35.42	35.40	35.69	35.66	8.21	0.666	0.676
4750	27.33	27.24	27.32	27.33	35.42	35.44	35.36	35.41	35.45	35.48	35.71	35.70	8.15	0.671	0.680
5000	27.46	27.39	27.46	27.45	35.56	35.57	35.48	35.52	35.55	35.52	35.78	35.76	8.14	0.671	0.681
5250	27.33	27.28	27.37	27.37	35.55	35.59	35.52	35.56	35.56	35.48	35.78	35.76	8.24	0.663	0.673
5460	27.17	27.12	27.16	27.22	35.48	35.51	35.45	35.46	35.43	35.51	35.71	35.71	8.33	0.656	0.666

Table A.11: 4 vol% Al_2O_3-Water Nanofluid

Power Input												Liquid Under Test	Date
Main Heater			Cap Heater			Side Heater (Horizontal)			Side Heater (Vertical)				
U (V)	I (A)	Q_{main} (W)	U (V)	I (A)	Q_{cap} (W)	U (V)	I (A)	Q_{side1} (W)	U (V)	I (A)	Q_{side2} (W)		
42.20	0.416	17.56	19.50	0.644	12.56	8.00	0.270	2.16	7.00	0.23	1.61	4vol% Al_2O_3-H2O NF fresh	19-May-04

Time (S)	Cold Plate Temperature (oC)				Hot Plate Temperature (oC)				Side Temperature (oC)		Cap Temperature (oC)		dT (°C)	Thermal Conductivity (W/m-k)	
	T_{outer1}	T_{inner1}	T_{outer2}	T_{inner2}	T_{lower1}	T_{lower2}	T_{upper1}	T_{upper2}	T_{side1}	T_{side2}	T_{cap1}	T_{cap2}			
	103(°C)	104(°C)	105(°C)	106(°C)	107(°C)	108(°C)	109(°C)	110(°C)	113(°C)	114(°C)	115(°C)	116(°C)		K	Ke
0	23.42	23.35	23.36	23.30	23.19	23.12	23.12	23.14	23.36	23.40	23.49	23.50	-0.17	-32.181	-32.964
250	24.72	24.70	24.68	24.69	29.86	29.82	29.60	29.59	28.00	28.53	26.51	26.51	5.15	1.073	1.092
500	25.55	25.50	25.54	25.53	32.24	32.23	32.09	32.11	30.51	30.79	29.40	29.41	6.72	0.821	0.834
750	25.84	25.76	25.82	25.83	33.23	33.23	33.10	33.15	32.01	32.21	31.32	31.36	7.43	0.743	0.754
1000	25.99	25.90	25.99	25.96	33.70	33.67	33.59	33.63	32.89	32.99	32.53	32.56	7.75	0.712	0.723
1250	26.30	26.22	26.30	26.28	34.08	34.05	33.98	34.00	33.60	33.77	33.47	33.49	7.81	0.707	0.718
1500	26.71	26.62	26.71	26.67	34.49	34.48	34.39	34.42	34.17	34.25	34.16	34.17	7.84	0.704	0.715
1750	27.05	26.97	27.04	27.02	34.87	34.89	34.80	34.83	34.63	34.73	34.69	34.69	7.88	0.700	0.710
1760	27.05	26.97	27.05	27.05	34.89	34.88	34.81	34.83	34.64	34.75	34.70	34.71	7.87	0.701	0.711
2000	27.27	27.20	27.27	27.28	35.19	35.19	35.11	35.14	34.98	35.07	35.06	35.07	7.95	0.694	0.704
2250	27.21	27.16	27.27	27.25	35.36	35.35	35.29	35.32	35.18	34.73	35.29	35.31	8.15	0.677	0.687
2500	27.02	26.95	27.04	27.02	35.25	35.25	35.18	35.23	35.16	35.03	35.32	35.34	8.27	0.668	0.677
2750	26.90	26.81	26.92	26.88	35.11	35.10	35.05	35.08	35.09	35.03	35.34	35.33	8.25	0.669	0.678
3000	27.02	26.94	27.05	27.00	35.13	35.13	35.07	35.07	35.17	35.02	35.42	35.41	8.16	0.677	0.687
3250	27.20	27.10	27.22	27.18	35.24	35.26	35.16	35.19	35.22	35.20	35.48	35.48	8.11	0.681	0.691
3500	27.39	27.30	27.39	27.35	35.40	35.38	35.31	35.34	35.34	35.36	35.59	35.59	8.07	0.684	0.694
3750	27.62	27.53	27.64	27.64	35.64	35.62	35.55	35.57	35.60	35.46	35.77	35.76	8.05	0.686	0.696
4000	27.56	27.50	27.57	27.59	35.74	35.75	35.66	35.70	35.68	35.57	35.92	35.90	8.20	0.673	0.683
4250	27.31	27.24	27.32	27.31	35.59	35.60	35.53	35.58	35.57	35.55	35.83	35.83	8.32	0.663	0.673
4500	27.04	26.98	27.06	27.07	35.39	35.37	35.34	35.37	35.42	35.35	35.71	35.71	8.36	0.660	0.670
4750	26.91	26.84	26.93	26.89	35.20	35.17	35.12	35.15	35.23	35.15	35.52	35.52	8.33	0.663	0.672
4830	26.86	26.79	26.88	26.84	35.15	35.13	35.08	35.10	35.20	35.11	35.48	35.48	8.32	0.663	0.673

Table A.12: 1 vol% CuO-Water Nanofluid

Power Input												Liquid Under Test	Date
Main Heater			Cap Heater			Side Heater (Horizontal)			Side Heater (Vertical)				
U (V)	I (A)	Q_{main} (W)	U (V)	I (A)	Q_{cap} (W)	U (V)	I (A)	Q_{side1} (W)	U (V)	I (A)	Q_{side2} (W)		
43.00	0.424	18.23	9.50	0.32	3.04	21.00	0.70	14.64	7.00	0.20	1.40	1vol% CuO-H2O NF fresh	19-July-04

Time (S)	Cold Plate Temperature (oC)				Hot Plate Temperature (oC)				Side Temperature (oC)		Cap Temperature (oC)		dT (°C)	Thermal Conductivity (W/m-k)	
	T_{outer1}	T_{inner1}	T_{outer2}	T_{inner2}	T_{lower1}	T_{lower2}	T_{upper1}	T_{upper2}	T_{side1}	T_{side2}	T_{cap1}	T_{cap2}			
	103(°C)	104(°C)	105(°C)	106(°C)	107(°C)	108(°C)	109(°C)	110(°C)	113(°C)	114(°C)	115(°C)	116(°C)		K	Ke
0	22.74	22.72	22.73	22.75	23.80	23.75	24.36	24.35	23.04	22.97	23.74	23.67	1.03	5.715	5.847
250	24.28	24.28	24.24	24.29	30.24	30.31	29.06	29.08	28.23	28.75	26.82	26.89	5.98	0.987	1.004
500	25.36	25.34	25.26	25.35	32.59	32.65	32.06	32.09	30.97	31.42	30.06	30.06	7.27	0.812	0.825
750	26.05	26.04	25.93	26.04	33.90	33.98	33.71	33.73	32.83	33.17	32.34	32.34	7.90	0.748	0.759
1000	26.51	26.49	26.39	26.48	34.74	34.80	34.70	34.71	34.10	34.40	33.92	33.90	8.28	0.713	0.724
1250	26.82	26.82	26.69	26.79	35.27	35.35	35.33	35.38	34.96	35.24	35.04	34.98	8.50	0.694	0.705
1500	27.07	27.06	26.93	27.04	35.68	35.75	35.79	35.83	35.58	35.78	35.76	35.72	8.67	0.681	0.691
1750	27.25	27.24	27.11	27.21	35.94	36.02	36.11	36.12	35.98	36.21	36.27	36.20	8.76	0.674	0.684
2000	27.36	27.33	27.20	27.31	36.14	36.18	36.33	36.33	36.25	36.41	36.60	36.56	8.83	0.668	0.678
2250	27.41	27.40	27.30	27.39	36.26	36.33	36.50	36.50	36.51	36.66	36.91	36.85	8.90	0.663	0.673
2500	27.49	27.48	27.36	27.48	36.39	36.45	36.61	36.64	36.76	36.81	37.10	37.05	8.94	0.660	0.670
2750	27.56	27.55	27.41	27.52	36.47	36.52	36.70	36.70	36.77	36.91	37.22	37.15	8.96	0.659	0.668
3000	27.59	27.58	27.43	27.57	36.53	36.59	36.74	36.78	36.87	36.97	37.31	37.24	8.98	0.657	0.666
3250	27.61	27.60	27.46	27.60	36.58	36.63	36.79	36.82	36.87	37.16	37.38	37.31	9.00	0.656	0.665
3500	27.63	27.61	27.49	27.59	36.60	36.66	36.84	36.87	36.94	37.10	37.41	37.33	9.03	0.654	0.663
3570	27.66	27.65	27.52	27.61	36.63	36.68	36.86	36.89	36.92	37.15	37.42	37.36	9.03	0.654	0.663

Table A.13: 2 vol% CuO-Water Nanofluid

Power Input												Liquid Under Test	Date
Main Heater			Cap Heater			Side Heater (Horizontal)			Side Heater (Vertical)				
U (V)	I (A)	Q_{main} (W)	U (V)	I (A)	Q_{cap} (W)	U (V)	I (A)	Q_{side1} (W)	U (V)	I (A)	Q_{side2} (W)		
44.00	0.434	19.10	9.50	0.32	21.00	21.00	0.70	14.64	7.00	0.20	1.40	2vol% CuO-H2O NF fresh	19-July-04

Time (S)	Cold Plate Temperature (oC)				Hot Plate Temperature (oC)				Side Temperature (oC)		Cap Temperature (oC)		dT (°C)	Thermal Conductivity (W/m-k)	
	T_{outer1}	T_{inner1}	T_{outer2}	T_{inner2}	T_{lower1}	T_{lower2}	T_{upper1}	T_{upper2}	T_{side1}	T_{side2}	T_{cap1}	T_{cap2}			
	103(°C)	104(°C)	105(°C)	106(°C)	107(°C)	108(°C)	109(°C)	110(°C)	113(°C)	114(°C)	115(°C)	116(°C)		K	Ke
0	21.69	21.68	21.71	21.74	21.87	21.83	21.93	21.91	22.32	22.30	22.60	22.52	0.14	44.011	45.067
250	23.13	23.19	23.09	23.19	28.97	29.10	27.70	27.74	27.05	27.44	25.52	25.53	5.84	1.058	1.077
500	24.23	24.28	24.18	24.31	31.71	31.81	31.19	31.23	29.83	30.23	28.74	28.75	7.46	0.828	0.842
750	24.97	25.00	24.92	25.05	33.16	33.26	32.99	33.02	31.73	32.02	31.06	31.05	8.19	0.755	0.767
1000	25.48	25.50	25.41	25.55	34.09	34.16	34.04	34.08	33.02	33.27	32.70	32.66	8.60	0.719	0.730
1250	25.82	25.86	25.74	25.90	34.66	34.74	34.71	34.75	33.93	34.15	33.85	33.80	8.82	0.701	0.711
1500	26.09	26.10	26.01	26.17	35.06	35.12	35.15	35.20	34.58	34.77	34.61	34.59	8.96	0.691	0.701
1750	26.33	26.28	26.17	26.37	35.42	35.41	35.48	35.52	35.05	35.24	35.22	35.18	9.09	0.680	0.690
2000	26.44	26.46	26.32	26.50	35.56	35.64	35.72	35.75	35.34	35.57	35.61	35.56	9.12	0.678	0.688
2250	26.49	26.51	26.39	26.56	35.70	35.74	35.88	35.90	35.57	35.69	35.87	35.82	9.18	0.673	0.683
2500	26.61	26.66	26.51	26.68	35.83	35.87	35.98	36.04	35.67	35.89	36.05	35.98	9.18	0.674	0.684
2750	26.66	26.70	26.58	26.74	35.89	35.94	36.10	36.12	35.90	36.04	36.24	36.19	9.19	0.673	0.683
3000	26.75	26.77	26.64	26.82	35.97	36.03	36.16	36.20	36.04	36.13	36.37	36.30	9.20	0.672	0.681
3250	26.71	26.74	26.62	26.80	36.00	36.04	36.20	36.24	36.02	36.17	36.44	36.36	9.25	0.669	0.678
3500	26.72	26.76	26.60	26.80	36.01	36.04	36.21	36.22	36.10	36.21	36.46	36.39	9.25	0.669	0.678
4000	26.88	26.92	26.77	26.94	36.12	36.17	36.31	36.34	36.12	36.33	36.54	36.47	9.22	0.671	0.681
4250	26.81	26.83	26.70	26.89	36.12	36.15	36.32	36.35	36.17	36.32	36.59	36.52	9.28	0.666	0.676
4500	26.75	26.80	26.68	26.87	36.03	36.12	36.31	36.30	36.17	36.29	36.56	36.51	9.24	0.669	0.679
4750	26.73	26.76	26.62	26.80	36.03	36.10	36.27	36.29	36.11	36.24	36.55	36.48	9.28	0.666	0.676
5000	26.67	26.71	26.56	26.75	35.99	36.06	36.23	36.25	36.06	36.06	36.51	36.44	9.30	0.665	0.675
5250	26.63	26.67	26.50	26.69	35.94	35.98	36.17	36.21	36.04	36.04	36.50	36.42	9.28	0.666	0.676
5500	26.59	26.62	26.48	26.66	35.91	35.96	36.13	36.16	35.96	35.96	36.43	36.36	9.30	0.665	0.675
5750	26.57	26.60	26.47	26.64	35.89	35.94	36.09	36.12	35.95	35.95	36.40	36.32	9.29	0.665	0.675
5940	26.56	26.57	26.45	26.61	35.87	35.91	36.07	36.09	35.97	35.97	36.39	36.33	9.30	0.665	0.675

Table A.14: 2.7 wt% CuO-Water Nanofluid

Power Input												Liquid Under Test	Date
Main Heater			Cap Heater			Side Heater (Horizontal)			Side Heater (Vertical)				
U (V)	I (A)	Q_{main} (W)	U (V)	I (A)	Q_{cap} (W)	U (V)	I (A)	Q_{side1} (W)	U (V)	I (A)	Q_{side2} (W)		
44.00	0.434	19.10	9.00	0.31	2.79	22.00	0.73	16.08	7.00	0.20	1.40	2.7wt% CuO-H_2O NF fresh	18-June-04

Time (S)	Cold Plate Temperature (oC)				Hot Plate Temperature (oC)				Side Temperature (oC)		Cap Temperature (oC)		dT (°C)	Thermal Conductivity (W/m-k)	
	T_{outer1}	T_{inner1}	T_{outer2}	T_{inner2}	T_{lower1}	T_{lower2}	T_{upper1}	T_{upper2}	T_{side1}	T_{side2}	T_{cap1}	T_{cap2}			
	103(°C)	104(°C)	105(°C)	106(°C)	107(°C)	108(°C)	109(°C)	110(°C)	113(°C)	114(°C)	115(°C)	116(°C)		K	Ke
0	22.74	22.73	22.75	22.76	22.72	22.68	22.70	22.70	23.00	22.97	23.14	23.09	-0.04	-143.80	-147.28
250	24.33	24.31	24.30	24.39	30.01	30.07	29.29	29.31	27.54	28.12	26.16	26.14	5.69	1.087	1.107
500	25.47	25.45	25.47	25.59	32.69	32.72	32.37	32.41	30.13	30.69	29.09	29.09	7.18	0.861	0.875
750	26.34	26.31	26.33	26.43	34.15	34.19	33.98	34.02	31.86	32.38	31.27	31.25	7.80	0.793	0.805
1000	26.83	26.83	26.82	26.97	35.01	35.04	34.93	34.97	33.02	33.52	32.77	32.71	8.13	0.761	0.772
1250	26.94	26.95	26.95	27.11	35.52	35.57	35.51	35.57	33.76	34.16	33.78	33.70	8.51	0.727	0.738
1500	26.89	26.88	26.88	27.04	35.64	35.69	35.67	35.74	34.05	34.52	34.29	34.22	8.71	0.710	0.721
1750	26.67	26.69	26.71	26.85	35.58	35.65	35.65	35.70	34.18	34.67	34.55	34.45	8.85	0.699	0.709
2000	26.61	26.56	26.60	26.76	35.48	35.54	35.56	35.60	34.31	34.63	34.65	34.54	8.85	0.699	0.709
2250	26.86	26.85	26.90	27.03	35.62	35.66	35.63	35.70	34.65	35.02	34.99	34.89	8.70	0.711	0.721
2500	27.17	27.15	27.19	27.31	35.86	35.93	35.89	35.94	34.98	35.30	35.32	35.23	8.66	0.714	0.725
2750	27.50	27.45	27.48	27.60	36.15	36.21	36.19	36.22	35.26	35.57	35.61	35.50	8.65	0.715	0.725
3000	27.74	27.71	27.76	27.87	36.44	36.47	36.47	36.48	35.51	35.86	35.84	35.75	8.66	0.714	0.725
3250	27.84	27.82	27.83	28.00	36.65	36.67	36.68	36.72	35.75	36.08	36.13	36.05	8.76	0.706	0.717
3500	27.66	27.65	27.65	27.83	36.65	36.67	36.71	36.74	35.70	36.02	36.20	36.10	8.92	0.693	0.703
3750	27.42	27.40	27.42	27.57	36.45	36.52	36.53	36.57	35.57	35.92	36.13	36.02	9.00	0.687	0.697
4000	27.13	27.12	27.16	27.32	36.20	36.25	36.31	36.34	35.38	35.73	35.98	35.86	9.01	0.686	0.696
4250	27.05	27.00	27.03	27.20	36.06	36.11	36.16	36.20	35.34	35.75	35.87	35.78	8.98	0.688	0.698
4500	26.90	26.86	26.93	27.04	35.91	35.95	36.01	36.03	35.33	35.73	35.80	35.70	8.98	0.689	0.699
4750	27.08	27.04	27.09	27.20	35.91	35.96	35.98	36.00	35.43	35.73	35.87	35.78	8.82	0.701	0.712
5000	27.33	27.27	27.29	27.44	36.07	36.12	36.11	36.14	35.58	35.86	35.96	35.88	8.74	0.707	0.718
5250	27.57	27.51	27.56	27.71	36.32	36.34	36.34	36.36	35.74	36.08	36.13	36.01	8.72	0.709	0.720
5500	27.83	27.78	27.84	27.96	36.57	36.59	36.59	36.61	36.08	36.47	36.38	36.28	8.71	0.710	0.721
5750	27.98	27.96	28.02	28.14	36.80	36.83	36.82	36.86	36.32	36.73	36.65	36.57	8.77	0.705	0.716
6000	27.86	27.83	27.87	28.03	36.84	36.88	36.91	36.96	36.42	36.75	36.82	36.72	8.93	0.692	0.703
6250	27.62	27.58	27.60	27.77	36.69	36.73	36.78	36.82	36.29	36.64	36.80	36.68	9.04	0.684	0.694

Table A.15: 1 volt% SiC-EG Nanofluid

Power Input												Liquid Under Test	Date
Main Heater			Cap Heater			Side Heater (Horizontal)			Side Heater (Vertical)				
U (V)	I (A)	Q_{main} (W)	U (V)	I (A)	Q_{cap} (W)	U (V)	I (A)	Q_{side1} (W)	U (V)	I (A)	Q_{side2} (W)		
31	0.306	9.49	9.00	0.31	2.79	21.00	0.695	14.60	7.00	0.20	1.40	1 vol% SiC-EG NF fresh	24-July-04

Time (S)	Cold Plate Temperature (oC)				Hot Plate Temperature (oC)				Side Temperature (oC)		Cap Temperature (oC)		dT (°C)	Thermal Conductivity (W/m-k)	
	T_{outer1} 103(°C)	T_{inner1} 104(°C)	T_{outer2} 105(°C)	T_{inner2} 106(°C)	T_{lower1} 107(°C)	T_{lower2} 108(°C)	T_{upper1} 109(°C)	T_{upper2} 110(°C)	T_{side1} 113(°C)	T_{side2} 114(°C)	T_{cap1} 115(°C)	T_{cap2} 116(°C)		K	Ke
0	21.82	21.80	21.82	21.83	22.15	22.14	22.20	22.20	22.26	22.19	22.42	22.34	0.33	9.244	9.461
250	22.61	22.54	22.56	22.55	27.11	27.15	26.31	26.32	26.94	27.69	25.29	25.32	4.59	0.661	0.671
500	23.38	23.27	23.31	23.27	30.06	30.09	29.55	29.58	29.53	30.06	28.33	28.35	6.81	0.445	0.450
750	23.96	23.86	23.87	23.83	31.98	32.01	31.65	31.70	31.30	31.64	30.53	30.52	8.15	0.372	0.374
1000	24.29	24.21	24.23	24.22	33.21	33.25	33.01	33.06	32.55	32.93	32.09	32.10	9.02	0.336	0.338
1250	24.59	24.50	24.50	24.50	34.08	34.13	33.98	34.02	33.44	33.63	33.22	33.20	9.61	0.316	0.317
1500	24.82	24.73	24.75	24.71	34.67	34.71	34.61	34.66	34.08	34.24	33.95	33.94	9.97	0.304	0.305
1750	25.16	25.04	25.04	25.03	35.12	35.14	35.09	35.09	34.56	34.74	34.59	34.55	10.09	0.300	0.301
2000	25.49	25.43	25.41	25.44	35.58	35.62	35.54	35.59	35.07	35.28	35.17	35.10	10.17	0.298	0.299
2250	25.86	25.78	25.77	25.77	35.99	36.03	35.98	36.02	35.43	35.70	35.60	35.55	10.24	0.296	0.297
2500	26.14	26.07	26.06	26.06	36.35	36.37	36.33	36.37	35.83	36.07	35.98	35.94	10.30	0.294	0.295
2750	26.48	26.39	26.37	26.38	36.71	36.73	36.70	36.73	36.18	36.41	36.36	36.30	10.34	0.293	0.294
3000	26.76	26.67	26.62	26.63	37.03	37.05	37.02	37.06	36.50	36.63	36.71	36.64	10.39	0.292	0.292
3250	26.71	26.65	26.60	26.63	37.25	37.29	37.26	37.33	36.77	36.86	37.03	36.97	10.63	0.285	0.286
3500	26.53	26.46	26.44	26.47	37.33	37.36	37.38	37.42	36.88	37.01	37.21	37.16	10.88	0.279	0.279
3750	26.36	26.28	26.25	26.26	37.28	37.31	37.35	37.41	36.83	36.86	37.21	37.16	11.02	0.275	0.275
4000	26.20	26.09	26.09	26.09	37.18	37.21	37.26	37.31	36.77	36.70	37.18	37.12	11.10	0.273	0.273
4250	26.08	26.00	25.97	25.99	37.08	37.10	37.15	37.20	36.69	36.68	37.11	37.06	11.10	0.273	0.273
4500	25.99	25.88	25.87	25.88	36.98	37.00	37.05	37.10	36.56	36.56	37.03	36.97	11.11	0.273	0.273
4750	25.94	25.84	25.84	25.85	36.87	36.89	36.96	37.00	36.49	36.57	36.96	36.89	11.04	0.275	0.275
5000	25.89	25.77	25.75	25.72	36.81	36.84	36.89	36.94	36.44	36.61	36.88	36.82	11.08	0.274	0.274
5250	25.83	25.71	25.73	25.73	36.75	36.77	36.81	36.87	36.35	36.36	36.86	36.74	11.04	0.275	0.275
5500	25.80	25.70	25.69	25.71	36.70	36.71	36.78	36.82	36.34	36.27	36.77	36.68	11.00	0.276	0.276
5750	25.79	25.66	25.65	25.65	36.67	36.70	36.74	36.80	36.31	36.38	36.74	36.67	11.03	0.275	0.275
6000	25.80	25.69	25.66	25.66	36.63	36.64	36.70	36.74	36.22	36.34	36.67	36.61	10.96	0.277	0.277
6250	25.68	25.56	25.55	25.54	36.55	36.58	36.62	36.68	36.17	36.17	36.61	36.54	11.02	0.275	0.275
6500	25.65	25.56	25.54	25.54	36.55	36.56	36.61	36.65	36.15	36.33	36.59	36.53	11.01	0.275	0.276
6710	25.70	25.58	25.56	25.55	36.51	36.55	36.59	36.63	36.15	36.14	36.57	36.50	10.97	0.276	0.277

Table A.16: 2 vol% SiC-EG Nanofluid

Power Input												Liquid Under Test	Date
Main Heater			Cap Heater			Side Heater (Horizontal)			Side Heater (Vertical)				
U (V)	I (A)	Q_{main} (W)	U (V)	I (A)	Q_{cap} (W)	U (V)	I (A)	Q_{side1} (W)	U (V)	I (A)	Q_{side2} (W)		
31	0.306	9.49	8.50	0.29	2.47	20.80	0.695	14.46	7.00	0.20	1.40	2 vol% SiC-EG NF fresh	24-July-04

Time (S)	Cold Plate Temperature (oC)				Hot Plate Temperature (oC)				Side Temperature (oC)		Cap Temperature (oC)		dT (°C)	Thermal Conductivity (W/m-k)	
	T_{outer1}	T_{inner1}	T_{outer2}	T_{inner2}	T_{lower1}	T_{lower2}	T_{upper1}	T_{upper2}	T_{side1}	T_{side2}	T_{cap1}	T_{cap2}		K	Ke
	103(°C)	104(°C)	105(°C)	106(°C)	107(°C)	108(°C)	109(°C)	110(°C)	113(°C)	114(°C)	115(°C)	116(°C)			
0	21.43	21.40	21.40	21.36	21.38	21.37	21.37	21.36	21.44	21.45	21.44	21.42	-0.01	-383.960	-393.238
250	22.39	22.35	22.34	22.31	26.26	26.34	25.08	25.11	26.03	26.57	24.32	24.41	3.97	0.774	0.786
500	23.49	23.45	23.41	23.36	29.52	29.59	28.78	28.81	29.01	29.45	27.70	27.79	6.15	0.500	0.505
750	24.10	24.02	23.99	23.95	31.67	31.74	31.22	31.26	30.98	31.29	30.17	30.21	7.72	0.398	0.401
1000	24.53	24.47	24.42	24.38	33.11	33.17	32.87	32.92	32.42	32.68	31.93	31.96	8.71	0.352	0.354
1250	24.87	24.79	24.73	24.70	34.08	34.12	33.93	33.98	33.38	33.62	33.17	33.19	9.35	0.328	0.330
1500	25.05	24.98	24.93	24.90	34.66	34.69	34.60	34.65	34.07	34.22	34.02	34.01	9.74	0.315	0.317
1750	25.18	25.11	25.06	25.04	35.05	35.12	35.06	35.11	34.56	34.71	34.61	34.59	10.01	0.307	0.308
2000	25.27	25.20	25.16	25.13	35.34	35.38	35.37	35.42	34.80	34.99	34.99	34.98	10.20	0.301	0.302
2250	25.55	25.46	25.43	25.41	35.59	35.64	35.62	35.67	35.14	35.19	35.32	35.27	10.18	0.302	0.303
2500	25.85	25.77	25.74	25.72	35.86	35.89	35.87	35.93	35.45	35.60	35.63	35.61	10.13	0.303	0.304
2750	26.16	26.10	26.03	26.03	36.13	36.19	36.17	36.22	35.79	35.90	35.95	35.93	10.10	0.304	0.305
3000	26.41	26.35	26.29	26.28	36.43	36.47	36.42	36.49	36.04	36.20	36.25	36.23	10.13	0.303	0.304
3250	26.71	26.65	26.59	26.59	36.73	36.77	36.76	36.80	36.46	36.63	36.62	36.60	10.13	0.303	0.304
3500	26.78	26.72	26.64	26.66	36.98	36.99	37.00	37.05	36.62	36.74	36.82	36.78	10.30	0.298	0.299
3750	26.52	26.47	26.40	26.41	36.99	37.03	37.06	37.14	36.53	36.87	36.89	36.84	10.57	0.291	0.291
4000	26.30	26.26	26.18	26.19	36.91	36.95	37.04	37.08	36.55	36.62	36.87	36.81	10.71	0.287	0.287
4250	26.27	26.20	26.12	26.12	36.81	36.85	36.92	36.97	36.51	36.52	36.80	36.74	10.67	0.288	0.288
4500	26.08	26.01	25.95	25.96	36.70	36.74	36.83	36.87	36.41	36.46	36.71	36.65	10.73	0.286	0.287
4750	25.99	25.87	25.87	25.86	36.58	36.64	36.73	36.74	36.27	36.31	36.61	36.53	10.75	0.286	0.286
5000	25.87	25.79	25.74	25.75	36.48	36.52	36.65	36.69	36.15	36.30	36.51	36.46	10.73	0.286	0.287
5250	25.79	25.69	25.63	25.62	36.32	36.38	36.48	36.49	35.99	36.17	36.34	36.29	10.70	0.287	0.288
5500	25.68	25.60	25.54	25.53	36.24	36.28	36.36	36.40	35.96	36.05	36.30	36.22	10.69	0.287	0.288
5670	25.70	25.60	25.54	25.53	36.17	36.22	36.29	36.34	35.86	36.01	36.20	36.14	10.63	0.289	0.289

Table A.17: 3 vol% SiC-EG Nanofluid

Power Input												Liquid Under Test	Date
Main Heater			Cap Heater			Side Heater (Horizontal)			Side Heater (Vertical)				
U (V)	I (A)	Q_{main} (W)	U (V)	I (A)	Q_{cap} (W)	U (V)	I (A)	Q_{side1} (W)	U (V)	I (A)	Q_{side2} (W)		
31	0.306	9.49	8.50	0.29	2.47	20.00	0.663	13.26	7.00	0.20	1.40	3 vol% SiC-EG NF fresh	24-July-04

Time (S)	Cold Plate Temperature (oC)				Hot Plate Temperature (oC)				Side Temperature (oC)		Cap Temperature (oC)		dT (°C)	Thermal Conductivity (W/m-k)	
	T_{outer1}	T_{inner1}	T_{outer2}	T_{inner2}	T_{lower1}	T_{lower2}	T_{upper1}	T_{upper2}	T_{side1}	T_{side2}	T_{cap1}	T_{cap2}		K	Ke
	103(°C)	104(°C)	105(°C)	106(°C)	107(°C)	108(°C)	109(°C)	110(°C)	113(°C)	114(°C)	115(°C)	116(°C)			
0	22.72	22.71	22.72	22.72	22.93	22.91	22.98	22.97	23.13	23.05	23.28	23.24	0.20	15.057	15.414
250	23.52	23.48	23.48	23.49	27.90	27.96	26.69	26.69	27.48	28.19	25.99	26.02	4.45	0.691	0.701
500	24.26	24.21	24.21	24.20	30.53	30.57	29.78	29.80	29.90	30.60	28.82	28.83	6.34	0.484	0.490
750	24.80	24.73	24.73	24.74	32.25	32.26	31.77	31.80	31.50	32.14	30.86	30.85	7.51	0.409	0.412
1000	25.17	25.08	25.08	25.08	33.35	33.38	33.09	33.13	32.69	33.12	32.34	32.34	8.29	0.371	0.373
1250	25.52	25.43	25.42	25.43	34.18	34.20	34.03	34.06	33.64	33.78	33.47	33.43	8.76	0.351	0.353
1500	25.77	25.68	25.66	25.68	34.72	34.73	34.63	34.67	34.27	34.42	34.21	34.19	9.05	0.339	0.341
1750	25.97	25.86	25.86	25.86	35.09	35.13	35.09	35.12	34.72	34.81	34.76	34.74	9.25	0.332	0.334
2000	26.06	25.97	25.95	25.98	35.42	35.43	35.41	35.48	35.06	35.15	35.20	35.15	9.45	0.325	0.326
2250	26.12	26.04	26.00	26.02	35.62	35.63	35.66	35.71	35.27	35.32	35.48	35.46	9.59	0.320	0.321
2500	26.12	26.02	25.98	25.99	35.72	35.70	35.80	35.81	35.40	35.51	35.65	35.61	9.71	0.316	0.318
2750	26.16	26.08	26.05	26.04	35.78	35.79	35.86	35.90	35.48	35.51	35.77	35.72	9.72	0.316	0.317
3000	26.13	26.04	26.02	26.04	35.84	35.84	35.94	35.98	35.57	35.50	35.89	35.81	9.80	0.313	0.314
3250	26.17	26.07	26.05	26.07	35.89	35.90	35.99	36.02	35.60	35.66	35.93	35.89	9.82	0.313	0.314
3500	26.14	26.05	26.03	26.04	35.88	35.90	35.98	36.02	35.62	35.62	35.94	35.89	9.84	0.312	0.313
3750	26.15	26.06	26.04	26.05	35.89	35.90	35.99	36.05	35.65	35.72	35.97	35.91	9.84	0.312	0.313
4000	26.15	26.07	26.04	26.04	35.89	35.91	35.99	36.03	35.59	35.69	35.97	35.91	9.84	0.312	0.313
4250	26.10	26.02	26.01	26.01	35.88	35.89	35.98	36.03	35.59	35.71	35.96	35.93	9.86	0.311	0.312
4500	26.09	26.00	25.99	26.00	35.83	35.85	35.94	35.98	35.61	35.57	35.92	35.88	9.84	0.312	0.313
4750	26.19	26.14	26.09	26.11	35.87	35.90	35.98	36.02	35.64	35.76	35.97	35.93	9.76	0.315	0.316
5000	26.10	26.01	25.97	25.99	35.90	35.90	36.00	36.05	35.62	35.64	35.96	35.90	9.90	0.310	0.311
5250	26.09	25.97	25.94	25.95	35.85	35.87	35.98	36.02	35.56	35.54	35.93	35.87	9.90	0.310	0.311
5500	26.03	25.94	25.89	25.93	35.83	35.84	35.94	35.98	35.53	35.69	35.91	35.84	9.90	0.310	0.311
5750	26.01	25.91	25.90	25.88	35.82	35.81	35.92	35.97	35.49	35.61	35.88	35.83	9.92	0.310	0.311
6000	26.01	25.91	25.89	25.91	35.80	35.81	35.90	35.93	35.51	35.60	35.86	35.81	9.89	0.311	0.312

Table B.1: DK48R1 flow meter calibration (coolant: D.I. water)

Flow Meter Reading (L/min)	Volume (ml)	Time (sec)
0.1	78.5	65.7
0.2	154	58
0.3	212	53.2
0.4	255	46.3
0.502	274	38.8
0.6	346	40.2
0.7	309	30.4
0.8	326	27.6

The linear regression model fitted for flowrate correction is $y = 0.9089x - 0.0268$

where, x is the flow meter reading and y is the corrected flow rate.

Table B.2: Thermal diodes calibration

Temperature from Oven Reading(^{o}C)	Data Logger Calibrated Temperature (^{o}C)	U1 diode (V)	U2 diode (V)	U3 diode (V)	U4 diode (V)
30	31.5	3.5382	3.5378	3.5376	3.5381
40	41.3	3.4482	3.4478	3.4477	3.4480
50	51.3	3.3573	3.3570	3.3570	3.3573
60	61.2	3.2666	3.2664	3.2663	3.2666
70	71.0	3.1758	3.1756	3.1755	3.1758
80	80.7	3.0850	3.0849	3.0848	3.0850
90	90.5	2.9940	2.9938	2.9937	2.9938
100	100.1	2.9031	2.9030	2.9030	2.9032

Thermal diodes	Equation of Calibration Curve
U1	$T_1 = -108.1U_1 + 414.14$
U2	$T_2 = -108.15U_2 + 414.29$
U3	$T_3 = -108.17U_3 + 414.33$
U4	$T_4 = -108.12U_4 + 414.20$

Note: T --diode temperature, U --diode voltage.

Table B.3 MCHS experimental results (coolant: D.I. water)

Flowrate (l/min)	U1 (V)	T1 (oC)	U2 (V)	T2 (oC)	U3 (V)	T3 (oC)	U4 (V)	T4 (oC)	T_{chip} (oC)	Δp (mbar)	T_r (oC)	T_{hi} (oC)	T_{HEo} (oC)	T_a (oC)	ΔTjr (oC)	ΔTji (oC)	ΔTja (oC)	Rjr (oC/W)	Rji (oC/W)	Rja (oC/W)	Heating Power (W)
0.072	3.381	48.6	3.384	48.2	3.315	55.6	3.310	56.3	52.2	4.7	23.5	23.9	23.4	21.3	28.7	28.2	30.9	0.481	0.474	0.518	59.627
	3.380	48.7	3.382	48.4	3.314	55.7	3.310	56.2	52.3	4.9	24.0	24.2	23.0	21.1	28.3	28.0	31.2	0.474	0.470	0.523	59.627
	3.382	48.5	3.385	48.1	3.316	55.5	3.310	56.2	52.1	4.8	23.7	23.8	22.9	20.8	28.4	28.2	31.3	0.475	0.473	0.524	59.694
	3.381	48.6	3.385	48.1	3.316	55.6	3.310	56.2	52.1	4.8	23.6	23.9	23.3	21.3	28.5	28.2	30.9	0.479	0.473	0.518	59.627
0.159	3.406	45.9	3.407	45.7	3.357	51.1	3.359	51.0	48.4	11.0	25.6	25.4	25.7	22.9	22.9	23.0	25.6	0.383	0.385	0.428	59.76
	3.403	46.2	3.403	46.1	3.354	51.5	3.355	51.4	48.8	11.0	25.9	25.6	25.0	21.1	22.9	23.2	27.7	0.383	0.388	0.464	59.76
	3.406	45.9	3.406	45.9	3.356	51.3	3.357	51.2	48.5	11.1	25.5	25.3	24.6	21.5	23.1	23.2	27.1	0.386	0.389	0.453	59.76
	3.409	45.6	3.409	45.5	3.360	50.8	3.360	50.8	48.2	11.1	25.2	24.9	24.3	21.4	23.0	23.2	26.8	0.385	0.389	0.448	59.76
0..239	3.421	44.3	3.421	44.2	3.376	49.1	3.379	48.8	46.6	19.7	25.3	25.0	25.6	22.2	21.3	21.6	24.4	0.356	0.360	0.408	59.826
	3.407	45.8	3.417	44.6	3.372	49.5	3.374	49.3	47.3	19.5	25.8	25.6	26.2	23.0	21.5	21.7	24.3	0.360	0.363	0.407	59.826
	3.416	44.8	3.415	44.8	3.370	49.7	3.373	49.4	47.2	19.5	25.8	25.5	25.2	21.3	21.4	21.7	25.9	0.358	0.362	0.433	59.826
	3.418	44.6	3.418	44.5	3.374	49.3	3.377	49.0	46.8	19.6	25.5	25.1	25.1	21.0	21.3	21.7	25.9	0.357	0.363	0.432	59.826
0.330	3.421	44.3	3.421	44.2	3.377	49.0	3.380	48.7	46.5	29.4	26.0	25.8	26.5	22.9	20.6	20.7	23.7	0.344	0.346	0.396	59.826
	3.418	44.6	3.418	44.5	3.374	49.3	3.377	49.0	46.9	29.3	26.3	25.9	26.2	22.1	20.6	20.9	24.8	0.344	0.350	0.414	59.826
	3.423	44.1	3.423	44.0	3.379	48.8	3.382	48.4	46.3	29.6	25.5	25.3	25.3	20.7	20.8	21.0	25.6	0.348	0.351	0.429	59.826
	3.427	43.6	3.427	43.5	3.383	48.3	3.386	48.0	45.9	29.9	25.1	24.8	25.0	20.4	20.8	21.0	25.5	0.347	0.352	0.426	59.826
0.424	3.436	42.6	3.436	42.6	3.393	47.3	3.397	46.9	44.8	40.8	24.7	24.4	24.9	21.2	20.2	20.4	23.7	0.337	0.341	0.395	59.893
	3.432	43.1	3.432	43.0	3.390	47.6	3.393	47.3	45.2	40.5	25.2	24.9	25.8	22.7	20.0	20.3	22.6	0.335	0.339	0.377	59.893
	3.428	43.5	3.428	43.4	3.385	48.1	3.389	47.8	45.7	40.4	25.6	25.2	25.5	20.6	20.1	20.5	25.1	0.336	0.342	0.420	59.826
	3.432	43.1	3.432	43.0	3.388	47.7	3.392	47.4	45.3	40.6	25.2	24.9	25.5	21.3	20.1	20.4	24.1	0.336	0.341	0.402	59.893
0.516	3.438	42.4	3.438	42.4	3.396	46.9	3.399	46.6	44.6	53.9	24.8	24.6	25.3	21.5	19.8	20.0	23.1	0.331	0.333	0.386	59.893
	3.437	42.5	3.437	42.4	3.395	47.0	3.399	46.7	44.6	53.8	24.9	24.6	25.3	21.4	19.8	20.0	23.3	0.330	0.334	0.389	59.893
	3.437	42.5	3.437	42.4	3.395	47.0	3.398	46.7	44.7	53.9	24.9	24.7	25.4	21.6	19.8	19.9	23.1	0.330	0.333	0.386	59.893

	3.438	42.5	3.438	42.4	3.395	47.0	3.399	46.7	44.6	53.9	24.8	24.6	25.1	21.5	19.9	20.0	23.2	0.331	0.334	0.387	59.893
0.610	3.441	42.0	3.441	42.0	3.400	46.5	3.403	46.2	44.2	68.4	24.7	24.5	25.1	21.0	19.5	19.7	23.2	0.326	0.328	0.388	59.893
	3.440	42.2	3.441	42.1	3.399	46.6	3.402	46.3	44.3	68.3	24.8	24.5	25.1	21.1	19.5	19.7	23.2	0.325	0.330	0.387	59.893
	3.440	42.2	3.440	42.1	3.399	46.6	3.402	46.3	44.3	68.2	24.8	24.6	25.2	21.4	19.5	19.7	22.9	0.326	0.328	0.383	59.893
	3.440	42.2	3.440	42.1	3.399	46.6	3.402	46.3	44.3	68.3	24.8	24.5	25.1	21.3	19.5	19.7	23.0	0.325	0.330	0.384	59.893
0.709	3.442	42.0	3.442	41.9	3.401	46.4	3.404	46.1	44.1	84.0	24.9	24.7	25.2	21.4	19.2	19.4	22.7	0.321	0.323	0.379	59.893
	3.442	41.9	3.442	41.9	3.402	46.3	3.405	46.0	44.0	84.0	24.8	24.6	25.1	21.5	19.2	19.4	22.6	0.321	0.324	0.377	59.893
	3.444	41.8	3.444	41.7	3.403	46.1	3.406	45.8	43.9	84.2	24.6	24.4	24.9	21.4	19.3	19.4	22.5	0.322	0.324	0.375	59.893
	3.443	41.9	3.443	41.9	3.402	46.3	3.405	46.0	44.0	84.0	24.8	24.6	25.2	21.9	19.2	19.4	22.1	0.321	0.324	0.370	59.893

Table B.4 MCHS experimental results (coolant: 0.7vol% Al_2O_3-water nanofluid)

Flowrate (l/min)	U1 (V)	T1 (oC)	U2 (V)	T2 (oC)	U3 (V)	T3 (oC)	U4 (V)	T4 (oC)	T_{chip} (oC)	Δp (mbar)	T_r (oC)	T_{hi} (oC)	T_{HEo} (oC)	T_a (oC)	ΔTjr (oC)	ΔTji (oC)	ΔTja (oC)	Rjr (oC/W)	Rji (oC/W)	Rja (oC/W)	Heating Power (W)
0.072	3.411	45.9	3.387	48.4	3.336	54.0	3.363	51.0	49.8	5.3	24.2	23.6	36.4	22.6	25.6	26.2	27.2	0.424	0.434	0.450	60.424
	3.409	46.1	3.385	48.6	3.333	54.3	3.361	51.3	50.1	5.3	24.2	24.0	36.9	21.6	25.9	26.1	28.5	0.428	0.432	0.471	
	3.417	45.2	3.393	47.8	3.340	53.5	3.368	50.5	49.2	5.4	23.5	23.2	36.1	20.9	25.7	26.0	28.3	0.426	0.431	0.469	
	3.416	45.3	3.392	47.9	3.339	53.6	3.367	50.6	49.4	5.4	23.8	23.2	35.8	22.6	25.6	26.2	26.8	0.423	0.433	0.443	
0.159	3.429	43.9	3.410	45.9	3.377	49.5	3.399	47.1	46.6	12.0	25.6	25.4	30.7	22.4	21.0	21.2	24.2	0.347	0.351	0.400	
	3.432	43.6	3.413	45.6	3.379	49.2	3.402	46.8	46.3	12.1	24.9	24.7	30.5	21.4	21.4	21.6	24.9	0.354	0.358	0.412	
	3.431	43.7	3.412	45.7	3.379	49.3	3.401	46.9	46.4	12.1	25.3	24.8	30.5	22.5	21.1	21.6	23.9	0.349	0.357	0.395	
	3.429	43.9	3.411	45.9	3.377	49.5	3.400	47.1	46.6	12.1	25.4	25.2	30.9	22.0	21.2	21.4	24.6	0.351	0.354	0.407	
0..239	3.438	42.9	3.422	44.6	3.395	47.6	3.415	45.4	45.1	20.3	25.3	24.9	28.6	21.1	19.8	20.2	24.0	0.328	0.335	0.398	
	3.444	42.3	3.427	44.0	3.399	47.1	3.420	44.9	44.6	20.9	24.9	24.6	28.1	21.8	19.7	20.0	22.8	0.326	0.331	0.377	
	3.438	42.9	3.422	44.7	3.394	47.6	3.415	45.4	45.2	20.9	25.5	25.1	28.5	22.1	19.7	20.1	23.1	0.325	0.332	0.382	
	3.435	43.3	3.418	45.0	3.390	48.0	3.411	45.8	45.5	20.0	25.8	25.6	29.3	21.6	19.7	19.9	23.9	0.327	0.330	0.396	
0.330	3.434	43.4	3.418	45.0	3.392	47.9	3.412	45.7	45.5	29.2	26.0	25.8	28.4	21.8	19.5	19.7	23.7	0.323	0.326	0.392	
	3.442	42.5	3.426	44.2	3.400	47.0	3.420	44.9	44.6	29.9	25.5	25.3	27.9	21.8	19.1	19.3	22.8	0.317	0.320	0.378	
	3.443	42.4	3.427	44.1	3.401	46.8	3.421	44.7	44.5	30.3	25.4	25.1	27.7	21.4	19.1	19.4	23.1	0.316	0.321	0.382	
0.424	3.452	41.4	3.436	43.1	3.411	45.8	3.431	43.7	43.5	39.6	24.8	24.5	26.7	21.2	18.7	19.0	22.3	0.309	0.314	0.369	
	3.450	41.7	3.434	43.3	3.409	46.0	3.429	43.9	43.7	39.5	24.9	24.7	26.7	20.9	18.8	19.0	22.8	0.312	0.315	0.378	
	3.451	41.5	3.435	43.2	3.410	45.9	3.429	43.8	43.6	39.6	25.0	24.7	26.6	21.3	18.6	18.9	22.3	0.308	0.313	0.369	
	3.451	41.5	3.436	43.1	3.411	45.8	3.430	43.7	43.5	39.7	24.8	24.6	26.6	21.2	18.7	18.9	22.3	0.310	0.313	0.370	
0.516	3.451	41.5	3.436	43.1	3.412	45.7	3.431	43.7	43.5	49.7	25.2	25.0	26.6	21.2	18.3	18.5	22.3	0.303	0.306	0.369	
	3.452	41.4	3.437	43.0	3.413	45.6	3.432	43.6	43.4	49.8	24.9	24.8	26.4	21.2	18.5	18.6	22.2	0.306	0.308	0.367	
	3.448	41.8	3.433	43.4	3.409	46.0	3.428	44.0	43.8	49.6	25.4	25.1	26.9	21.8	18.4	18.7	22.0	0.305	0.309	0.364	
0.610	3.441	42.6	3.426	44.2	3.402	46.8	3.421	44.8	44.6	48.9	26.2	26.0	27.6	23.0	18.4	18.6	21.6	0.304	0.307	0.357	
	3.444	42.2	3.429	43.9	3.405	46.5	3.424	44.4	44.2	60.7	26.0	25.8	27.2	22.3	18.2	18.4	21.9	0.302	0.305	0.363	

	3.441	42.6	3.426	44.2	3.402	46.8	3.421	44.7	44.6	60.6	26.4	26.1	27.6	22.5	18.2	18.5	22.1	0.301	0.306	0.365	
	3.450	41.6	3.435	43.2	3.411	45.7	3.430	43.7	43.6	61.7	25.3	25.1	26.6	21.2	18.3	18.5	22.4	0.302	0.306	0.370	
0.709	3.452	41.4	3.437	43.0	3.413	45.6	3.432	43.6	43.4	61.8	25.3	25.0	26.5	21.6	18.1	18.4	21.8	0.300	0.305	0.361	
	3.445	42.2	3.406	46.3	3.381	49.0	3.426	44.2	45.4	76.6	25.0	24.9	26.2	21.2	20.4	20.5	24.2	0.338	0.340	0.401	
	3.455	41.1	3.440	42.7	3.415	45.4	3.435	43.2	43.1	74.6	25.0	24.7	26.1	21.2	18.1	18.4	21.9	0.300	0.305	0.362	
	3.454	41.1	3.439	42.8	3.415	45.4	3.435	43.2	43.1	74.5	25.2	25.0	26.2	21.6	17.9	18.1	21.5	0.297	0.300	0.356	

Table B.5 MCHS experimental results (coolant: 2vol% Al_2O_3-water nanofluid)

Flowrate (l/min)	U1 (V)	T1 (oC)	U2 (V)	T2 (oC)	U3 (V)	T3 (oC)	U4 (V)	T4 (oC)	T_{chip} (oC)	Δp (mbar)	T_r (oC)	T_{hi} (oC)	T_{HEo} (oC)	T_a (oC)	ΔTjr (oC)	ΔTji (oC)	ΔTja (oC)	Rjr (oC/W)	Rji (oC/W)	Rja (oC/W)	Heating Power (W)
0.256	3.422	44.2	3.420	44.3	3.404	46.0	3.404	46.1	45.2	54.5	26.5	26.4	26.4	21.5	18.7	18.7	23.7	0.312	0.313	0.395	59.893
	3.427	43.6	3.425	43.7	3.409	45.5	3.409	45.5	44.6	54.5	26.0	25.9	26.2	22.4	18.6	18.7	22.2	0.311	0.312	0.371	59.893
	3.421	44.3	3.419	44.4	3.403	46.1	3.404	46.1	45.2	53.4	26.6	26.4	26.8	22.9	18.7	18.8	22.4	0.311	0.314	0.373	59.893
0.344	3.432	43.1	3.430	43.2	3.416	44.8	3.415	44.9	44.0	69.4	26.1	26.0	26.7	22.6	17.9	18.0	21.4	0.299	0.300	0.358	59.893
	3.429	43.4	3.427	43.5	3.413	45.1	3.412	45.2	44.3	69.2	26.2	26.2	26.6	22.1	18.1	18.1	22.2	0.303	0.302	0.371	59.893
	3.436	42.7	3.434	42.8	3.420	44.3	3.419	44.5	43.6	70.4	25.6	25.5	25.9	20.9	18.0	18.0	22.7	0.300	0.301	0.379	59.893
	3.439	42.4	3.437	42.4	3.423	44.0	3.422	44.1	43.2	70.9	25.2	25.2	25.7	21.6	18.1	18.0	21.7	0.301	0.301	0.362	59.893
0.415	3.441	42.1	3.440	42.1	3.426	43.6	3.425	43.8	42.9	81.6	25.5	25.3	25.9	21.6	17.4	17.6	21.4	0.291	0.293	0.356	59.959
	3.437	42.5	3.436	42.6	3.421	44.2	3.420	44.3	43.4	81.6	25.9	25.8	26.4	22.4	17.5	17.6	21.0	0.293	0.293	0.351	59.893
	3.433	42.9	3.432	43.0	3.418	44.5	3.418	44.6	43.7	81.3	26.3	26.1	26.7	22.7	17.5	17.6	21.1	0.292	0.294	0.352	59.893
	3.432	43.0	3.431	43.1	3.418	44.5	3.417	44.7	43.8	81.5	26.0	25.9	26.3	20.7	17.8	17.9	23.1	0.298	0.299	0.386	59.893
0.583	3.445	41.7	3.444	41.7	3.429	43.3	3.429	43.4	42.5	97.4	25.4	25.1	25.6	21.1	17.1	17.4	21.5	0.286	0.290	0.358	59.959
	3.448	41.4	3.447	41.4	3.432	43.0	3.432	43.1	42.2	98.9	25.1	24.8	25.4	21.4	17.1	17.4	20.8	0.286	0.290	0.348	59.959
	3.439	42.3	3.438	42.3	3.424	43.9	3.424	44.0	43.1	97.5	26.1	25.9	26.5	22.5	17.0	17.2	20.7	0.284	0.287	0.344	59.959
	3.435	42.7	3.434	42.8	3.419	44.4	3.419	44.5	43.6	97.8	26.5	26.3	26.9	22.7	17.1	17.3	20.9	0.286	0.288	0.349	59.893
0.664	3.449	41.2	3.448	41.2	3.434	42.8	3.433	42.9	42.0	110.5	25.2	24.9	25.4	21.1	16.9	17.1	21.0	0.281	0.285	0.350	59.959
	3.450	41.1	3.449	41.2	3.434	42.8	3.434	42.9	42.0	110.9	25.2	25.0	25.6	22.0	16.8	16.9	20.0	0.280	0.283	0.334	59.959
	3.445	41.7	3.444	41.7	3.429	43.3	3.429	43.4	42.5	110.3	25.7	25.5	26.2	22.5	16.8	17.0	20.1	0.281	0.284	0.335	59.959
	3.440	42.2	3.439	42.2	3.424	43.8	3.424	44.0	43.1	108.7	26.2	26.0	26.7	22.8	16.9	17.0	20.3	0.282	0.284	0.338	59.959
0.753	3.444	41.7	3.444	41.7	3.430	43.3	3.429	43.4	42.5	123.5	25.9	25.7	26.2	22.3	16.6	16.8	20.3	0.277	0.280	0.337	60.026
	3.442	42.0	3.441	42.0	3.426	43.6	3.425	43.8	42.9	123.6	26.2	26.0	26.5	22.7	16.7	16.9	20.2	0.278	0.281	0.337	60.026
	3.439	42.3	3.439	42.3	3.424	43.9	3.423	44.0	43.1	123.6	26.5	26.4	26.8	22.8	16.6	16.7	20.4	0.277	0.278	0.339	60.026
	3.445	41.7	3.445	41.6	3.430	43.2	3.429	43.3	42.4	125.1	25.7	25.4	25.9	21.3	16.8	17.0	21.2	0.279	0.284	0.353	60.026

Table B.6 MCHS experimental results (coolant: 3vol% Al_2O_3-water nanofluid)

Flowrate (l/min)	U1 (V)	T1 (oC)	U2 (V)	T2 (oC)	U3 (V)	T3 (oC)	U4 (V)	T4 (oC)	T_{chip} (oC)	Δp (mbar)	T_r (oC)	T_{hi} (oC)	T_{HEo} (oC)	T_a (oC)	ΔTjr (oC)	ΔTji (oC)	ΔTja (oC)	Rjr (oC/W)	Rji (oC/W)	Rja (oC/W)	Heating Power (W)
0.227	3.396	47.0	3.399	46.6	3.398	46.7	3.396	47.0	46.8	70.8	26.2	26.2	26.6	21.4	20.6	20.6	25.4	0.345	0.344	0.425	59.826
	3.395	47.1	3.399	46.6	3.397	46.8	3.396	47.0	46.8	72.1	26.3	26.3	26.5	21.5	20.6	20.5	25.4	0.345	0.344	0.425	59.694
	3.394	47.2	3.398	46.7	3.396	46.9	3.395	47.1	47.0	71.2	26.5	26.5	26.8	21.8	20.5	20.4	25.2	0.343	0.342	0.422	59.694
0.354	3.397	46.9	3.400	46.4	3.412	45.1	3.405	45.9	46.1	84.9	28.2	28.0	27.0	22.8	17.9	18.1	23.3	0.300	0.302	0.390	59.826
	3.395	47.1	3.399	46.6	3.411	45.3	3.403	46.2	46.3	85.9	28.3	28.1	26.7	22.6	18.0	18.2	23.7	0.301	0.304	0.397	59.826
	3.401	46.4	3.405	45.9	3.417	44.7	3.409	45.5	45.6	88.8	27.6	27.3	25.9	21.5	18.1	18.3	24.2	0.302	0.306	0.404	59.893
	3.406	45.9	3.410	45.3	3.422	44.1	3.414	45.0	45.1	90.4	27.1	26.9	25.8	22.0	18.0	18.2	23.1	0.301	0.303	0.386	59.893
0.482	3.417	44.7	3.417	44.6	3.428	43.4	3.424	43.9	44.2	98.4	27.1	27.0	26.2	21.9	17.1	17.1	22.3	0.285	0.286	0.372	59.893
	3.414	45.0	3.414	44.9	3.424	43.8	3.421	44.3	44.5	97.9	27.5	27.3	26.4	22.4	17.0	17.2	22.1	0.285	0.287	0.370	59.893
	3.409	45.5	3.409	45.4	3.420	44.3	3.417	44.7	45.0	97.2	28.1	27.8	27.0	22.9	16.9	17.2	22.1	0.283	0.287	0.369	59.893
	3.414	45.1	3.413	45.0	3.424	43.9	3.421	44.3	44.6	97.6	27.5	27.1	26.0	21.4	17.1	17.4	23.2	0.285	0.291	0.387	59.893
0.595	3.421	44.2	3.421	44.2	3.434	42.8	3.432	43.0	43.6	109.4	27.1	26.8	27.0	23.1	16.5	16.7	20.5	0.275	0.279	0.342	59.959
	3.419	44.4	3.419	44.4	3.432	43.1	3.430	43.3	43.8	108.6	27.2	27.0	27.1	22.8	16.6	16.8	21.0	0.278	0.280	0.351	59.893
	3.427	43.7	3.426	43.7	3.438	42.3	3.437	42.5	43.0	111.2	26.4	26.2	26.1	21.5	16.7	16.8	21.6	0.278	0.281	0.360	59.959
	3.431	43.1	3.431	43.1	3.443	41.8	3.442	42.0	42.5	112.4	25.9	25.7	25.8	21.8	16.6	16.8	20.7	0.277	0.280	0.346	59.959
0.679	3.431	43.2	3.430	43.2	3.443	41.8	3.441	42.1	42.6	121.4	26.3	26.0	26.2	22.5	16.3	16.6	20.1	0.272	0.276	0.336	59.959
	3.426	43.7	3.426	43.7	3.439	42.2	3.438	42.4	43.0	121.2	26.7	26.5	26.5	22.8	16.3	16.5	20.2	0.272	0.275	0.338	59.959
	3.424	44.0	3.423	44.0	3.436	42.6	3.435	42.8	43.3	120.7	27.0	26.8	26.8	23.0	16.3	16.5	20.3	0.272	0.275	0.339	59.959
	3.422	44.1	3.422	44.1	3.435	42.7	3.434	42.9	43.5	120.5	27.1	26.9	26.9	22.9	16.4	16.5	20.6	0.273	0.276	0.343	59.959
0.777	3.425	43.8	3.425	43.8	3.435	42.7	3.433	42.9	43.3	135.8	27.0	26.9	26.7	22.3	16.3	16.4	21.0	0.272	0.273	0.351	60.026
	3.431	43.2	3.430	43.2	3.440	42.1	3.439	42.3	42.7	137.8	26.3	26.1	26.1	21.2	16.4	16.6	21.5	0.274	0.276	0.359	60.026
	3.434	42.8	3.434	42.8	3.445	41.6	3.443	41.8	42.3	139.1	26.0	25.8	25.7	21.3	16.3	16.5	21.0	0.272	0.274	0.350	60.026
	3.432	43.1	3.432	43.0	3.443	41.9	3.441	42.1	42.5	138.8	26.3	26.2	26.2	22.2	16.2	16.3	20.3	0.270	0.271	0.339	60.026

Table B.7 MCHS experimental results (coolant: 1vol% SiC-water nanofluid)

Flowrate (l/min)	U1 (V)	T1 (oC)	U2 (V)	T2 (oC)	U3 (V)	T3 (oC)	U4 (V)	T4 (oC)	T_{chip} (oC)	Δp (mbar)	T_r (oC)	T_{hi} (oC)	T_{HEo} (oC)	T_a (oC)	ΔTjr (oC)	ΔTji (oC)	ΔTja (oC)	Rjr (oC/W)	Rji (oC/W)	Rja (oC/W)	Heating Power (W)
0.862	3.449	41.2	3.450	41.0	3.449	41.2	3.452	40.9	41.1	125.1	24.3	24.4	25.7	20.9	16.7	16.6	20.2	0.279	0.277	0.336	60.0256
	3.451	41.0	3.452	40.8	3.450	41.0	3.453	40.7	40.9	125.2	24.1	24.2	25.5	21.0	16.8	16.7	19.9	0.279	0.278	0.332	
	3.451	41.0	3.452	40.8	3.450	41.0	3.454	40.7	40.9	125.8	24.1	24.2	25.5	20.7	16.8	16.7	20.2	0.279	0.278	0.337	
	3.452	40.9	3.453	40.7	3.451	40.9	3.455	40.6	40.8	125.7	24.0	24.1	25.4	20.6	16.7	16.6	20.2	0.279	0.277	0.337	
0.698	3.446	41.5	3.449	41.2	3.445	41.6	3.449	41.2	41.4	93.2	24.4	24.4	25.9	20.9	16.9	16.9	20.5	0.282	0.282	0.341	
	3.448	41.3	3.451	41.0	3.447	41.4	3.451	41.0	41.2	93.7	24.2	24.2	25.7	20.6	16.9	17.0	20.6	0.282	0.283	0.344	
	3.448	41.3	3.451	41.0	3.447	41.4	3.451	41.0	41.2	93.3	24.2	24.2	25.7	20.9	16.9	17.0	20.3	0.282	0.283	0.339	
	3.445	41.7	3.447	41.4	3.443	41.8	3.447	41.5	41.6	92.9	24.7	24.7	26.2	22.2	16.8	16.9	19.4	0.281	0.281	0.324	
0.532	3.434	42.9	3.436	42.5	3.432	43.0	3.436	42.6	42.8	63.4	25.5	25.4	27.3	21.7	17.3	17.3	21.1	0.289	0.289	0.352	
	3.436	42.6	3.439	42.3	3.435	42.7	3.439	42.3	42.5	64.0	25.1	25.1	27.0	21.5	17.3	17.4	21.0	0.289	0.289	0.350	
	3.437	42.5	3.439	42.3	3.435	42.7	3.439	42.3	42.4	63.3	25.0	25.0	26.9	21.1	17.4	17.4	21.4	0.290	0.290	0.356	
	3.441	42.1	3.443	41.8	3.439	42.3	3.442	41.9	42.0	64.3	24.6	24.6	26.5	20.9	17.4	17.4	21.2	0.290	0.290	0.353	
0.389	3.431	43.1	3.433	42.8	3.428	43.5	3.432	43.1	43.1	42.4	25.3	25.1	27.6	20.9	17.9	18.0	22.3	0.298	0.300	0.371	
	3.434	42.9	3.436	42.6	3.431	43.2	3.435	42.8	42.8	42.6	24.9	24.9	27.4	21.3	17.9	17.9	21.6	0.298	0.298	0.359	
	3.436	42.7	3.438	42.4	3.432	43.0	3.437	42.5	42.6	42.8	24.8	24.7	27.2	21.4	17.8	17.9	21.3	0.296	0.298	0.354	
	3.437	42.5	3.439	42.2	3.434	42.8	3.438	42.4	42.5	42.9	24.6	24.5	27.0	21.4	17.8	18.0	21.1	0.297	0.299	0.352	
0.247	3.420	44.3	3.422	44.1	3.414	45.0	3.419	44.5	44.5	25.8	26.0	25.7	29.4	23.0	18.5	18.7	21.5	0.308	0.312	0.358	
	3.423	44.1	3.424	43.8	3.416	44.7	3.421	44.2	44.2	26.1	25.5	25.3	29.0	21.7	18.8	18.9	22.5	0.313	0.315	0.376	
	3.429	43.4	3.430	43.2	3.422	44.1	3.427	43.7	43.6	26.1	24.8	24.7	28.5	21.3	18.8	18.9	22.3	0.312	0.314	0.372	
	3.431	43.2	3.433	42.9	3.424	43.8	3.429	43.4	43.3	26.4	24.6	24.4	28.2	21.3	18.7	18.9	22.0	0.311	0.315	0.367	
0.106	3.422	44.2	3.423	44.0	3.404	46.1	3.409	45.5	44.9	10.8	23.4	23.1	31.2	20.8	21.5	21.8	24.2	0.358	0.363	0.403	
	3.422	44.2	3.423	44.0	3.403	46.1	3.409	45.6	45.0	10.8	23.4	23.2	31.2	20.9	21.5	21.7	24.1	0.358	0.362	0.401	
	3.422	44.1	3.423	43.9	3.404	46.1	3.409	45.5	44.9	10.8	23.3	23.1	31.1	20.8	21.6	21.8	24.1	0.359	0.363	0.402	
	3.422	44.1	3.424	43.9	3.404	46.0	3.410	45.5	44.9	10.8	23.3	23.1	31.0	21.4	21.5	21.7	23.5	0.359	0.362	0.392	

0.071	3.381	48.6	3.381	48.5	3.355	51.3	3.359	50.9	49.8	6.3	23.3	23.2	36.1	21.7	26.5	26.6	28.2	0.441	0.443	0.469
	3.381	48.6	3.381	48.6	3.354	51.4	3.361	50.7	49.8	6.2	23.2	23.0	36.0	21.3	26.6	26.8	28.5	0.443	0.446	0.476
	3.383	48.4	3.382	48.5	3.359	50.9	3.362	50.6	49.6	6.0	23.0	22.8	35.9	21.0	26.5	26.7	28.6	0.442	0.446	0.477
	3.382	48.4	3.382	48.4	3.357	51.1	3.361	50.7	49.7	6.1	22.9	22.7	35.8	21.1	26.7	26.9	28.6	0.445	0.449	0.476

Appendix C: Experimental Procedures of Nanofluids Thermal Conductivity Characterization

I. System Assembly

- Assemble the apparatus following the schematic of the apparatus setup.
- All the thermocouples should be properly installed according to the apparatus setup and tested to be in good function.
- Carefully adjust the seat and support of the apparatus to ensure its horizontality.
- Connect the pipes, pump, compact heat exchanger and the cooling slab of the thermal conductivity measurement apparatus following the schematic of the experimental setup.
- Conduct hydraulic testing and solve all the leakage problems before testing.
- Connect all the thermocouples to the Agilent 34970A data logger for temperature measurement. The software (Benchlink) for data logger should be properly installed and the communication protocol of computer and data logger should be set to RS232.

II. Power Supply Connection

1) Connect Keithley 228A voltage/current source to the main heater for heating power supply.
2) Connect TTi PL330 power supply (1) to the side compensate horizontal heater.
3) Connect Topward TPS-4000 power supply to the side vertical guard heater.
4) Connect TTi TSX1820P power supply to the top guard heater.
5) Connect TTi PL330 power supply (2) to the HG0024 micro pump (24V DC) and the heat exchanger fans (230V DC).
6) Keep all the power supply off during the preparation. The power input for different fluid varies. The recommended power inputs are given in Table A.1 of Appendix A.

III. Sample Loading

1) Calculate the sample volume to be added according to the thickness of the PTFE spacer used. The fluid sample volume for the 1mm and 2mm thick spacers can be 15ml and 20ml, respectively. Overloading of fluid will give rise to measurement inaccuracy.
2) Put fluid sample in apparatus and carefully adjust three spacers in order to make them evenly distributed in the chamber. Gas bubbles are carefully avoided.
3) Put the hotplate in the center of the chamber and adjust the location to avoid its contact with the cell frame.
4) Assemble the cap of the apparatus and tighten using screws. Seal the cap center hole to avoid air circulation between the chamber and the ambient.

IV. Thermal Testing

1) Turn on pump and heat exchanger fans.
2) Turn on the data logger and start its temperature scan.
3) Turn on the power supply for the main heater and other guard heaters.
4) Adjust the heating power of the main heater to maintain enough temperature difference between the cold and hot plates of the apparatus.
5) Adjust the heating power of the guard heaters to minimize the heat loss. The temperature difference among chamber cap, cell frame and the hot plate should be controlled within 0.5^{o}C.
6) The temperature of different locations in the apparatus was monitored at a 10 seconds interval. Each experimental run should be conducted long enough to reach steady state (normally above 70 minutes) and the temperature reading deviation should be controlled to be less than 1%.

7) After the apparatus reaches the steady state and temperature readings are taken, stop the temperature scanning process of the data logger first and then turn off all the heaters.
8) Turn off pump and heat exchanger fans.
9) Take out the sample and clean the apparatus chamber.

Appendix D: Experimental Procedures of Thermal Performance Characterization of Nanofluid-Cooled MCHS Cooling System

I. Power supply connection

- Connect Keithley 228A voltage/current source to thermal test board for heating power supply.
- Connect Keithley 2400 source-meter to thermal test board for measurement of diode forward-bias voltages which can be used to calculate chip temperature.
- Connect power supply to the heat exchanger fans (230V AC), HG0024 micro pump (24V DC) and pressure transducer (16V DC).
- Keep all the power supply off during the preparation.

II. Flow system connection

- Connect the pipes, valves, connectors, filter, flow meter and pump following the schematic of the experimental setup.
- Connect the pressure transducer to main fluid flow tubing through two pressure ports.
- Assemble the MCHS with the Perspex cover plate by screws and connect the inlet and outlet of the cover to the piping system.

III. Hydraulic testing

- Conduct hydraulic testing to check leakage for all the tubes, valves, connectors as well as the O ring seal of MCHS and the inlet, outlet connecters of the MCHS cover.
- Air trapped in the tubes especially the air bubbles in the two tubes connected to the two ports of pressure transducer should be removed to avoid measurement errors.
- The hydraulic testing should be carried out at the allowable highest measurement flowrate by increasing the rotational speed of the pump gradually.
- Leakage issues must be solved before running the thermal testing.

IV. Assembly of the MCHS with the thermal test board

- Apply thermal interface material, either thermal grease or PCM, to the chip of the thermal test board. For thermal grease, put a drop of thermal grease at the center of the chip and spread it out evenly. For PCM, apply a layer of the PCM over the entire chip surface area.
- Manage the tubes and connectors to make a torque-free mounting between the thermal test chip and the MCHS.
- Bolt spring-loaded screws with same spring length to ensure uniform force between the MCHS and thermal test chip. Uneven mounting causes non-event contacts between the chip and heat sink base.

V. Thermal testing

1. Switch on the power supplies to all the test equipment except the Keithley 228A power supply for chip heating. The Keithley 228A power supply should not be activated until a certain flow rate of fluid flow is available.
2. Correct the pressure transducer LCD display value to zero at no flow condition.
3. Switch on the pump and gradually increase to ¾ of the full speed range.
4. Adjust to a flow rate of 0.5 *l*/min and run for 20 minutes to get the initial chip diode readings and thus calculate the chip temperature T_j.
5. Switch on Keithley 228A voltage/current source with a low power supply (eg. Q=20W) to the thermal test chip. Beginning with a low heating power is essential for an unknown thermal interface material and new heat sink design.
6. The following quantities are required to be recorded:
   - Pressure drop ΔP
   - Inlet and outlet temperature T_{in} and T_{out}
   - Heat sink base temperature T_b, when single channel heat sink is under testing

- Ambient temperature T_a
- Diode forward-bias voltages and thus the chip temperature T_j

Procedures for recording temperature and pressure:

The temperature readings had been found to deviate less than 1% after running around 40 minutes at a given flowrate. In view of this, both pressure drop and chip temperatures were first recorded after running the test for the first 20 minutes and then recorded every 5 minutes until steady-state was reached. Usually a total of 3 readings are required to get a set of steady-state readings.

7. Reduce the flow rate to 0.1 *l*/min and increase the flowrate with a step increment of 0.1 *l*/min till the maximum flowrate of 1.0 *l*/min is reached. Record the temperature readings following the procedure mentioned above for each increment.
8. Increase the heating power by around 20W and record the thermal data readings as mentioned in steps 6 and 7, until the heating power limitation is reached for the thermal test chip.
9. Switch off all the equipments and the power supplies. The power supply for the heating of chip, Keithley 228A, must be deactivated first.
10. End of experiment.